Brain tumors
preclinical imaging and novel therapies

Tonny Lagerweij

Printing of this thesis was financially supported by:
Stichting STOPhersentumoren.nl
Stichting Semmy
Perkin Elmer, distributor of IVIS

ISBN: 978-94-6295-801-2
Layout and Cover design: Tonny Lagerweij
Printing: ProefschriftMaken|| www.proefschriftmaken.nl

VRIJE UNIVERSITEIT

Brain tumors
preclinical imaging and novel therapies

ACADEMISCH PROEFSCHRIFT

ter verkrijging van de graad Doctor aan
de Vrije Universiteit Amsterdam,
op gezag van de rector magnificus
prof.dr. V. Subramaniam,
in het openbaar te verdedigen
ten overstaan van de promotiecommissie
van de Faculteit der Geneeskunde
op dinsdag 23 januari 2018 om 11:45 uur
in de aula van de universiteit,
De Boelelaan 1105

door
Teunis Lagerweij
geboren te Ede

promotoren:	prof.dr. T. Wurdinger
	prof.dr. W. P. Vandertop
copromotoren:	dr. D. P. Noske
	dr. E. Hulleman

TABLE OF CONTENTS |

CHAPTER 1 |

GENERAL INTRODUCTION

INTRODUCTION

Primary brain tumors are a diverse group of malignancies, arising from different cell types within the central nervous system (CNS). They display a large heterogeneity, both between patients as within one tumor. Because of this heterogeneity, more than 100 different (sub)types of brain tumors have been identified. Until recently, CNS tumor classification was based mainly on histopathological features [1]. However, it was recognized that genetic and epigenetic aberrations should be added to the 2007 classification as findings from large-scale genomic studies and epigenetic profiling have identified human glioblastoma genes and core pathways involved in glioma genesis [2–6]. This has resulted in the renewed 2016 WHO classification where schemes for the diagnosis of CNS tumors include genetic and epigenetic signatures and diagnosis is based on a layered, morphological-molecular diagnostic approach [7,8]. Besides heterogeneity between patients, there is also a great intra-tumoral heterogeneity. This is reflected already by the old name of the most common primary brain tumor, glioblastoma multiforme (GBM), in which multiform indicated the many different aspects which are presented in these tumors [4,9–13]. Treatment of patients is hampered by this heterogeneous appearance of the tumors, as well as by the location of the tumor within the delicate brain tissue. Also, intrinsic and acquired resistance to treatment and the presence of the blood-brain-barrier (BBB) represent major challenges in the treatment of these patients.

In this thesis, we focus on improving therapy of pediatric medulloblastoma and diffuse intrinsic pontine glioma and adult glioblastoma by novel treatment strategies. In order to quantify and visualize the tumor progression, advanced imaging tools were used to monitor therapeutic efficacy.

PEDIATRIC BRAIN TUMORS

Brain tumors are the most common solid tumors in children accounting for the majority of cancer related deaths in this age group. Most pediatric brain tumors are primary tumors, thus originating in the CNS. Childhood brain tumors frequently appear in different locations and behave differently than brain tumors in adults. In children, 15.1% of the brain tumors are located in the cerebellum, and a proportion of 10.1% of the tumors is located in the brain stem [14]. The most common pediatric brain tumors are embryonic tumors: In order of increasing age, the most prominent ones are medulloblastoma in children age 0-4 years; pilocytic astrocytoma at ages 5-9 years and malignant glioma in age group 10-14 years [15].

Treatment options vary between tumor type and are strongly influenced by the age of the child. Although, in some occasions the prognosis for children with brain tumors is much better than for adults with similar conditions, adverse side effects of the anti-cancer therapy could limit treatment efficacy, especially in young children. Unfortunately, for a subset of childhood tumors, such as pediatric high grade gliomas (pHGG), patient outcome is still dismal as 70-90% of these patients die within 2 years of diagnosis [15–19]

Diffuse pontine glioma

Diffuse pontine glioma (DIPG) is a high-grade glioma in the brainstem, mostly in children. With the new 2016 WHO classification, these tumors are included in the group of diffuse midline glioma. However, because this new nomenclature is not common practice yet, the old name, DIPG, will still be used throughout this thesis. Although DIPG is rare, approximately 10 children per year in The Netherlands, this disease is the most deadly pediatric neoplasm, with a 5 years survival approaching to zero percent [20,21]. The symptoms of DIPG usually develop rapidly before diagnosis, thus reflecting the fast growth and location of these tumors. These symptoms include problems in controlling eye movements, speech, chewing and swallowing; weakness in arms and legs and subsequent problems with walking and coordination. The diagnosis is based on MRI, but conventional MRI cannot predict survival in childhood DIPG [22]. In 2012, several genomic studies of DIPG tissue have identified mutations in genes encoding histone 3 [6,23]. These H3K27 alterations appeared as the founding event in DIPG. Two main histone H3 variants can be identified which drive two distinct oncogenic programmes: The H3.3-K27M-mutated DIPG -which has a proneural/oligodendroglial phenotype and a pro-metastatic gene expression with PDGFRA activation-, and the H3.1-K27M-mutated DIPG -which exhibit a mesenchymal/astrocytic phenotype and a pro-angiogenic/hypoxic signature-. Patients with tumors harboring the K27M mutation in H3.3 (*H3F3A*) have an even worse clinical response as those with a mutation in H3.1 (*HIST1H3b/C*). The patients with the H3F3A variant relapsed significantly earlier and exhibited more metastatic recurrences than those patients with H3.1 variant [4,24,25].

Because DIPG is incurable, most treatments are mainly palliative. There are no strict guidelines for the treatment of DIPG, resulting in individualized therapy and a heterogeneous application of treatment schedules. Most DIPG patients are treated with radiotherapy or by combined radiotherapy/chemotherapy. The most widely prescribed chemotherapeutic agents are temozolomide and vincristine/carboplatin. [20]. Surgical resection is not possible due to the location of the tumor. With current therapies, the median overall survival is only 9.5 months.

Medulloblastoma

Medulloblastomas, a highly aggressive WHO-grade IV embryonal tumor, located in the cerebellum, are mainly occurring in the first decade of life, with a peak incidence between 0 and 4 years of age. Medulloblastomas constitute 15-20% of all childhood brain malignancies. Currently risk stratification into high- and standard risk groups primarily depended on variables such as age, presence of metastasis, extent of resection and histological subtypes [26,27]. More recently, molecular characterization showed that medulloblastomas can be classified into four subgroups: WNT-activated, SHH-activated, Group 3 and Group 4. The SHH-activated subgroup can be divided further into TP53-mutant and TP53-wildtype subgroups [8–10,28–30]. These classifications allow the definition of risk groups based on current survival rates. Patients with WNT-activated subtype have the best prognosis (>90% survival) whereas patients of Group 3 with metastasis and patients of SHH-activated with PT53-mutations have the worst prognosis of all subtypes with a 5-year overall survival of 50% [26].
Treatment consists of surgical removal of as much of the tumor as feasible, followed by craniospinal radiation and adjuvant chemotherapy. Based on the age of the child, extent of surgical resection and metastasis, a patient is assigned to either the standard risk group or the high-risk group. Standard risk patients are treated with reduce-dose radiation (23.4 Gy) whereas high risk patients are treated with a higher radiation dose (36 Gy). Adjuvant chemotherapy consists of different combinations of therapeutic agents, including cisplatin, lomustine, vincristine, cyclophosphamide and etoposide [31,32]. Very young children, generally defined as those less than 3 years of age, are typically not treated by radiotherapy due to the devastating neurocognitive outcome associated with this treatment. Patients in this age group are treated by chemotherapy only, to delay or avoid the radiotherapy [17,33–35]. Other means to limit exposure of healthy tissue to the harmful radiation include technical advantages in radiation equipment such as stereotactic radiosurgery and strategies to enhance radiotherapeutic efficacy by so called radiosensitizers, including quercetin and protein kinase inhibition such as the WEE1 or MRK/ZAK pathways [36–39]. With current therapies, 70-80% of children with average risk medulloblastoma have a 5 years progression free survival. And even in high-risk patients, long term PFS is 60-65% [34]. New understanding of the biology of medulloblastoma and the classification into distinct molecular subtypes will further facilitate the stratification of patients to the optimal treatment options.

ADULT BRAIN TUMORS

Glioblastoma (GBM) is the most common and aggressive primary brain tumor in adults. GBM can develop both *de novo* or via progression from primary low-grade glioma (LGG). Median age of diagnosis of primary GBMs is 62 years whereas secondary GBMs are often diagnosed in younger patients at a median age of 44 years [8]. The incidence is slightly higher in males than in females (ratio 1.6 to 1). GBMs are generally located in the cerebral hemispheres and show an infiltrative growth. The tumors are histologically characterized by nuclear atypia, mitoses, endothelial proliferation and/or necrosis [40]. Within one tumor, many different aspects could be present simultaneously. This heterogeneity might be represented by area-specific chromosome aberrations, mutations and gene-expression profiles [41–43]. Three key signaling pathways are deregulated, namely the RB (retinoblastoma), p53 and RTK/RAS/PI(3)K pathways [2]. Amplification of the epidermal growth factor receptor (*EGFR*) gene is the most frequent genetic change associated with GBM, which results in over-expression of the transmembrane tyrosine kinase receptor. The amplified EGFR frequently expresses EGFRvIII, a truncated variant of the receptor which is constitutive activated without necessity of ligand binding. EGFRvIII has been shown to increase proliferation and migration of GBM cells. Cells expressing EGFRvIII cause wild-type EGFR-expressing cells to accelerate their proliferation by upregulation of IL-6. Furthermore, EGFRvIII can promote angiogenesis by activation of the *src* oncogene [44–46].

In the 2016 CNS WHO classification, glioblastomas are divided into IDH-wildtype and IDH-mutant. The IDH-wildtype are about 90% of the GBM cases and corresponds closely to primary GBM. Patients in this subgroup have a median survival of 15 months after treatment with surgery, radiotherapy and chemotherapy. Commonly found mutations are in the TERT promotor (72%), TP53 (27%), EGFR amplification (35%) and PTEN mutations. IDH-mutant GBM corresponds closely to secondary GBMs. Median survival of these patients is 31 months after treatment. Typical genetic alterations include ATRX mutations (71%), TP53 mutations (81%). Patients with GBM are treated by a combination of surgery, radiation and chemotherapy. Due to the delicate region and infiltrative nature of GBM, radical surgery is never possible and inevitably some tumor cells will remain behind, which will give rise to tumor recurrence. The introduction of radiotherapy after surgical resection improved brain cancer treatment. In the case of GBM, radiotherapy was the first postsurgical adjuvant therapy that consistently demonstrated efficacy, typically doubling median survival from 4 – 6 months to 10 – 11 months [47]. Adding temozolomide (TMZ) chemotherapy has resulted in a further increase of median survival to 15.6 months after diagnosis. The current standard of care for GBM treatment is surgical resection to the maximal extent feasible, followed by radiotherapy concomitantly with temozolomide (TMZ) therapy and followed by six additional cycles of adjuvant TMZ alone [48,49]. TMZ is an alkylating/methylating agent of DNA. This

methylation damages the DNA which causes death of the cell. Unfortunately, TMZ therapy delays tumor relapse and consequent improvement of survival in only a part of the GBM patient population. One explanation for this therapy resistance is the presence of a DNA repair mechanism in the treated cells, such as expression of O-6-alkylguanine DNA alkyl transferase (AGT) which is encoded by the methylguanine-DNA methyltransferase (MGMT) gene. AGT removes the alkyl groups from the O^6 position of guanine residues, thus decreasing the therapeutic efficacy of TMZ. Epigenetic silencing of the MGMT promoter by methylation diminishes AGT expression and has been associated with longer survival of patients treated with alkylating agents. This methylation status of the MGMT promoter has shown to be a predictor of TMZ efficacy. However, this MGMT status is not the only factor involved in therapy resistance, paving the way for additional research to improve current therapies [50,51].

BRAIN TUMOR THERAPY

Many chemotherapies which are effective in non-CNS malignancies, are ineffective in brain tumor treatment. One obstacle to brain tumor treatment is the existence of the blood-brain barrier. Under normal circumstances, this barrier functions as a 'filter' to protect the brain from harmful substances. However, this barrier also prevents chemotherapy and other drugs to reach the brain in patients, thereby rendering the tumor resistant to therapy. One way to circumvent this BBB and allow effective delivery of pharmaceuticals at the tumor location is by convection-enhanced delivery (CED). With this technique, the pharmaceutical compound is administered under constant pressure into the tumor, and adjacent brain tissue. The volume of CED, and the placement of the catheters through which the compound is injected, are chosen such that the compound will reach the whole tumor core [52,53]. Besides a means to pass the BBB, CED is also useful for compounds which have severe systemic toxic effects. Due to the direct administration into the brain tumor, high local concentrations will be achieved whereas systemic levels are minimal [54,55]. Other methods which are explored to deliver compounds across the BBB into a brain tumor are the use of PEGylated vesicles and the use of viruses as delivery vehicle [56–58]. Also, ways to temporarily disrupt the BBB, thus allowing the compounds to pass this BBB, are evaluated. These include the use of microbubbles which can be activated locally by ultrasound to disrupt the BBB as well as methods such as TNF injections or high osmotic fluids which will open the BBB temporarily [59–63].

Currently, most therapies, including radiotherapy and TMZ chemotherapy are mainly targeted towards dividing cells. But cancer cells are not solely dividing cells. Cascades of aberrant signals within the cancer cells promote survival, accelerate growth, recruit blood vessels, enhance nourishment (Warburg effect), educate the immune system towards a pro-tumorigenic environment and lead to other effects which sustain life of the cancer cell [64,65]. Consequently, many of these aspects are potential targets for therapies in the treatment of cancer. An example of this is anti-angiogenic therapy. As GBMs are highly vascularized, it was postulated that inhibition of angiogenic factors, particularly VEGF, would be an effective way to control this disease. VEGF is upregulated in response to hypoxia, although overexpression of oncogenes (*Src,* ras) or the absence of tumor suppressor genes (p53) can also upregulate VEGF expression. Several strategies to target VEGF have been developed. Reduction of the amount of available extracellular VEGF is accomplished by anti-VEGF antibodies like bevacizumab or the use of soluble receptors like aflibercept. Other strategies are directed towards the VEGF-receptor, such as vandetanib and sunitinib. Also, methods to target the VEGF induced intracellular signaling pathways such as phosphatidylinositol-3-kinase (PI3K), Akt and ERK pathways. Although anti-angiogenic therapies were effective in some glioma animal models, experiences with anti-angiogenic mono-therapies were disappointing. This might be due to the fact that tumors may use alternative ways, such as vessel co-option, to obtain blood supply or the fact that even single GBM cells have the capacity to migrate, thus escaping hypoxic areas [66–69]. Anti-angiogenesis treatment may also lead to ischemic stress which attracts and activates pro-tumorigenic macrophages.

Besides the BBB and angiogenesis, other factors play a role in the poor response of brain tumors to treatment. Intratumoral heterogeneity, which is the presence of multiple, epigenetically and genetically different subpopulations of cells within a single tumor, might contribute largely to treatment failure [70]. This heterogeneity may result in tumors where multiple driver receptor tyrosine kinase (RTK) amplifications are presented and activated in adjacent tumor cells. Similarly, intercellular heterogeneous expression of the MGMT DNA repair gene has been shown in pediatric medulloblastoma where MGMT positive and MGMT negative cells were intermingled [71]. Transfer of these driver mutations or transfer of MGMT repair system from therapy resistant cells towards more sensitive cells plays a role in treatment failure. This tumor heterogeneity prompts for the use of combinations of treatments against several targets, either simultaneous or consecutive. As therapy resistance can be transferred from one cell to another [72–74], novel ways to block this transfer of resistance are being explored to enhance therapy efficacy.

Another major factor in tumor progression is the role of the immune system. In normal situations, the immune system removes abnormal cells before they transform into cancer cells. However, tumor cells have not only escaped this immune surveillance, but merely

educated the immune cells to enhance tumor growth [75–77]. In GBM, up to 30% of the tumor bulk consists of tumor associated macrophages/microglia (TAMs). These TAMs stimulate angiogenesis and drive the T-cells towards an anti-inflammatory Th2 response [78,79]. In preclinical research, reduction of the number of TAMs by engagement of CSF-1R was effective in delaying tumor progression, but also other immune therapeutically approaches are being explored in the context of brain tumor therapy [76,80,81].

PRECLINICAL MODELS

Cancer cell lines are pivotal to study biochemical pathways *in vitro*. With the use of human and animal cancer cell lines, many fundamental questions about tumor development and progression have been raised, and answered. However, when one wants to study the complex interplay of tumor cells and their micro-environment, effects of the blood-brain-barrier or adverse effects on a organism, animal models are inevitable. These animal models are tools to translate knowledge from *in vitro* research towards clinical practice as they provide means to characterize physiological interactions where *in vitro* systems are insufficient to answer these interactions [82]. Animal models are used to address scientific questions, evaluate pharmacokinetics, efficacy and safety of novel therapeutics, and biomarker discovery. These models include chicken embryo chorioallantoic membrane (CAM) assay, zebrafish , dogs, rat and mouse models [83–85]. Ideally animal models for brain tumor research should recapitulate the complexity of the human body and brain, and reflect all aspects of human brain tumors including initiation and progression of tumor, migration of tumor cells, presence of relevant tumor markers, and interaction with the micro-environment, thus covering the diversity of all human brain tumor types and furthermore reflecting the intratumoral heterogeneity as seen in humans [86,87].

For most preclinical animal research, the mouse is the experimental model of choice. Great advantages of the mouse as experimental models are the highly developed methodology for genetic manipulation, and the wide availability of mouse specific reagents, such as antibodies. Moreover, the possibility to use immune deficient mice with xenografts of human tissues makes mouse models particularly attractive for oncology research. These arguments already recapitulate two of the most used strategies to reproduce brain tumors in animals which will be described below namely genetically-engineered mouse models and (xenograft) transplantation models.

Genetically-engineered mouse models (GEMMs)

Genetically-engineered mouse models (GEMMs) include transgenic-, knockout- and knockin mouse models. GEMMs are a valuable tool for determining target function, verifying selectivity, predicting toxicity and drug discovery [88]. These models have the advantages of defined genetic modifications that are known to be involved in human malignancies. Furthermore, GEMMs develop reliably tumors at the correct anatomical site, and have properties very similar to those of their human counterpart [89]. Development of the first patented animal, the OncoMouse [90], made it possible to study the role of oncogenes and environmental stimuli which are necessary for tumor development and progression. Since the introduction of technologies to culture mouse blastocyst cells and the genetic modification technologies in the 1980s, thousands of models have been generated. Another important milestone in the development of GEMMs was the Cre/LoxP system [91,92]. This technique offers the advent of inducible transgenic systems, thus allowing temporal and spatial regulation of gene-expression. At that time, appropriate engineering of these genetic models was still cumbersome and time consuming. Nowadays, much faster production of transgenic animals can be obtained by current genetic modification techniques using CRISPR/Cas9 or TALENs-mediated genome editing [93,94].

Despite the aforementioned advantages, GEMMs do not cover all aspects of brain tumors. GEMMs are generated for only a single, known target or at most a limited combination of targets. Furthermore, GEMMS do not reflect the tumor heterogeneity found in human cancers. One approach to reflect better the initiation of cancer is by a less targeted way of tumor induction. For instance by injection of tumorigenic viruses into the brain or by injection of chemicals [95,96]. This will result in a more random tumor induction and may present better the natural tumor initiation. Due to this more random tumor initiation, likely an inhomogeneous tumor will develop which reflects biological tumor heterogeneity.

Transplantation models

Xenograft transplantation of patient derived tumor material into immune compromised mice give tumors that partially retain histological features and molecular characteristics of human cancer. Tumor cells of different types or subtypes of brain tumors can be injected into immune compromised animals, thus giving raise of human tumors. When primary cells, e.g. directly obtained from biopsy, autopsy or surgery are used, part of the intratumoral heterogeneity will be covered by the full grown xenografted tumor [97]. Traditionally, new treatments were often assessed in subcutaneous tumor models (heterotopic) due to their convenience, low costs and wide availability [98–100]. But, as recognized already long ago, to duplicate *in vivo* conditions even better, brain tumors should be transplanted into the brains of mice [101,102]. These orthotopic xenografts have proven to be valuable for identification of new therapeutic strategies in many occasions.

Most often, xenograft studies are performed in immune deficient nude or scid mice. However, a disadvantage of immune compromised mice is the lack or altered tumor immunology and the absence of a natural microenvironment. Although human xenograft models in immune competent mice has been described to be feasible and it was shown that these models recapitulates glioblastoma-microenvironment interactions [103], more often syngeneic murine models are being used to study immunological interactions and immunotherapy [104,105]. In these syngeneic mouse models, murine cancer cells are injected into immune competent mice which allows the evaluation of immunological based therapies. Alternatively, the use of humanized mice could be considered to study the role of immune therapeutically approaches [106,107].

PRECLINICAL IMAGING

Beyond advancing our knowledge about basic cancer biology, mouse tumor models also comprise a stringent means to evaluate the *in vivo* efficacy of therapeutic intervention strategies. As described by De Jong et al, translation of *in vitro* research to clinical practice is mainly a two-step procedure. During the first step, where translation from laboratory findings towards preclinical models takes place, imaging tools such as bioluminescent imaging, fluorescent imaging and intravital microscopy play a major role. During the second step, where preclinical *in vivo* findings are translated to clinical findings, a more prominent role is given to imaging techniques which are also being used in the clinic [82]. The most efficient way of utilizing mouse models is through longitudinal studies. Through application of a suite of imaging techniques, it is now possible to measure a broad range of tumor-relevant parameters in a single animal at different time points. The greatest advantages of preclinical imaging techniques include the reduction of biological variability along with the substantial reduction in the number of animals required for a particular study, fully complying with 3R (Replacement, Reduction and Refinement) policies [108,109].

To visualize and quantify progression of disease, numerous techniques are available for preclinical imaging, including positron emitting tomography (PET), computed tomography (CT), magnetic resonance imaging (MRI), bioluminescence imaging (BLI) and intravital microscopy (IVM). Except for IVM and BLI, these imaging modalities are also widely used in clinical applications where these are routinely used for diagnosis and follow-up of human diseases (Figure 1). This use of translational imaging techniques facilitates the correlation between preclinical and clinical data (bench-to-bedside model).

Every imaging technique has its own limitations and advantages. Each imaging modality has its strengths and weaknesses which define its use in visualization of different stages of disease or in drug development process (Table 1). For example, MRI and CT are in general label free and are well suited for visualization of anatomical detail. However, they lack molecular specificity whereas the nuclear imaging techniques PET and SPECT allow functional imaging of tumor biology [82]. PET is more sensitive than SPECT, whereas SPECT can be used to visualize multiple nuclear tracers simultaneous. Techniques such as PET, MRI, CT, SPECT and ultrasound (US) have great translational capabilities as these techniques are already used in the clinic.

Bioluminescence imaging (BLI)

Bioluminescence is the production of light by a living organism. Many bacteria can produce light as over 700 strains of luminous bacteria are isolated. But also other organisms such as fireflies, jellyfish and squids are capable of bioluminescence. Several luciferase genes were isolated and cloned from these organisms, including firefly luciferase (Fluc), gaussia luciferase (Gluc) and renilla luciferase [110–113]. Introduction of these genes into cancer cells allows to study biological events such as intracranial tumor development, treatment efficacy, and to monitor metastasis [114], because the luminescent signal corresponds highly with tumor burden and predicts animal survival [115,116]. A major advantage of the use of these luciferase genes is the absolute lack of background signal. As only these genetically modified cells will emit light in the presence of the luciferin substrate, BLI shows higher sensitivity as compared to imaging techniques such as PET or MRI, allowing detection of small number of cells [117]. Because this technique is inexpensive, fast, sensitive and simple to operate, BLI is efficient for longitudinal studies and drug discovery research. A disadvantage of BLI is that this technique does not allow real quantification of data. Because visible light is highly quenched by tissues and erythrocytes, as well as by bone structures and fur of the animals, signal intensity is largely dependent on the location and depth of the cells to be visualized and therefore not proportionally related to the number of bioluminescent cells.

Intravital microscopy (IVM)

Light microscopy provide means to visualize cellular and even subcellular details. Intravital microscopy makes use of such light microscopes to observe biological systems at high spatial, and temporal resolution in a living animal. The use of optical imaging for *in vivo* imaging is still mainly limited to preclinical imaging, largely because of the limited penetration depth of visible light into intact tissue. However, advances in instrumentation, especially the use of longer wavelengths for multiphoton microscopy, have improved light penetration and will probably continue to do so. Furthermore the potential of translating optical imaging towards the clinic has been shown by recent studies of fluorescence-guided surgery [118,119] and label free imaging by using second- and third harmonic imaging [120] . Intravital fluorescence

microscopy can be performed non-invasive on superficial structures [121–124]. If deeper tissues, or tissues covered by bones or tissues in the skull have to be visualized by intravital microscopy, optical windows are needed to visualize cellular and vascular processes [115,125–130]. Limitations of intravital imaging are the small field of view and limited imaging depth. Imaging depth is limited due to absorption and reflection of photons. The use of higher wavelengths, as in multiphoton imaging and by the use of near-infrared dyes, has improved imaging depth, but still it is under 2 mm [131,132].

Positron Emitting Tomography (PET)

Small animal PET-imaging was boosted by the development of dedicated small animal PET scanners, which became available during the 1990's [133–135] . Preclinical PET-imaging is increasingly used to assess efficacy of therapeutic interventions and to validate applications of current and novel radiotracers for translation to human applications. Due to developments such as thinner scintillator sizes and smaller bore sizes, preclinical devices have a reduction in spatial resolution of approximately 3-fold as compared to the clinical scanners. But still, this improvement in resolution is insufficient to create an equal sampling size in mice and humans because a human is about 3000 times the size of a mouse. Although sensitivity is low compared to BLI and spatial resolution is far less as compared to MRI, PET-imaging has its own advantages. Positron emitting radionuclides can be coupled to many different types of molecules. This allows imaging of biological processes such as proliferation, DNA damage and repair and angiogenesis thus allowing to get functional, quantitative information about physiological processes in tissues or organs [136,137].

Computed Tomography (CT)

X-ray imaging makes use of electromagnetic radiation (X-rays) and the differential absorption of these X-rays by water, bone, fat and air to make cross-sections of the body. Computational combination of X-rays taken from different angles allows 3D reconstruction of the scanned object. The main advantage of CT is the high contrast between bone and soft tissues. Soft tissues have often similar densities of contrast as their surrounding tissues, which makes CT less suitable for imaging of soft tissues. Although contrast agents are available to enhance contrast, the use of iodinated contrast agents to discern organs and vessels in mice is challenging. Because mice have a physiological heart rate between 500-620 bpm, these contrast agents are cleared quickly from the circulation. Moreover, image resolution of CT images is limited to about 50 µm, making the visualization of minute structures such as vessels in small animal models difficult [138]. CT imaging is often used for anatomical localization of tumors in combination with other imaging modalities such as PET or BLI, and for image-guided stereotactic cranial irradiation [139,140].

Magnetic Resonance Imaging (MRI)

The ability of MRI to confer anatomic detail are unmatched. However, overall it is low in throughput, is labor intensive, time-consuming and requires expensive instrumentation. MR in preclinical brain tumor imaging is most used to screen and monitor tumor growth and to correlate imaging phenotypes with tumor histology [103,141]. High spatial resolution (down to 25 µm) is obtained by applying high strength magnetic fields, up to 15.2 Tesla, but for characterization of the growth of preclinical tumor models, low-field (1T) magnetic resonance imaging, which gives a spatial resolution of 100 µm, is often sufficient [142,143]. MRI can be used to study blood-brain-barrier integrity with the use of MRI contrast agents such as gadolinium [144].

Ultrasound (US) / Photo-Acoustic (PA) imaging

Ultrasound (US) imaging uses registration of reflected high-frequency sound waves which are translated into 2D and 3D images. Preclinical ultrasound devices are specifically developed for small animal research, with frequencies ranging from 9 MHz to 80 MHz. Due to its high data capturing rate, up to 1000 frames per second, US is capable to visualize blood flow *in vivo.*

Photo-acoustic imaging (PA) is a special type of acoustic imaging where a laser delivers energy to biological tissues. This energy is absorbed and converted to heat which results in the production of a high-frequency sound wave which can be registered with an ultrasound probe. As the energy absorption is associated on properties such as oxygen saturation of hemoglobulin, PA imaging can be applied to visualize oxygenation levels in a tumor [145]. Both US and PA have limited penetration trough bone tissues. Imaging of brain tissues or tumors is therefore limited to the more superficial areas. Alternatively imaging windows have to be created, or part of the skull has to be removed to allow imaging of deeper located brain areas [126,128].

Figure 1. (next page) Overview of various imaging techniques for preclinical brain tumor research. **a** Positron emission tomography (PET) image of the distribution of ^{89}Zr-bevacizumab in mice. **b** T1 weighed magnetic resonance image (MRI) of a mouse xenografted with U251FM GBM cells. **c** T2-weighed MRI. **d** Computed tomography (CT) image. **e** Ultrasound (US) image of a mouse with GBM8FM brain tumor. **f** Photo-acoustic (PA) image of the same region. **g** Bioluminescent light imaging (BLI) of a mouse with an intracranial E98FM tumor and some drop-metastasis in the spinal cord. **h** Intravital microscopy of diffuse growing GBM8FM cells in the brain of a mouse. **i** Superficial blood vessels imaged by intravital microscopy through a cranial window. **j** Immunohistology; lectin labeled blood vessels (green) and GBM8 tumor cells (red). **k** Hematoxylin & eosin stained GBM8 tissue. **l** Co-registration of ^{89}Zr-bevacizumab PET scan with anatomical CT data. **m** Co-registration of GBM8FM BLI data with 3D X-ray anatomical data. **n** 3D brain vasculature of a health mouse of CLARITY cleared tissue.

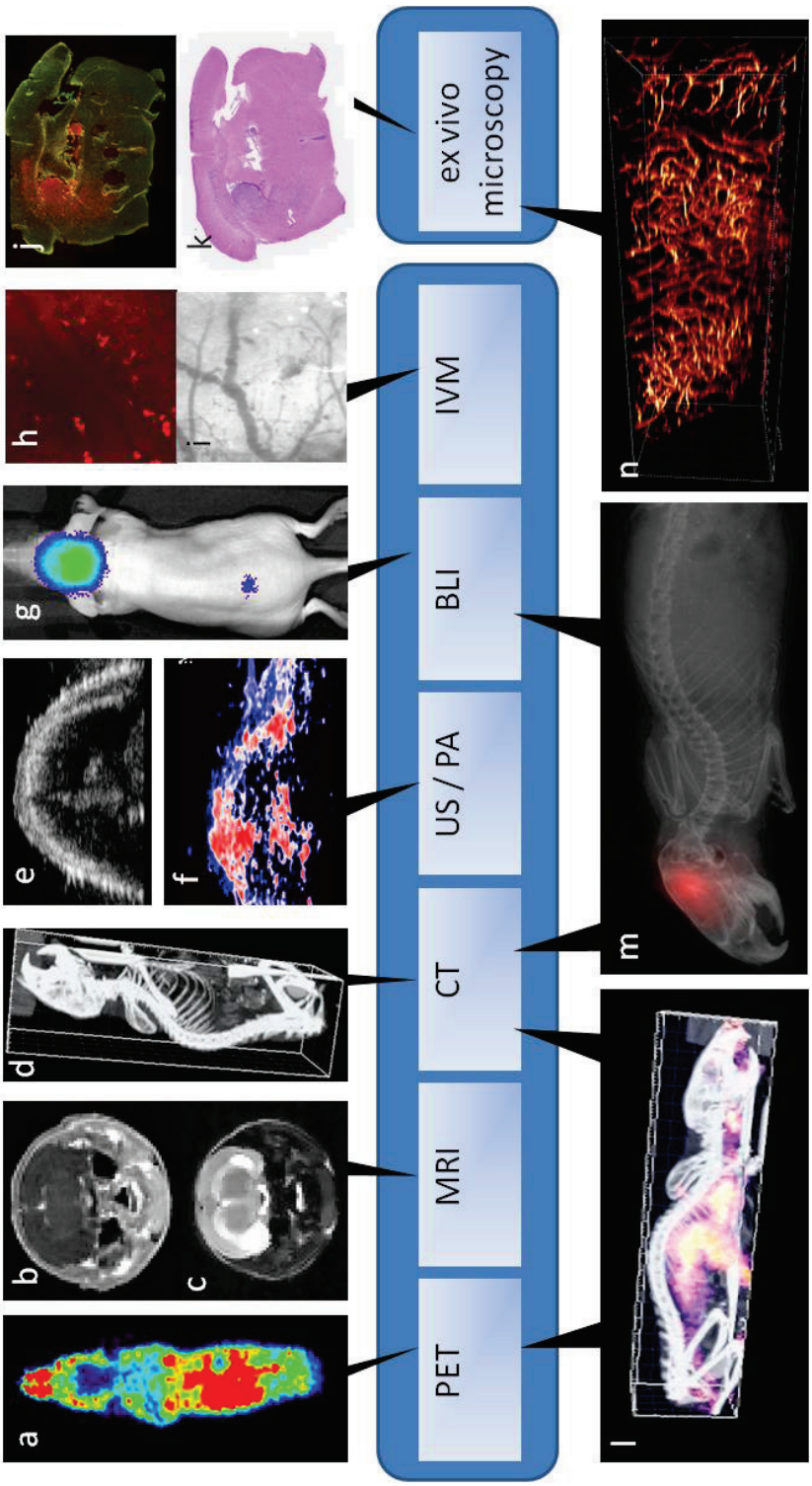

Figure 1 (legend see previous page**)**

Ex vivo: 3D microscopy

Microscopical imaging has been indispensable in tumor diagnosis and research. Up to now, cancer diagnosis depends largely on histological analysis of formalin-fixed, paraffin-embedded (PPFE) tissue slides. To visualize cells or structures, the tissues are usually stained by chemical procedures, such as hematoxylin and eosin (H&E) staining, or histochemical staining using antibodies against specific targets. Traditional histological assessment of tissues limits proper insight in 3D tissues structure. Imaging of serial sections and subsequent 3D reconstruction has been developed successfully, but its application remained limited to small volumes of tissue [146–150]. Furthermore, mechanical slicing and manual aligning of tissue slides is a time-consuming and error-prone procedure. This has led to the development of methods for optical slicing avoiding mechanical slicing of tissue. Optical slicing has become feasible because of developments in microscope, laser, optics and detector technologies, such as improved confocal microscopes with long working distance objects, multiphoton laser scanning microscopes and light sheet microscopes [151–153]. Because light scattering and absorbance hinders proper imaging of large samples, samples need to be cleared by optical tissue clearing (OTC) to render transparent tissues. Many OTC's have been developed, including BABB, Scale, 3Disco, ClearT, SeeDB, CLARITY, CUBIC, PACT/PARS, iDISCO, ACT-PRESTO [149,154–157], reviewed by Azaripour [158]. Other advantages which allowed 3D imaging of cells and structures in optical cleared tissues are developments of stable and strong fluorescent labels such as Alexa Fluor and Dylight labels, and animals which express endogenous fluorescence. Major advances for 3D imaging of larger pieces of tissues are being expected from more efficient labeling of the structures of interest [159–163].

Imaging Modality	Spatial Resolution	Acquisition time	Imaging depth	Contrast agents / molecular probes	Clinical translational	Quantitative degree	Morphological imaging	Key use
MRI	25 - 100 µm	mins to hours	no limit	gadolinium, iron particles	yes	++	+++	anatomical imaging (soft tissues)
US	30 - 50 µm	mins	mm - cms	microbubbles, nanoparticles	yes	+ to ++	+++	vascular imaging
BLI	1 - 10 mm	secs to mins	1 - 2 cm	luciferases	no	- to +/-	-	research
FLUOR	0.2 - 10 mm	secs to mins	1 - 2 cm	fluorecent labels	yes	- to +/-	-	research
IVM	5 µm	secs to hours	1 - 2 mm	fluorescent labels	no	- to +/-	+/-	research
CT	30 - 50 µm	mins	no limit	iodine	yes	+ to ++	++	anatomical imaging (bone tissues)
SPECT	1 - 2 mm	mins to hour	no limit	isotopes (^{99m}Tc, ^{123}I, ^{125}I, ^{67}Ga)	yes	+++	+	metabolic imaging
PET	1 - 2 mm	mins to hour	no limit	isotopes (^{18}F, ^{89}Zr, ^{68}Ga)	yes	+++	+	metabolic imaging

Table 1: Main characteristics of preclinical imaging modalities. Information partly sourced from [164–167] Spatial resolution=minimum distance between two objects that can be distinguished separately MRI: Magnetic Resonance Imaging, US: Ultrasound, BLI: Bioluminescence Imaging, FLUOR: Fluorescence imaging, IVM: Intravital microscopy, CT: Computed Tomography, SPECT: single-photon emission computed tomography, PET: Positron emitting tomography

THESIS OUTLINE

The general aim of the research presented in this thesis is to explore novel therapeutic strategies for the treatment of high grade brain cancer. To this end we have used brain tumor models in mice, which we used to study the efficacy of several therapeutics or administration routes. The focus was on imaging tumor progression and therapy efficacy.
In the first part of this thesis we pay attention to treatment and imaging options in DIPG, a pediatric high-grade tumor in the brainstem. In chapter 2 we describe a method for delivery of carmustine directly into a brainstem tumor by convection-enhanced delivery. The safety and efficacy of this CED-method was evaluated by histological and bioluminescence imaging in tumor bearing mice.

This CED technique which was further explored to test feasibility of local delivery of doxorubicin to treat pediatric DIPG and thalamic high-grade glioma is described in chapter 3.

As high-grade tumors are highly angiogenic, anti-angiogenic therapies could be beneficial in the treatment of these tumors. In chapter 4, we use PET-imaging and distribution studies in orthotopic (intracranial) and heterotopic (subcutaneous) DIPG and high-grade glioma animal models to study whether VEGF-expression is dependent on the tumor microenvironment.

In chapter 5, we screened a library of chemical compounds to identify possible radiosensitizers in order to study, in an orthotopic xenograft model for medulloblastoma, whether administration of the radiosensitizer quercetin around the time of radiation increases the radiation efficacy and prolonged survival in this preclinical animal model.

Chapter 6 addresses a novel way to inhibit tumor progression. Because extracellular vesicles (EVs) are important in tumor progression, we identify chemokine receptors on the tumor cells which are involved in EV interaction. Next, we evaluate if therapeutic intervention inhibits the EV-interactions and their consequent effects on tumor progression and the prevention of temozolomide resistance.

Finally, in chapter 7, we describe a method for 3D-histology of the brain and the use of this technique to visualize, and quantify blood-vessels in healthy brain and the topological orientation of tumor cells towards the vasculature in tumors.

Chapter 8 discusses the results of these studies and the use of preclinical imaging models in the field of brain tumor research, concluding with the implications for future research to improve treatment strategies of brain cancer.

CHAPTER 2 |

CONVECTION-ENHANCED DELIVERY OF CARMUSTINE TO THE MURINE BRAINSTEM: A FEASIBILITY STUDY

Tonny Lagerweij*, A. Charlotte P. Sewing*, Viola Caretti*, Pepijn Schellen, Marc H.A. Jansen, Dannis G. van Vuurden, Sander Idema, Carla F.M. Molthoff, W. Peter Vandertop, Gertjan J.L. Kaspers, David P. Noske, Esther Hulleman

Published in: *J. Neurosci. Methods* 2014;238:88-94.

* These authors contributed equally to this work

ABSTRACT

Systemic delivery of therapeutic agents remains ineffective against diffuse intrinsic pontine glioma (DIPG), possibly due to an intact blood–brain-barrier (BBB) and to dose-limiting toxicity of systemic chemotherapeutic agents. Convection-enhanced delivery (CED) into the brainstem may provide an effective local delivery alternative for DIPG patients.

The aim of this study is to develop a method to perform CED into the murine brainstem and to test this method using the chemotherapeutic agent carmustine (BiCNU). To this end, a newly designed murine CED catheter was tested *in vitro* and *in vivo.* After determination of safety and distribution, mice bearing VUMC-DIPG-3 and E98FM-DIPG brainstem tumors were treated with carmustine dissolved in 5% dextrose (DW) or carmustine dissolved in 10% ethanol.

Our results show that CED into the murine brainstem is feasible and well tolerated by mice with and without brainstem tumors. CED of carmustine dissolved in 5% DW increased median survival of mice with VUMC-DIPG-3 and E98FM-DIPG tumors with 35% and 25% respectively. Dissolving carmustine in 10% ethanol further improved survival to 45% in mice with E98FM-DIPG tumors.

INTRODUCTION

Diffuse intrinsic pontine glioma (DIPG) is a fatal brain malignancy in children, for which prognosis has not improved in the last 40 years [168,169]. Although recent *in vitro* studies have shown DIPG cells to be sensitive to both classic chemotherapeutic drugs and novel targeted agents [170], multiple clinical trials have so far been unsuccessful [169]. A possible reason for this failure is the inability of therapeutic agents to reach tumor cells, due to a relatively intact blood–brain-barrier (BBB) [171,172]. The BBB constitutes a physiological barrier to safeguard the central nervous system from exposure to both endogenous and exogenous toxins, thereby also preventing effective delivery of chemotherapy to the tumor parenchyma [173]. Therefore, convection-enhanced delivery (CED), a local drug delivery method, may be a promising delivery approach to more effectively treat DIPG patients [174,175]. CED relies on a continuous hydrostatic pressure gradient, which propels therapeutic agents over relevant anatomical volumes, at a speed several orders of magnitude greater than simple diffusion [176]. Local drug concentrations achieved by CED can be up to 10,000-fold higher as compared to intravenous drug administration, while minimizing systemic exposure [177]. Because of a wider distribution, CED could be preferred over intrathecal-, intraventricular- and intra-arterial drug administration or polymer-wafer implantation in brain tumor patients [178–180]. The use of CED as a treatment strategy for DIPG patients has matured from preclinical studies showing feasibility in rats [181,182], to safety and distribution studies in non-human primates [183,184] and phase I/II clinical trials in children [185]. To our current knowledge, four studies have been published, describing follow up of five pediatric patients treated with CED in the brainstem, four of which were suffering from a DIPG [53,186–188]. These studies have shown CED in DIPG to be feasible and safe but have yet to show a survival benefit. To further improve CED for more (pre-clinical) research is needed.

Even though the safety and efficacy of CED in the brainstem has been assessed in rat non-tumor [181] and non-DIPG brainstem tumor models in rats [182], no study has shown the feasibility of CED in the murine brainstem. Since true primary DIPG-xenograft and genetically-engineered models of DIPG are currently only available in mice [189,190], we decided to conduct a safety and efficacy study of CED in the murine brainstem using the chemotherapeutic agent carmustine (BiCNU, 1,3-bis-(chloroethyl)- 1-nitrosourea). Carmustine is an alkylating agent with a clear differential toxicity to pediatric high grade glioma and DIPG cells *in vitro* compared to astrocytes [170]. Dose-limiting systemic toxicity makes carmustine unsuitable for intravenous therapy in brain tumor patients [191], but its efficacy against glioma cells and the lack of toxicity to astrocytes at clinically relevant concentrations [170], makes it an excellent candidate for local therapy. Currently, carmustine is the only FDA-approved treatment for intracerebral chemotherapy of adult glioblastoma [168,192]. In addition, interstitial carmustine

administration by wafers has shown to be safe in pediatric brain tumor patients [193,194]. In this study we evaluated carmustine dissolved in 5% dextrose (DW) which is known to be safe in rats. Subsequently, we tested the safety of 10% ethanol administration to the murine brainstem, because dissolving carmustine in 10% ethanol could improve distribution and allows for a better translation into the clinic [195]. As a final test we studied the *in vivo* efficacy of local delivery of carmustine via CED dissolved in both vehicles (5% DW and 10% ethanol). For this purpose we employed our recently developed VUMC-DIPG-3 [196] model and our previously established E98-Fluc-mCherry (E98-FM) DIPG model [197].

MATERIALS and METHODS

Convection-enhanced delivery *in vitro*

The CED-system was tested *in vitro* by performing CED of trypan blue in 0.6% agarose gel, which has been previously described as a reliable model to simulate CED in the brain parenchyma [198]. CED was performed at a speed of 0.5 µl/min for 30 min. Total infusion volume was 15 µl. Five minutes after the end of the procedure, the inner cannula was withdrawn and after 1 min the guide was also withdrawn at a speed of 1 mm/min. Distribution and backflow were assessed by observing trypan blue distribution in the agarose gel.

Carmustine

For the *in vivo* experiments carmustine (BiCNU), (Bristol-Myers- Squibb, Princeton, NJ), was resuspended to a concentration of 3.3 mg/ml in either 5% DW (pH <4), or 10% ethanol. Carmustine dose was measured *in vitro* before and after the CED procedure using HPLC–UV in both vehicles.

Animals used for convection-enhanced delivery experiments

Animal experiments were performed in accordance with the Dutch law on animal experimentation and the protocol was approved by the committee on animal experimentation of the VU University Medical Center (VUMC). All tumor models (E98FM-DIPG, total $n = 31$, VUMC-DIPG 3, total $n = 12$) were established in immune deficient 6-week-old athymic nude-foxn1^{nu} mice to allow for adequate engraftment. Toxicity studies of 10% ethanol infusion (total $n = 15$) were performed on 6-week-old balb/c mice with an intact immune system to study the full scope of possible tissue reactions. All mice were housed under specific pathogen-free conditions in a 12-h light–dark cycle and were offered food and water *ad libitum.* Weights were measured, and clinical scores were assigned daily after the CED procedure (toxicity and efficacy studies). Clinical scores ranged from 0 to 4 and referred to 0: normal active behavior, 1: subtle inactivity or subtle neurological symptoms, 2: mild to moderate

inactivity or neurological symptoms, 3: severe neurological symptoms, inactivity, loss of reflexes, inadequate grooming, 4: dead. Half point scores were assigned to mice that were behaving in between two scores.

Orthotopic DIPG mouse models

A single-cell suspension was prepared after harvesting subcutaneous E98-FM and VUMC-DIPG-3 tumors. E98-FM cells were originally isolated from an adult GBM patient [197] and the genotypic murine-DIPG model: VUMC-DIPG-3 was established after injection of DIPG material collected during autopsy [196,199]. E98-FM cells and VUMC-DIPG 3 cells were injected as previously described [197], Coordinates from lambda for tumor-cell injections were: −1.0 mm *X*, −0.8 mm *Y*, 4.5 mm *Z*. Coordinates were based on "The mouse brain in stereotaxic coordinates" by Franklin and Paxinos, 3rd edition [200]. For the DIPG-E98-FM model, tumor growth was monitored twice weekly by bioluminescence imaging (BLI), as previously reported [197].

Convection-enhanced delivery *in vivo*

Before the CED-procedure, animals were injected subcutaneously with the analgesic buprenorphine 0.05–1 mg/kg and then anesthetized with isoflurane 2.5–3% in 100% oxygen. After placing the animals in a stereotactic frame on a heated platform, the CED-catheter was introduced into the pons (coordinates from lambda: −1.0 mm *X*, −0.8 mm *Y*, 4.5 mm *Z*) and the drug was infused (15 µl in 30 min). After the procedure, the catheter was removed, and the animals were returned to their cages to recover and resumed normal active behavior within 3–12 h.

Convection-enhanced delivery efficacy studies

At day five (VUMC-DIPG-3) or day seven to nine, depending on bioluminescence signal in E98-FM, after intracranial injection of tumor cells for the establishment of orthotopic pontine tumors, mice were stratified on the basis of BLI signal intensities into different treatment groups (E98-FM) or randomly assigned to one of the two groups (VUMC-DIPG-3). Animals were assigned to receive CED with carmustine in DW 5% (VUMC-DIPG-3 and E98FM-DIPG) or 10% ethanol (E98FM-DIPG) or only DW 5% or 10% ethanol vehicle. Researchers were blinded as to which treatment group mice belonged to. Follow-up included daily observations and weight measurement and measurement of BLI signal twice a week (E98-FM). Clinical scores were assigned ranging from 0 (normal active behavior) to 4 (dead). Endpoints were defined as weight loss more than 15%, severe neurological symptoms or severe inactivity. Mice were sacrificed *via* pentobarbital overdose. Brains were removed and fixed in 3.7% formaldehyde solution in PBS (phosphate buffered saline). Blood was withdrawn from

the tail vein before CED and a week thereafter, allowing the monitoring of alanine aminotransferase (ALAT), aspartate aminotransferase (ASAT) and creatinine levels using standard laboratory techniques used at the VUMC.

Tissue staining and histological scoring of mice receiving convection-enhanced delivery with 10% ethanol

Hematoxylin and eosin (H&E) staining was performed on 5 µm formalin-fixed, paraffin-embedded tissue sections cut in the coronal plane from non-tumor baring balb/c mice 2 or 21 days after CED with 10% ethanol or distilled water, using a standard H&E protocol. Sections were selected at the site of the needle tract and 100 µm both rostrally and posteriorly. Two researchers and an independent neuropathologist performed assessment of tissue damage and inflammation. They were blinded to the experimental procedure that the animals underwent.

Statistics

Differences in survival were analyzed by Kaplan–Meier curves and log rank tests for significance in the efficacy studies. Non-parametric Kruskal–Wallis test followed by a Dunn's *posthoc* test was used to determine differences in ALAT, ASAT and creatinine levels and differences in BLI signal. The weight loss of mice treated with 10% ethanol was analyzed using a generalized linear model (GLM) and carmustine dose measured before and after CED in 10% ethanol and 5% DW was analyzed using a two-tailed *t*-test. A $p < 0.05$ was considered statistically significant.

RESULTS

Convection-enhanced delivery *in vitro* provides a symmetrical distribution with minimal backflow

A stepped design catheter was developed incorporating an inner cannula (Hamilton Comp., Reno, NV) into an outer needle (Fig. 1a and b). The use of a stepped design reduces the risk of backflow or mechanical tissue injury and allows for a higher infusion rate [53] (Fig. 1a and b). The cannula has an outer and inner diameter of 0.24 and 0.11 mm, respectively; the outer guide has an outer and inner diameter of 0.52 and 0.26 mm, respectively.This catheter was connected *via* a tubing system (Fig. 1c) to a 300 µl disposable syringe inserted into a syringe pump (PHD 2000, Harvard Apparatus Inc., Holliston, MA). A pressure transducer was put in place to assure continuous pressure during the infusion and prompt detection of any issues in delivery (Fig. 1c). The inner cannula was inserted 2.5 mm into the agarose and further lowered to 4.5 mm using a dedicated screw system to ensure the inner cannula followed a straight line minimizing backflow and damage to the brainstem (Fig. 1a). The CED catheter was tested *in vitro* by performing CED of trypan blue in 0.6% agarose gel. Rate of infusion (0.5 µl/min) and total volume (15 µl) were chosen based on previous pre-clinical studies[201], clinical relevance (size of pons in relation to volume infused), and presumed feasibility (supplemental Table 1). Only minor leakage could be detected due to needle- and guide withdrawal and trypan blue was distributed as a symmetrical sphere in the agarose gel (Fig. 1d).

Convection-enhanced delivery into the murine brainstem is feasible and safe

Next, using the same settings, CED of trypan blue was performed *in vivo* to confirm proper infusate delivery. Mice were sacrificed after surgery to confirm infusion at the correct anatomical location (Fig. 1e and f). Trypan blue could be identified in the brainstem area (Fig. 1e and f). To assess safety of CED with carmustine in the brainstem, vehicle solution (5% DW) or carmustine (3.3 mg/kg in 5% DW) was infused in balb/c mice using the same settings as previously described. Mice recovered promptly from the surgery and no acute or chronic toxicities were observed during a two months follow-up.

10% ethanol can be safely administered to the brainstem via convection-enhanced delivery

To exclude toxicity of 10% ethanol infused directly in the brainstem by CED, non-tumor bearing mice were treated with 15 µl of 10% ethanol or vehicle. One vehicle-treated mouse died during the procedure due to a technical problem (inaccurately fixed catheter). Both 10% ethanol and vehicle-treated mice showed a transient

clinical deterioration and increase in weight loss after the CED procedure. All mice recovered completely, and no significant difference could be detected in clinical score or weight loss between treatment groups (Fig. 2a and b and supplemental Table 1, supplemental Figure 1). Histological evaluation of H&E stained brain sections from three separate locations around the needle tract showed substantial early tissue damage at day two (Fig. 2c and Table 1) and more subtle late changes at day 21 (Fig. 2d and Table 1). There were no differences between 10% ethanol and vehicle-treated brain tissues.

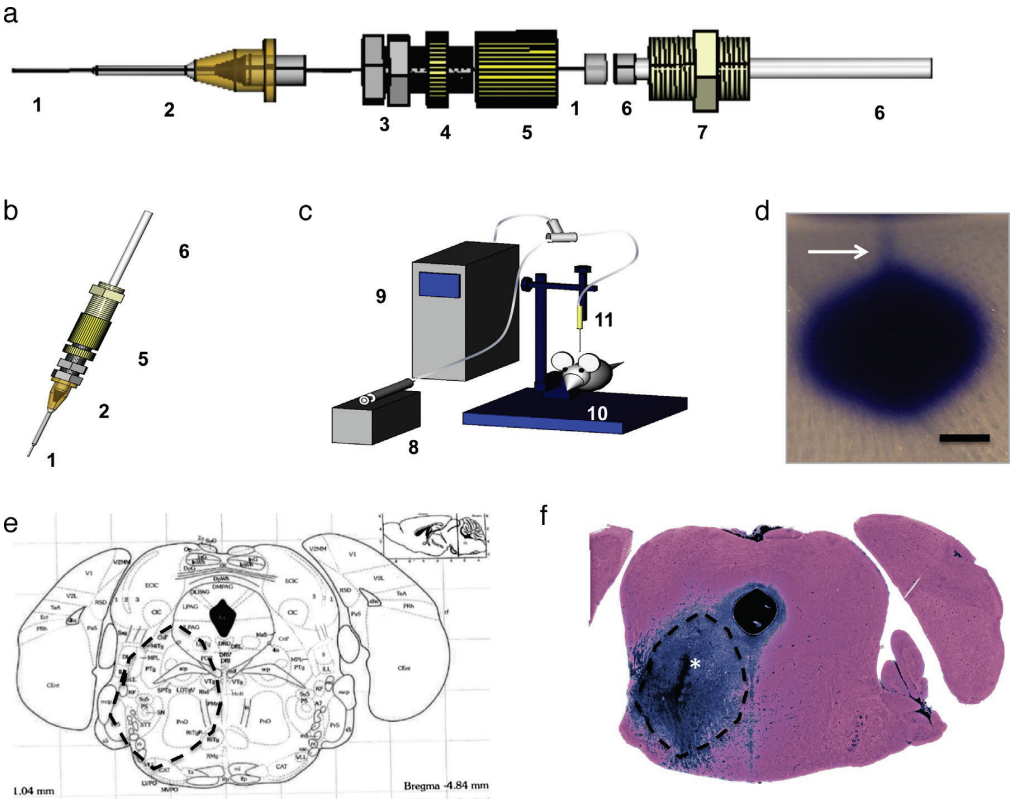

Figure 1 (a) Stepped design CED catheter with separate parts shown (b) stepped design CED catheter 3D image (c) CED setup for *in vivo* convection-enhanced delivery. Legend (a–c): 1: inner cannula (32G needle, OD 0.24 mm, ID 0.11 mm); 2: guide needle (25G, OD 0.52 mm, ID 0.26 mm); 3: nuts (for fixation in the stereotactic frame); 4: blocking screw; 5: adjusting screw (part one); 6: flexible catheter; 7: adjusting screw (part two); 8: infusion pump; 9: pressure transducer; 10 stereotactic frame; 11 stepped catheter (d) CED of trypan blue in 0.6% agarose gel. The arrowhead indicates minimal backflow of trypan blue after termination of CED. Scale bar: 1 mm. (e) Anatomy of the mouse brainstem at the level of the pons from Franklin & Paxinos: the mouse brain in stereotaxic coordinates[200]. (f) Image of the brainstem of a balb/c mouse sacrificed directly after CED of trypan blue

counterstained with eosin corresponding to (e) Asterisk shows needle-track (e) dotted line shows infused area in (e and f). The area infused contains intended pontine regions including the pontine reticular nucleus, motor and sensory nucleus of the trigeminal nerve, superior olivary complex and to a lesser extend areas outside the pons including the superior cerebellar peduncles and bordering on the periaqueductal gray matter[200]. Contrast in this picture was enhanced using Adobe Photoshop Elements 11.

Dissolving carmustine in 10% ethanol increases its efficacy *in vivo*

To enable translation to the clinic, we investigated whether this significantly increased survival could be further improved by dissolving carmustine in 10% ethanol and used the well-established E98FM-DIPG orthotopic mouse model. Accordingly, we injected E98-FM cells into the murine pons as previously described [197]. Some mice experienced transient clinical symptoms after injection of E98-FM cells, but no differences were detected between groups (Fig. 3e–h). At day seven to nine, depending on BLI signal, mice bearing E98FM tumors were treated with either carmustine dissolved in 5% DW or vehicle (5% DW) or carmustine dissolved in 10% ethanol or vehicle (10% ethanol). It should be noted that the differences in BLI between the groups were relatively large, despite not being statistically significant (Table 2). Due to the CED procedure, clinical scores rose transiently in some animals (Fig. 3e–h) and in vehicle treated groups, mice rapidly deteriorated due to tumor growth, starting at day 14 (Fig. 3e and f). Mice treated with CED of carmustine dissolved in ethanol demonstrated a significant decrease in tumor growth two weeks after CED, measured by bioluminescent imaging ($p < 0.05$) (Fig. 3i and j). CED of carmustine dissolved in 5% DW significantly increased median survival time with 25% compared to CED of 5% DW only ($p < 0.01$) (Fig. 3k). In comparison, CED of carmustine dissolved in 10% ethanol increased median survival time by 45% ($p < 0.01$) and resulted in one animal without any clinical symptoms or measurable BLI signal after 60 days of follow up (Fig. 3k). Dissolving carmustine in 10% ethanol instead of DW 5% increased survival by 36% ($p < 0.05$). CED with 10% ethanol vehicle itself did not increase survival significantly compared to CED with 5% DW ($p = 0.15$). HPLC–UV measurements before and after CED in both vehicles showed availability of carmustine to be 30% higher when using 10% ethanol compared to 5% DW as vehicle ($p < 0.05$). Carmustine concentration was similar when measured after the CED procedure, suggesting chemical stability in both vehicles (supplemental figure 2).

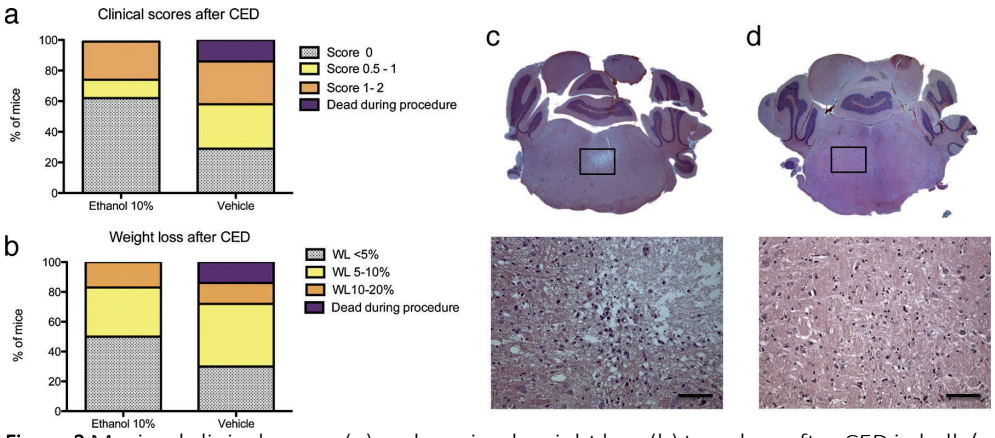

Figure 2 Maximal clinical scores (a) and maximal weight loss (b) two days after CED in balb/c mice treated with CED of 15 µl 10% ethanol or vehicle (distilled water). (c) H&E staining from a 5 µm brain section cut in the coronal plane approximately 100 µm posterior from the needle tract two days after CED of 15 µl 10% ethanol in an 8 weeks old Balb/c non-tumor bearing mouse. Higher magnification shows loss of tissue and necrotic nuclei. (d) Section in the coronal plane 50 µm posteriorly from the needle tract, 3 weeks after CED of 15 µl 10% ethanol. Changes include glial scaring, macrophage influx and some loss of tissue. Scale bars are equal to 100 µm.

	Acute (day 2 after CED)	**Chronic (day 21 after CED)**
Ethanol 10%	Necrosis, oedema and loss of tissue around the needle tract (N=4)	Inflammation (macrophages), glial scaring, some loss of tissue around needle tract (N=4)
Vehicle	Necrosis, oedema and loss of tissue around the needle tract (N=3) Severe necrosis and tissue loss (N=1)	Inflammation (macrophages), glial scaring, some loss of tissue around needle tract (N=4)

Table 1: Histological findings 2 or 21 days after CED with 10% ethanol or vehicle

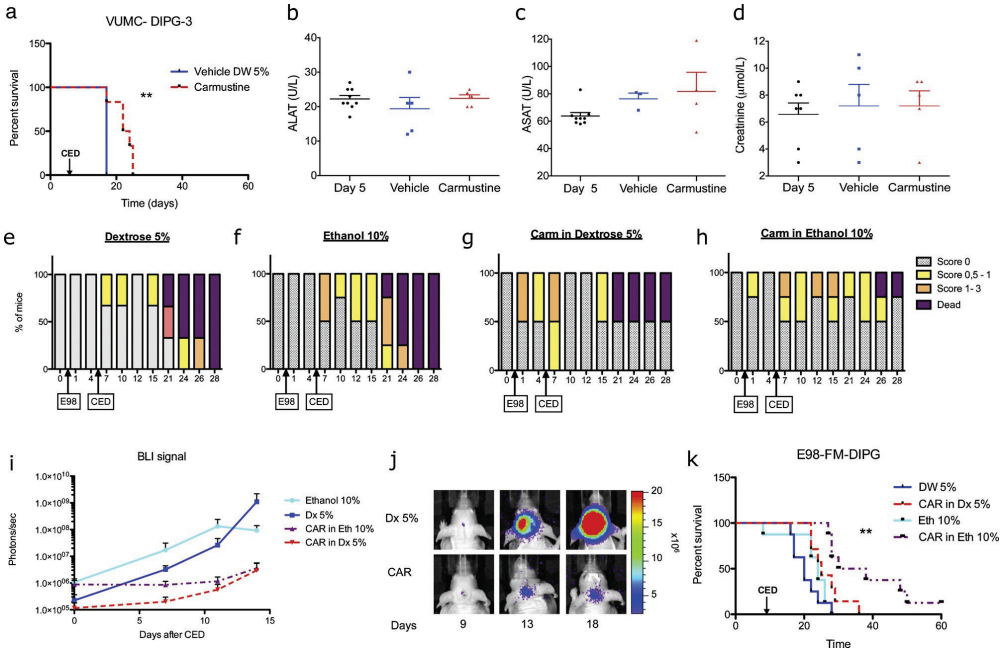

Figure 3 Kaplan–Meier survival curves of mice bearing VUMC-DIPG-3 tumors treated with CED of carmustine 5% dextrose (red) or vehicle 5% dextrose (blue) Arrow indicates day of treatment with CED; $^{**}p < 0.01$ (b–d) ALAT, ASAT, and creatinine blood values from all mice bearing VUMC-DIPG-3 tumors at the day of CED treatment and seven days later, n.s. = not significant. Error bars indicate standard error of the mean (SEM). (e–h) Clinical scores of a representative group (total $n = 14$) of E98FM bearing mice treated with CED from day 0 (before implantation of E98FM cells) until day 28. Clinical scores refer to 0: normal active behavior, 1: subtle inactivity or subtle neurological symptoms, 2: mild to moderate inactivity or neurological symptoms, 3: severe neurological symptoms, inactivity, loss of reflexes, inadequate grooming, 4: dead. Transient symptoms after IC-injection of E98FM cells and CED, clinical score rapidly increasing from day 12 in vehicle groups. No increase of clinical score in carmustine-treated animals. No difference in CED-associated clinical scores between treatment groups. (i) Firefly luciferase bioluminescence imaging of E98-FM DIPG tumor bearing mice treated with CED of carmustine (dissolved in 10% ethanol or 5% DW) or vehicle over time; $^{*}p < 0.05$, Kruskal–Wallis nonparametric test. (j) Representative bioluminescence images of E98-FM DIPG tumor bearing mice treated with either Carmustine 5% DW or 5% DW. Color bar represents photons/second. (k) Kaplan–Meier survival curves of mice bearing E98FM-DIPG tumors treated with CED of carmustine 5% DW (red), carmustine 10% ethanol (purple) or vehicle 5% DW (blue) or 10% ethanol (cyan). Arrow indicates day of treatment with CED; $^{**}p < 0.01$.

DISCUSSION

In this study, we show for the first time that CED in the mouse brainstem is reproducible, safe and has potential to show a significant survival benefit. The methods and results presented here set the foundation for future preclinical studies in orthotopic DIPG mouse models, including efficacy and distribution studies using different therapeutic agents and drug carrier systems such as liposomes. As stated earlier, no significant improvement in survival has been achieved for children affected by DIPG in the last 40 years. Unlike other gliomas that present a leaky BBB, the permanence of an intact BBB could in part explain DIPG resistance to therapeutic agents delivered systemically [202]. Whether potential chemotherapeutic agents actually reach the tumor after systemic delivery is largely unknown and should be further studied using advanced molecular imaging techniques such as positron emission tomography (PET) scans or experimental systems. When therapeutic levels of agents, shown to be effective *in vitro*, cannot be established in the tumor due to the effects of the BBB or dose-limiting toxicity, CED may overcome these issues [175,179]. Therefore, CED is anticipated to play an important role in future potentially successful treatment regimens, intensifying the need for *in vivo* techniques to study CED in the brainstem. Currently, clinical CED is performed in phase I/II clinical trials in children with DIPG. Lonser et al. treated a four-year-old DIPG patient with fusion protein interleukin 13 – pseudomonas exotoxin (IL-13-PE) (volume 1.4 ml in 6 h with infusion rate 0.5–10 µl/min) at time of progression. The patient showed only transient worsening of symptoms and died four month after infusion [53]. Anderson et al. treated two children age five and six years with topotecan (volume 6.04 or 5.3 ml in ± 100 h, infusion rate between 0.3 and 2 µl/min). Both children did show only transient worsening of neurological symptoms after the CED procedure [186]. Follow-up MRI showed a slight decrease of tumor size, but the patients did not experience prolonged survival. Barua et al. reported treating a 5-year-old DIPG patient with CED of carboplatin (volume 9 ml in 20 h, five times in nine days, with infusion rate 0.5–10 µl/min) at tumor progression. One month after treatment the patient showed mild clinical improvement and MRI changes that could be attributed to tumor necrosis. The patient died two month after CED from tumor progression outside the field of infusion [187]. Even though clear progress has been made in demonstrating the feasibility of CED in DIPG patients, many questions remain that could be answered by *in vivo* studies. Although our preclinical CED setup was designed to mimic the clinical situation as accurately as possible, infusion time difference varies significantly between clinical CED and preclinical CED as presented here. This difference is caused by limitations in the acceptable duration of anesthesia in mice. Implanting flexible catheters that remain

in the brain parenchyma of the mice would allow for continuous administration without anesthesia. This infusion technique has been performed in the rat brainstem [203], but due to the size of the murine brainstem this will be technically challenging. It could be argued that the small size of the murine brainstem also limits studying the benefits of convection in CED, because small molecules can, in time, diffuse over relative anatomical distances in this model. However, since the biological half-life of carmustine is relatively short, our method still poses an unique opportunity to study the efficacy of drugs such as carmustine *in vivo* orthotopically.

	Median BLI at start CED	Days after IC-injection	Total N
Ethanol 10%	1.10E+06	7 - 8	8
Dextrose 5%	6.59E+04	7 - 9	7
CAR in Ethanol 10%	5.91E+05	7 - 8	8
CAR in Dextrose 5%	9.44E+04	7 - 9	8

Table 2: Median BLI of E98FM-DIPG at start CED

We show CED with carmustine using 5% DW as a vehicle to be effective in a primary model of DIPG, however carmustine dissolved in ethanol 10% proved significantly more effective. Adequate distribution of a therapeutic agent is key to the efficacy of locally delivered therapy. Chemical structure (large molecules) and solvability (lipophilicity) of the infused compound can negatively influence volume of distribution in tissue after CED [201]. Carmustine is a lipophilic drug that, for intravenous use and for local delivery, including into brain tumors, has long been dissolved in 100% ethanol to improve delivery [195]. Using 100% ethanol allowed for safe intra-tumoral injection up to a carmustine concentration of 60 mg/ml in GBM patients, although adverse events of 100% ethanol were reported when used for intra-arterial delivery [195]. Currently it is thought that a minimum of 10% ethanol or 5% DW solution with pH <4, can be used as a vehicle for carmustine, up to a maximum concentration of 3.3 mg/ml [195]. Both vehicles will maintain the stability of the drug, however the safety and efficacy of CED with 10% ethanol in the brainstem is unknown. It has been noted that carmustine in 5% DW remains a suspension, possibly influencing the distribution of the compound and thereby its efficacy. In this study efficacy significantly improved upon dissolving carmustine in 10% ethanol. This improvement is likely due to a better solvability and sub-sequential availability of the drug and is

therefore of preference in a clinical setting. Of note in this respect, 10% ethanol could be administered to the normal murine brainstem without additional clinical or histological abnormalities. Murine studies like these will enable faster and more effective translation to the clinic and our results encourage exploring the possibility of a clinical trial studying CED of carmustine in DIPG.

Funding

This work was supported by the Semmy foundation and KIKA (research project number 69), Children Cancer-Free (http://www.kika.nl and http:// www.stichtingsemmy.nl)

Acknowledgements

We are thankful to Fred Buijs (Department of Nuclear Medicine & PET Research) for technical support with CED, to Professor Pieter Wesseling, M.D. (Department of Pathology VUMC) for histological assessment of murine brain tissue after CED, Fatma El-Khouly and René Vos (Department of Clinical Pharmacology, VUMC) for the measurements of carmustine concentration and to Thomas Würdinger, PhD. (Neuro-oncology Research Group, VUMC) for critical revision of the manuscript.

CHAPTER 3 |

PRECLINICAL EVALUATION OF CONVECTION-ENHANCED DELIVERY WITH LIPOSOMAL DOXORUBICIN TO TREAT PEDIATRIC DIFFUSE INTRINSIC PONTINE GLIOMA AND THALAMIC HIGH-GRADE GLIOMA

A. Charlotte P. Sewing, Tonny Lagerweij, Dannis G. van Vuurden, Michaël H.Meel, Susanna J. E. Veringa, Angel M. Carcaboso, Pieter J. Gaillard, W. Peter Vandertop, Pieter Wesseling, David Noske, Gertjan J. L. Kaspers, Esther Hulleman

Published in: J. Neurosurg. Pediatr. 2017;19(5):518-530

ABSTRACT

Pediatric high-grade gliomas (pHGGs) including diffuse intrinsic pontine gliomas (DIPGs) are primary brain tumors with high mortality and morbidity. Because of their poor brain penetrance, systemic chemotherapy regimens have failed to deliver satisfactory results; however, convection-enhanced delivery (CED) may be an alternative mode of drug delivery. Anthracyclines are potent chemotherapeutics that have been successfully delivered via CED in preclinical supratentorial glioma models. This study aims to assess the potency of anthracyclines against DIPG and pHGG cell lines *in vitro* and to evaluate the efficacy of CED with anthracyclines in orthotopic pontine and thalamic tumor models.

The sensitivity of primary pHGG cell lines to a range of anthracyclines was tested *in vitro*. Preclinical CED of free doxorubicin and PEGylated liposomal doxorubicin (PLD) to the brainstem and thalamus of naïve nude mice was performed. The maximum tolerated dose (MTD) was determined based on the observation of clinical symptoms, and brains were analyzed after H&E staining. Efficacy of the MTD was tested in adult glioma E98-FM-DIPG and E98-FM-thalamus models and in the HSJD-DIPG-007-Fluc primary DIPG model.

Both pHGG and DIPG cells were sensitive to anthracyclines *in vitro*. Doxorubicin was selected for further preclinical evaluation. Convection-enhanced delivery of the MTD of free doxorubicin and PLD in the pons was 0.02 mg/ml, and the dose tolerated in the thalamus was 10 times higher (0.2 mg/ml). Free doxorubicin or PLD via CED was ineffective against E98-FM-DIPG or HSJD-DIPG-007-Fluc in the brainstem; however, when applied in the thalamus, 0.2 mg/ml of PLD slowed down tumor growth and increased survival in a subset of animals with small tumors.

Local delivery of doxorubicin to the brainstem causes severe toxicity, even at doxorubicin concentrations that are safe in the thalamus. As a consequence, the authors could not establish a therapeutic window for treating orthotopic brainstem tumors in mice. For tumors in the thalamus, therapeutic concentrations to slow down tumor growth could be reached. These data suggest that anatomical location determines the severity of toxicity after local delivery of therapeutic agents and that caution should be used when translating data from supratentorial CED studies to treat infratentorial tumors.

INTRODUCTION

Diffuse intrinsic pontine glioma (DIPG) and thalamic glioma are diffusely infiltrating midline gliomas, often harboring histone H3K27M mutations and most frequently observed in childhood [204]. These tumors have very high mortality and morbidity as effective treatment strategies still do not exist [205,206], despite significant progress in understanding the biological processes that play a role in the development and progression of these tumors [23,24,125,207–209]. Tumor cells are highly resistant to chemo- and radiotherapy, and the presence of the blood-brain barrier (BBB) prevents drugs from reaching the bulk tumor and infiltrating tumor cells in sufficient concentrations [22,210].

None of the clinical trials performed in DIPG and pediatric high-grade glioma (pHGG), which have used a large number of different chemotherapeutic agents such as cytostatic agents, targeted antibodies, and small-molecule inhibitors, has yet to show a clear benefit that can be translated to standard clinical practice [209,211]. Recently, preclinical research has identified pHGG and DIPG cell lines to be sensitive to a number of "classic" cytostatic agents, especially some anthracycline drugs [170]. Anthracyclines are the cornerstones of many chemotherapeutic treatment regimens in a wide variety of cancer types in both adults and children [212]. They are, despite their assumed value, associated with serious adverse events, including debilitating or even life-threatening cardiotoxicity [213]. Almost all anthracyclines have been identified as strong substrates of ATP-binding cassette transporters (ABC transporters), P-gP, MRP1, and BCRP, causing limited brain penetration [214,215]. The limited brain penetrance of anthracyclines in brain tumors with an intact BBB, such as diffuse gliomas, may also explain these agents' lack of efficacy when used in the treatment of pHGG including DIPG.

Convection-enhanced delivery (CED) is a local delivery technique that is being considered a potential drug delivery strategy in DIPG and other brain tumors as it circumvents the BBB [53,63,186,187,201,216]. Drug distribution is facilitated by a pressure gradient at the tip of the infusion catheter, resulting in bulk flow through the interstitial spaces of the brain [217,218]. However, choosing the right drug to administer via CED is difficult: it should be effective against pHGG cells, have favorable chemical properties to enable adequate distribution, and give no or limited toxicity in healthy brain tissue [187,201,218]. Using liposomal formulations of a drug can potentially improve distribution, bioavailability, biological half-life, and efficacy after CED, as suggested by several preclinical studies [219–222].

In the present study, we aimed to investigate the translational potential of anthracyclines in the treatment of DIPG and pHGG using CED. Preclinical animal studies have already shown the potential for local delivery of anthracyclines to treat brain tumor models, but no study has investigated the administration of these chemotherapeutic drugs directly to the pons or thalamus [220,221]. We studied the efficacy of different anthracyclines *in vitro* and determined

the feasibility of delivering these agents to delicate brain areas such as the brainstem and thalamus. Subsequently, we investigated the efficacy of nanoliposomal and free anthracyclines in treating orthotopic high-grade tumors in the brainstem and thalamus *in vivo*.

MATERIALS and METHODS

Expression of Topoisomerase Type IIA in DIPG and pHGG

Because topoisomerase Type IIA (TOPIIA) expression is associated with a good clinical response to treatment with anthracyclines in a number of cancer types [223,224], *TOPIIA* mRNA expression in DIPG (n = 27) [225] and pHGG (n = 53) [226] was determined *in silico* by using publicly available data sets and compared with a data set of nonmalignant brain tissue (44 tissue samples) [227], low-grade brainstem glioma (LG-BSG; 6 samples) [225], and adult HGG (284 samples)[228]. These data sets included tumor material from biopsy (adult and pediatric HGG and DIPG), resection (adult and pediatric HGG), and autopsy (DIPG). All expression analyses were performed using R2, a web-based microarray analysis and visualization platform (http://r2.amc.nl).

Processing of Tumor Material and Cell Cultures

Single-cell cultures were established from biopsy samples derived from pediatric glioblastoma multiforme (GBM), anaplastic astrocytoma, anaplastic oligodendroglioma, and DIPG. Informed consent was obtained according to institutionally approved protocols. Tumor pieces were collected into DMEM (PAA Laboratories GmbH) and washed twice with phosphate-buffered saline (PBS) to remove blood clots. Samples were sliced into small (3–5 mm^3) pieces and either mechanically dissociated by filtering through a cell strainer (BD Falcon Biosciences) or dissociated by incubation with Accutase (PAA Laboratories GmbH). Single cells were seeded in DMEM-F12 constituted with stable glutamine, 10% fetal bovine serum (Perbio Science Nederland B.V.), 1% penicillin-streptomycin (PAA Laboratories GmbH), and 0.5% sodium pyruvate. For primary astrocytes, 15% fetal bovine serum was used. Cells were grown at 37°C in a 5% CO_2 humidified atmosphere. Primary cell cultures were genetically characterized using karyotyping or array comparative genomic hybridization (CGH), as previously described by Veringa et al [170]. The primary HSJD-DIPG-007 cell line was established from DIPG material obtained at Hospital Sant Joan de Déu (Barcelona, Spain) from a 6-year-old patient after autopsy and was confirmed to have an H3F3A (K27M) and ACVR1 (R206H) mutation [229]. The HSJD-DIPG-007-Fluc was cultured in serum-free tumor stem medium, as previously described[230].

Drug Treatment

The primary pediatric glioma and astrocyte cultures were exposed to different anthracycline drugs (idarubicin, epirubicin, mitoxantrone, doxorubicin, and daunorubicin) at concentrations ranging from 0.01 to 1000 nM. A total of 1500 cells were seeded per well in 96-well tissue culture plates. After 96 hours, cell survival was assessed with the Acumen eX3 laser cytometer (TTO Labtech) using 300 mM of DAPI (Sigma-Aldrich) as readout. Results were analyzed using Acumen Explorer software, calculating the survival percentage for each compound tested in the assay. Each experiment was performed at least 4 times.

Drugs

Clinical formulations of the idarubicin, epirubicin, and daunorubicin used for the *in vitro* drug screens were supplied by the Department of Pharmacology of the VU University Medical Center (VUMC). Free and PEGylated liposomal doxorubicin (PLD) were supplied by 2-BBB Medicines BV. The PLD was prepared according to the commercial doxil/caelyx preparation method, that is, using active doxorubicin loading against an ammonium sulfate gradient, as previously described [231]. Mean liposome size was 95 nm and contained 2 mg/ml of doxorubicin, more than 90% of which was encapsulated in the liposomes. The liposomes were stored in liposome buffer (9.4% sucrose with histidine, 1.55 mg/ml; Sigma-Aldrich) at 4°C for no longer than 3 months after production. The vehicle was previously shown to be nontoxic in mice [231]. For details on the stability of doxorubicin and its liposomal formulation, we refer to previously published data by Barenholz and Gaillard et al. [231,232]

Animals

Animal experiments were performed in accordance with the Dutch law on animal experimentation, and the protocol was approved by the committee on animal experimentation of the VUMC. Athymic nude-foxn1^{nu} mice (6 weeks old, total of 112 mice used in all experiments) were purchased from Harlan, were kept under filter top conditions, and received food and water ad libitum.

Orthotopic DIPG Mouse Models

The E98 adult GBM cell line[233] was transduced to express firefly luciferase (Fluc) and mCherry (E98-FM cells) and cultured in DMEM supplemented with 10% fetal calf serum and penicillin-streptomycin. These cells were injected subcutaneously into female athymic nude mice (6–8 weeks of age, 1 mouse per batch of intracranially injected cells) to expand the number of cells [197]. When the subcutaneous tumor reached a diameter of 1 cm, the tumor was removed, and a single-cell suspension was prepared by mechanical disruption through a 100-µm nylon cell strainer. The HSJD-DIPG-007-Fluc cells were injected directly from culture after mechanical dissociation and counting. The cells were washed once with PBS and concentrated to 10^5 cells/µl (both E98-FM and HSJD-DIPG-007-Fluc). Mice were

stereotactically injected with 5 − 10^5 cells in a final volume of 5 µl into either the pons (x: −1.0 mm, y: −0.8 mm, and z: 4.5 mm from the lambda) or the thalamus (x: 1.5, y: −2, and z: −3.2 from the bregma). Coordinates were based on *The Mouse Brain in Stereotaxic Coordinates* by Franklin and Paxinos [200] and were previously validated using injections of trypan blue (data not shown).

Convection-Enhanced Delivery i*n vivo*

The CED procedure was performed using a stepped catheter specifically designed for this purpose (Fig. 1A), as we have described elsewhere [234]. *In vivo* targeting of the brainstem was determined by infusion of trypan blue via CED (Fig. 1C), and MRI was performed after infusion of 15 µl of gadolinium 5 µM (Dotarem, Guerbet; Fig. 1D). Imaging was performed on 3 mice anesthetized with isoflurane inhalation (1.5 L O_2 /min and 2.5% isoflurane) using a preclinical PET-MRI system (nanoScan system, Mediso Medical Imaging Systems). The T1-weighted images were acquired and analyzed using MIPAV software (Medical Image Processing, Analysis, and Visualization, version 7.2.0, National Institutes of Health). To perform *in vivo* CED, animals were injected with buprenorphine 0.05–1 mg/kg and anesthetized with isoflurane 2%–3% in 100% O_2 . After placing the animals in a stereotactic frame on a heated platform (37°C), we introduced the CED catheter into the pons (30 mice for toxicity studies, 24 mice for efficacy studies) or thalamus (9 mice for toxicity studies, 24 mice for efficacy studies; Fig. 1B). The coordinates used for CED were the same as those used for intracranial injections. During 30 minutes, a total of 15 µl of free doxorubicin, PLD, or vehicle was infused in the murine brain with a flow velocity of 0.5 µl/min. After the procedure, animals were returned to their cages to recover and resumed normal active behavior within 3–12 hours.

Toxicity Study

Convection-enhanced delivery toxicity (3 mice per dose and location) of 0.02 mg/ml (35 µM, pons), 0.2 mg/ml (345 µM, pons and thalamus), or 2 mg/ml (3448 µM, pons) of doxorubicin or PLD was determined based on clinical observations, including weight loss and clinical score. Clinical scores ranged from 0 to 4 and referred to normal active behavior (0); subtle inactivity or subtle neurological symptoms (1); mild to moderate inactivity or neurological symptoms (2); severe neurological symptoms, inactivity, loss of reflexes, and inadequate grooming (3); and death (4). Half-point scores were assigned to mice that were behaving in a manner between 2 scores. End points due to toxicity were defined as weight loss more than 15%, severe neurological symptoms, or severe inactivity. When none of these clinical end points were met, mice were euthanized 6 weeks after CED to determine histological toxicity. The maximum tolerated dose (MTD) was selected based on clinical features after treatment of 3 mice (no end point reached in all 3 animals, no clinical score > 2).

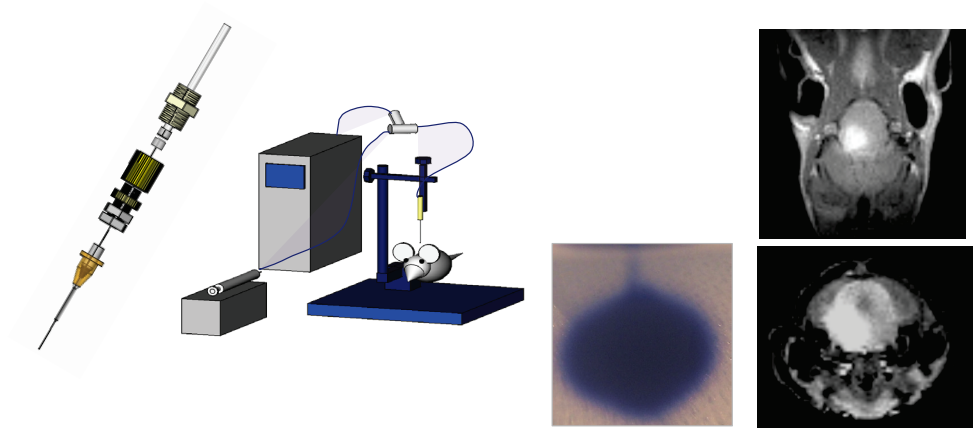

A CED catheter **B** *in vivo* CED setup **C** Trypan blue **D** T1 CED gadolinium

Figure 1. Schematic overview of preclinical CED including CED catheter (A) and stereotactic infusion setup (B). Infusion of 15 µl of trypan blue to the selected stereotactic coordinates (C, upper) and in agarose gel (C, lower). T1-weighted MR images (D) obtained directly after infusion of 15 µl of gadolinium. Panels A, B, and C reprinted from Sewing et al: *J Neurosci Methods 238:*88–94, 2014.

Convection-Enhanced Delivery and Intravenous Efficacy Studies

The start of treatment was determined by a rise in the bioluminescent imaging (BLI) signal, indicating tumor engraftment and growth. At Day 7 or 8 after intracranial injection of tumor cells to establish orthotopic brain tumors, mice were stratified on the basis of BLI signal intensities into different treatment groups. For the CED studies, animals harboring a pontine (E98-FM-DIPG or HSJD-DIPG-007-Fluc) or thalamic (E98-FM-thalamus) tumor were assigned to undergo CED of 0.02 mg/ml (35 µM) or 0.2 mg/ml (345 µM) of free doxorubicin or PLD, or vehicle (NaCl 0.9%; 4 mice for pons, 8 mice for thalamus per treatment group). For the intravenous studies, mice (4 per group) were assigned to receive PLD (18 mg/kg, once a week for 2 weeks) or vehicle (NaCl 0.9%) injected intravenously into the tail vein (3 mice/treatment group). Dosing was performed at the previously described MTD [235]. Follow-up included daily observations, assignment of clinical scores, and weight measurement as well as twice weekly measurement of the BLI signal (E98-FM). End points were defined as weight loss more than 15%, severe neurological symptoms, or severe inactivity. Researchers were blinded to treatment group. Mice were euthanized via pentobarbital overdose. Brains were removed and fixed in 3.7% PBS-buffered formaldehyde. Differences in survival were analyzed with Kaplan-Meier curves and log-rank tests for significance. Nonparametric Kruskal-Wallis test followed by Dunn's post hoc test was used to determine differences in the BLI signal. A p value < 0.05 was considered statistically significant.

Tissue Staining and Histological Scoring

Hematoxylin and eosin (H & E) staining was performed on 4-µm formalin-fixed, paraffin-embedded tissue sections cut in the coronal plane, using a standard H & E protocol. To determine histological toxicity in non–tumor-bearing animals, sections were selected at the site of the needle tract and 100 µm both rostrally and posteriorly. Two researchers (A.C.P.S. and T.L.) and an independent neuropathologist (P.W.) assessed tissue damage and inflammation. They were blinded to the experimental procedure that the animals underwent.

RESULTS

Anthracyclines as Promising Drugs to Treat pHGG and DIPG

Topoisomerase Type IIA was significantly overexpressed in pHGG and DIPG as compared with levels in LG-BSG and normal brain ($p < 0.01$; Fig. 2A and B). Cytotoxicity of clinically available anthracyclines was tested *in vitro* against pHGG and DIPG primary cells and showed moderate to excellent sensitivity with half maximal inhibitory concentration (IC50) values ranging from 1 µM to 10 pM (Fig. 2C–G). Doxorubicin proved to be particularly active against DIPG cells (Fig. 2G). Next, the potency of doxorubicin was tested against E98-FM cells, used to establish orthotopic E98-FM-DIPG and E98-FM-thalamus models[197,233], and normal human astrocytes, showing an excellent therapeutic window (Fig. 2H). For doxorubicin, used in subsequent *in vivo* experiments, IC50 values ranged from 1 nM in the VUMC-DIPG-A cell line to 0.8 µM in the VUMC-HGG-05 cell line. HSJD-DIPG-007-Fluc had an intermediate sensitivity profile (IC50 40 nM; Supplemental Fig. 2).

Clinical Toxicity of Doxorubicin Determined by Anatomical Location

Convection-enhanced delivery of high-dose (2 mg/ml) doxorubicin and PLD to the pons led to severe clinical toxicity (Fig. 3A). Severe symptoms occurred later after the CED procedure in the PLD-treated animals (6 days) than in the animals treated with free doxorubicin (1–3 days), and the difference in survival and weight loss was statistically significant ($p < 0.05$; Table 1 and Supplemental Fig. 1). Eventually, all animals treated with high-dose doxorubicin in the brainstem had to be euthanized because of unacceptable toxicity. Symptoms consisted of weight loss (> 15%) and neurological deficits including paresis and loss of balance.

Severe clinical toxicity still occurred with CED of medium-dose (0.2 mg/ml) doxorubicin to the pons. All animals in the free-doxorubicin group had to be euthanized. In the PLD group, 1 animal had to be euthanized because of severe symptoms and 1 animal had clear neurological symptoms but remained active, with weight loss within acceptable limits (< 15%); these neurological symptoms regressed after approximately 3 weeks (Table 1 and Fig. 3B).

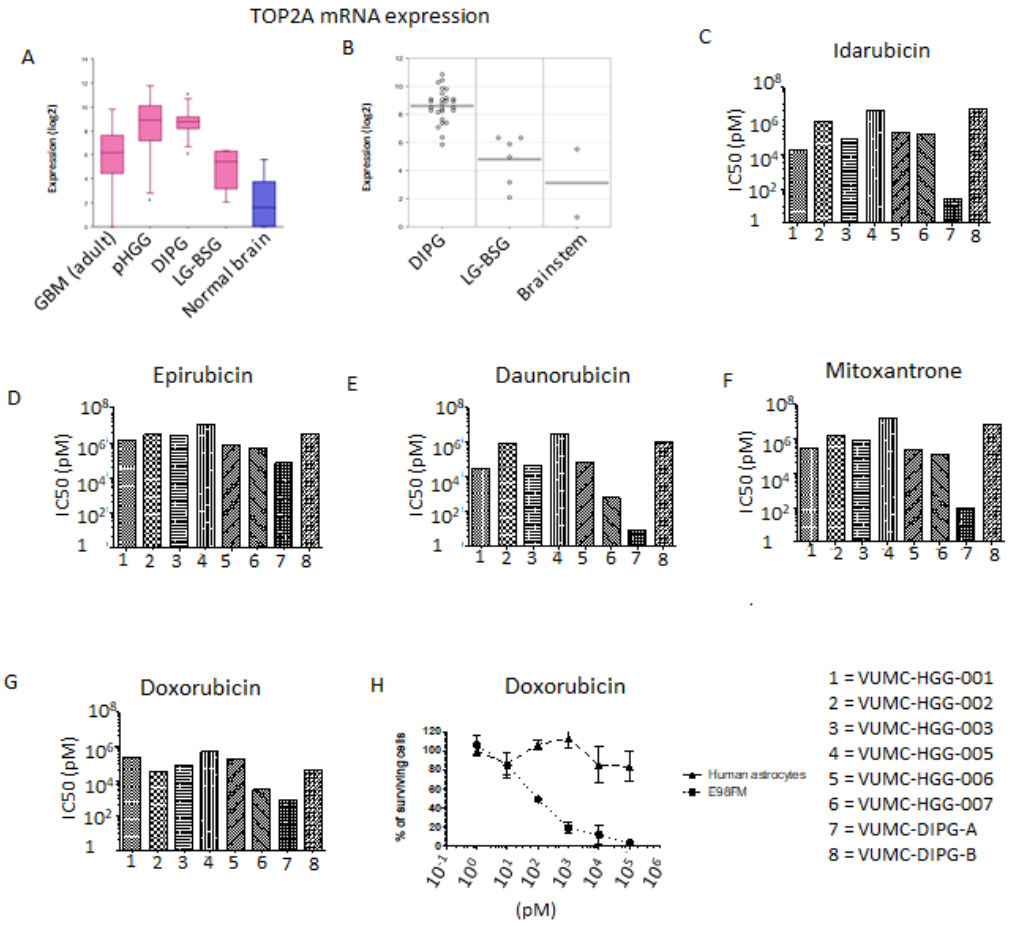

Figure 2. Expression of TOPIIA (A) in adult GBM, pHGG, DIPG, LG-BSG, and normal brain. TOPIIA expression (B) in DIPG, LG-BSG, and normal brainstem (individual cases plotted), as assessed by mining a publicly available database (http://r2.amc.nl). Sensitivity (IC50) of pHGG and DIPG cell lines to idarubicin (C), epirubicin (D), daunorubicin (E), mitoxantrone (F), and doxorubicin (G). Sensitivity of normal human astrocytes and E98-FM cells to doxorubicin (H). Numbers 1–8 refer to VUMC-HGG and VUMC-DIPG cell lines.

None of the animals treated with low-dose (0.02 mg/ml) doxorubicin or PLD to the pons showed significant clinical toxicity, as illustrated by the absence of clinical symptoms after CED (data not shown). In our experience, weight loss or inadequate weight gain in the animals is a sensitive symptom of toxicity, and all animals treated with 0.02 mg/ml showed normal weight gain after treatment (Fig. 3C). To find out the MTD of doxorubicin for injection into the pons, mice were treated via CED with doses of 0.1 and 0.04 mg/ml as well. These

doses still caused intolerable symptoms that were beyond the criteria set for MTD (clinical end point reached > 1 animal, clinical score > 2, data not shown).
Toxicity of CED of doxorubicin to the thalamus was significantly less pronounced. Medium-dose (0.2 mg/ml) free doxorubicin and PLD could be delivered to the thalamus without any clinical symptoms or weight loss (Fig. 3D). Given the severe toxicity seen after treatment with 2 mg/ml of doxorubicin to the pons, this dose level was not further assessed in the thalamus because of ethical considerations.

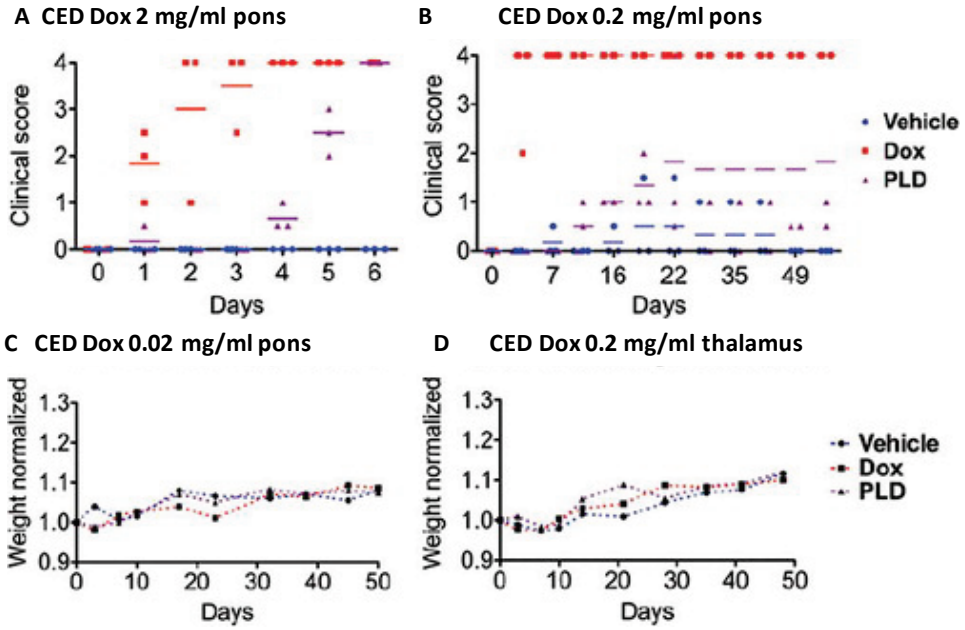

Figure 3. Clinical symptoms of mice treated via CED of doxorubicin (Dox) in the brainstem and thalamus. Clinical scores (0–4) of mice treated with high-dose (A, 2 mg/ml) or intermediate-dose (B, 0.2 mg/ml) free doxorubicin (*red*), PLD (*purple*), or vehicle (*blue*) in the brainstem. Normalized weight gain of mice (C) treated with vehicle, 0.02 mg/ml of free doxorubicin, or 0.02 mg/ml PLD in the brainstem. Normalized weight gain of mice (D) treated with vehicle, 0.2 mg/ml of free doxorubicin, or 0.2 mg/ml of PLD in the thalamus.

Location	Dose & Formulation	Euthanized After CED (days)
Pons	**High**	
	Doxorubicin	1–3
	PLD	5–6
	Middle	
	Doxorubicin	2–3
	PLD	20–56
	Low	
	Doxorubicin	56
	PLD	56
	Vehicle	56
Thalamus	**Middle**	
	Doxorubicin	56
	PLD	56
	Vehicle	56

Table 1. Number of days after CED that mice were euthanized because they reached the clinical end point or the end of follow-up

Histological Toxicity of CED Related to Dose and Formulation of Doxorubicin

After the mice were euthanized, their brains were histologically analyzed. Animals were euthanized 6 weeks after treatment unless they had to be euthanized at an earlier time point because of unacceptable clinical symptoms (CED to the pons with high- and medium-dose free doxorubicin and high-dose PLD; Table 1).In the pons tissues obtained 6 days after high-dose (2 mg/ml) PLD treatment, we consistently noted a sharply demarcated lesion with incomplete necrosis, dispersed macrophages, and relative sparing of the microvessels (Fig. 4A). In animals treated with high-dose free doxorubicin (2 mg/ml, clinical end point reached 1–3 days after treatment), lesions were much less circumscribed and showed insipient necrosis of intervascular tissue and more widespread spongy changes of the neuropil (Fig. 4B).

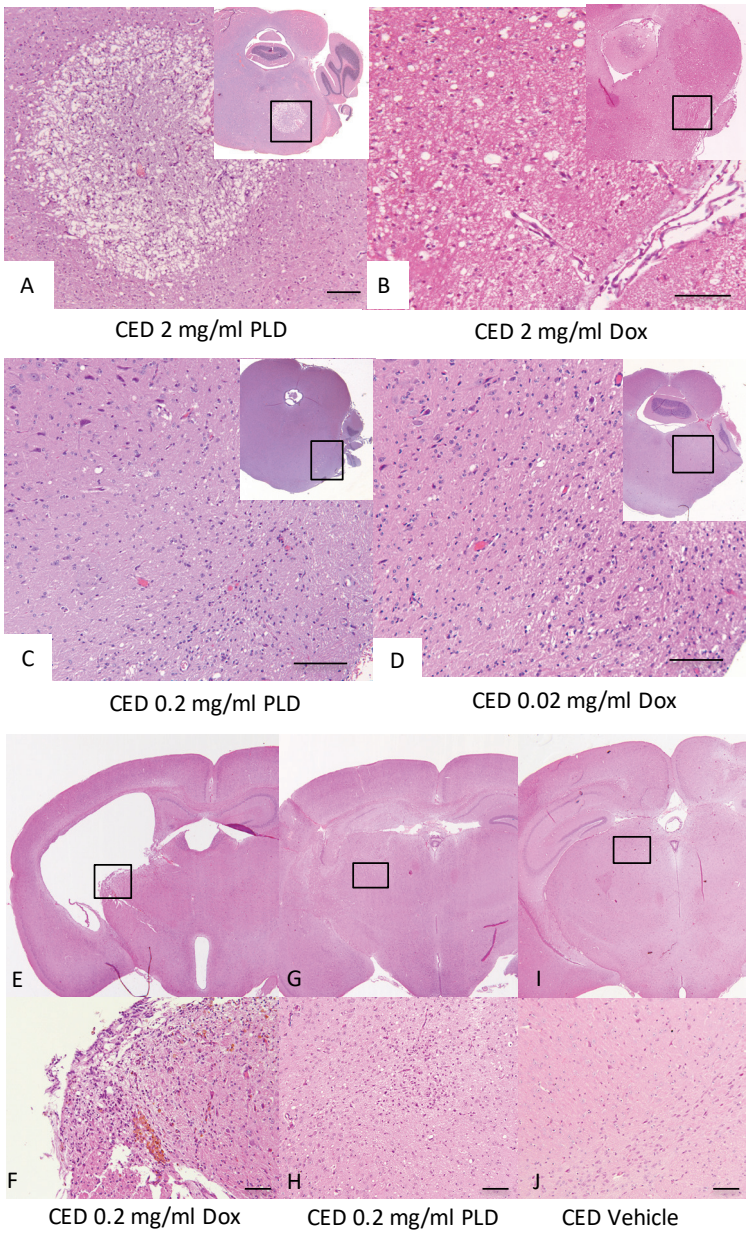

Figure 4. *Black squares* indicate enlarged areas. Brain slices from the pontine area of mice treated with 2 mg/ml of PLD (A), 2 mg/ml of free doxorubicin (B), 0.2 mg/ml of PLD (C), or 0.02 mg/ml of free doxorubicin (D). Brain slices from the thalamic area of mice treated via CED of intermediate-dose (0.2 mg/ml) free doxorubicin (E and F), PLD (G and H), or vehicle (I and J). H & E. Bar = 100 µm.

In brains treated with medium-dose (0.2 mg/ml) doxorubicin to the brainstem, the tissue damage was more variable. In sharp contrast to the functional neurological deficits demonstrated in these animals, histological abnormalities at 2–3 days after treatment were generally absent. After treatment with 0.2 mg/ml of PLD (brains analyzed 3–6 weeks after CED), some focal gliosis and deposition of iron pigment was found (Fig. 4C). Six weeks after treatment with low-dose (0.02 mg/ml) free doxorubicin, the brainstem showed only focal areas with more coarse texture, consistent with astrogliosis (Fig. 4D), similar to what was found in some of the animals treated with low-dose PLD or vehicle only. After 6 weeks of follow-up, brains treated with 0.2 mg/ml of free doxorubicin to the thalamus showed clear toxicity characterized by a variably circumscribed area of tissue decay, pericellular thickening of the walls of microvessels, some iron pigment deposition (partly in macrophages), and some proliferation of (myo)fibroblasts (Fig. 4E and F). Brains treated with 0.2 mg/ml of PLD still showed similar but less pronounced lesions (Fig. 4G and H). No histological abnormalities were detected in animals treated with vehicle to the thalamus (Fig. 4I and J).

E98-FM Cells and the Formation of Diffuse Infiltrative High-Grade Tumors in the Pons and Thalamus

Adult GBM-derived E98-FM cells have been described to grow as diffuse tumors in the pons, with histological and clinical features quite similar to human DIPG [197]. To study CED in diffuse HGGs in the thalamus, we established thalamic tumors using E98-FM cells. To this end, we injected E98-FM cells into previously validated thalamic coordinates and followed *in vivo* tumor growth using BLI. A subset of mice injected with E98-FM to the thalamus and pons were euthanized at set time points, and their brains were analyzed to study the size and histological features of the tumors (Fig. 5A–C and G–I). Others were followed until the previously determined clinical end point (weight loss, severe neurological symptoms, or severe inactivity; Fig. 5M and N). Histological assessment showed diffuse infiltrative tumors located in the thalamus with tumor size proportionate to the bioluminescence signal. Median survival of mice with E98-FM-thalamus was 23.5 days (8 mice; Fig. 5M); for those with E98-FM-DIPG, median survival was 22 days (6 mice; Fig. 5N).

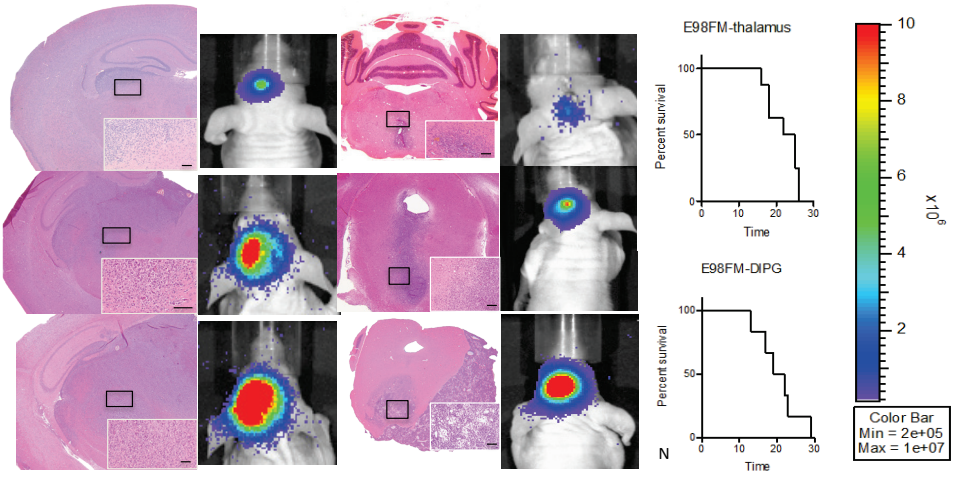

Figure 5. Validation of the E98-FM tumor model in the pons and thalamus. Progression of E98-FM tumors after injection to the thalamus or pons at Days 7 (A and G), 14 (B and H), and 21 (C and I). Corresponding BLI signals (D and J, E and K, and F and L, respectively) and survival curves (M and N). Eight mice per tumor line listed. Bar = 100 µm.

Treatment of E98-FM-DIPG and E98-FM-Thalamus with Free Doxorubicin or PLD

Both E98-FM-DIPG and HSJD-DIPG-007-Fluc, and E98-FM-thalamus tumors were treated via CED of free doxorubicin, PLD, or vehicle at the MTD determined in the previous toxicity experiments. The treatment and follow-up schedule are depicted in Fig. 6. Median survival of E98-FM-DIPG and HSJD-DIPG-007-Fluc animals treated with free doxorubicin or PLD at a low dose (0.02 mg/ml) did not differ significantly from animals treated with vehicle (Fig. 7A and G), and the bioluminescence signal was not significantly different for the E98-FM-DIPG and HSJS-DIPG-007-Fluc groups, regardless of treatment (Fig. 7B and H). Of note, one mouse with HSJD-DIPG-007-Fluc treated with PLD survived beyond the 90 days of follow-up. In mice with E98-FM-thalamus tumors treated with a medium dose (0.2 mg/ml), the bioluminescence signal of the tumors was significantly lower in the mice treated with PLD than in those treated with vehicle or free doxorubicin (Fig. 7D). Survival did not differ significantly for the whole E98-FM-thalamus tumor group, regardless of treatment; however, 2 of 8 animals treated with PLD had a prolonged decrease in BLI signal and prolonged survival (Fig. 7C). Treating mice with E98-FM-DIPG tumors with intravenous PLD did not significantly influence clinical course (Fig. 7E) or bioluminescence signal (Fig. 7F).

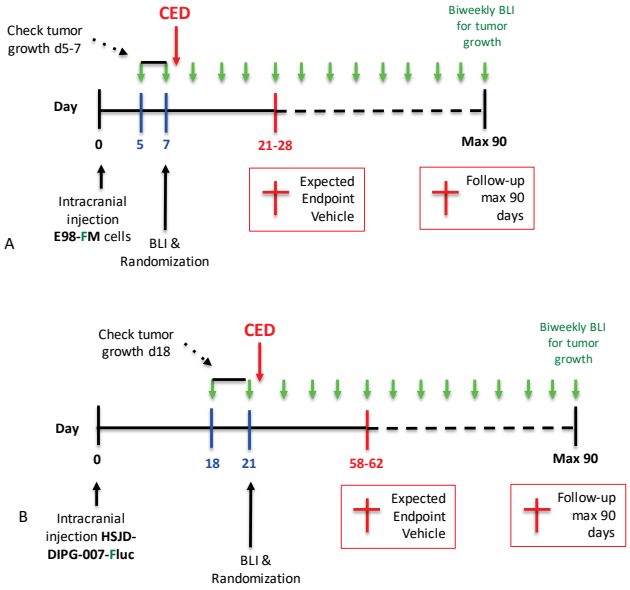

Figure 6. Schematic of the treatment and follow-up for E98-FM-DIPG and E98-FM-thalamus (A) and HSJD-DIPG-007-Fluc (B).

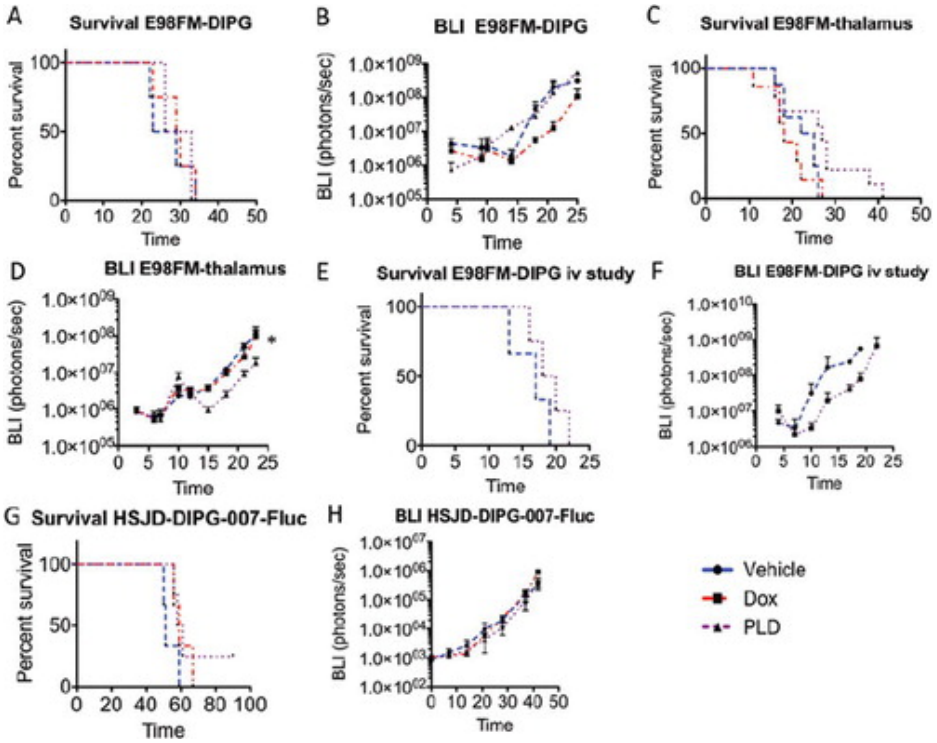

Figure 7. Survival and corresponding BLI data of mice with E98-FM-DIPG (A and B) or E98-FM-thalamus (C and D) treated with free doxorubicin (*red*), PLD (*purple*), or vehicle (*blue*). Survival (E) and BLI (F) data of mice treated with intravenous (iv) PLD or vehicle. Survival (G) and BLI (H) data of HSJD-DIPG-007-Fluc mice treated with 0.02 mg/ml of doxorubicin, PLD, or vehicle. *$p < 0.05$.

Influence of E98-FM Tumor Size on Efficacy of PLD Treatment via CED

In the efficacy study using E98-FM-thalamus orthotopic tumors, we found a significant difference in the bioluminescence signal in the 1st week after treatment with 0.2 mg/ml PLD and noticed a survival benefit in a small proportion (2 of 8) of the mice. To determine whether this survival benefit was due to a true treatment-dependent decrease in tumor burden or just a random occurrence, we studied these animals in more detail. One noticeable difference in animals that responded to treatment was a relatively low bioluminescence signal at the start of treatment. Even though the median BLI signal was not significantly different between groups, there was great variation in the signal at the start of treatment (Fig. 8A, D, and G). We studied the response of each individual animal in relation to the bioluminescence signal at the start of treatment. Thereto, we stratified mice into low ($< 10^6$photons/sec), medium ($< 10^7$ photons/sec), or high ($> 10^7$ photons/sec) tumor burden at the start of treatment. By doing so, we found that mice with E98-FM-thalamus tumors with a low tumor burden showed response to treatment with 0.2 mg/ml of PLD (Fig. 8F), while no responsive subgroup could be identified in the E98-FM-DIPG or HSJD-DIPG-007-Fluc tumors treated either via CED (PLD or doxorubicin; Fig. 8C and Supplemental Fig. 3) or intravenously (Fig. 8I). In these mice, the BLI signal rose exponentially without change, in a manner similar to that in vehicle-treated animals. This finding suggests that tumor size at the start of treatment has substantial influence on the efficacy of CED of PLD at the MTD in the thalamus but not in tumors in the pons treated at the MTD via CED or intravenously.

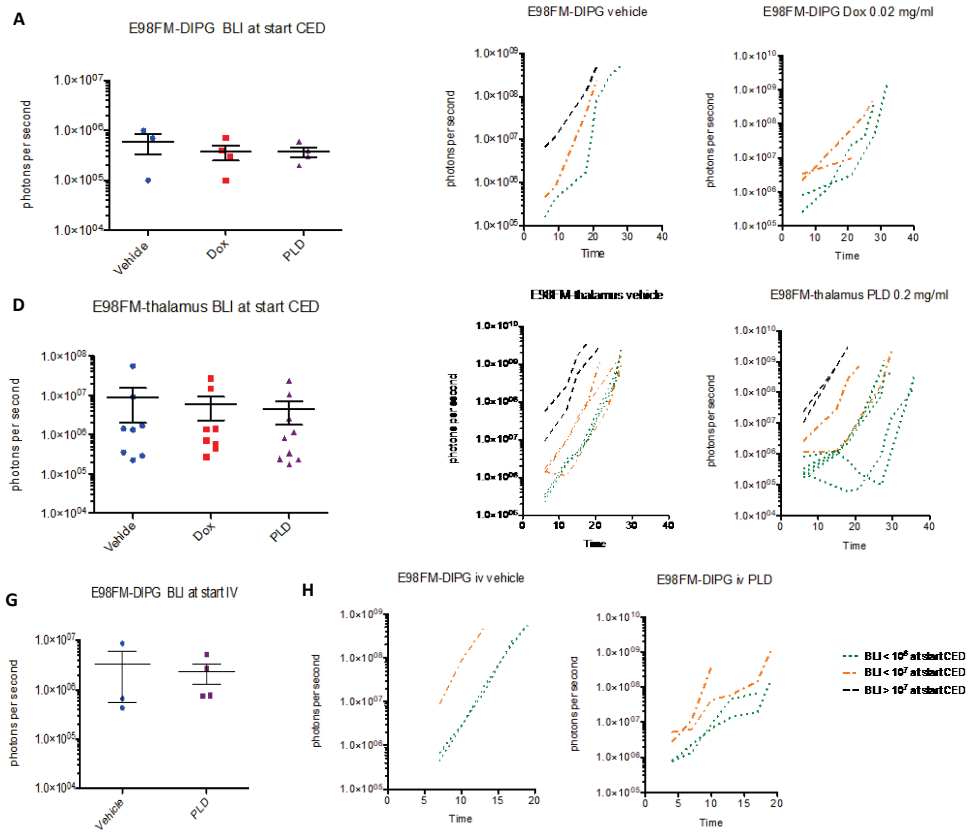

Figure 8. Bioluminescent imaging response at the start of CED for E98-FM-DIPG (A) or E98-FM-thalamus (D) or E98-FM-iv (G) treated with free doxorubicin (*red*), PLD (*purple*), or vehicle (*blue*). The BLI response of individual mice was related to the bioluminescent signal at the start of CED. E98-FM-DIPG treated with vehicle (B) or low-dose doxorubicin (C), E98-FM-thalamus treated with vehicle (E) or intermediate-dose PLD (F), or intravenous (iv) administration of vehicle (H) or PLD (18 mg/kg once a week for 2 weeks, I).

DISCUSSION

Using *in silico* and *in vitro* experiments, we identified anthracyclines as an interesting class of chemotherapeutics that could potentially be administered for the treatment of DIPG and pHGG. Topoisomerase Type IIA, previously shown to be correlated with anthracycline efficacy in patients [223,224], was highly expressed in both DIPG and pHGG compared with levels in normal brain and brainstem. Furthermore, we showed that pHGG and DIPG cells were sensitive to anthracyclines *in vitro*. The severity of toxicity after local delivery via CED, however, limits effective treatment *in vivo*.

Anthracyclines' method of action has not been fully elucidated but is thought to be multifactorial. The best-known effect of anthracycline drugs is the inhibition of TOPII, which is necessary to avoid supercoiling of DNA in dividing cells. Inhibition of TOPII leads to double-stranded breaks and subsequent cell death via apoptosis. Just a few clinical trials of anthracyclines have been conducted in children with pHGG, DIPG, or other recurrent or progressive brain tumors [235–237]. Results have been variable thus far. In one study, 4 of 8 patients with recurrent or progressive pHGG responded with stable disease for a period of 9–48 weeks on a regimen of PLD and oral topotecan, but the toxicity of this systemic treatment was high [237]. In another study, children with recurrent or progressive brain tumors were treated with liposomal daunorubicin, resulting in a treatment response in 6 of 14 children, with relatively mild toxicities [236]. Interestingly, our *in vitro* data showed that some DIPG cells (VUMC-DIPG-A) appeared to be ultrasensitive to 4 of 5 anthracyclines tested, with IC50 values well below those needed to treat all other cell lines in this panel and other glioma cell lines reported in the literature [238]. Only this particular cell line carries a mutation in histone gene *H3F3A* at lysine 27 (K27M) [24], which can be found in approximately 60% of DIPGs [23]. This mutation alters the organization of chromatin by the inability of EZH2 to trimethylate lysine 27. The absence of Lys27 trimethylation causes a more open chromatin structure and leads to gross changes in expression profiles of various cell types [6,239,240]. It was recently discovered that certain anthracyclines, including doxorubicin and daunorubicin, can cause histone eviction, especially in chromatin regions with an absence in trimethylation at lysine 27 [241]. This mechanism could potentially add to the sensitivity of *H3F3A*-mutated DIPG cells to anthracyclines. Further experiments to elucidate the role of histone eviction are beyond the scope of this paper. Unfortunately, the VUMC-DIPG-A cell line does not engraft after inoculation in the brain of mice and thus could not be used to perform the *in vivo* efficacy experiment. Therefore, another H3F3A K27M mutated cell line (HSJD-DIPG-007-Fluc), which was not part of our initial screen, was used. This cell line was intermediately sensitive to doxorubicin *in vitro*, but no efficacy of low-dose doxorubicin via CED could be established using our methods.

Despite their potential, these compounds' limited penetration of the brain after systemic delivery greatly constricts their clinical use in the treatment of brain tumors. In this study, we investigated the feasibility of using CED for local delivery of doxorubicin in the brainstem and thalamus. To our surprise, doxorubicin showed an MTD that was 100 times lower than the dose previously described to be safe for local delivery in the rat striatum [220]. In our experience, anatomical location clearly influenced clinical toxicity after CED. The tolerable dose when treating mice via CED of doxorubicin to the thalamus was 10 times higher than the MTD to the brainstem. Meanwhile, histological analysis of brains after CED showed similar tissue damage in the infused regions. Why this difference in toxicity occurs is not completely understood. We hypothesize that damage to the brainstem, including the pons, is more likely to produce functional deficits as compared with damage to structures in the thalamus, a phenomenon that is well known in human neurology. Of note, we only studied indirect distribution of doxorubicin by observing the spread of histological toxicity. In theory, it is possible that the distribution of free doxorubicin or PLD differs between the pons and the thalamus, causing differences in clinical presentation after CED. In this study, we also did not investigate more subtle defects in performance in mice treated with moderately high-dose doxorubicin in the thalamus. In doing so, we may have observed functional deficits that escaped our attention using basic observations. The expected tolerable dose in the thalamus still differed 10-fold from safe concentrations delivered to the striatum of rats described in the literature. Although toxicity after CED appears to be related to concentration and not total dose [242], this finding could still be explained by the use of a relatively large volume (15 µl) compared with the volume used in most CED studies using rats (average 20 µl). Furthermore, additional toxicity could be species or even strain related.

Liposomal formulation of doxorubicin gave rise to clinical symptoms in mice much later than did the free doxorubicin, but despite this lag time, free and liposomal doxorubicin had similar MTDs. The distribution of PLD was more sphere-like, as illustrated by the circumscribed lesions found in the brains of animals treated with high doses. The high protein affinity of free doxorubicin (nearly 98%) could lead to poor distribution, and the PLD used in this study should have had a nearly ideal size (100 nm in diameter [231]) for convection through the brain interstitial spaces [222]. Our data imply that PLD indeed gives a more gradual release of doxorubicin and a wider area of distribution after CED. Both effects may enhance efficacy of CED in patients.

The low-dose doxorubicin (MTD pons) was ineffective in treating a diffusely growing orthotopic DIPG model with a single delivery, suggesting that no therapeutic window could be reached and that a one-time infusion of doxorubicin via CED would most likely have no role in the treatment of DIPG. This result is contrasted by data from our *in vitro* experiments showing cytotoxicity at much lower *in vitro* IC50 values than those delivered to tumors *in vivo* (up to a theoretical million-fold difference) and a substantial difference in cell survival between E98-FM and normal human astrocytes (Fig. 2H). The difference between *in vitro*

efficacy and *in vivo* lack of efficacy could be attributable to inadequate coverage of the tumor due to inadequate distribution or fast efflux of doxorubicin from the brain by efflux pumps [243], causing a much lower area under the curve than with *in vitro* treatment. When using the 10-fold higher dose (MTD thalamus), PLD was effective in slowing down tumor growth in the thalamus. These findings suggest that data from supratentorial CED studies cannot be directly translated to design trials to treat infratentorial tumors and stress the need for selective agents to avoid excessive toxicity to healthy surrounding tissue, especially to treat tumors in delicate areas of the brain. One preclinical study has already shown that infusing the more targeted small-molecule inhibitors dasatinib, everolimus, and perifosine can be safely performed in the rat pons using long-term CED [244].

Using our methods, we were able to infuse a substantial area of the pons, but even when treating this area, CED was only effective when tumors were still very small. This is particularly problematic considering the small size of the murine pons compared with the human pons. Translating this knowledge to a clinical setting would imply treating only small, very-early-stage tumors. Since this is not the clinical reality of DIPG and thalamic HGG, CED will require drugs with a very high therapeutic index or long-term continuous infusions with lower-concentration drugs. To achieve the latter, it will be necessary to apply more sophisticated techniques such as using multiple infusion catheters and computer modeling for targeted infusion [187,245] or brain-penetrating nanoparticles with regulated release [222,244]. These projects are ongoing, and results from clinical studies are eagerly awaited. To advance CED to an effective treatment strategy for pHGG including DIPG will be a clinical, biological, and technical challenge requiring a comprehensive multidisciplinary approach.

Conclusions

In vitro studies showed that anthracyclines, especially doxorubicin, are effective against pHGG and DIPG cells, while sparing normal human astrocytes. Convection-enhanced delivery can be used to achieve an adequate concentration of doxorubicin at the site of the tumor. However, preclinical evaluation of CED with free and liposomal doxorubicin showed that no therapeutic window could be reached in the pons to locally treat diffuse orthotopic brainstem tumors in mice because of excessive toxicity. The administration of higher-dose doxorubicin in orthotopic tumors within the thalamus was tolerated and effective in slowing down tumor growth. This preclinical study raises awareness that results obtained from supratentorial CED studies cannot be directly translated to the treatment of infratentorial tumors.

Acknowledgments

This research was made possible by the support of the Semmy Foundation, the Stichting Kika (Children-Cancer-free), and the Egbers Foundation.

Supplementary Figures

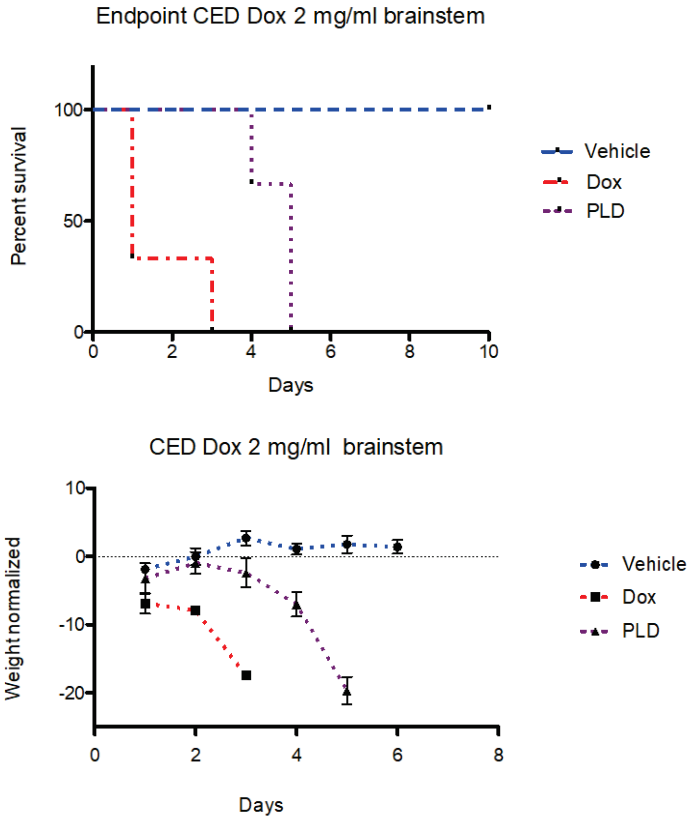

Supplemental Figure 1 (A) Kaplan-Meier curve of naïve mice treated with 2 mg/ml free doxorubicin (red), PLD (purple) or vehicle (blue) **(B)** Normalized weight curves of naïve mice treated with 2 mg/ml free doxorubicin (red), PLD (purple) or vehicle (blue)

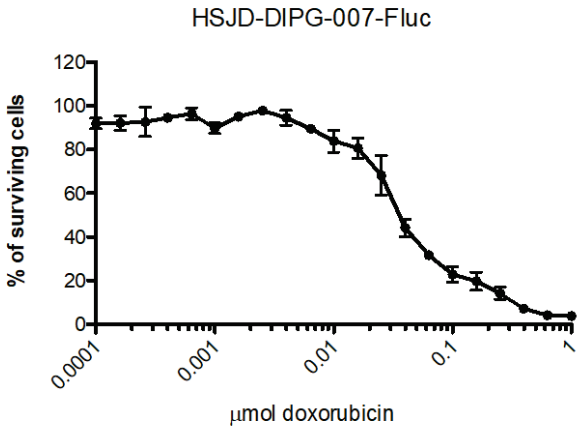

Supplemental Figure 2. *In vitro* sensitivity of HSJD-DIPG-007-Fluc to doxorubicin

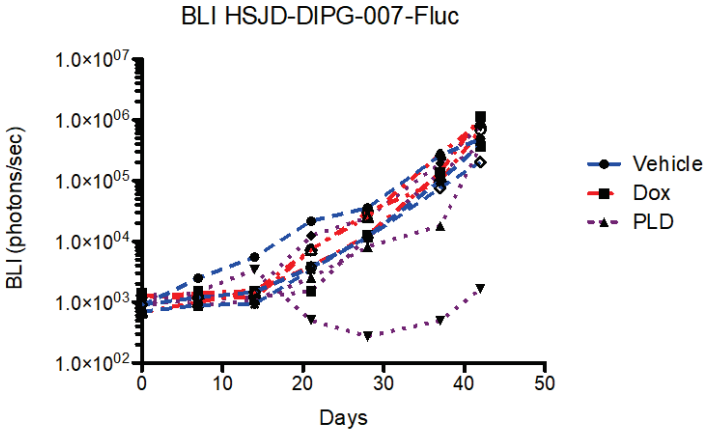

Supplemental Figure 3. BLI data of HSJD-DIPG-007-Fluc treated with doxorubicin, PLD or vehicle, plotted for each individual mouse and showing one long-term survivor treated with PLD.

CHAPTER 4 |

BEVACIZUMAB TARGETING DIFFUSE INTRINSIC PONTINE GLIOMA: RESULTS OF ^{89}ZR-BEVACIZUMAB PET IMAGING IN BRAIN TUMOR MODELS

T. Lagerweij*, A.C.P. Sewing*, M.H.A. Jansen*, D.J. Vugts, D.G. van Vuurden, C.F.M. Molthoff, V. Caretti, S.J.E. Veringa, N. Petersen, A.M. Carcaboso, D.P. Noske, W.P. Vandertop, P. Wesseling , G.A.M.S. van Dongen, G.J.L. Kaspers, E. Hulleman

Published in: Mol. Cancer Ther. 2016; 25:2166-2174

* These authors contributed equally to this work

ABSTRACT

The role of the vascular endothelial growth factor (VEGF)-inhibitor bevacizumab in the treatment of diffuse intrinsic pontine glioma (DIPG) in children is unclear. The aim of this study was to determine the biodistribution and uptake of zirconium-89 (^{89}Zr)-labeled bevacizumab in DIPG mouse models.

Human E98-FM, U251-FM glioma cells and HSJD-DIPG-07-FLUC DIPG primary cells were injected into the subcutis, pons, or striatum of athymic nude mice. Tumor growth was monitored by bioluminescence imaging (BLI) and visualized by Magnetic Resonance Imaging (MRI). Seventy-two to 96 hours after intraperitoneal ^{89}Zr-bevacizumab injections, mice were imaged by Positron Emitting Tomography (PET) and biodistribution was analyzed *ex vivo.*

Data from a publicly available database showed up-regulation of VEGF expression in human DIPG and pediatric high-grade glioma (pHGG). However, in our preclinical tumor models no significant ^{89}Zr-bevacizumab uptake could be detected in orthotopic gliomas located in the pons and striatum at an early or late stage of the disease. The E98-FM, and to a lesser extent the U251-FM and HSJD-DIPG-07 subcutaneous tumors, showed high accumulation of ^{89}Zr-bevacizumab. VEGF expression could not be demonstrated in the intracranial tumors by in situ hybridization (ISH), but was clearly present in the perinecrotic regions of the subcutaneous E98-FM tumors.

The poor uptake of ^{89}Zr-bevacizumab in orthotopic diffuse infiltrative tumors in the pons and striatum and high uptake in subcutaneous E98-FM-tumors, suggests that VEGF targeting with bevacizumab has limited efficacy for diffuse infiltrative parts of glial brain tumors in mice. Translating these results to a clinical setting would imply that treatment with bevacizumab in children with DIPG is only justified after demonstrating the presence and targeting of VEGF in the tumor by applying techniques such as ^{89}Zr-bevacizumab immuno-PET studies. We aim to confirm this observation in a clinical PET study with DIPG patients.

INTRODUCTION

Recent advances in molecular and cellular cancer biology have resulted in the identification of critical molecular tumor targets involved in the different phases of tumor growth and spreading. This knowledge has boosted the rational design of novel drugs, especially monoclonal antibodies and tyrosine kinase inhibitors. However, broad application of these targeted therapies to treat brain tumors has lagged behind in daily clinical practice. By using molecular positron emission tomography (PET) imaging, target expression, bio-distribution can be studied concurrently in a relatively non-invasive manner. It potentially allows the identification of those patients who may, or may not, benefit from targeted therapy.

A disease that may benefit from molecular imaging is diffuse intrinsic pontine glioma (DIPG), a childhood malignancy located in the brainstem. In the past 40 years the outcome of patients with DIPG has remained unchanged, with less than 10% of the patients being alive two years from diagnosis [168,169]. Given the lack of gadolinium uptake on MRI in DIPG tumors [22], it is plausible that the blood brain barrier (BBB) in DIPG often remains intact which might explain the resistance to systemic chemotherapy in these patients.

A well-studied drug target in gliomas is the vascular endothelial growth factor (VEGF), a signal protein stimulating angiogenesis and increasing vessel permeability [246]. Overexpression of VEGF-A, its receptor VEGFR2, or both, have been implicated as poor prognostic markers in various clinical studies [246,247]. Bevacizumab is a recombinant humanized monoclonal antibody that selectively binds with high affinity to all isoforms of human VEGF-A, and neutralizes their biologic activity [246,248]. Studies in adult patients with recurrent high-grade gliomas (HGG) reported high radiological response rates with bevacizumab treatment [248–250] but recently two large phase III randomized studies showed no improvement in overall survival with bevacizumab treatment in an upfront setting [251–253]. Bevacizumab has been studied in a number of non-randomized trials in pediatric brain tumor patients. Efficacy in these trials has been variable, with a subset of patients showing clear radiological and/or clinical improvement. The role of bevacizumab in the treatment of DIPG patients is even less clear, but is currently studied in several trials [254–257], (NCT00890786 and NCT01182350; clinicaltrials.gov; NTR2391 Trialregister.nl).

No validated methods are available to identify patients who may potentially benefit from bevacizumab treatment. Lack of clinical effect may be due to either poor transport of bevacizumab into the tumor microenvironment due to an intact BBB, or a lack of VEGF expression. In this study, we analyzed VEGF(R) expression in adult and childhood high-grade gliomas, including DIPG tumors. Furthermore, we studied bevacizumab distribution *in vivo* using molecular PET-imaging with ^{89}Zirconium-labeled bevacizumab in murine DIPG models [197].

MATERIALS and METHODS

VEGF-A and VEGFR2 mRNA expression profiles

VEGF-A and VEGFR2 (KDR) mRNA expression in DIPG (n=27) and pediatric high-grade glioma (pHGG) (n=53) were determined *in silico*, using publicly available datasets, and compared to a dataset of non-malignant brain tissue (n=44), low grade brainstem glioma (n= 6) and adult HGG (n=284). These datasets include tumor material from biopsy, resection and autopsy (DIPG). Differences were analyzed by two-way ANOVA and a $p < 0.01$ was considered significant. As a validation of these findings, VEGF associated gene expression was studied in normal brain, low grade brainstem glioma (LG-BSG), DIPG and GBM by creating a heat map using K-means clustering. All expression analyses were performed using R2, a web-based microarray analysis and visualization platform (http://r2.amc.nl).

Immunohistochemistry and in situ hybridization

Formalin-fixed paraffin-embedded slides were sectioned from xenograft tumors and brain tissue and subjected to immunohistochemical (IHC) staining. Briefly, after deparaffinization and heat induced antigen retrieval, sections were incubated with primary mouse anti-Ki67 antibodies (clone MIB-1, DAKO) overnight at 4°C. Thereafter slides were washed and incubated with HRP-conjugated EnVision (DAKO) and subsequently stained by DAB with hematoxylin counterstaining.

For *in situ* hybridization (ISH), tumors were cut in 5 µm slices and incubated with VEGF probes against the human VEGF coding sequence using a previously described protocol [258]. Samples were evaluated by microscopy with a Zeiss Axioskip microscope (HBO100W/Z), equipped with a Canon digital camera and imaging software (Canon PowerShot A640, Canon Utilities, ZoomBrowser Ex. 5.7, Canon Inc., Tokyo, Japan).

Labeling and quality control of ^{89}Zr-bevacizumab

Bevacizumab was labeled with zirconium-89 using *N*-succinyl-desferrioxamine (*N*-suc-Df) as described previously [259]. In short: the chelator, desferrioxamine, was succinylated to *N*-suc-Df. Next, the hydroxamate groups were blocked with iron and the succinyl group was activated as its TFP-ester (Fe-*N*-suc-Df-TFP ester). Bevacizumab (6 mg/mL) was reacted with two equivalents of Fe-*N*-suc-Df-TFP ester at pH 9 for 30 min at room temperature. Hereafter, iron was removed at pH 4.2-4.5 with an excess of ethylenediaminetetraacetic acid (EDTA) for 30 min at 35°C and *N*-suc-Df-bevacizumab was purified by size exclusion chromatography using a PD-10 column. Radiolabeling of *N*-suc-Df-bevacizumab was performed in HEPES buffer: to 200 µL ^{89}Zr in 1M oxalic acid 90 µL 2M Na_2CO_3 was added. After 3 min 300 µL 0.5 M HEPES, *N*-suc-Df-bevacizumab and 700 µL 0.5 M HEPES

were added. After 60 minutes reaction time ^{89}Zr-*N*-suc-Df-bevacizumab was purified by PD10 using 5 mg/mL gentisic acid in 0.9% NaCl (pH 4.9-5.4) as the mobile phase.

Radiochemical purity and antibody integrity were determined using instant thin-layer chromatography (iTLC), high-performance liquid chromatography (HPLC) and sodium dodecylsulfate-polyacrylamide gel electrophoresis followed by phosphor imager analysis. For analysis of immunoreactivity an ELISA based assay was used. iTLC analysis of ^{89}Zr-bevacizumab was performed on TEC control chromatography strips (Biodex). As the mobile phase, citrate buffer (20 mmol/L, pH 5.0) containing 10% acetonitrile was used. HPLC analyses of bevacizumab modification and radiolabeling were performed using a Jasco HPLC system equipped with a Superdex^{TM} 200 10/30 GL size exclusion column (GE healthcare Life sciences) using a mixture of 0.05 M sodium phosphate, 0.15 M sodium chloride (pH 6.8) and 0.01 M NaN_3 as the eluent at a flow rate of 0.5 mL/min. The radioactivity of the eluate was monitored using an inline NaI(Tl) radiodetector (RaytestSockett).

Cell lines and animal models

Animal experiments were performed in accordance with the European Community Council Directive 2010/63/EU for laboratory animal care and the Dutch Law on animal experimentation. The experimental protocol was validated and approved by the local committee on animal experimentation of the VU University Medical Center. Athymic Nude-Foxn1^{nu} mice (six weeks old) were purchased from Harlan/Envigo (Horst, The Netherlands) and kept under filter top conditions and received food and water *ad libitum*.

The primary HSJD-DIPG-07 cell line was established from DIPG tumor material obtained after autopsy from a 6-year-old patient and was confirmed to have a H3F3A (K27M) and ACVR1 (R206H) mutation [260]. The E98 cell line was obtained from Radboud University Medical Center Nijmegen [261], the U251 glioma cell line from ATCC. All cell lines were transduced in our laboratory to express firefly luciferase (FLUC) and/or mCherry [261,262]. Cell lines were mycoplasm negative and were authenticated by STR-analysis modified from De Weger et al. [263]

E98-FM cells were injected subcutaneously in female athymic nude mice (7-9 weeks of age) to expand the number of cells [197]. When the subcutaneous tumor reached a diameter of 1 cm, the tumor was removed and a single cell suspension was prepared by mechanical disruption through a 100 µm nylon cell strainer. HSJD-DIPG-07-FLUC was cultured in tumor stem medium (TSM) [24], U251-FM in DMEM supplemented with 10% FCS and penicillin/ streptomycin. Shortly before stereotactic injection, cells were washed once with phosphate buffered saline (PBS) and concentrated to $1x10^5$ cells per µl. Mice were

stereotactically injected with $5x10^5$ cells in a final volume of 5 µL into either the pons or striatum, or injected subcutaneously with $3x10^6$ cells in a final volume of 100 µl/flank. Coordinates used for intracranial injections were -1.0 mm X, -0.8 mm Y, 4,5 mm Z from the lambda for pontine tumors and 0.5 mm X, 2 mm Y, −2 mm Z from the bregma for the striatum tumors. Coordinates were previously validated and based on "The mouse brain in stereotaxic coordinates" by Franklin and Paxinos [200]. Tumor engraftment was monitored by bioluminescence measurement of the Fluc signal. For E98-FM, early stage tumors in the pons (n=8), striatum (n=7) and s.c. xenografts (n=3) were allowed to grow for 18 days and late stage tumors (n=9, striatum; n=3, subcutaneous) for 35 days after xenograft injection. E98 xenograft tumors in the pons were not available 35 days post injection, because injection of E98FM cells in the pons would result in death of the mice due to tumor growth within three weeks. For HSJD-DIPG07-FLUC and U251-FM tumors (pons, striatum, subcutaneous) were evaluated, at days 78 and 22 respectively (Figure 2A)

Two to three days before the endpoint of the study, mice were injected intraperitoneally (i.p.) with ^{89}Zr-labeled bevacizumab (40 µg, 5 MBq for PET analysis and *ex vivo* biodistribution or 185 kBq for *ex vivo* biodistribution only).

PET-imaging and *ex vivo* analysis

The distribution of ^{89}Zr-bevacizumab was determined 72 hours (*ex vivo* only) or 96 hours (PET followed by *ex vivo* analysis) after administration, as a minimum of 72 hours interval between injection and scanning has previously been shown to achieve optimal tumor-to-nontumor ratios [264]. Scanning of E98-FM tumors was performed using a LSO/LYSO double layer ECAT High-resolution Research Tomograph (HRRT, CTI/Siemens, Knoxville, TN, USA): a small animal and human brain 3-dimensional (3D) scanner with high spatial resolution (2.3–3.4 mm full width at half maximum) and high sensitivity [265]. Mice were anesthetized by isoflurane inhalation anesthesia (1.5 L 0_2 /minute and 2.5% isoflurane) before positioning in the HRRT. A static transmission scan (6 min) using a rotating 740 MBq ^{137}Cs point source was performed. Prior to positioning the mice in the HRRT, a canula was placed i.p. to enable later injection of ^{18}F(-). Static images of 60 minutes acquisition time were obtained. Immediately thereafter ^{18}F(-) was injected i.p (10 MBq/mouse) for co-localization of bone structures (static images of 60 minutes acquisition). Body temperature was controlled with a heated platform (kept at 37 °C).

Mice with HSJD-DIPG07-FLUC or U251-FM tumors and where tumor growth was confirmed by increase of BLI signal were imaged using another, preclinical, PET system, (Nanoscan PET-CT, MEDISO, Budapest, Hungary), 72 hours after ^{89}Zr-bevacizumab injection. PET images were analyzed using AMIDE software*. (Amide's a Medical Image Data Examiner, version 1.0.1)* [266]

Magnetic Resonance Imaging (MRI)

Mice with representative HSJD-DIPG-07-FLUC or U251-FM tumors were selected for MRI based on the intensity of the bioluminescence signal. Gadolinium (750 µmol, Dotarem) was administered i.v. immediately before imaging. Mice were anesthetized by isoflurane inhalation anaesthesia (1.5 L 0 $_2$ /minute and 2.5% isoflurane), placed in a preclinical PET-MRI system (Nanoscan system, MEDISO, Budapest, Hungary) and T1 and T2 weighed images were acquired. MRI images were analyzed using MIPAV software (*Medical Image Processing, Analysis, and Visualization, version 7.2.0*).

Ex vivo analysis

Immediately after PET-imaging, animals were sacrificed for *ex vivo* tissue distribution analysis. Blood, urine, tumor and various tissues were excised, rinsed in PBS to remove residual blood, and weighed. Radioactivity in blood and tissues (in percentage injected dose per gram of tissue: % ID/g) was determined using an LKB 1282 gammacounter (Compugamma,LKB Wallac, Turku, Finland). Differences in the amount of radioactivity in healthy brain regions versus subcutaneous-, pontine-, and striatal tumors were analysed by Kruskal-Wallis test with Dunn's Multiple Comparison posthoc testing. A $p<0.05$ was considered statistically significant.

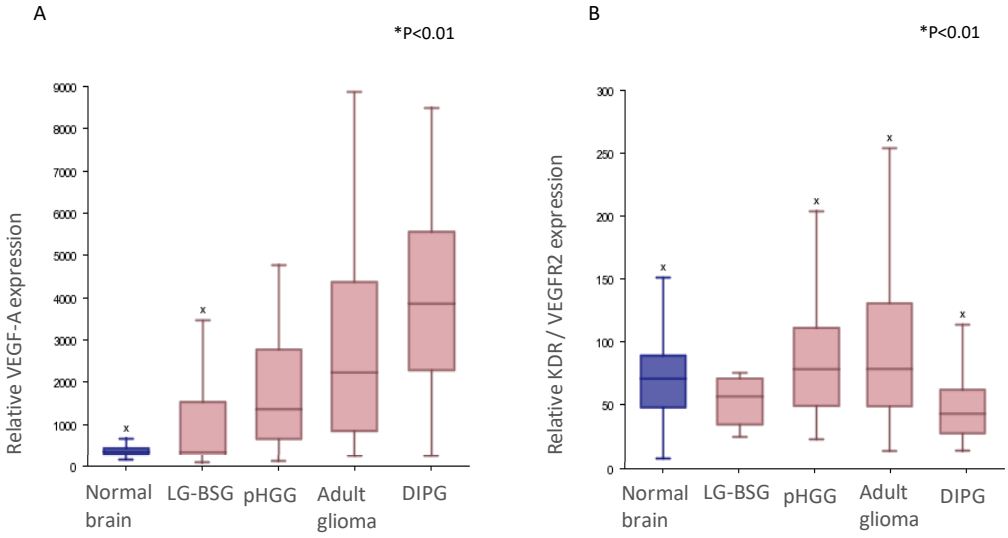

Figure 1: Expression profiles of VEGF-A and VEGFR2

1A: Box-plots representing relative median mRNA expression in diffuse intrinsic pontine glioma (DIPG) (n=27) and pediatric high grade glioma (pHGG) (n=53), versus datasets of normal brain tissue (n=44, blue), low grade brainstem glioma (n= 6) and adult HGG (n=284). VEGF-A overexpression is shown in DIPG compared to normal brain and compared to adult glioma. **1B**: VEGFR2 is not overexpressed in DIPG and pediatric glioma compared to normal brain. * P<0.01, ANOVA

VEGF-A, VEGFR2 and VEGF associated gene expression in DIPG A search in a publicly available mRNA expression database curated by the Amsterdam Medical Center (R2.amc.nl) revealed that *VEGF-A* mRNA is overexpressed in DIPG compared to normal brain and compared to low grade brainstem glioma (LG-BSG) and non-pontine adult- and pediatric HGG (Figure 1a; $p<0.01$, ANOVA). VEGFR2 (KDR) mRNA expression was low in both pediatric and adult glioma, compared to normal brain (Figure 1b; $p<0.01$, ANOVA). A heatmap generated using K-means clustering of expression of VEGF-A associated genes confirmed an aberrant VEGF-A pathway to be more prominent in DIPG compared to LG-BSG. Most DIPG (red) samples clustered together with pediatric GBM (green) and LG-BSG (blue) clustered with normal brain tissue (purple) (supplemental Figure 1).

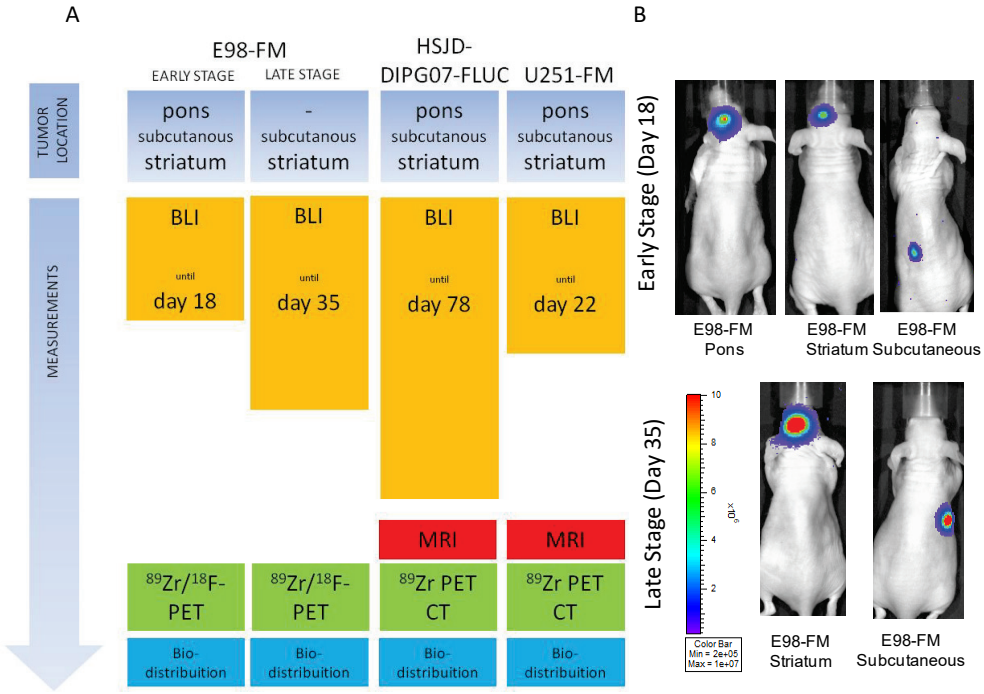

Figure 2A: Schematic overview of the experiment. Cells are injected at day 0 in the pons, striatum or subcutis (early stage tumors) or the striatum and subcutis (late stage E98-FM tumors). Tumor progression was monitored by bioluminescent imaging. The time point for 89Zr-bevacizumab injection was dependent on the growth speed of used cell lines. This injection was done 72-96 hours before PET scanning. MRI, PET or PET/CT imaging was followed by *ex vivo* measurement of ^{89}Zr-bevacizumab accumulation in tissues (Bio-distribution) . **2B**: Charged couple device (CCD) camera images of mice bearing E98-FM tumors. BLI images were obtained at the study endpoint, day 18 (early stage, upper panel) and day 35 (late stage, lower panel).

Biodistribution of ^{89}Zr-bevacizumab

After tumor growth was confirmed by increase in bioluminescence (BLI) signal, ^{89}Zr-bevacizumab was injected in these animals. 72 – 96 hours after i.p. injection of ^{89}Zr-bevacizumab, animals were imaged by PET; a schematic overview of the experiment is given in Figure 2, with representative BLI figures of E98-FM engrafted mice shown in Figure 2b. ^{89}Zr-bevacizumab uptake was not visualized in the E98 gliomas located in the pons (only early stage, Figure 3a) or in the striatum at early or late stage. The rest of the brain showed no uptake of ^{89}Zr-bevacizumab either, independently of the presence of a tumor. However, subcutaneous E98 tumors showed high accumulation of ^{89}Zr-bevacizumab indicated by a red hotspot (Figure 3a).

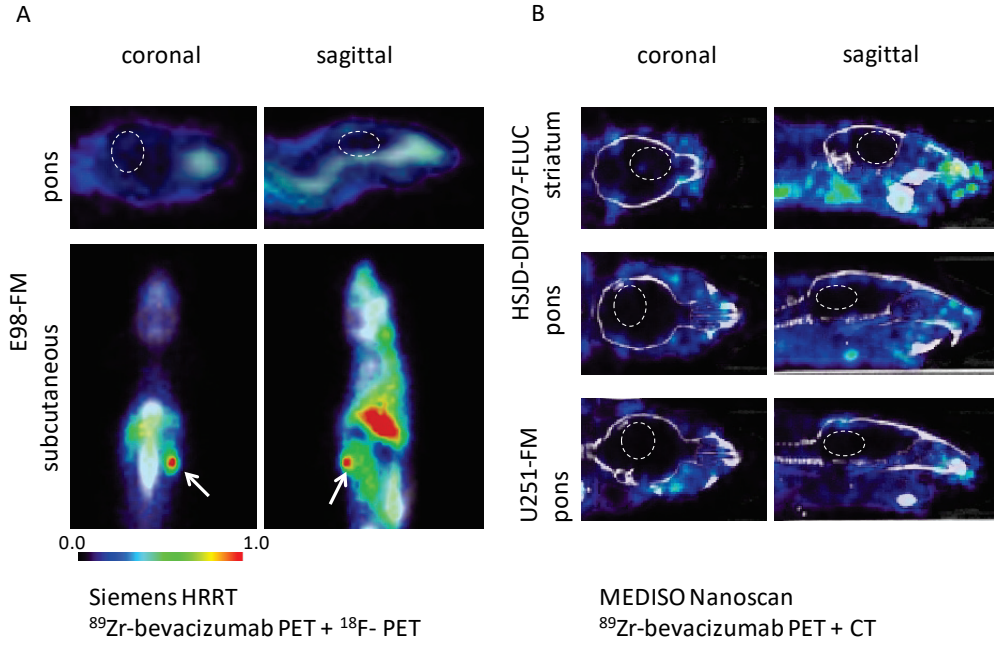

Figure 3A: ^{89}Zr-PET combined with ^{18}F- imaging of mice with an E98 tumor located in the pons (upper panels), or subcutaneous (bottom panels). White circles indicate expected location of intracranial tumors. While no uptake of ^{89}Zr-bevacizumab is observed in the pontine tumor, the subcutaneous tumor shows a PET hot spot reflecting ^{89}Zr-bevacizumab accumulation in the tumor (arrow). In all animals, high intensity (visualized by red color code) is seen in the heart and liver of the mice, reflecting ^{89}Zr-bevacizumab in the blood pool.. Images acquired with Siemens HRRT. **3B**: Immuno-PET scanning of mice with HSJD-DIPG07-Fluc (upper and middle panels) or U251FM tumors (bottom panels) confirmed the lack of bevacizumab uptake in intracranial tumors. Image acquired with MEDISO Nanoscan PET-CT system. White circles indicate expected location of intracranial tumors. *Ex vivo* tissue distribution measurements confirmed that no significant ^{89}Zr-bevacizumab uptake was detected in the brain or brain tumor at any stage of disease, while there was high uptake in the subcutaneous tumor ($p < 0.01$) (Figure 4a).

Besides accumulation in the subcutaneous tumor with an average level of 50% ID/g, ^{89}Zr-bevacizumab was measured in all animals (to a lesser extent) in the blood pool and in well-perfused organs, such as the liver, spleen and lungs (Figure 5). Experiments using the two other cell lines (U251FM and HSJD-DIPG-07-FLUC) showed comparable results. Using these cell lines, no uptake of ^{89}Zr-bevacizumab was visualized on PET in any of the xenografts (Figure 3b). *Ex vivo* biodistribution analysis showed higher ^{89}Zr-bevacizumab uptake in subcutaneous HSJD-DIPG-07-FlUC tumors ($p<0.05$) as compared to brain (areas) without tumor (Figure 4b). The subcutaneous U251FM tumors showed no significant increase in ^{89}Zr-bevacizumab uptake (Figure 4c) as compared to non-tumor brain. Of note, both HSJD-DIPG-07-FLUC and U251FM cells formed only very small subcutaneous tumors during the time window in which mice baring intracranial tumors had reached human endpoints (78 vs. 22 days after tumor injection).

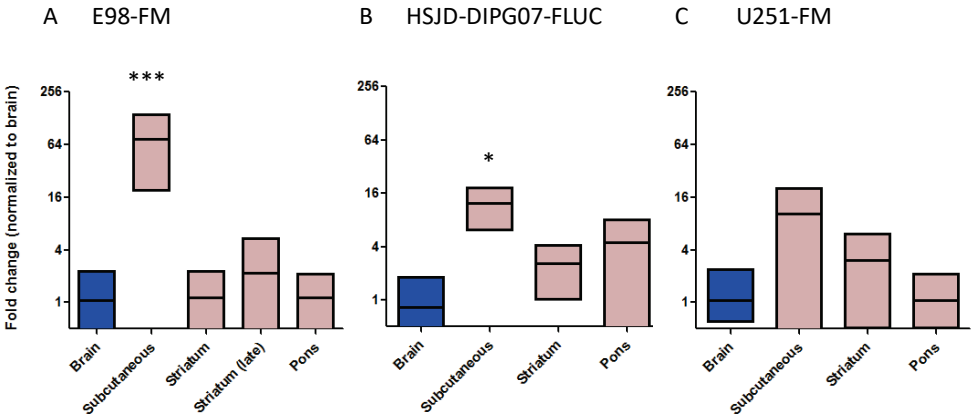

Figure 4: ^{89}Zr-bevacizumab measured *ex vivo* by a gamma-counter and normalized to counts found in healthy brain tissue (brain tissue of animals without xenografted brain tumors). **4A**: Uptake is significantly higher in the subcutaneous E98-FM tumors (***$p<0.01$), but there is no significant difference in uptake in pontine or striatal xenografts at any stage of the disease compared to normal brain. **4B:** Uptake in subcutaneous DIPG7-Fluc tumors is higher than in normal brain(*$p<0.05$). **4C**: No significant differences between U251-FM tumors (s.c. or intracranial) versus normal brain.

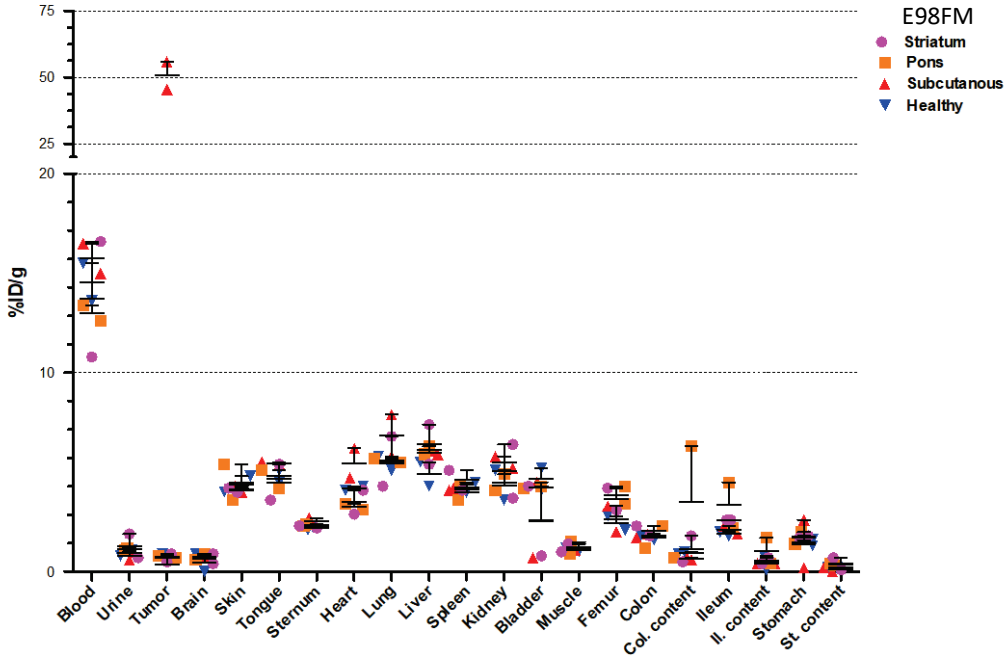

Figure 5: ^{89}Zr-bevacizumab uptake measured *ex vivo* by radioactivity of the specific organs and the tumor after dissection, expressed as percentage of the injected dose per gram tissue in E98-FM tumor bearing animals. Note the high uptake in subcutaneous tumors, compared to the negligible uptake in the intracerebral tumors.

In situ-hybridization of VEGF

To determine whether the differences in ^{89}Zr-bevacizumab uptake in the subcutaneous and the intracranial tumors were due to an impaired distribution of ^{89}Zr-bevacizumab into the brain or to a differential expression of its target (or both), VEGF expression was analyzed in the different xenografts. *In situ* hybridization confirmed expression of VEGF in the subcutaneous E98FM tumor (Figure 6a), while VEGF expression was absent in E98FM-brain tumors (Figure 6b) and brain tissue without a xenograft. Of note, in the subcutaneous tumors, VEGF was preferentially expressed in perinecrotic areas, while necrosis was absent in all of the striatal and pontine tumors. A Ki67 (Mib-1) staining was performed to confirm presence of proliferating tumor tissue (Figures 6c,d). In HSJD-DIPG-07-FLUC and U251FM tumors, VEGF mRNA expression was not detectable in striatal and pontine gliomas. The subcutaneous tumors were too small to adequately perform VEGF ISH and therefore no conclusions could be drawn regarding VEGF expression in these s.c. tumors.

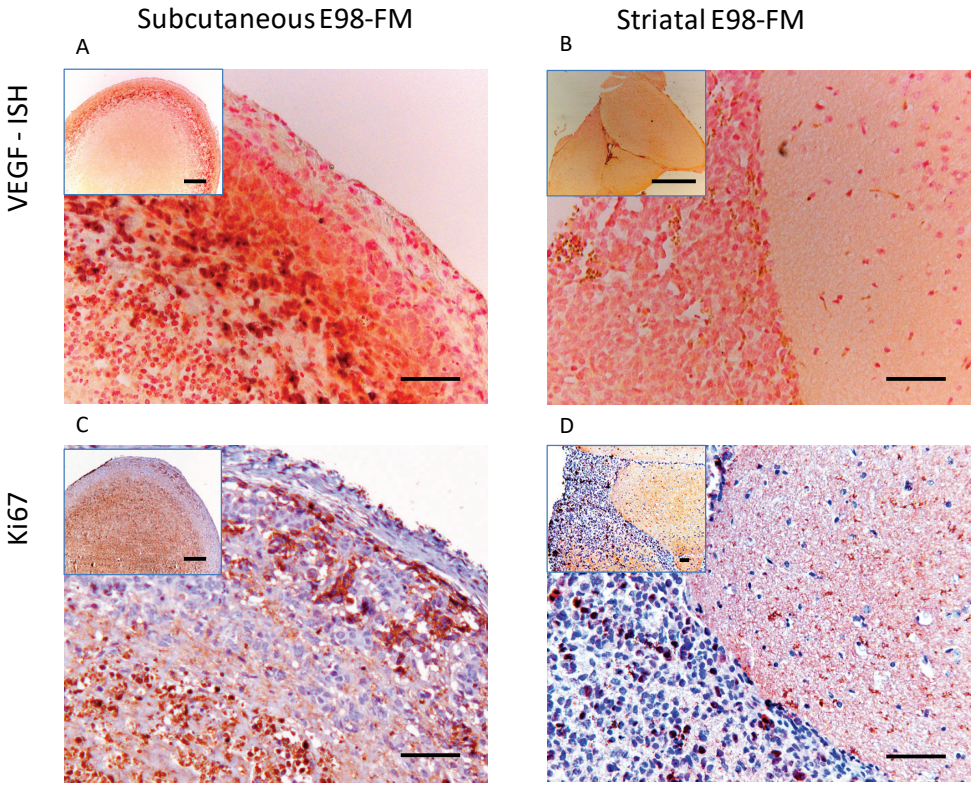

Figure 6: VEGF expression in DIPG tumors as assessed by VEGF *in situ* hybridization (ISH). **6A**: Positive VEGF staining in subcutaneous E98-FM tumor cells (magn. 20x, insert 2,5x). The tumor shows extensive necrosis surrounded by VEGF positive cells. **6B**: No VEGF mRNA is detected in the E98-FM tumor tissue in the striatum (magn. 20x, insert 1.25x). **6C**: Ki67 staining shows the presence of proliferating tumor cells in the subcutaneous tumor tissue (magn. 20x, insert 2.5x). **6D**: Ki67 positive tumor cells in the striatal E98-FM tumor (magn. 20x, insert 10x)

Magnetic Resonance Imaging.

To visualize disruption of the blood-brain-barrier, mice with HSJD-DIPG07-FLUC and U251-FM intracranial tumors were imaged by MRI after intravenous administration of gadolinium. In the diffusely growing HSJD-DIPG07-FLUC tumor, gadolinium enhancement on T1 weighed images was limited (Figure 7a, arrow), whereas gadolinium enhancement was clearly visible in the U251-FM tumor (Figure 7c, arrow). On T2 weighed images, tumors were not clearly visible (Figures 7b, d; arrow).

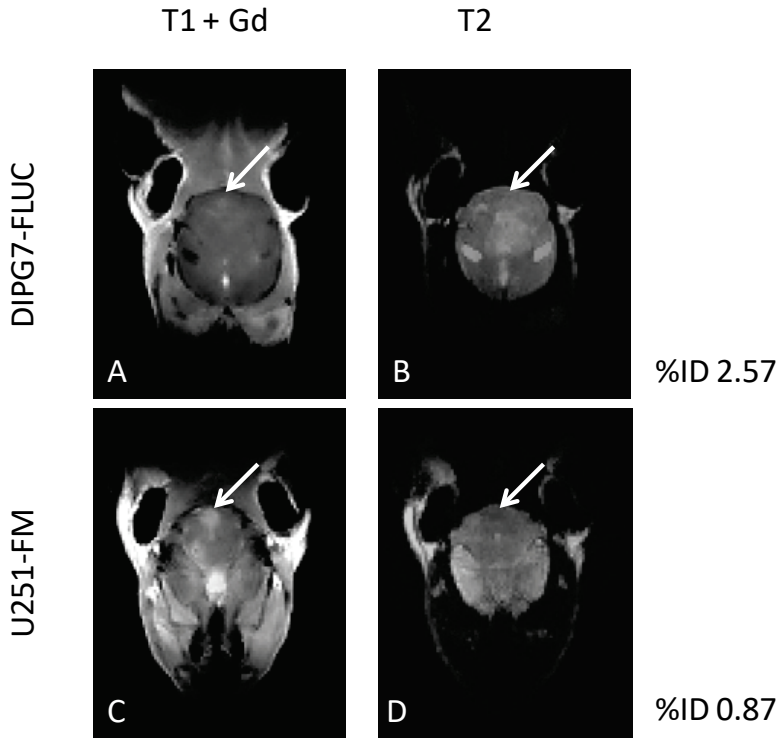

Figure 7: MRI scans of pontine tumors. The 89Zr-bevacizumab uptake in the tumors of these two mice is presented as %ID/g. 7A: Limited gadolinium contrast enhancement in the tumor area (arrow) on T1 scan. 7B: HSJD-DIPG07-Fluc tumor is poorly visible on T2 weighed MRI image (arrow). 7C: Clear gadolinium contrast enhancement in the U251-FM tumor area (T1 weighed MRI scan) indicates disruption of the blood-brain-barrier. 7D: U251-FM tumor is visible on T2 weighed MRI scan.

DISCUSSION

The potential benefit of bevacizumab in the treatment of DIPG is unclear, as efficacy depends on expression of VEGF-A as well as appropriate drug distribution [267]. We used molecular PET-imaging to study the influence of location and stage of disease on biodistribution of ^{89}Zr-bevacizumab in three glioma mouse models (pontine, striatal, subcutaneous) using three different cell lines. The E98-FM pontine and striatal and HSJD-DIPG-07 pontine xenograft models have previously been described to resemble the diffuse phenotype of human DIPG and other diffuse high grade gliomas [197,229,233]. U251 has been described as an intracranial murine tumor model that recapitulates most of the key figures of adult GBM [268]. We found no significant uptake of ^{89}Zr-bevacizumab in the intracranial tumor models at any stage of the disease, nor in the normal/non-neoplastic surrounding brain. In contrast, high accumulation of ^{89}Zr–bevacizumab was observed in the subcutaneous E98-xenograft and moderate uptake in the subcutaneous HSJD-DIPG07-FLUC.

We initially hypothesized that lack of ^{89}Zr–bevacizumab uptake could be explained solely by poor distribution into the brain, as large molecules like monoclonal antibodies may not be able to pass the BBB. This hypothesis is supported by the absence of enhancement of the tumor on MRI after administration of gadolinium in animals with HSJD-DIPG-07-FLUC pontine tumors. However, MRI analysis of U251-FM tumors in the brainstem of mice showed clear gadolinium enhancement, which is indicative of "leaky" blood vessels in the tumor. Furthermore, VEGF expression of the E98FM glioma cells - analyzed by ISH – also differed between tumor locations: E98FM gliomas in both striatum and pons appeared VEGF-negative, while the s.c. E98FM tumors were partly VEGF-positive. The differences in VEGF expression of the tumors in distinct locations originating from the same cell line, confirms that the orthotopic microenvironment and the resulting growth pattern significantly influence gene expression in glioma cells, a phenomenon that has been described previously (19, 20). Moreover, it has been shown that in GBM, VEGF is predominantly overexpressed in hypoxic, perinecrotic cells [269,270]. Indeed, in our study the VEGF expression in subcutaneous E98FM tumors was especially present around areas of necrosis, whereas in intracranial E98FM tumors necrosis and VEGF expression were lacking and this also coincided with lack of bevacizimab uptake studied *ex vivo* and by PET. Of note, bevacizumab does not bind to murine VEGF-A [271], but as typically the neoplastic cells are upregulating VEGF expression in tumor angiogenesis we consider it unlikely that stromal cell-derived mouse VEGF-A plays an important role in this particular xenograft model. [233]

In contrast to our preclinical findings, the *in silico* analysis that we performed in this study, indicates that human DIPG tumors have relatively high expression levels of VEGF mRNA. However, the majority of tumors (23 out of 27) used for the microarray experiments were

collected *post-mortem* [225,272] and therefore these samples represent the end-stage of the disease, and are post-radiation therapy. In the end-stage of the disease, DIPG is known to have necrotic areas with microvascular proliferations and blood-brain barrier disruption, compatible with the histology of a GBM, which is associated with high VEGF expression. Although the numbers are low, it is important to point out that VEGF-A expression levels in samples obtained pre-treatment were low compared to expression in post-mortem/end-stage samples (supplemental Figure 2). In addition, biopsy samples that were included in the analysis are frequently directed at contrast-enhancing regions, and this 'biased sampling' may well lead to overestimation of the role of VEGF in the tumor as a whole. We are currently studying the differences in VEGF-A expression in autopsy-derived DIPG tissue between the perinecrotic areas and the more diffusely growing tumor parts without necrosis.

Experimental and clinical research in both adult and pediatric high grade glioma and DIPG has suggested that there is a complex relation between a histologically diffuse growth pattern of tumors, VEGF expression and availability and BBB integrity [210,258,273–276]. Traditionally, VEGF is viewed as the main cause of increased BBB permeability in CNS tumors as represented by contrast-enhancing lesions on MRI [277]. More recently, anti-VEGF therapy is thought to potentially induce a more diffuse and distant spread of tumor cells [210,274]. In contrast to adult high grade gliomas, gadolinium contrast enhancement on MRI in DIPGs at diagnosis is generally limited, with 50% of the patients showing no enhancement at all [22]. The lack of gadolinium enhancement suggests an intact BBB, at least for large molecules, in a substantial percentage of the patients, coinciding with low VEGF expression and inability of bevacizumab to target the tumor [211].

Results from our preclinical PET, MRI with gadolinium contrast and ISH studies suggest that this relation is not so straightforward, pressing the need for studying VEGF targeting in patients treated with anti-VEGF therapy. One could however argue, whether high local tumor accumulation of bevacizumab is at all needed to obtain potential therapeutic effects in DIPG. Bevacizumab is capable of decreasing VEGF levels to undetectable range in less than 20 days in a large cohort of adult cancer patients [278], but only a subgroup of patients responded to anti-VEGF therapy. This suggest simply decreasing VEGF in the blood-pool is, at least for the tumor types studied, not sufficient to treat all tumors, and presence and targeting of VEGF should therefore be confirmed to identify those patients that will benefit from treatment [278–280].

The results of immuno-PET-imaging and VEGF-ISH in these DIPG models are in line with the poor clinical response rates thus far obtained with bevacizumab in children with DIPG [254]. The data presented suggest that no adequate uptake of bevacizumab will occur in diffusely growing gliomas, which present with BBB disruption but without drastically increased VEGF expression. Therefore we suggest that bevacizumab treatment is only justified if targeting

of VEGF by bevacizumab has been visualized by immuno-PET scan. We aim to confirm this hypothesis in a clinical PET study with DIPG patients.

Future directions

This study underlies the importance of using strong biological and biodistributional rationale before using any therapy in any patient. Following the results of this study, we developed a molecular drug imaging trial with ^{89}Zr-bevacizumab in children with DIPG (study number NTR3518 www.trialregister.nl). This technique aims to further unravel the role of bevacizumab treatment in DIPG. Ideally, such molecular imaging is combined with VEGF-A and VEGFR2 expression analysis on tumor tissue originating from biopsies taken from several (contrast-enhancing and non-enhancing) parts of the tumor. Because DIPG can generally be diagnosed based on its typical radiological presentation and the delicate nature of the brain involved, taking biopsies from DIPGs is still no common practice and bioptic sampling of multiple regions is even more cumbersome. In general, integrating molecular imaging with radiolabelled drugs (classic cytostatic agents, small molecules, other monoclonal antibodies) in the treatment of childhood brain cancer provides an insight in drug targeting and might help to personalize treatment and thereby to avoid unnecessary side effects of drugs that do not reach the tumor.

Acknowledgements

We are thankful to Ricardo Vos, Iris Mes and Alex Poot (Department of Radiology & Nuclear Medicine, VUmc) for technical support with labelling of PET tracers and PET-imaging. Piotr Waranecki and Yanyan Veldman (Neuro-oncology Research Group, VUmc) for technical assistance and animal handling. DIPG research at our institution has been made possible by the invaluable support of the Semmy Foundation, Stichting Egbers and of Stichting Kika (Children-Cancer-free).

Conflict of Interest

DIPG research is funded by the Semmy and Egbers foundation as well as by Stichting Kika (Children-Cancer-free). The sponsors had no role in the preparation and execution of the study nor in the writing of the manuscript.

Supplementary Figures

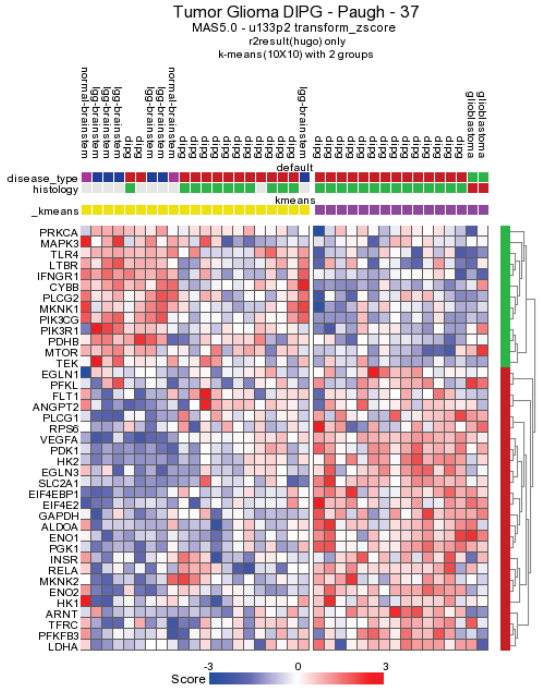

Supplemental Figure 1: Heatmap of VEGF-A associated genes generated using Spearman's rank correlation; LG-BSG samples (blue) in the disease type histology (upper legends) cluster with normal brain (purple). DIPG (red) clusters with GBM (green). DIPG (green), pHGG/GBM (red).

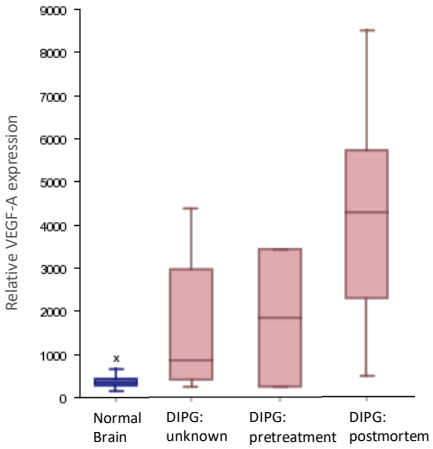

Supplemental Figure 2: VEGF mRNA expression in DIPG in comparison to normal brain (n=31) as analyzed by R2 (R2.amc.nl), clustered by stage of disease; unknown (n=10), pretreatment (n=2) and postmortem (n=23)

CHAPTER 5 |

A CHEMICAL SCREEN FOR MEDULLOBLASTOMA IDENTIFIES QUERCETIN AS A PUTATIVE RADIOSENSITIZER

Tonny Lagerweij*, Lotte Hiddingh*, Dennis Biesmans, Matheus H.W. Crommentuijn, Jacqueline Cloos, Xiao-Nan Li, Mari Kogiso, Bakhos A. Tannous, W. Peter Vandertop, David P. Noske, Gertjan J.L. Kaspers, Tom Würdinger, and Esther Hulleman

Published in: Oncotarget, 2016 7(24): 35776-35788

* These authors contributed equally to this work

ABSTRACT

Treatment of medulloblastoma in children fails in approximately 30% of patients, and is often accompanied by severe late sequelae. Therefore, more effective drugs are needed that spare normal tissue and diminish long-term side effects. Since radiotherapy plays a pivotal role in the treatment of medulloblastoma, we set out to identify novel drugs that could potentiate the effect of ionizing radiation selectively.
A small molecule library, consisting of 960 chemical compounds, was screened for its ability to sensitize towards irradiation, using two independent read-out systems.

This small molecule screen identified the flavonoid quercetin as a novel radiosensitizer and we show that quercetin can sensitize the medulloblastoma cell lines DAOY, D283-med, and, to a lesser extent, D458-med to ionizing radiation at low micromolar concentrations. Quercetin enhanced the *in vitro* radiation sensitivity of medulloblastoma cells in clonogenic survival assays at doses used in fractionated radiation schemes. Furthermore, quercetin did not affect the proliferation of neural precursor cells or normal human fibroblasts. DAOY and D283-med were identified as a SHH and a group 3 subtype medulloblastoma, respectively, which may indicate a subgroup-independent effect of quercetin on the radiation response. Importantly, *in vivo* experiments confirmed the radiosensitizing properties of quercetin, as administration of this flavonoid at the time of irradiation significantly prolonged survival in orthotopically xenografted mice.

Together, these findings indicate that quercetin is a potent radiosensitizer for medulloblastoma cells that may be a promising lead for the treatment of medulloblastoma in patients.

INTRODUCTION

Medulloblastoma, the most common malignant brain tumor in children, accounts for approximately 20% of all intracranial childhood tumors [281]. Medulloblastomas are invasive neuroepithelial tumors that are thought to arise from the progenitor cells of the dorsal brain stem, or from precursor cells in the cerebellum [282,283]. Currently, patients are stratified into two groups based on histological features and clinical criteria: the standard- and high-risk groups. Treatment of standard-risk medulloblastoma patients consists of surgery and reduced-dose craniospinal radiotherapy, followed by an additional boost aimed at the primary tumor site, and adjuvant chemotherapy. In high-risk patients, a higher craniospinal dose is used [284,285]. Although such treatment has resulted in remarkable improvement in outcome, this therapy still fails in approximately 30% of medulloblastoma patients [286]. Moreover, such therapy causes severe long-term side effects that significantly impact quality of life [16–18,33,287–289]. There is a need for alternative therapies that allow to lower the total dose of irradiation or increase the radiation efficacy. Besides new radiotherapy techniques that limit the radiation doses to surrounding healthy tissues [290–292], new chemotherapeutics that specifically sensitize the tumor to irradiation may provide alternative therapies [293,294].

We screened a commercially available small molecule library consisting of 960 compounds (ActiTarg-K960) with a diversity of chemical structures to identify radiosensitizers for medulloblastoma. Chemical structures represented by these compounds have been reported to exert kinase inhibitory functions and screening of these compounds would help in the identification of new chemical directions for hit optimization. However, to our surprise, we identified a known chemical compound, quercetin (3,3',4'5,7-pentahydroxyflavone), a flavonoid found in fruits, vegetables and grains, as a radiosensitizer for human medulloblastoma cells. Quercetin treatment at low micromolar concentrations did not affect cell proliferation when used as monotherapy, while the combination with irradiation significantly decreased medulloblastoma cell growth. Importantly, this sensitizing effect was not found on neural precursor cells, or normal human fibroblasts. In addition, quercetin treatment enhanced the *in vitro* sensitivity of medulloblastoma cell lines in clonogenic survival assays. However, the radiosensitizing effect was not observed in two primary medulloblastoma cell cultures. Finally, we observed that quercetin administration to orthotopically xenograft mice around the time of irradiation significantly prolonged survival. Since quercetin sensitizes medulloblastoma cells in our experiments at doses used in fractionated radiation schemes, and the quercetin concentrations used can easily be achieved by oral administration, we suggest that the use of quercetin should be further evaluated in clinical trials in medulloblastoma patients in the near future.

MATERIALS and METHODS

Cell culture and lentiviral infections

Mouse C17.2 neural precursor cells, human primary fibroblasts and D283-Med, D458-Med, DAOY medulloblastoma cell lines were cultured at 37°C in a 5% CO_2 humidified atmosphere in DMEM plus 10% fetal calf serum, 100IU/ml penicillin and 100μg/ml streptomycin (PAA Laboratories GmbH, Austria). Pools of D283-med FM/GC or DAOY FM/GC cells were generated by infection with lentiviral vectors, expressing the reporter gene combinations *Firefly* luciferase/mCherry (FM) or *Gaussia* luciferase/Cerulean (GC), as described previously [111]. Fluorescence microscopy was used to assess the success rate of transductions and cell viability. For intracranial injections, cells were harvested and suspended in PBS at a concentration of $1x10^8$ cells/ml. The cells used in this study were not authenticated.

Primary cell culture VU371 was derived from tumor tissue, surgically removed from a patient diagnosed with medulloblastoma at the VU University Medical Center. Informed consent was obtained according to institutionally approved protocols. ICb-1299MB is a patient derived orthotopic xenograft mouse model of group 4 medulloblastoma [295] and the xenograft cells were kindly provided by Dr. Xiao-Nan Li and Dr. Mari Kogiso (Baylor College of Medicine, Houston, TX, USA). VU371 and ICb-1299MB were cultured at 37°C in a 5% CO_2 humidified atmosphere in NBM (NeuroBasal Medium)(Invitrogen) supplemented with neural stem cell supplement (NSCS), N2, stable glutamine (PAA), epidermal growth factor (EGF), and basic fibroblast growth factor (bFGF)(PeproTech).

Chemicals

The ActiTarg-K960 chemical library, consisting of 960 putative kinase inhibitory compounds, was obtained from TimTec (Newark, Delaware, USA). Ninety-one percent of these compounds conform to four Lipinski criteria and 97% to three Lipinski criteria, suggesting they have desirable pharmacologic properties [296]. Quercetin dihydrate (Calbiochem, USA) was dissolved in dimethyl sulfoxide (DMSO; Sigma-Aldrich, USA), with a final DMSO concentration of 0.1% for *in vitro* experiments or a final DMSO concentration of 5% for *in vivo* experiments.

Chemical library screen

Seven hundred and fifty DAOY cells were plated per well in 96-well plates. The next day, cells in each well were treated with a different compound from the ActiTarg-K960 library at a 1 μM concentration. Treatment was performed with drugs in paired 96-well plates, where one plate was exposed to 4 Gy in a Gammacell® 220 Research Irradiator (MDS Nordion, Canada) 30 minutes after addition of the compounds, and the other plate was a non-irradiated control. Four days later, cell survival was evaluated by measuring Gaussia luciferase (Gluc)

activity [297], or by means of the Acumen eX3 laser scanning cytometer (TTP LabTech, UK). Results were analyzed using Acumen Explorer software, calculating the percentage survival for each compound tested with the assay.

Survival assays

Responsiveness of D283-med, D458-med (1,000 cells/well, or $1x10^4$ cells/flask), or DAOY (1,500 cells/well) medulloblastoma cells to quercetin (1 μM) was determined in a cell proliferation assay by use of the Acumen eX3 laser scanning cytometer as described above, and confirmed by cell counts using a Bürker hemocytometer. Viability of primary cells, VU371 and ICb-1299MB (2,000 cells/well), after treatment with 1 μM quercetin and 0.7 Gy irradiation was determined with Cell Titer Glo assay (Promega) according to manufacturer's protocol. In addition, a clonogenic assay was performed with different doses of irradiation (0-3 Gy). Therefore, exponentially growing D283-med and D458-med cells were plated in triplicate in 6-well plates at concentrations ranging from 200-2,000 cells/well, and grown for 14 days in MethoCult®H4001 with 0, 0.5, or 1 μM quercetin. Colonies were counted visually and plating efficiency (PE) was calculated by dividing the number of colonies counted by the number of cells plated. Surviving fractions (SF) were then calculated by dividing the PE by the PE of the non-irradiated control per drug concentration. Duplicate experiments were performed for each cell line. Analysis of inhibitory concentrations was performed using SigmaPlot 11.0 (Systat Software, Inc. San Jose, CA, USA).

qRT-PCR

Quantitative RT-PCR (qRT-PCR) analysis was performed to determine expression of the medulloblastoma subgroup classifiers WIF1, SFRP1, NPR3, and KCNA in medulloblastoma cell lines and a normal cerebellum sample. Total RNA was isolated using the TRIzol RNA isolation protocol (Invitrogen, Carlsbad, CA, USA) and equal amounts of RNA were converted to cDNA using the Omniscript kit (Qiagen). Primer sequences for WIF1, SFRP1, NPR3, and KCNA transcripts were previously described by Zhao *et al.* [298] and primers were manufactured by Biolegio (Nijmegen, The Netherlands). Gene expression of the subgroup classifiers in medulloblastoma cells was normalized to GAPDH expression levels and the Ct values were used to calculate the relative fold difference in mRNA levels (ΔΔCt method) compared to normal cerebellum.

D283-med orthotopic xenograft mouse model

Female athymic nude-Fox1nu mice (age 8-10 weeks; Harlan, Horst, The Netherlands) were maintained in accordance with the guidelines and regulations set out by the VU University committee on research animal care. For intracranial injections, mice were anesthetized with 2.5% isoflurane in oxygen, and a volume of 5 μl ($0.5x10^6$ D283-med FM-GC cells) was injected stereotactically into the cerebellum at a rate of 2 μl per minute, using a Hamilton 10 μl

syringe with a 26G needle. Coordinates for injection were determined according to the mouse brain atlas [299]: 2.0 mm lateral, 2.5 mm ventral of lambda, and at a 2.0 mm depth. Before start of the treatment (three weeks after injection of the tumor cells) tumor engraftment was determined by measuring *Firefly* luciferase (Fluc) activity. Based on this activity, mice were randomized into four treatment protocols: vehicle (5% DMSO), quercetin, DMSO/irradiation (4 Gy), and quercetin/irradiation (4 Gy). Mice without tumor engraftment (Fluc activity <80,000 photons/sec at three weeks after implantation) were excluded from the experiment. Quercetin (100 mg/kg) was administered intraperitoneally at six time points: 30 and 60 minutes before-, or after irradiation, 0 hours, and 24 hours after irradiation. Mice not receiving quercetin were treated with the same volume of DMSO dissolved in PBS, at the same time intervals as the quercetin treated mice. To enable precise positioning of the radiation beam on the head and neck area of the mice, the animals were anesthetized with ketamine/xylazine. Mice that were not irradiated were anesthetized just before the zero hours' time point. Tumor growth was monitored semi-weekly by bioluminescent imaging (BLI). In short, 150 µl D-luciferin (0.03 g/L, Gold Biotechnology, St. Louis, USA) was injected intraperitoneally and 10 minutes after administration mice were anesthetized with isoflurane inhalation anesthesia, positioned in the IVIS camera and the bioluminescence signal was determined with the IVIS Lumina CCD camera. In addition, the mice were monitored daily for discomfort and weight loss. When moderate to severe symptoms were present (weight loss of >20% or severe neurological deficits), animals were sacrificed and brains were removed and formalin-fixed.

Statistical analysis

A coefficient of variation (CV) and Z' factor were calculated to assess the reproducibility and robustness of the small molecule screens, as described by Zhang *et al.* [300], where $CV=SD/\mu$ and $Z' = 1-(3\sigma_{c+} +3\sigma_{c-})/|\mu_{c+} -\mu_{c-}|$. Statistical significance of treatment was assessed using the Mann-Whitney U test. Kaplan-Meier survival curves were generated with GraphPad Prism 5. Median survival of the groups was calculated and survival curves were compared with the Log-rank (Mantel-Cox) test. The *p* values <0.05 were considered statistically significant.

RESULTS

Identification of quercetin as a radiosensitizer for medulloblastoma

In order to enable the identification of novel radiosensitizers for medulloblastoma, a small molecule screen was performed using DAOY medulloblastoma cells that were transduced with a lentiviral *Gaussia* luciferase (Gluc) vector co-expressing the fluorescent 'Cerulean' (CFP) reporter [111]. Expression of these genes allowed to monitor cell survival by bioluminescent and fluorescent read-out of cell viability. To optimize screening conditions, the well-to-well and plate-to-plate variation, number of DAOY cells, and the dose of irradiation were determined. For the well-to-well and plate-to-plate variation, aliquots of Gluc-conditioned medium were distributed over 96-well plates and assayed for luciferase activity as described previously [297]. In four independent experiments a variation coefficient (CV) of < 7% was observed (Fig. 1A), indicating only minimal variation in pipetting errors, substrate stability and measurement errors. An even better CV of < 2% was observed (Fig. 1A) for the plates measured by Acumen technology, where equal numbers of cells were plated and detected by CFP expression. Robustness of the assays was determined by calculating the Z' factor as described by Zhang *et al.* [300], where Z'=0.84 for the Gluc assay and Z'=0.56 for the Acumen screen. Since both assays allowed to monitor cell viability at different time points after treatment, we optimized our screening conditions – number of cells, dose of irradiation, and drug concentrations – by measuring Gluc secretion or cell numbers in time (Fig. 1B-D). This resulted in a four-day assay, using 750 DAOY cells per well with 4 Gy irradiation. In addition, a drug concentration of 1 µM was chosen, since this showed good results in a pilot experiment using eight different, randomly chosen small molecules (Fig. 1D), and yielded positive hits in a drug screen performed previously by our group [297]. Once all conditions were established, cells were seeded in 96-well plates, and treated the next day with compounds from the ActiTarg-K960 drug library (TimTec) consisting of 960 putative kinase inhibitors, or with 0.1% DMSO as an internal control. The compounds were added in duplicate plates, where one set was irradiated to identify putative radiosensitizers, while the other set was left non-irradiated to assess cytotoxicity of the compounds as monotherapy. A reduction of >75% of cell growth after four days of incubation as compared to the DMSO controls was considered to be significant (Fig. 2A). In four separate screens, a total of 23 compounds were identified that consistently inhibited cell growth or sensitized towards irradiation, with 12 compounds inducing cell death independently of irradiation, and 11 compounds functioning as radiosensitizers (Table 1 and Supplementary Fig. S1). Cytotoxicity of these 23 compounds was subsequently determined on primary human fibroblasts and on C17.2 neuronal precursor cells (NPCs), to assess the therapeutic window (Table 1).

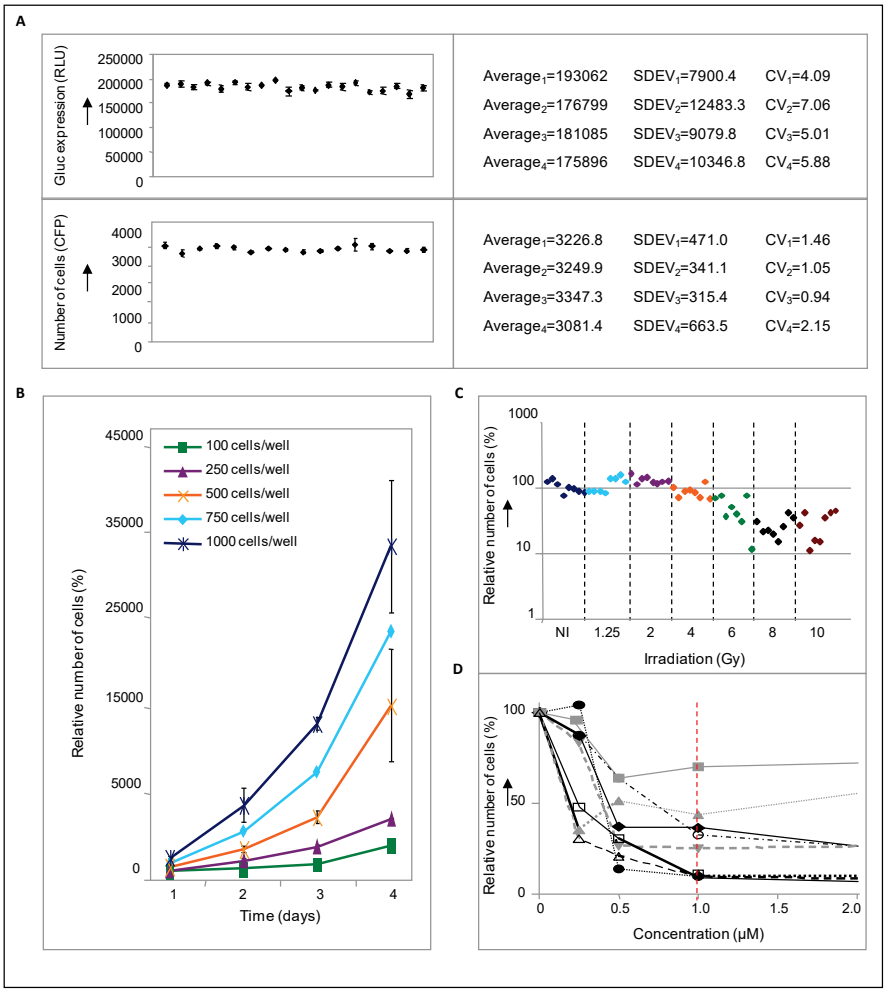

Figure 1. Determination of screening conditions. **A**, reproducibility of Gluc measurements (upper panel) or cell counts as measured by Acumen technology (lower panel). Aliquots of Gluc-containing medium or equal numbers of cells were plated in 96-well plates in quadruplicate, and measured to assess plate-to-plate and well-to-well variation (RLU=relative luciferase units). Data are presented as means ± SD. The corresponding coefficients of variation (CV) are depicted in the right-hand panels. **B**, growth curves of DAOY medulloblastoma cells. One hundred, 250, 500, 750, or 1000 cells were plated per well and set at 100%. Relative cell numbers were measured at different time points after plating as indicated in the figure. A plating density of 750 cells/well resulted in exponentially growing cells after 4 days of incubation that could be monitored without much variation. Data are presented as means ± SD (n=3). **C**, graphic representation of the irradiation response in DAOY cells. Growth of non-irradiated (NI) cells is set at 100%. For each irradiation dose 8 samples were measured. **D**, concentration curves of DAOY medulloblastoma cells treated for four days with 0, 0.5, 1, or 2 µM of different drugs. Compounds were chosen randomly from the TimTec library: ST027883 (-■-), ST004727 (-●-), ST053862 (-▲-), ST012157 (-▼-), ST012256 (-♦-), ST029265 (-○-), ST036501 (-□-), ST052055 (-△-). A drug concentration of 1 µM was (red dotted line) was used for the final screen.

This smaller screen narrowed our list of putative novel compounds for use in medulloblastoma down to five: two radiosensitizing agents and three compounds that have been identified as inducers of cell death in DAOY cells independently of irradiation (Fig. 2B). The flavonoid quercetin was among the radiosensitizing compounds that has been shown to enhance radiation-induced cell death in rat hepatoma cells.[301,302] Treatment with quercetin 30 minutes prior to irradiation resulted in a 5-fold reduction in cell growth (~20% cell survival), while treatment with quercetin alone did not significantly affect cell viability compared to cells treated with the solvent DMSO (Fig. 2C). Irradiation without addition of quercetin resulted in a 2-fold reduction in cell numbers. As mentioned above, these results were not observed in primary human fibroblasts or neuronal precursor cells (Fig. 2C).

Quercetin sensitizes medulloblastoma cells to radiation *in vitro*

Since quercetin has been reported to effectively cross the blood-brain-barrier [303], we hypothesized that this compound could be an attractive agent for the treatment of medulloblastoma. Therefore, we investigated if similar effects could be observed in additional medulloblastoma cell lines. D283-med, D458-med, and DAOY cells were incubated with 1 µM quercetin 30 minutes prior to irradiation, and cell numbers were determined at 4 days after treatment (Fig. 3A). Although the responses were less pronounced in the D458-med cells, a radiosensitizing effect of quercetin was observed in all cell lines, while quercetin treatment by itself did not inhibit cell proliferation. To further confirm the radiosensitizing potential of quercetin, dose-dependent clonogenic survival assays were performed. DAOY cells appeared unfit for these experiments, since they did not form clones. However, treatment of D283-med and D458-med medulloblastoma cells with 0.5 µM or 1 µM quercetin showed radiosensitization in both cell lines (Fig. 3B), even at radiobiologically relevant irradiation doses of 1 Gy or 2 Gy used in fractionated radiation schemes. These results strengthen our hypothesis that quercetin is a putative radiosensitizer for medulloblastoma. Next, we tested the radiosensitizing effect of quercetin on two primary medulloblastoma cell cultures, VU371 and ICb-1299MB [298]. Similar as for the cell lines, cells were treated with 1 µM quercetin 30 minutes prior to irradiation, and viability was determined four days after treatment (Fig. 3C). Again, quercetin by itself did not reduce cell viability, however, these cells are highly sensitive to radiation (data not shown). Therefore, cells were irradiated with the lowest technical dose possible, 0.7 Gy, which already significantly impaired viability. We did not observe an enhanced radiation response in combination with quercetin in these cells. Since medulloblastomas have been subclassified into four molecular subgroups [10], we determined to which subgroups the used cell lines belong. Expression of four subgroup classifier genes was assessed by qRT-PCR, which was previously described by Zhao et al. [298] (Supplementary Fig. S2A+B). DAOY was identified as a SHH medulloblastoma while D283-med, D458-med, and VU371 seem to belong to the group

3 subtype (Fig. 3D and Supplementary Fig. S2A+B). ICb-1299MB was previously classified as a group 4 medulloblastoma [298].

Quercetin treatment improves radiation efficacy in a xenograft tumor model

To further evaluate if quercetin can function as a novel agent in the treatment of medulloblastoma, we investigated the effect of this compound in an *in vivo* setting, using an orthotopic xenograft mouse model. Therefore, luciferase-expressing D283-med cells were implanted stereotactically into the left cerebellar hemisphere of nude mice. In two independent experiments, 31 out of 36 mice developed primary tumors, as judged by bioluminescent imaging (BLI) three weeks after implantation. These mice were then randomly assigned into four groups, and treated with vehicle (5% DMSO) or quercetin, either alone or in combination with irradiation. Since quercetin has a half-life of only 20 minutes *in vivo* [304], six consecutive injections with quercetin (100 mg/kg) were given at different time points around the time of irradiation (60 or 30 minutes before, 30 or 60 minutes after irradiation, 0 hours and 24 hours after irradiation). Quercetin treatment did not induce any neurological symptoms or other adverse events. Tumor growth was monitored twice a week by BLI. In addition, the mice were monitored daily for discomfort and weight loss. Although the BLI signal of the tumors did not differ between the various groups, survival analysis indicated a significant extension of the group that received ionizing radiation in combination with quercetin as compared to the vehicle-treated group ($p=0.0052$), the quercetin group ($p<0.0001$), or the group that only received radiotherapy ($p=0.002$; Fig. 4A). All animals treated with the combination of quercetin and irradiation survived for more than 24 days after treatment, with a median survival time of 32 days. Animals that did not receive irradiation (either vehicle- or quercetin-treated) had a median survival of only 12-17 days (Fig. 4B).

Figure 2. **(next page)** A small molecule screen identifies quercetin as a radiosensitizer in medulloblastoma cells. **A**, example of a scatter plot of Gluc values (left panels) and Acumen read-out (right panels), representing cell survival after treatment of DAOY cells with 1 µM of the ActiTarg-K960 small molecule library in the presence, or absence of irradiation (4 Gy). The fluorescence in the single wells as measured by the Acumen is represented as relative intensities of the color green, where black corresponds with little cells and green with many cells. When using Gluc as a read-out, cell viability was measured by luciferase activity and corrected for the toxicity of the solvent, 0.1% DMSO (set to 100%). A reduction of >75% of cell growth was considered to be significant, as indicated by a dashed line. Each dot represents a single well; in position F05 a cytotoxic agent is identified, in position C09 a radiosensitizer. A representative 96-well plate is shown. **B**, structure formulae of compounds that induce cell death in DAOY medulloblastoma cells but show limited cytotoxicity on primary human fibroblasts and on C17.2 neuronal precursor cells (NPCs). Two radiosensitizing agents and three compounds that induce cell death independently of irradiation have been identified. **C**, graphic representation of relative cell survival in DAOY medulloblastoma cells (left panel), primary human fibroblasts (PHF, middle panel), or neural precursor cells (NPC, right panel) after quercetin (QC)

treatment and/or irradiation (IR), as extracted from the small molecule screen. Data are presented as means ± SD (n=3). ** p<0.005, Mann-Whitney U test.

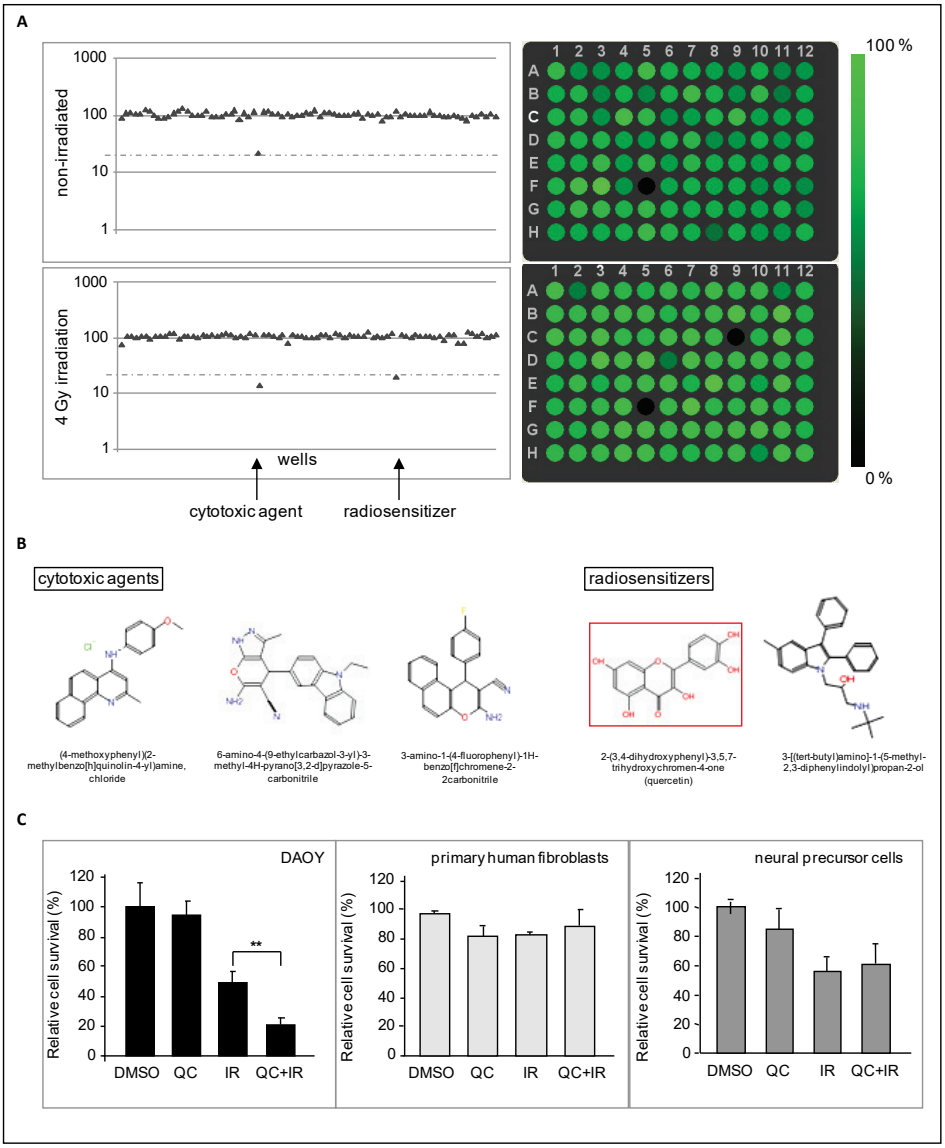

Figure 2 (legend on previous page)

IUPAC name	structure formula	Molecular weight (Da)	common name	Fibroblasts	Neural Precursor Cells
(4-methoxyphenyl)(2-methylbenzo[h]quinolin-4-yl)amine, chloride	C21H19ClN2O	350,85		OK	OK
6-amino-4-(9-ethylcarbazol-3-yl)-3-methyl-4H-pyrano[3,2-d]pyrazole-5-carbonitrile	C22H19N5O	369,43		OK	OK
3-amino-1-(4-fluorophenyl)-1H-benzo[f]chromene-2-carbonitrile	C20H13FN2O	316,33		OK	OK
5-bromo-4-(4-cyclohexyl-5-phenyl(1,2,4-triazol-3-ylthio))-2-phenyl-2-hydropyri dazin-3-one	C24H22BrN5OS	508,44		OK	+/-
4,5-dichloro-2-[(4-fluorophenyl)methyl]-2-hydropyridazin-3-one	C11H7Cl2FN2O	273,09		+/-	+/-
3-[((1E)-2-(2-pyridyl)-1-azavinyl)amino]-6-methyl-4H-1,2,4-triazin-5-one	C10H10N6O	230,23		+/-	cell death
3-[((1E)-2-(2-pyridyl)-1-azavinyl)amino]-4H-1,2,4-triazin-5-one	C9H8N6O	216,2		+/-	cell death
1-cyclohexylazoline-2,5-dione	C10H13NO2	179,22	N-cyclohexylmaleimide	cell death	cell death
4,7-dimethylpyridino[3,2-h]quinoline, oxamethane	C14H14N2O	226,28	neocuproine	cell death	cell death
2,9-dimethylpyridino[3,2-h]quinoline	C14H12N2	208,26	neocuproine	cell death	cell death
5-((2E)-5,5-dichloropenta-2,4-dienoyl)-6-methylpyran-2-one	C11H8Cl2O3	259,09		cell death	cell death
(8-chloro(4H-benzo[e][1,3-thiazolo[5,4-c]thiin-2-yl))naphthylamine	C20H13ClN2S2	380,92		cell death	cell death

2-(3,4-dihydroxyphenyl)-3,5,7-trihydroxychromen-4-one	C15H10O7	302,24	quercetin	OK	OK
3-[(tert-butylamino]-1-(5-methyl-2,3-diphenylindolyl)propan-2-ol	C28H32N2O	412,57		OK	OK
5-(4,6-dimethylpyrimidin-2-ylthio)-4-nitrobenzo[c]1,2,5-thiadiazole	C12H9N5O2S2	319,37		+/-	OK
3-(indol-3-ylmethylene)benzo[b]pyran-2,4-dione	C18H11NO3	289,29		+/-	cell death
5-[(1E)-2-(4-bromo-3-chlorophenyl)-2-azavinyl]-2-nitrothiophene	C11H6BrClN2O2S	345,6		+/-	cell death
5-[(1E)-2-(2,4-dichlorophenyl)-2-azavinyl]-2-nitrothiophene	C11H6Cl2N2O2S	301,15		+/-	cell death
5-[(1E)-2-(4-iodophenyl)-2-azavinyl]-2-nitrothiophene	C11H7IN2O2S	358,16		cell death	cell death
6-(tert-butyl)-2-[3-(tert-butyl)-5-bromo-2-hydroxyphenylthio]-4-bromophenol	C20H24Br2O2S	488,28		cell death	cell death
[(5-nitro-2-thienyl)methylene]methane-1,1-dicarbonitrile	C8H3N3O2S	205,2		cell death	cell death
9-((1E)-2-nitrovinyl)anthracene	C16H11NO2	249,27		cell death	cell death
dl2,3,4,5,6-pentafluorophenyl ketone	C13F10O	362,13		cell death	cell death

Table 1. Overview of compounds that induce cell death in DAOY medulloblastoma cells, as identified by a small molecule screen. Chemical compounds that repetitively induced cell death (upper panel) or functioned as radiosensitizers (lower panel) are represented. NPC=neural precursor cells; OK= no cell death as compared to control, +/- = ≤ 50% cell death.

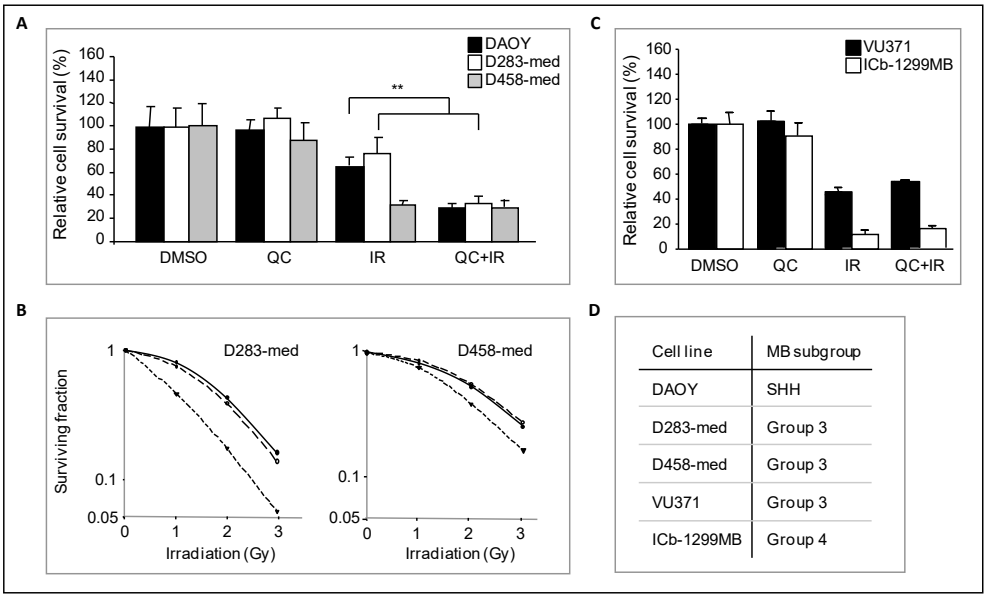

Figure 3. Quercetin sensitizes towards irradiation in a panel of medulloblastoma cells. A, graphic representation of relative cell survival of DAOY, D283-med, and D458-med cells after 4 days of quercetin treatment in the presence or absence of irradiation (4 Gy). Cell numbers were determined by visual counts, using a Bürker hemacytometer. Vehicle treated cells are set at 100%. Data are presented as means ± SD (n=3). ** $p<0.005$, Mann-Whitney U test. **B**, clonogenic survival of D283-med (left panel) and D458-med (right panel) medulloblastoma cells, 14 days after irradiation (0-3Gy). Cells were treated with 0 µM (-●-), 0,5 µM (-o-), or 1 µM (-▼-) quercetin 30 minutes prior to irradiation. A representative experiment is shown. **C**, graphic representation of relative cell survival of VU371 and ICb-1299MB cells after 4 days of quercetin treatment in the presence or absence of irradiation (0.7 Gy). Cell viability was determined by Cell Titer Glo assay. Vehicle treated cells are set at 100%. Data are presented as means ± SD. **D**, molecular subgroup classification of DAOY, D283-med, D458-med, VU371, and ICb-1299MB cells. Expression levels of subgroup classifiers WIF1, SFRP1, NPR3, and KCNA were determined by qRT-PCR to determine to which subgroups the used medulloblastoma cells belong.

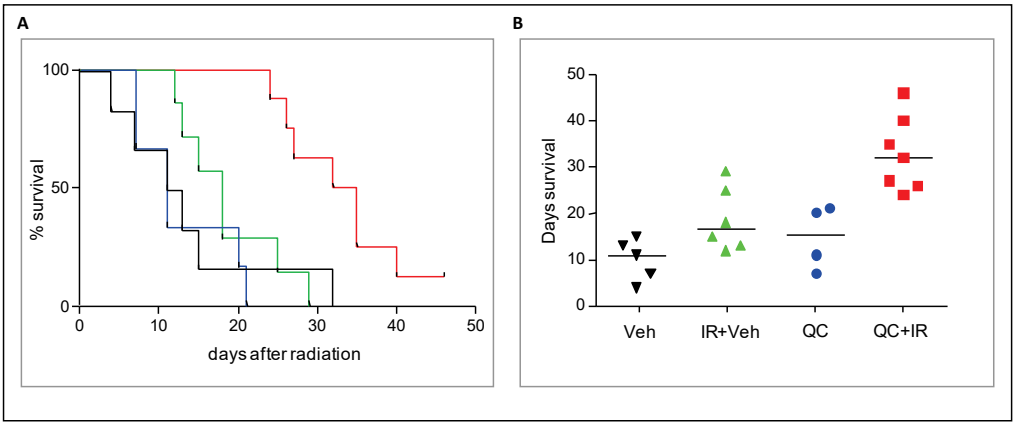

Figure 4. Effect of quercetin treatment in combination with irradiation on survival in a xenograft mouse model. A, Kaplan-Meier survival analysis of medulloblastoma-bearing mice treated with quercetin (blue line), vehicle (5% DMSO – black line), vehicle and irradiation (green line), and quercetin in combination with irradiation (red line). A significant survival extension of the group that received ionizing radiation in combination with quercetin as compared to the vehicle-treated group ($p=0.0052$), the quercetin group ($p<0.0001$), or the group that only received radiotherapy ($p=0.002$) was observed. **B,** graphical representation of survival in days; medians are indicated as horizontal lines.

DISCUSSION

In the past decade, a better understanding of the biology and heterogeneity of childhood medulloblastomas has allowed an improved patient stratification and risk-adapted treatment strategies. However, despite these novel insights, therapy still fails in approximately 30% of patients and is often accompanied by severe long-term sequelae. Thus, there still is a need for alternative therapies that allow to lower the total dose of irradiation, reducing the long-term side effects, and/or increase the radiation efficacy. We show here that the flavonoid quercetin can sensitize medulloblastoma cells to irradiation, and that administration of quercetin during radiotherapy significantly improves survival in mice harboring medulloblastoma.

Quercetin was identified as a 'ready-to-use' radiosensitizer in a small molecule screen for medulloblastoma cells, using two independent read-out systems. The small molecule screen consisted of 960 compounds with a diversity of chemical structures that have been reported to exert kinase inhibitory properties. In this screen 23 compounds were repeatedly identified that could inhibit cell growth (n=12), or sensitize towards irradiation (n=11). Strikingly, two of the compounds that induced cell death independently of irradiation had similar structures, as did three of the 11 compounds that functioned as a radiosensitizer (nitrophenes, Supplementary Fig. S1). However, most of those drugs also induced cell death in primary human fibroblasts or neuronal progenitor cells, rendering them unfit for the development of novel and tumor-specific therapies. Unlike those compounds, quercetin did not affect the proliferation of neuronal precursor cells or normal human fibroblasts, nor showed any toxicity in the absence of ionizing radiation. This is in concordance with previous studies that report selective activity of quercetin as a sensitizer to chemotherapeutics on cancer cells, but not in normal cells, even though higher quercetin concentrations (ranging from 5-200 μM) were used in these studies [305–307]. Importantly, the low micromolar concentrations used in our experiments are in the range of the plasma concentrations that can be reached in humans and are considered to be safe [308]. Quercetin is found in a broad range of fruits and vegetables such as apples, onions and tomatoes, and present in plasma at the nanomolar range (<100 nM) through our dietary intake, but micromolar concentrations have been reported after supplementation [309,310].

The observation that the concentrations needed for therapeutic benefit can be easily achieved by oral administration, and the fact that quercetin is cheap and readily available, renders this flavonoid an interesting option for the treatment of children with medulloblastoma. Another motive to consider quercetin as a radiosensitizer for this type of brain tumors, is the previously reported observation that quercetin can pass the blood-brain

barrier (BBB)[311,312]. The BBB is a natural boundary between circulating blood and cerebrospinal fluid that protects the brain from toxins and potentially harmful substances (reviewed by Agarwal *et al.* [313]). Although beneficial under normal circumstances, the presence of this BBB constitutes a major obstacle for drug delivery in the treatment of brain tumors. Importantly, quercetin has not only been shown to pass the BBB in *in vitro* systems, but has also been shown to accumulate in the brain after oral administration in rats [303]. Moreover, quercetin has been shown to function as a neuroprotective agent, both *in vitro* and *in vivo* following ischemia, trauma, or other forms of induced brain damage [303,314–316]. Of particular interest in the context of medulloblastoma treatment is the observation that administration of quercetin can improve learning and memory deficits in animals that were subjected to brain damaging agents [317–319].

The neuroprotective effect of quercetin has been suggested to be due to its anti-oxidative properties. Quercetin is a potent anti-oxidant that can scavenge free radicals and bind transition metal ions. However, alternative mechanisms, such as modulation of signal transduction pathways or effects on gene expression have also been reported. Quercetin can modulate the activity of many kinases and other enzymes (reviewed by Russo *et al.* [320]), which may explain the diversity of its actions. Besides neuroprotective properties, quercetin has been described to prevent cardiovascular diseases [321], to function as a chemopreventive agent [322], to have anti-proliferative and growth-suppressing effects [323], to induce senescence and autophagy [324,325], and to have anti-inflammatory and anti-angiogenic activities [326,327]. Each property or action appears to depend on the dose and model system used. Of note are the inhibition of the Wnt/β-catenin pathway, which plays an important role in one of the four medulloblastoma subgroups [10], and the inhibition of the Hepatocyte Growth Factor (HGF)-induced cell migration in medulloblastoma by quercetin [328]. Furthermore, quercetin has been reported to induce radiosensitization in tumor cells other than medulloblastoma by targeting the ATM-mediated pathway, which is critical in the DNA damage response [37]. Which pathway or mechanism is involved in the radiosensitization of medulloblastoma cells by quercetin is not exactly known at the moment.

Four distinct molecular subtypes of medulloblastoma have been identified [10]. Subclassification of the cell lines used in this study showed that the SHH and group 3 subtypes were represented. DAOY was identified as a SHH medulloblastoma, which was also suggested by Pambid *et al.* [329]. D283-med and D458-med belong to the group 3 medulloblastomas as was reported before for D458-med [9,330]. We observed radiosensitization after treatment with quercetin in DAOY and D283-med and, to a lesser extent, in D458-med cells. This indicates that the mechanism underlying the improved radiation response caused by quercetin may represent a general effect on medulloblastoma cells and, thus, is likely to be subtype-independent. The primary cell cultures used in this study belong to the group 3 and group 4

subtypes. We did not detect a radiosensitizing effect of quercetin in these cells, since these cells are highly radiosensitive *in vitro* and there is no window in which quercetin can exert its effect. This was also seen in D458-med cells, which show high sensitivity to radiation. It would be of interest to examine the efficacy of quercetin in radioresistant primary medulloblastoma cell cultures. In addition, the response of primary cell cultures *in vitro* may not necessarily represent the response in the cerebellar environment. Therefore, we are setting up more primary cell lines of the different subtypes and use these to develop orthotopic mouse models to study the effect of quercetin as a radiosensitizer in medulloblastoma in an environment that is more comparable to that of the original tumor. However, the results presented here indicate that quercetin functions as a potent radiosensitizer in medulloblastoma cells at easily achievable concentrations, providing a promising lead for treatment of children with this type of brain tumor.

Acknowledgements

We thank Laurine Wedekind for technical assistance and Stichting VUmc-CCA for their contribution to acquire the Acumen eX3.

Supplementary Figures

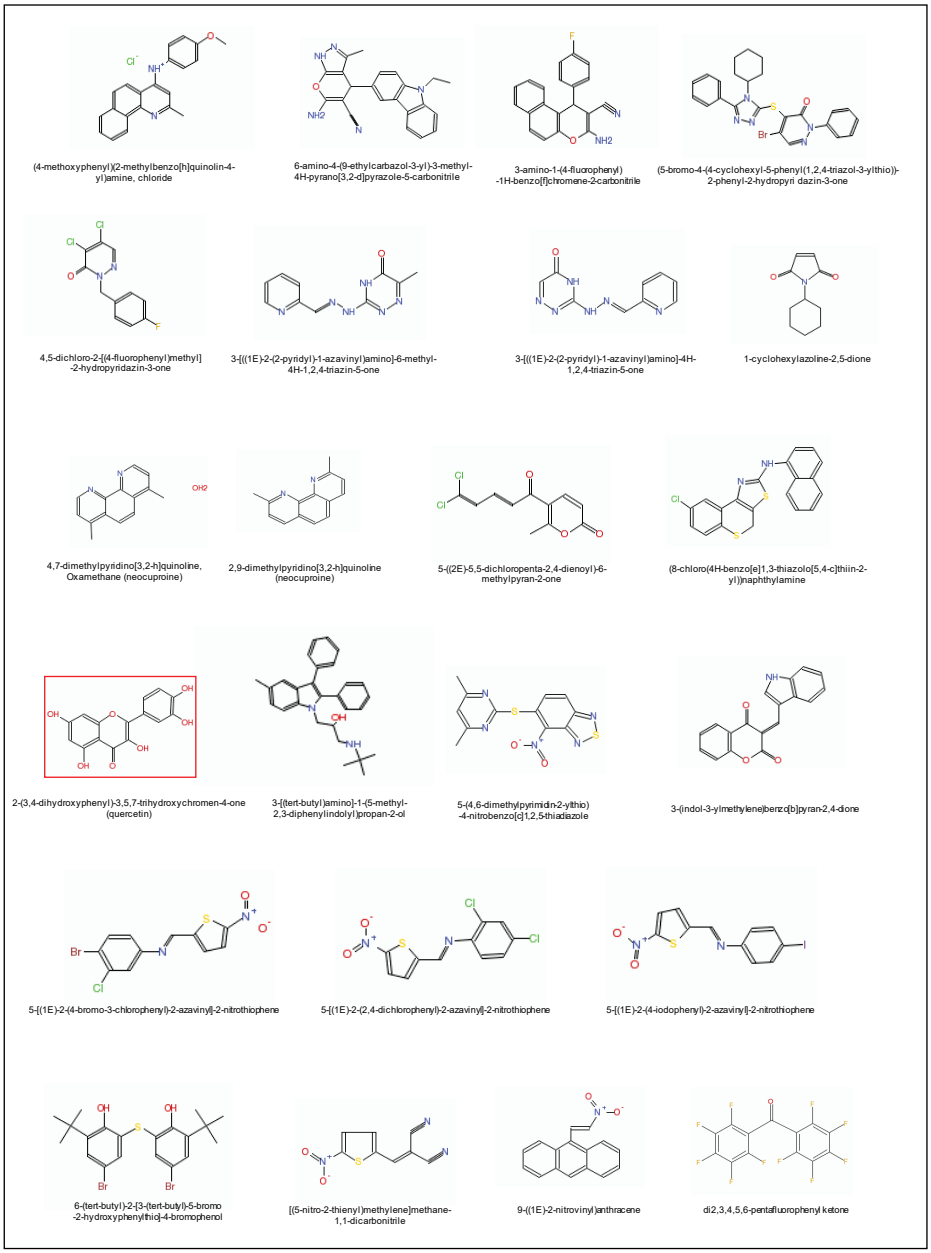

Supplementary Figure S1. Structure formulae of compounds that induce cell death in DAOY medulloblastoma cells, as identified by a small molecule screen. Chemical compounds that repetitively induced cell death (upper twelve) or functioned as radiosensitizers (lower structures) are represented.

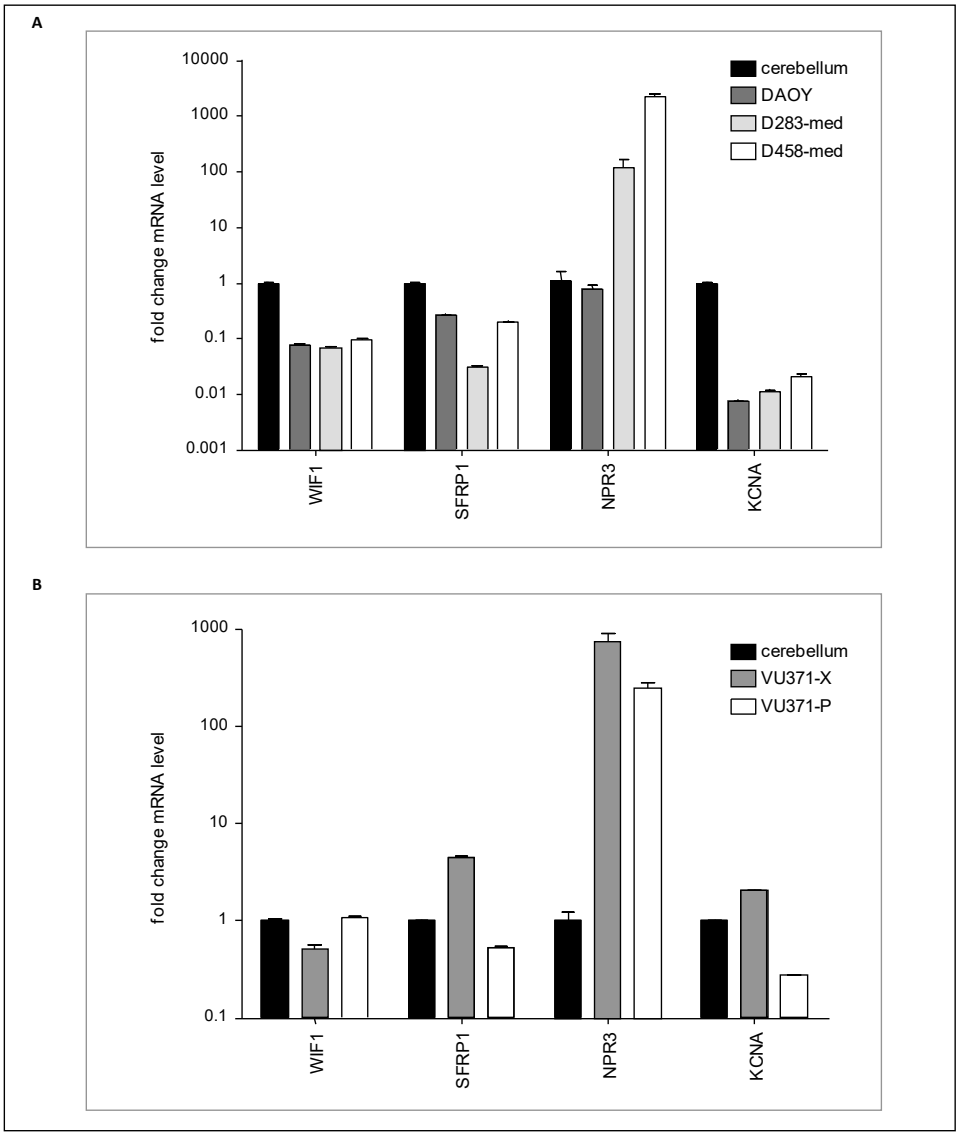

Supplementary Figure S2. Expression levels of subgroup classifiers WIF1, SFRP1, NPR3, and KCNA in medulloblastoma cells compared to normal cerebellum. A, expression levels of WIF1, SFRP1, NPR3, and KCNA in DAOY, D283-med, and D458-med compared to normal cerebellum. DAOY was identified as a SHH medulloblastoma, D283-med and D458-med were identified as group 3 medulloblastomas. **B,** expression levels of WIF1, SFRP1, NPR3, and KCNA in VU371 cells from a xenograft tumor and VU371 cells from the original tumor as compared to expression in normal cerebellum. VU371 was identified as a group 3 medulloblastoma. The subgroup type was preserved after serial transplantation of tumor cells in the cerebellum of mice.

CHAPTER 6 |

Glioblastoma-derived extracellular vesicles induce proliferation and temozolomide resistance via chemokine receptor CCR8

Jordi Berenguer, Tonny Lagerweij, Xi Wen Zhao, Sophie Dusoswa, Petra van der Stoop, Bart Westerman, Danijela Koppers-Lalic, Mark C. de Gooijer, Marloes Zoetemelk, Anoek Zomer, Matheus H. W. Crommentuijn, Laurine E. Wedekind, Àlan López-López, Alberta Giovanazzi, Marina Bruch-Oms, Ida H. van der Meulen-Muileman, Rogier M. Reijmers, Toin H. van Kuppevelt, Juan-Jesús García-Vallejo, Yvette van Kooyk, Bakhos A. Tannous, Pieter Wesseling, W. Peter Vandertop, David P. Noske, Victor W. van Beusechem, Jacco van Rheenen, D. Michiel Pegtel, Olaf van Tellingen, Thomas Wurdinger

Submitted

ABSTRACT

Cancer cells release extracellular vesicles (EVs) that contain functional biomolecules such as RNA and proteins. EVs are transferred to recipient cancer cells and can promote tumor progression and therapy resistance. In contrast to most viral uptake mechanisms, EV uptake mechanisms are currently poorly understood. Through RNAi screening we have discovered a novel EV uptake mechanism involving a triple interaction between the chemokine receptor CCR8 on the cells, glycans exposed on EVs and the soluble ligand CCL18. This ligand acts as bridging molecule, connecting EVs to cancer cells. We show that glioblastoma EVs promote cell proliferation and resistance to the alkylating agent temozolomide (TMZ). Using *in vitro* and *in vivo* stem-like glioblastoma models we demonstrate that EV-induced phenotypes are neutralized by the small molecule CCR8 inhibitor R243. Interference with chemokine receptors may offer therapeutic opportunities against EV-mediated cross-talk in glioblastoma, and perhaps other diseases in which EV glycosylation plays a role.

INTRODUCTION

Intracellular vesicles (EVs), including exosomes and shed microvesicles, are membranous vesicles released by most, if not all, cell types. EVs contain active molecules such as proteins, lipids and nucleic acids, that can exert biological functions once taken up by recipient cells. EV-mediated communication is of particular importance in tumor progression and therapy resistance. For several cancer types it was demonstrated that migratory and metastatic potential can be phenocopied from one cell to another by EVs [125,331–335], and that tumor growth is enhanced by EVs in many cancer types, including glioblastoma (GBM) [336–339]. EVs are involved in many aspects of the communication between tumors and their microenvironment, such as cell migration and homing, EV-mediated propagation of GBM heterogeneity and MGMT promotor methylation status-dependent TMZ resistance [340–343]. Tumor EVs also exert a protective effect against several chemotherapeutic agents by delivering a variety of resistance-inducing molecules such as P-glycoprotein (P-gp), TrpC5, and non-coding RNAs [344–348]

Despite the promising therapeutic potential of blocking EV uptake in cancer, this approach is not extensively exploited due to the scarce knowledge of EV uptake mechanisms. EV uptake is considered to depend on the EV donor and recipient cell type, their physiological state, and the presence or absence of interfering molecules in the extracellular microenvironment [349–351]. Although direct fusion of EVs and plasma membranes has been reported for melanoma cells [352], multiple studies point to interactions involving endocytic pathways. Proteinase K treatment of either recipient cells or EVs strongly reduces EV uptake in several cell types, implying a role of membrane proteins in the internalization process [353–355]. EV uptake is also inhibited at 4°C, indicating an active, energy-dependent process [353,356,357]. Co-localization studies and assays employing pathway-specific inhibitors revealed involvement of both clathrin-dependent and clathrin-independent endocytosis, including caveolin-mediated endocytosis, macropinocytosis and phagocytosis [351]. These observations seem compatible with receptor-mediated EV uptake mechanisms, similar as for many enveloped viruses [358,359]. To date only few specific cellular receptors for EVs have been proposed. In an early study, Tim1 and Tim2 receptors were proposed to bind phosphatidylserine exposed on EV membranes on pre-B cells overexpressing these receptors [360]. Integrins have also been shown to act as EV receptors by binding lysophosphatidic acid from the EV surface [361]. Furthermore, heparan sulfate proteoglycans (HSPGs) on the plasma membrane were reported to function as EV receptors, in a mechanism in which fibronectin acts as a bridging molecule that interacts with both cellular and exosomal HSPGs [362,363].

GBM is the most common primary malignant tumor of the central nervous system in adults and known to release large amounts of EVs [339,364,365]. Affected patients have an extremely poor prognosis with a median survival of only 15 months following treatment [366]. Standard

of care currently consists of tumor resection combined with radiotherapy and concomitant and adjuvant chemotherapy with the alkylating agent temozolomide (TMZ). Although tumors may initially respond to this regimen, recurrences are inevitable and occur even while patients are still receiving adjuvant TMZ [49]. Here we show that GBM EVs are inducers of cell proliferation and capable of triggering TMZ resistance in recipient GBM cells. Using RNAi screening we identified the chemokine receptor CCR8 as a receptor for EVs, allowing for binding and entry of EVs decorated with glycans that interact with the chemokine CCL18.

MATERIALS and METHODS

Animal models

Animal experiments were performed in accordance with the European Community Council Directive 2010/63/EU. The experimental protocol was validated and approved by the local committee on animal experimentation of the VU University medical center or The Netherlands Cancer Institute . Athymic Nude-Fox1nu mice were purchased from Harlan/Envigo (Horst, The Netherlands). They were kept under filter top conditions and received food and water ad libitum.

Antibodies and chemicals

MC148 was purchased from B-Bridge international and was dissolved in PBS. R243 was custom synthesized by MercaChem (Nijmegen, The Netherlands) and was dissolved in dimethyl-sulfoxide (DMSO). Temozolomide (dissolved in DMSO), 4',6-diamidino-2-phenylindole (DAPI), Dynasore, heparin, heparinase III, Dynasore and PKH67 were obtained from Sigma. BrdU was from Life Technologies and recombinant CCL18 and human Epidermal Growth Factor (hEGF) were from R&D. Basic-Fibroblast Growth Factor (b-FGF) was purchased from PeproTech. The antibodies used in this work were obtained from the following manufacturers: mouse anti-CD63 (Clone NKI/C3) from Fisher Scientific. Mouse anti-Alix and mouse anti-β-Actin were purchased from Santa Cruz. Mouse anti-Cre and gold-conjugated rabbit anti-goat are from Sigma. Rabbit anti-BrdU from Rockland. Rabbit anti-CCR8 and rabbit anti-GFP from Abcam. Goat anti-CCL18 from Origene. Rabbit anti phospho-ERK (Phospho-p44/42 MAPK (Erk1/2) (Thr202/Tyr204)) from Cell Signaling. HRP-conjugated goat anti-mouse, HRP-conjugated goat anti-rabbit and HRP-conjugated rabbit anti-goat used as secondary antibodies in Western blots were from Dako. IRDYE 800CW mouse anti-rabbit and IRDYE® 680RD goat anti-mouse also employed for Western blot were from Li Cor. Alexa Fluor 405 and goat anti-rabbit Alexa Fluor 594 from Life Technologies. Protein A-gold (purchased from Cell Microscopy Core, University Medical Center Utrecht), goat-anti-biotin-Gold (Aureon). Phage display antibodies (kindly provided by Van Kuppevelt, Nijmegen) to detect three types of glycosaminoglycans: VSV-tagged anti-heparan sulfate (HS4E4), VSV-tagged anti-chondroitin sulfate (1O3H10) and VSV-tagged anti-dermatan sulfate (GD3A12).

Western blot analysis

For Western blot analysis on p-ERK, cells 5 x 10^5 cells were seeded in 24-well plates and isolated EVs (or PBS in the control wells) were added at a final concentration of 100 ng/µl at the moment of seeding and once more 18 h later. At 12 h after second EV addition, the cells were harvested, washed with PBS and lysed in RIPA buffer (150 mM NaCl, 50 mM Tris-HCl (pH 8.0), 1% NP-40, 0.5% deoxycholate, 0.1% SDS) supplemented with Protease Inhibitor Cocktail (Roche Applied Sciences). For Alix, CD63 and CCL18 analysis, 40 µg of EVs were

directly lysed in RIPA buffer supplemented with protease inhibitor cocktail. After lysis, cell or EV samples were loaded in SDS-PAGE gels using NuPAGE® Novex 4–12% Bis-Tris 1.0 mm gel (Life Technologies) and the NuPAGE® system from Life Technologies and were transferred onto 0.45 µm pore-Immobilon-P PVDF Membrane (Millipore). After blotting, membranes were blocked for 30 min in 5% milk (Campina) for CCL18, Alix, and CD63 analyses and in Rockland Blocking Buffer (Rockland) for phospho-ERK and β-Actin and incubated overnight with primary antibodies (diluted in blocking buffer) at 4°C. After three washes with Tris-Buffered Saline + 0.1% Tween (TBS-T), membranes were incubated with secondary antibodies (diluted in blocking buffer) for 1.5 h and washed again three times with TBS-T before being developed using Amersham ECL Plus Western Blotting Detection System (GE Healthcare) (CCL-18, Alix, and CD63) or scanned in a LI-COR Odyssey scanner (Biosciences) according to the manufacturers' instructions (phospho-ERK and β-actin).

Transmission electron microscopy

GBM8 EVs were diluted 1:1 with PBS and coated for a minimum of 10 min on Formfar coated copper grids (Electron Microscopy Sciences (EMS)). For the analysis of size distribution, grids were washed five times after coating, fixed in 1% glutaraldehyde (EMS), and incubated in 0.5% uranil acetate (SPI Supplies) / 2% methyl cellulose (SIGMA). A total of nine images (three images per grid from three separate grids) were acquired using a transmission electron microscope (Philips CM100 Bio Twin), connected to a CCD camera (Olympus, Morada G2) and analyzed in iTEM version 5.2 software. Diameters of all EVs found on these images were measured in iTEM, resulting in a total of 944 measurements. For immuno-gold stainings, grids were coated with EVs 1:1 diluted in PBS, washed five times with PBS supplemented with 1% BSA (PBA), blocked for 5 min in PBA and 10 min in a commercial blocking reagent (Aureon) or 10% rabbit serum (obtained from the Animal facility VU University medical center). After a minimum of 30 min incubation with primary antibodies, grids were washed again five times with PBA before incubation for 20 min with secondary reagents. Lastly grids were washed, fixed in 1% glutaraldehyde, and incubated in 0.5% uranil acetate/2% methyl cellulose before imaging. Image acquisition was performed using a transmission electron microscope connected to a CCD camera and iTEM software.

EV interaction analysis

For EV interaction experiments, subconfluent cultures were incubated with 10 ng/µl of PKH67-labeled EVs (if not stated otherwise) for 18 hours. Although it is firmly established that uptake of EVs is rapid and becomes saturated at 2-3 after incubation, we have incubated overnight (18 hours), because we were not only interested in EV binding, but also in subsequent processes such as internalization, accumulation, and cellular distribution where interference could potentially prevent EV function. When indicated, cells or EVs were treated with recombinant CCL18, anti-CCL18 neutralizing antibody, heparin (25 µg/ml),

heparinase III, MC148 or R243 (20 µM unless indicated otherwise) for 1 h before EV addition, except for heparinase III, treatment (2 miU every 2 h for 6 h at 37°C). After overnight incubation with labeled EVs, cells were washed with PBS before fluorescence analysis. $PKH67^+$ cells were either directly quantified in a Leica DM6000 microscope or analyzed by flow cytometry. Since GBM8 medium contains heparin, GBM8 uptake experiments were carried out in heparin-reduced medium (0.2 µg/ml).

RNA isolation and RT-PCR

A total of 5 x 10^5 cells or 40 µg of EVs were lysed in lysis/binding buffer and RNA was isolated using the total RNA extraction protocol from the MiRVANA kit (Ambion) following manufacturer's indications. After isolation, RNA integrity and concentration were determined on an Agilent 2100 Bioanalyzer using Agilent Small RNA kit (Agilent Technologies, Germany), concentration of the samples was adjusted to the minimum concentration of the samples analyzed and cDNA was synthesized using Omniscript RT kit for RNA samples above 50 ng or with Sensiscript RT kit when RT reactions contained less than 50 ng (both kits were from Qiagen) following manufacturer's instructions.

Small RNA sequencing and data analysis

The RNA quality from GBM cell lines and matched EVs was analyzed on Agilent 2100 Bioanalyzer using Agilent Small RNA kit (Agilent Technologies, Germany). Maximum sample input (6 µl) was prepared for sequencing using the Illumina TruSeq small RNA Preparation Kit according to the manufacturer (Illumina). RNAseq was performed on a HiSeq 2500 (Illumina) pair-end 125 nucleotide length read, using equimolar amounts for each sample. Sequencing reads analysis was done by using the sRNAbench analysis package as described previously (Barturen et al., 2014; Koppers-Lalic et al., 2014). Briefly after adapter trimming and unique reads grouping, reads were aligned to the human genome (UCSC hg19) using the Bowtie 1.1.2. To provide annotations for RNA elements that mapped to human genome, several databases were used, including miRBase (version 21) for mature and pre-miRNA sequences and NCBI Reference Sequences (RefSeq Release 69, January 2nd 2015). Apart from the main sRNAbench program, a differential expression module based on edgeR (Robinson et al., 2010) was used to generate an expression matrix of all miRNAs detected. Note that by using edgeR, sRNAbench applies implicitly TMM normalization in the detection of differentially expressed small RNAs, which was reported to be among the most stable methods (Dillies et al., 2013; Maza et al., 2013).

Relative cell number quantifications

Relative number of cells in GBM8 spheres were estimated by calculating GBM8 sphere volumes, assuming the volume of a neurosphere to be proportional to the number of cells comprising it. When seeded at low density in round-bottom, cell-repellent 96-well plates

(Greiner Bio-One), GBM8 cells form a single, nearly perfectly spherical neurosphere. Using a Leica DM 3000B motorized microscope equipped with a Pulnix JAI RMC-1327GE camera, pictures of individual spheres were taken and the area covered by the sphere was calculated using ImageJ software. Radius of the sphere was calculated as the square root of the area divided by Pi, and relative sphere volume was calculated by taking four thirds of Pi multiplied by the third power of the calculated radius. When stated, R243 and/or TMZ (20 µM or otherwise indicated concentrations) were directly added to the culture medium immediately after seeding the cells. EVs were added at a final concentration of 100 ng/µl once 30 min after drug treatments and again 24 h later. Spheres were measured between from 5 to 7 days after treatments. IC_{50} value determination for R243 on GBM8 cells, as well as TMZ/R243 synergy studies were performed using CellTiter-Glo kit (Promega), and GBM-FM relative cell numbers in Figure 2D were estimated by luciferase assay (Promega). Both assays were performed following manufacturer's recommendations.

Development of Cre and mTmG lines and *in vitro* Cre-mT/mG EV transfer studies

The Cre-expressing GBM8 cell line was generated by lentiviral transduction of the plasmid Puro.Cre empty vector (Addgene #17408), followed by puromycin selection for one month. Homogeneity of Cre expression in GBM8-Cre cells was verified by immunocytochemistry. GBM8 mT/mG cells were generated by releasing the entire (linearized) mT/mG cassette from ROSA26 mT/mG plasmid (Addgene #17787) by restriction with AscI, AccI and PmeI (New England Biolabs), band purification and electroporation with a microporator MP-100 (Digital Bio, Seoul, South Korea) following manufacturer's instructions with a single pulse of 1400 V for 40 milliseconds. After 1 month in culture, cells still expressing mTomato protein were sorted by flow cytometry in a FACSARIA instrument (BD Biosciences). Functionality of the mT/mG cassette was verified by incubating the lenti Puro.Cre virus directly on GBM8-mT/mG cells and observing appearance of mG^+ cells 96 h later. For EV transfer studies, 1 x 10^4 GBM8-mT/mG cells were seeded in 6-well plates and Cre-donor EV isolates were added at a final concentration of 10 and 40 ng/µl. An equivalent volume of PBS was added as negative control. Alternatively, a total 10^4 GBM8-mT/mG and GBM8-Cre cells were co-cultured at 1/10 and 1/100 ratios of mT/mG vs Cre cells. As a negative control, GBM8-mT/mG cells were co-cultured with parental Cre^- cells. After 12 days in culture, wells were inspected for the presence of spheres with GFP^+ cells in a Leica DM IL microscope equipped with a DFC345 FX camera. Results were expressed as % of GFP^+ spheres relative to the total spheres.

In vivo Cre-mT/mG EV transfer studies

Shortly before intracranial injection, GBM8-mTmG were washed once with phosphate buffered saline (PBS) and concentrated to 1.2 x 10^5 cells per µl. Mice were stereotactically injected with 6 x 10^5 cells in a final volume of 5 µl into the striatum. All intracranial injections were performed using isoflurane inhalation anesthesia (1.5 L O_2 /min; 2% isoflurane) and

appropriate systemic and topical analgesia. Coordinates used for intracranial injections were 0.5 mm X, 2 mm Y, -2.5 mm Z from the bregma (1). Three days after injection of GBM8-mTmG tumor cells, 10 µl vesicle suspension (15 µg) was injected into the tumor, using the same coordinates. Vesicles were harvested by ultracentrifugation from Cre-containing GBM8 cells of from parental cells. For tumor-to-tumor crosstalk, GBM8-mTmG cells, GBM8-Cre cells and GBM8 parental cells were prepared and concentrated as indicated above. GBM8-mTmG cells were injected in the striatum of the left hemisphere, whereas GBM8-Cre (n = 6) or GBM8 parental cells (n = 6) were injected in the right hemisphere. Three weeks after tumor injection, mice were sacrificed and cryosections (8 µm thick) of brains were prepared. Fluorescence of endogenous mTomato and/or GFP in the left hemisphere was imaged in DAPI stained cryosections using a Zeiss Fluorescence microscope.

GPCR siRNA screening

For the GPCR siRNA screening, HEK-293T cells were plated in 96-well plates at a density of 5 x 10^4 cells/ml. After an overnight incubation, cells were transfected with a siGENOME Smartpool siRNA library-G Protein-Coupled Receptors (50 nM, Dharmacon) using Lipofectamine 2000 as a transfection reagent following manufacturer's indications. This library contains siRNAs against 512 individual GPCRs and GPCR-associated genes. After 48 h, 20 ng/µl of PKH67-labeled EVs were added to the plates. As controls for EV uptake reduction, every plate was loaded with a standard curve of labeled EVs (20, 10, 5 and 0 ng/µl) on untransfected cells. After overnight incubation with stained EVs, plates were washed twice with PBS, nuclei were stained with DAPI and plates were scanned in an Acumen eX3 (TTP LabTech, Melbourne, UK) microplate cytometer. After this overnight incubation time, the fluorescence signal represents the sum of multiple EV interactions and processes, including cell-surface bound EVs and intracellular EVs. Fluorescence levels were normalized by mean fluorescence intensity of all the plates excluding controls and divided by the number of nuclei determined by DAPI staining.

siRNA validation transfection

For siRNA screening validation on top-8 EV uptake-inhibiting GPCRs, new siRNAs against them were obtained from another manufacturer (Qiagen FlexiTube siRNAS: PTGIR_1: SI00019250, C5R1_1: SI00027412, TRAR3_1 (TAAR9): SI00159208, ADORA2A_1: SI00013874, MRGX2_1: SI00147994, CXCL3_1: SI00032662, CCR8_7: SI03027843, GPR172B_1: SI00120295). siRNAs were transfected in HEK-293T cells with Lipofectamine 2000 following manufacturer's instructions. Efficient mRNA knock-down of target genes was verified by quantitative real-time PCR (data not shown). siRNA screening results were also validated in GBM8 cells by electroporation of Qiagen's siRNAs with a microporator MP-100 (Digital Bio, Seoul, South Korea) following manufacturer's instructions with a single pulse of 1400 V for 40 milliseconds. At 48 h after transfection, HEK-293T and GBM8 cells were

incubated overnight with 20 ng/µl of PKH67-labeled EVs, washed twice with PBS and subjected to fluorescent EV uptake analysis. As a control for EV uptake inhibition in GBM8 cells, siRNA control cells were treated with Dynasore (80 µM), a Dynamin2 inhibitor know to impair EV uptake (Mulcahy et al., 2014Mulcahy et al., 2014) for 30 min before incubation with labelled EVs.

Flow cytometry

For FACS analysis, cells were washed in PBS, resuspended in PBS supplemented with 1% BSA (PBS-BSA) and analyzed with FACSDiva software in a BD Fortessa instrument. Collected data was processed with flowJoX software. CCR8 expression analysis was carried out by incubating cells with anti CCR8 antibody for 30 min on ice, washing them three times with PBS-BSA and incubating them with an Alexa Fluor 405-coupled secondary antibody for another 30 min. Cells were analyzed after three more washes with PBS-BSA. For the BrdU incorporation assay, cells were seeded at a density of 4 x 10^5 cells/ml and EVs (or PBS in the control wells) were added at a final concentration of 100 ng/µl at the moment of seeding and once more 18 h later. At 12 h after second EV addition, cells were incubated for 2 h with BrdU and washed with PBS prior fixation with 4% paraformaldehyde (PFA) for 15 min. Membranes were permeabilized with 100% cold methanol and cells were washed with DNAse buffer (10 mM Tris, 2.5 mM $MgCl_2$, 0.1 mM $CaCl_2$) and treated with DNAseI diluted in DNAse buffer at RT for 20 min. Cells were washed in ICC wash buffer (1x PBS, 0.1% Triton TX-100, 0.05% Azida, 1% BSA), blocked in wash buffer containing 10% fetal bovine serum (FBS) for 20 min at room temperature and incubated overnight with anti-BrdU primary antibody at 4°C. After three wash steps, Alexa Fluor 405-coupled secondary antibody was incubated at RT for 2 h. Before analysis by flow cytometry, samples were washed three times in ICC wash buffer.

CCR8 and CCL18 expression and patient survival analysis

Expression and Kaplan Meier analyses were performed using the R2 online platform (R2.amc.nl). To distinguish expression levels of GBM versus normal brain tissue, MAS5.0 normalized, u133p2 microarray data of the (1) French Tumor Glioma Dataset (GSE16011,) containing 276 glioma samples of all histology and 8 control samples [115] (2) The Sun Tumor Glioma dataset (GSE4290) containing 157 tumor samples including 26 astrocytomas, 50 oligodendrogliomas and 81 glioblastomas, (3) Hegi Tumor Glioblastoma dataset (GSE7696), containing 80 glioblastoma specimens of patients were compared to (4) Eight normal samples present in the French dataset; (5) the Berchtold Normal Brain regions dataset (GSE11882) containing 176 samples from hippocampus, entorhinal cortex, superior-frontal gyrus, and postcentral gyrus brain tissues) and (6) the Harris Normal Brain PFC dataset (GSE13564), containing 44 prefrontal cortex brain tissues. Kaplan Meier analyses were performed using the French dataset. The significance of the difference in expression levels of CCR8 and CCL18 between tumor versus normal brain tissues was determined using a t-

test. The significance of the Kaplan analyses was tested using a Mann-Whitney test. For this, the most optimal expression threshold point was determined.

Immunocytochemistry, Immunohistochemistry, tissue microarray and chemokine array

For immunocytochemistry, attachment of cells to glass coverslips was induced by adding 10% FBS for 2 h. Then, coverslips were washed with PBS, fixed with 4% PFA for 15 min and treated with cold methanol. After a wash in ICC wash buffer, coverslips were blocked in ICC wash buffer containing 10% FBS for 20 min at room temperature and incubated overnight with anti-Cre or anti-CCR8 primary antibodies at 4°C. After three wash steps, Alexa Fluor 488-coupled (Cre) or Alexa Fluor 594-coupled (CCR8) secondary antibodies were incubated at RT for 2 h. Slides were washed three times before and after DAPI counterstain and mounted with Vectashield (Vector Laboratories) on glass slides. For analysis of GBM8 mT/mG xenografts, brain cryosections (10 µm thick) were fixed in 4% PFA, washed three times with PBS for 10 min before and after counterstaining with DAPI and mounted on glass coverslips with Vectashield. Pictures were taken with a Leica DM6000 microscope and processed with ImageJ software. GFP Immunohistochemistry was performed on cryopreserved tissue slides following standard procedures. Slides were scanned using Aperio Scanscope and processed with ImageScope software (Leica) (Abcam; ab 6556; 1:1000). Tissue micro array – GL805a (TMA) containing glioblastoma samples and control tissues was purchased from US Biomax Inc. After deparaffination and microwave induced antigen retrieval (Tris-EDTA pH9.0), TMA's were stained with anti-CCR8 antibody (E77, Abcam) and anti-rabbit/mouse EnVision-HRP (DAKO). For negative staining, the first antibody was omitted. CCR8 expression was calculated based on the stained area (0-4) and staining intensity (0-4), thus resulting in a maximal value of 16. To detect chemokines secreted by GBM8 cells, Proteome Profiler™ Human Chemokine Array Kit (R&D Systems) was used to detect secreted chemokines in GBM8 conditioned medium following manufacturer's instructions. Briefly, array membranes were blocked and incubated for 2 h with conditioned medium collected from cells growing at 2.5 x 10^5 cells/ml for 24 h and diluted 1:1 in blocking buffer. After washing, membranes were incubated with a cocktail of biotinylated human chemokine antibodies in blocking buffer at RT for 2 h and then incubated with horseradish peroxidase (HRP)-conjugated streptavidin in blocking buffer overnight at 4°C following further washes, After three washes, membranes were developed using Chemi Reagent Mix and visualized on X-ray film (GE healthcare).

Enzyme-linked immunosorbent assay

To detect EV-associated molecules, a fixed concentration of 5 ng/µl or serial dilutions of isolated EVs were coated overnight at 4°C in coating buffer (0.2 M $NaHCO_3$, pH 9.2) on ELISA plates. Plates were washed twice with TSM buffer (20 mM Tris, pH 7.4, 150 mM NaCl, 1 mM $CaCl_2$, 2 mM $MgCl_2$) and blocked with 1% BSA in TSM for 1 h at room

temperature. Plates were then incubated with primary antibodies at a fixed concentration (1 µg/ml) or in serial dilutions (from 4 µg/ml to 62.5 ng/ml) in TSM buffer with 1% BSA for 1 h at room temperature. After three washes with TSM buffer, plates were incubated with secondary antibodies at RT for 1 h, washed again three times, and the reaction was developed, using 3,3',5,5'-tetramethylbenzidine (TMB) as a substrate (Sigma Aldrich). Signal intensities were acquired with a Biotek Synergy HT microplate reader.

In vivo R243 + TMZ treatment

Treatment with R243 (1.0 mg/kg, i.p. once daily) or vehicle (1% DMSO in PBS) was started at day 4 after tumor injection and continued until day 8. At day 5, animals were treated once with 10 mg/kg TMZ, i.p., or vehicle (4% DMSO in PBS). Stocks of R243 (100 µM; 35.7 mg/ml) were prepared in DMSO and stored at -20°C. Working solutions were prepared freshly before each administration by diluting R243 stock solution in PBS.

Bioluminescence imaging

Tumor progression was followed by measuring firefly luciferase (Fluc) signal by a charge-coupled device (CCD) camera, using the Xenogen-IVIS Lumina system under isoflurane anesthesia. Mice were injected intraperitoneally with 150 µl D-luciferin (100 mg/kg). Regions of interest were defined on the head of the mice. The photon flux (p/s) in these regions were used as a total measurement of Fluc activity. Photon flux was normalized to the group means at day 8 (Figure 5E). Disease progression was defined as the time point at which for two consecutive measurements an increase in BLI was observed.

Pharmacokinetic studies

WT FVB mice and transgenic *Abcg2*$^{-/-}$, *Abcb1a/b*$^{-/-}$ and *Abcg2; Abcb1a/b*$^{-/-}$ FVB mice were used in pharmacokinetic studies. R243 was administered i.v. at a dose of 10 mg/kg in a formulation containing 2 mg/ml R243 in DMSO:Cremophor EL:saline (1:1:8). Blood and brains were collected 1 h after administration. Plasma was obtained by centrifugation (5 min, 5000 rpm, 4°C) and brains were weighed and homogenized using a FastPrep®-24 (MP-Biomedicals, NY, USA) in 1% (w/v) bovine serum albumin in water. R243 was extracted by liquid-liquid extraction using ethyl acetate and measured using LC-MS/MS.

In vitro translocation assays

Conventional bidirectional translocation assays were performed using parental MDCK cells as described previously (Lin et al., 2013Lin et al., 2013). R243 was added to either the apical or basolateral side of a Transwell microporous polycarbonate membrane filters (3.0 µm pore size, 24 mm diameter; Costar Corning, Corning, NY, USA) at a concentration of 100 nM and translocation over time was measured using LC-MS/MS. Complete R243 translocation was reached when an equilibrium between both compartments was established.

Supplemental information

Supplemental Figures and Table are available online.

Accession numbers

The raw sequencing data are deposited at a public database. The NCBI SRA accession number for the small RNA sequencing by Illumina Hi-Seq 2500 reported in this paper is SRP092232. Small RNA sequencing data used in the analysis for supplementary Fig. 9 is presented in Supplementary Table S1 with the list of human miRNAs detected in GBM8 cells and their paired EVs. Individual miRNA sequencing reads mapped to human miRNAs are detected in cells and their paired EVs. Highlighted in yellow are miRNAs represented in supplementary Fig. 9. RPM, reads per million of normalized reads (relative expression).

RESULTS

GBM EVs induce a proliferative phenotype in recipient GBM cells.

To confirm the pro-tumoral capacity of EVs on GBM cells we isolated EVs from GBM-conditioned media by differential ultracentrifugation [367,368]. EVs isolated from stem-like GBM8 cells (a primary stem-like GBM cell type) had a diameter ranging from 30 to 200 nm as measured by EM (Fig. 1a), similarly as EVs isolated from U87 and U251 GBM cells (Supplementary Fig. 1a, b), and expressed the EV markers Alix and CD63 (Fig. 1b and Supplementary Fig. 1c). GBM8 cells were incubated with isolated and PKH67-labeled GBM8 EVs, resulting in a dotted fluorescent pattern, indicating efficient EV binding (Fig. 1c), similar results were obtained for U251 and U87 (Supplementary Fig. 1d). Using FACS analysis, the proportion of $PKH67^+$ cells after incubation with labeled EVs showed a sigmoidal log-linear dose-response relationship with the amount of PKH67-labeled EVs added (R=0.9998). Co-incubation of PKH67-labeled EVs with increasing concentrations of unlabeled EVs resulted in a dose-dependent reduction in mean fluorescence intensity (Supplementary Figs 1e, f)(39,40). These results prompted us to quantify EV-mediated proliferation. We incubated GBM8 cells with fresh EV-depleted medium or with medium supplemented with isolated GBM EVs, resulting in enlarged stem-like GBM8 neurospheres and an increase in total cell number in cells supplemented with exogenous EVs (Fig. 1d). The EV-mediated induction of proliferation was significant and dose-dependent, increasing GBM8 stem-like cell numbers by 2.4-fold when cells were incubated with 250 ng/µl of isolated EVs (Fig. 1f). Addition of exogenous EVs resulted in a 1.5-fold increase in 5-bromo-2'-deoxyuridine (BrdU) incorporation, indicating that the observed increase in cell number is at least partially due to an enhanced proliferation rate (Fig. 1g). EV exposure also induced activation of the MAPK-ERK pathway, as evidenced by an increase in phospho-ERK levels (Fig. 1e). Because MAPK-ERK activation also is implicated in TMZ resistance in GBM cells [369], we validated the effects of TMZ treatment in the presence of EVs. After determining the IC_{50} value of TMZ on GBM8 cells (~20 µM, Supplementary Fig. 3), we treated cells with 20 µM TMZ in the presence or absence of 100 ng/µl of purified EVs. As shown in Fig. 1h, addition of exogenous EVs indeed resulted in strong protection against TMZ-mediated cell kill, although a partial contribution of a concomitant induction of cellular proliferation is not excluded.

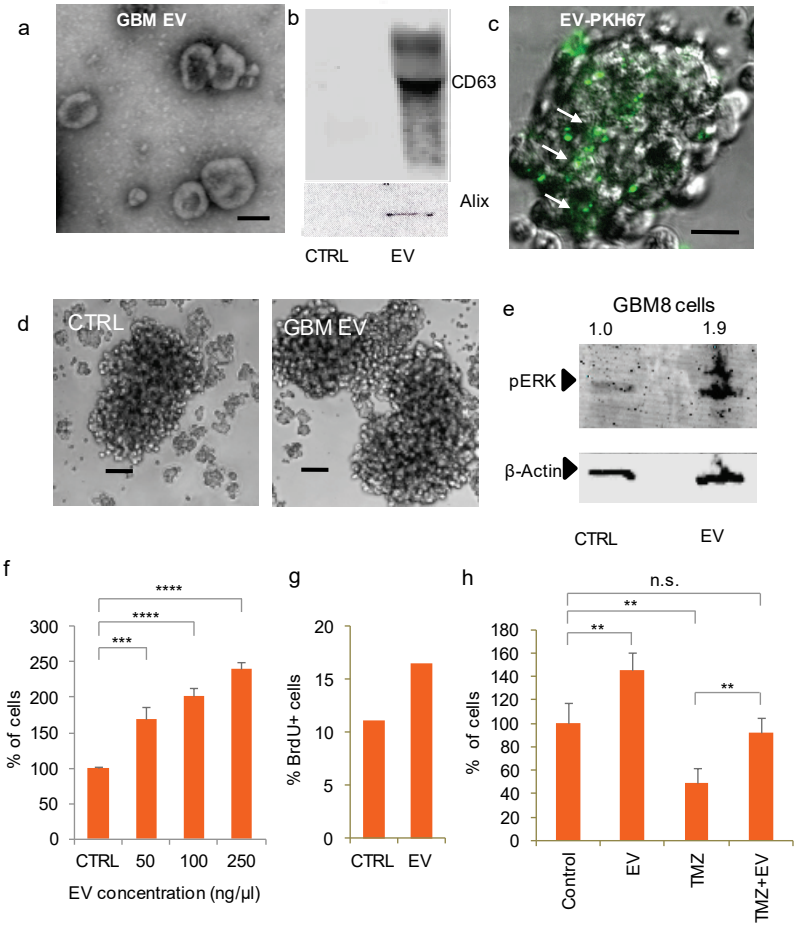

Figure 1. GBM cells can exchange functional RNA via EVs. (**a**) EM image of GBM8 EVs isolated by differential centrifugation (scale bar: 100 nm). (**b**) Western blot analysis of EV markers CD63 and Alix on EVs isolated from GBM8 cells. Control: Supernatant from the 70,000 x g centrifugation step. (**c**) GBM8 cells incubated overnight with PKH67-labeled GBM8 EVs. Arrows indicate PKH67$^+$ cells which have taken up EVs (scale bar: 10 µm). (**d**) GBM8 cells incubated with 100 ng/µl of isolated EVs show enlarged neurospheres (right picture) as compared with cells incubated with control supernatant from the last centrifugation step (left picture) (scale bars: 100 µm). (**e**) Western blot analysis of phospho-ERK on cells incubated as in (**g**), β-actin was used as a loading control. Numbers above blot represent relative phospho-ERK band intensities. (**f**) Luciferase assay on GBM8-FM cells incubated with increasing concentrations of isolated EVs indicates dose-dependent increase in cell number. The bar graphs show the means ± standard deviation (SD) of three independent experiments. ***indicates p-value ≤0.001 and **** indicates p-value ≤0.0001 as determined by one-way analysis of variance (ANOVA). (**g**) BrdU incorporation assay reveals increased proliferation rate in cells incubated with 100 ng/µl as compared to control-incubated cells. (**h**) GBM8 spheres were treated with TMZ for 96 h in the presence or absence of 100 ng/µl of GBM8 isolated EVs and relative cell numbers were estimated by calculating sphere volume. The data is normalized to control-treated cells (100%) and bar graphs show the means ± SD of four independent experiments. ** indicates p-value ≤0.01, *** indicates p-value ≤0.001 as determined by ANOVA.

To determine whether functional transfer by EVs occurs at physiologically relevant levels, we used a color switch system based on EV-mediated Cre recombinase mRNA transfer [125]. Reporter mT/mG cells contain a floxed copy of membrane-tagged Tomato (mT). Upon Cre-mediated recombination the mT sequence is excised allowing expression of a membrane-tagged GFP (mG) located immediately downstream, resulting in a color switch from mT^+ (red) to mG^+ (green) (Supplementary Fig. 2a). Cre protein expression in stably transduced EV donor cells was confirmed by immunocytochemistry (Supplementary Fig. 2b), and RT-PCR analysis revealed presence of Cre mRNA in EVs isolated from these donor cells (Supplementary Fig. 2c). Next, addition of purified Cre^+ EVs isolated from Cre donor cells induced patches of mG^+ cells in recipient GBM8-mT/mG stem-like neurospheres (Supplementary Fig. 2d), and Cre activity was also transferred from Cre donor cells to mT/mG recipient cells in co-culture experiments in which no exogenous EVs were added (Supplementary Fig. 2e).
Altogether these results indicate that GBM EVs can transfer cargo, and that EV interaction results in activation of the MAPK-ERK pathway, induces proliferation and that EVs can reverse TMZ sensitivity.

CCR8 acts as an EV receptor

To identify cellular receptors involved in EV uptake we performed siRNA screening using PKH67-labelled EV uptake by HEK-293T cells as readout. HEK-293T cells were selected because the conditions for siRNA screening of these cells were considered more favorable as compared to primary stem-like GBM neurospheres. We selected a siRNA library against G-protein coupled receptors (GPCRs) because of the highly versatile roles of GPCRs in many cellular processes, including viral entry, and because many GPCRs are potentially druggable. After testing that GBM EVs are efficiently taken up by HEK-293T cells and that EV uptake is dose-dependent (Supplementary Fig. 4a, b), we transfected the GPCR siRNA library. At 48 h after transfection, cells were incubated overnight with labeled EVs and fluorescent cells were recorded (Supplementary Fig. 4c). A total of 65 of 512 siRNAs caused a reduction in fluorescent signal stronger than 30% from which we selected the top-8 for further validation with an independent set of siRNAs (Fig. 2a). CCR8 inhibition caused a strong and consistent reduction in EV uptake in both HEK-293T and GBM8 cells and therefore was selected for further studies (Fig. 2b and Supplementary Fig. 4d).

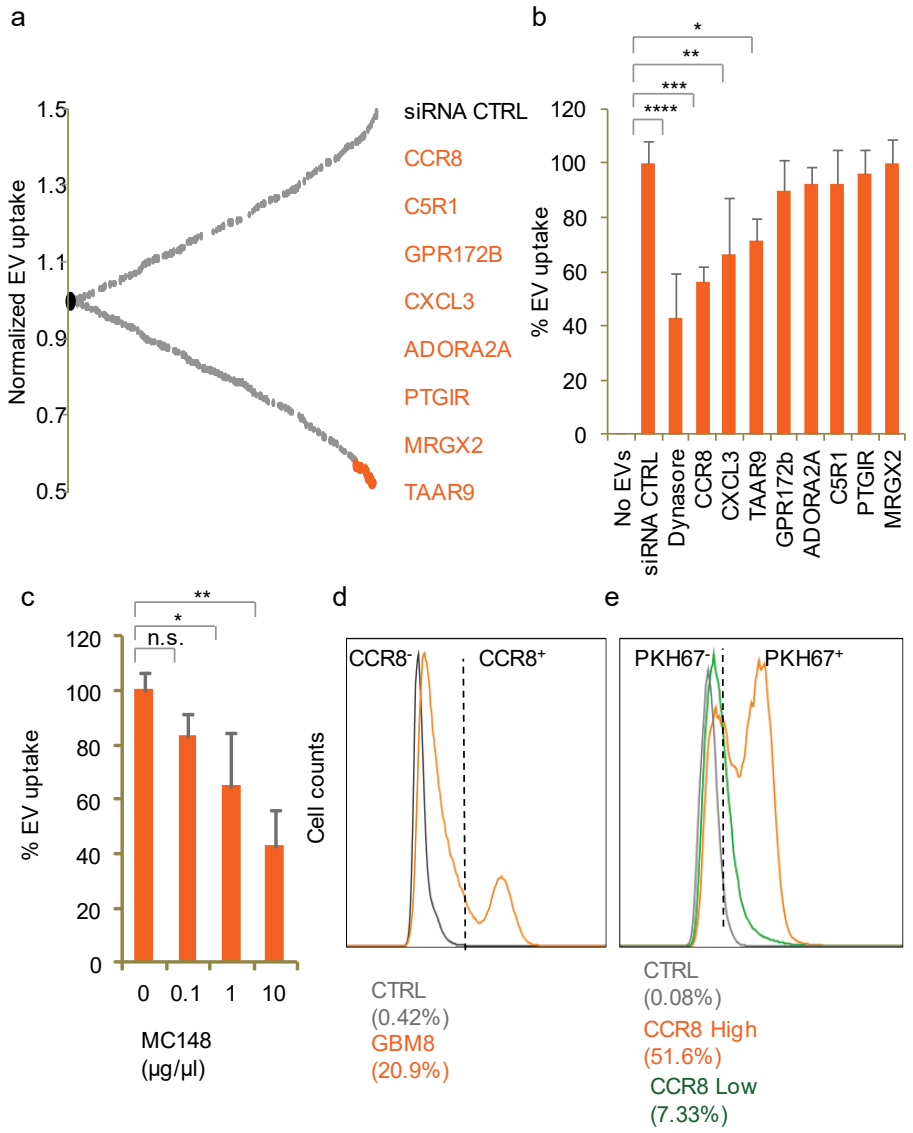

Figure 2. CCR8 acts as an EV receptor (**a**) GPCR siRNA screening result on HEK-293T cells. Normalized PKH67 fluorescence is displayed on the Y-axis, and each dot represents a siRNA against an individual GPCR Top-8 EV uptake-reducing siRNAs are highlighted in orange and indicated at the right side. (**b**) siRNA screening validation on GBM8 cells with an independent set of siRNAs. Normalized PKH67 fluorescence (EV uptake) is displayed on the Y-axis. Treatment of cells with Dynasore served as a control for EV uptake reduction. (**c**) CCR8 inhibitor MC148 reduces EV uptake in a dose-dependent fashion. (**d**) FACS analysis of CCR8 expression in GBM8 cells. Negative control: No anti-CCR8 primary antibody **(e)** PKH67 fluorescence (representative of EV uptake) of $CCR8^-$ (green) compared to $CCR8^+$ (orange) GBM8 cells. Negative control (grey): GBM8 cells not incubated with PKH67 EVs.

CCR8 is a beta chemokine receptor with a known role in induction of chemotaxis in Th2 cells via its two ligands CCL1 and CCL18 [370], and functions as a co-receptor for enveloped viruses including HIV [371,372]. The CCR8 axis has been found to be activated in urothelial and renal carcinomas resulting in immune response impairment, and it is responsible for apoptosis inhibition in lymphoma [373,374]. Furthermore, CCR8 function in melanoma cells is essential for the entry of metastatic cells into lymph nodes [375]. We show the relevance of CCR8 on EV uptake in GBM8 cells by the dose-dependent reduction of uptake in the presence of increasing concentrations of MC148, a highly selective virus-encoded CCR8 antagonist [376] (Fig. 2c). According to the CCR8 expression levels, GBM8 cells can be divided in two populations. One population expresses undetectable levels of CCR8 ($CCR8^-$ cells), whereas the other population shows significant CCR8 immunoreactivity ($CCR8^+$ cells) (Fig. 2d and Supplementary Fig. 4e). In several independent experiments, we have observed variable proportions of $CCR8^+$ GBM cells, ranging from 20-80%. Interestingly, when we combined labeled EV uptake with CCR8 immunostaining, we observed that a significantly larger proportion of $CCR8^+$ cells take up PKH67-labeled EVs than do CCR8- cells (Fig. 2e), strongly suggesting that CCR8 participates in the uptake process.

CCR8 inhibition neutralizes EV-induced phenotypes *in vitro*

R243 is a small molecule which functionally inhibits CCR8 both *in vivo* and *in vitro* [377]. We therefore synthesized a batch of R243 to test its effect on inhibiting EV uptake (chemical synthesis scheme in Supplementary Fig. 5a). As expected, R243 treatment strongly impaired EV uptake (Fig. 3a, b). We then tested whether R243 could counteract EV-induced phenotypes on recipient GBM cells. After determining the IC_{50} value of R243 on GBM8 cells (44 µM, Supplementary Fig. 5b), we pre-treated GBM8 cells with R243 (20 µM) for 30 min, incubated the cells with isolated EVs and measured the total number of GBM cells after 96 h. As shown in Fig. 3c, R243 alone had no measurable effect on GBM cell growth, whereas R243 pre-treatment was able to completely block EV-induced GBM cell growth. Next, we studied whether TMZ and R243 have synergistic effects. Combined treatment of GBM cells resulted in enhanced potency of TMZ, with combination indexes [378] down to 0.8 (Fig. 3d). We studied the effects of R243 on GBM cells treated with TMZ in the presence of isolated EVs. Interestingly, although EV supplementation alone restored cell-numbers after TMZ treatment, R243 treatment partially prevented this EV-induced resistance to TMZ (Fig. 3e). As shown in Supplementary Fig. 5c-g, R243 reduced EV uptake by three different GBM lines tested, although with variable potency. We also observed a significant effect of the drug on A375 cells (malignant melanoma), but not on A549 cells (lung carcinoma). These results suggest that CCR8 may also function as an EV receptor on certain non-GBM cell types.

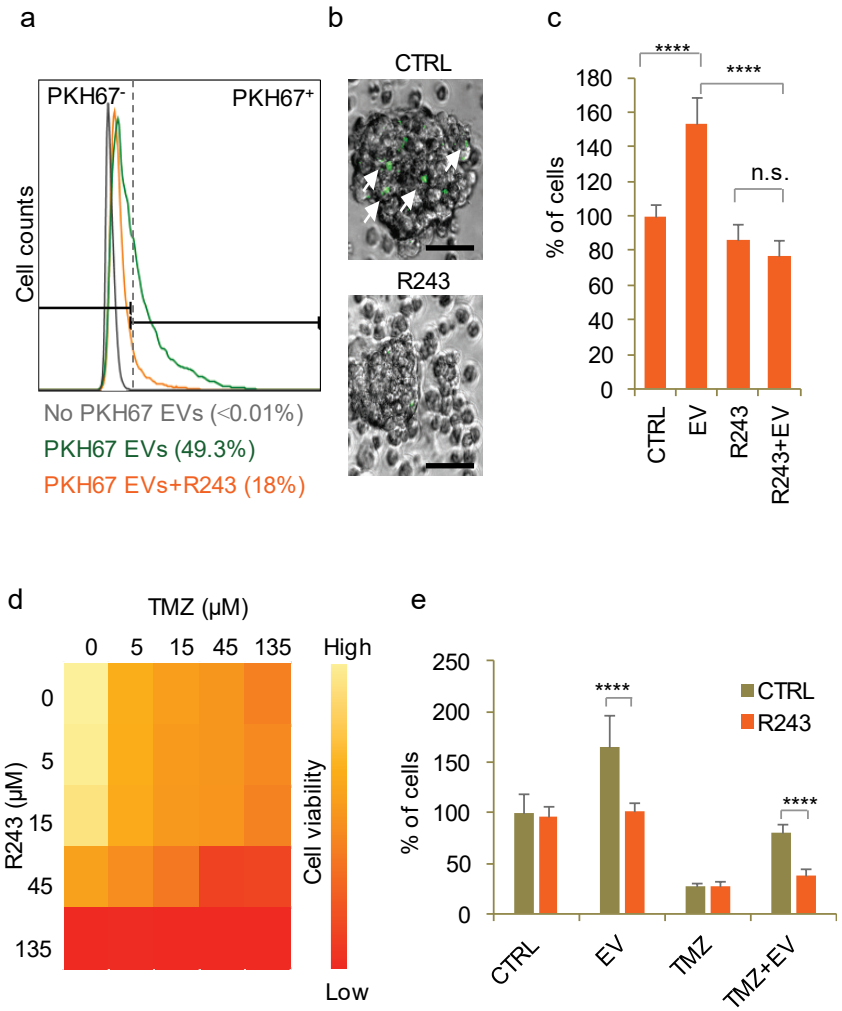

Figure 3. CCR8 inhibition neutralizes EV-induced phenotypes *in vitro*. (**a**) PKH67 uptake analysis of cells treated with vehicle (green) or with R243 (orange). Control: No PKH67 EVs (grey). (**b**) Representative pictures of cells incubated as in (a) (scale bars: 25 µm). (**c**) Relative cell number of cells incubated with and without GBM8 EVs in the presence or absence of R243. Values are normalized to control (vehicle, no EVs) and bar graphs show the means ± SD of six independent experiments. (**d**) CellTiter-Glo viability assay (Promega) on GBM8 cells treated with variable concentrations of TMZ and R243. Darker orange represents less viability. (**e**) Relative cell number of GBM8 spheres incubated with or without 100 ng/µl of GBM8 EVs and treated with TMZ in combination with R243 (orange bars) or vehicle (grey bars). Bars show the means ± SD of 4 independent experiments. For all experiments * indicates p-value ≤0.05, ** indicates p-value ≤0.01, *** indicates p-value ≤0.001 as determined by ANOVA.

CCR8 and CCL18 expression levels are increased in GBM and are an indicator of poor prognosis

To determine whether CCR8 expression has implications in tumor progression in GBM patients, we performed immunostaining against CCR8 on a tissue microarray (TMA) from glioma samples of patients with different glioma grades, including grade IV GBM. Tumor cells exhibited different immunoreactivity patterns which we scored depending on the intensity of the staining. Blinded classification of array specimens revealed a significant increase in CCR8 expression in grade IV GBM as compared to normal (non-tumoral) brain tissues (Fig. 4a, b and Supplementary Fig. 6). We also performed metadata analysis on publicly available microarray data using the R2 Analysis and Visualization Platform (http://r2.amc.nl). Results showed increased mRNA levels of both CCR8 and its natural ligand CCL18 in GBM as compared to normal brain samples (Fig. 4c, d). Moreover, survival analyses indicate that both CCR8 and CCL18 are indicators of poor prognosis in GBM patients (Fig. 4e, f).

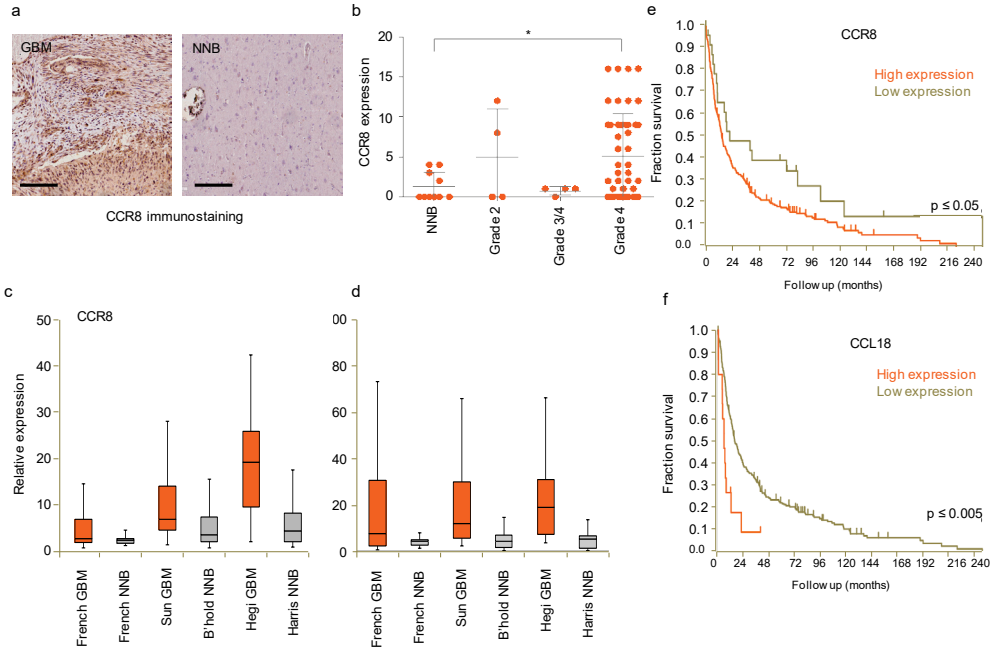

Figure 4. CCR8 and CCL18 expression levels are increased in GBM and are an indicator of poor prognosis. (**a**) Representative pictures of a GBM TMA immunostained against CCR8 (scale bar: 200 µm). (**b**) Scoring of CCR8 immunoreactivity on TMA of GBM of different grades and healthy tissue. * indicates p-value ≤0.05 (t-test). (**c,d**) CCR8 and CCL18 mRNA expression analysis on datasets using R2 Analysis and Visualization Platform. X axis shows the dataset used. (**e,f**) Survival analysis of patients expressing high and low levels of CCR8 and CCL18 mRNA, respectively. For expression and Kaplan-Meyer analyses R2 online platform (R2.amc.nl) was used. Differential expression was tested by t-test and significance of Kaplan analysis by Mann-Whitney test. P values for CCR8 expression were 10^{-10} (Sun / Bechtold), 9^{-9} (Hegi / Harris) and >0.05 for the French dataset. P values for CCL18 expression were 0.004 (Sun / Bechtold), 0.05 (Hegi / Harris) and 0.0003 for the French dataset.

Pharmacological inhibition of CCR8 delays tumor growth after TMZ treatment

A common problem in the development of drugs for GBM treatment is the blood-brain barrier (BBB). Therefore, we first verified that R243 is capable of reaching the brain. Specific transporter proteins, which are present on the BBB, are known for their role in blocking drug delivery to the brain [63]. By using wildtype mice and transgenic mice deficient for the transporters Abcg2 and Abcb1a/b, we show that these drug transporters have no meaningful impact on the brain penetration of R243 (Fig. 5a-c). Intriguingly, the brain-to-plasma ratio of R243 was 35 in wildtype mice, unusually high, pointing to a remarkable accumulation of R243 into the brain (Fig. 5d). Next, to test the effects of R243 on GBM *in vivo*, we employed a version of GBM8 cells (GBM8-FM) stably expressing mCherry protein and firefly luciferase, which allows monitoring of tumor growth bioluminescence imaging. Subsequently, we tested with the Cre-mT/mG EV reporter system the ability of *in vivo* transfer of EV cargo. We orthotopically injected GBM8-mT/mG recipient cells in the brain of nude mice (n = 6). Three days after implantation of the recipient reporter cells, we injected EVs isolated from Cre^+ (n = 3) or Cre^- (n = 3) donor cells in the brains of these mice. Two weeks later the mice were sacrificed, and the brains were resected, sliced and analyzed by fluorescent microscopy. The tumor tissues consisted mostly of red mT^+ cells, but tumor areas with abundant mG^+ cells were also observed in 3 out of 3 mice injected with Cre^+ EVs, in contrast to the brains of the 3 mice injected with Cre^- control EVs, where no mG^+ cells were detected (Supplementary Fig. 7a). Next, we investigated whether physiological levels of locally produced Cre^+ EVs - by co-injection of GBM8-Cre donor cells with GBM8-mT/mG recipient cells - can also result in functional transfer of Cre. Hence, we co-injected mice with mT/mG recipient cells and Cre^+ or Cre^- donor cells in opposite hemispheres of the brain in order to minimize the risk of cell contact-dependent Cre transfer. Again, the brains of 3 out of 3 mice co-injected with Cre^+ cells displayed patches of mG^+ cells in mT/mG tumors, in contrast to mice co-injected with Cre^- GBM cells which resulted only in mT^+ cells (Supplementary Fig. 7b, c). The presence of mG^+ cells was further validated by anti-GFP immunostaining of mouse brain slices (Supplementary Fig. 7d). These results demonstrate that EVs can indeed provide functional transfer of RNA molecules in orthotopic brain tumors, albeit that the efficiency of the Cre–mT/mG reporter system under these conditions is relatively low. We than tested if we could inhibit the EV mediated protumoral effects *in vivo*, by the administration of the CCR8 inhibitor R243. As shown in Fig. 5e, f, R243 administration did show a trend in reducing primary GBM stem-like xenograft growth in nude mice (n = 6), although no significant effects were measured. However, when we administered R243 before and after TMZ treatment in nude mice (n = 6), the effect of TMZ was significantly enhanced, and tumor recurrence was significantly delayed as compared to TMZ treatment in the absence of R243 (Fig. 5e, f). In conclusion, under these conditions R243 only showed a minor non-significant effect when administered alone, and perhaps repeated dosing and/or earlier treatment would be more beneficial. However, administration of R243 in combination with TMZ did demonstrate a

significant delay of recurrence after TMZ treatment and warrants further preclinical testing (Fig. 5g).

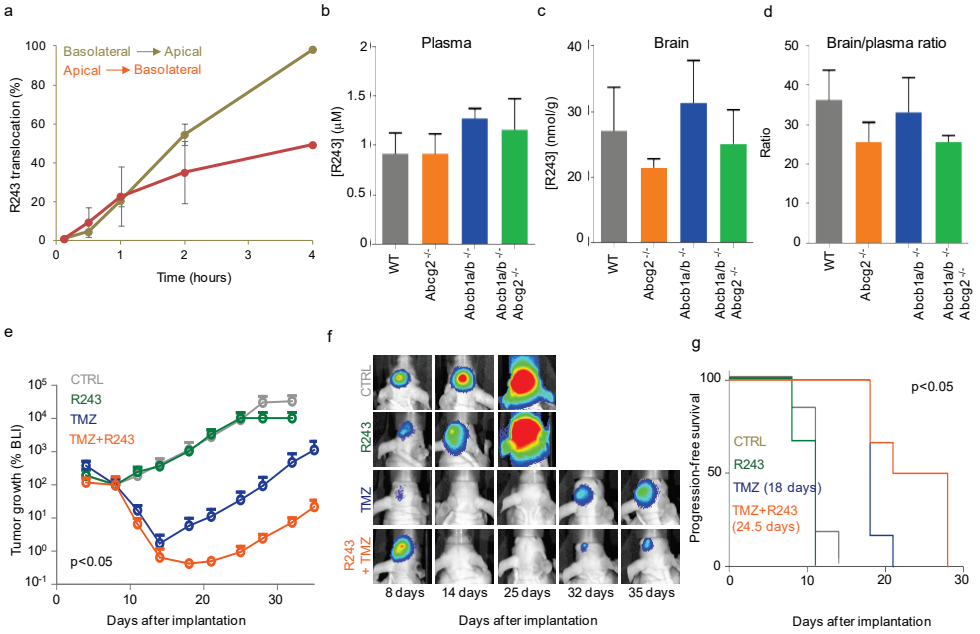

Figure 5. Pharmacological inhibition of CCR8 delays tumor growth after TMZ treatment. (**a**) R243 transwell translocation assay for the drug transporter P-gp using MDCK cells. Percentage of R243 translocation from basolateral to apical (grey line) and from apical to basolateral (orange line) is plotted in Y-axis. (**b-d**) R243 levels were measured in plasma (**b**) and in brain (**c**) 1 h after i.v. injection of the drug, and brain-to-plasma ratio was calculated (**d**). No statistical differences were measured by ANOVA. (**e-g**) BLI tumor growth analysis of GBM8 mouse xenografts treated with vehicle (grey); R243, 1.0 mg/kg (green); TMZ, 10 mg/kg (blue) or R243 and TMZ combined (orange). Mice were treated with R243 once daily from day 4 to day 8 after tumor injection and TMZ was administered a single time at day 5. The y-axis represents the median BLI normalized to day 8. The p-value was determined by t-test on the area under the curve for TMZ vs. TMZ+R243. Representative BLI images are shown in (**f**) and progression-free survival is calculated in (**g**). P-value on median progression-free survival was determined by the Log-rank (Mantel-Cox) test.

CCL18 acts as a bridging molecule between GAGs on EVs and cellular CCR8

We performed uptake analyses in the presence of CCL1 and CCL18, the two known ligands of CCR8, as well as with neutralizing antibodies directed against these chemokines. Whereas CCL1 or its neutralizing antibody had no effect on EV uptake (data not shown), recombinant CCL18 addition significantly increased EV uptake, and the CCL18 neutralizing antibody decreased uptake (Fig. 6a, b). These results suggest that CCL18 plays a mediating role in the EV uptake via CCR8. Chemokine arrays were used to determine that GBM8 cells secrete many chemokines, including CCL18 (Supplementary Fig. 8a). Given that EV membranes are highly glycosylated [379,380], and that chemokines bind with high affinity to glycans [381,382], we

considered the possibility that CCL18 could be acting as a bridging molecule between glycans on the EV membrane and the cellular receptor CCR8. We incubated isolated EVs with recombinant CCL18 overnight, washed the EVs with PBS and purified them again. Western blot analysis revealed that CCL18 can be detected in the EV pellet but not in the supernatant, confirming effective binding of CCL18 to EVs (Supplementary Fig. 8b). We incubated ELISA plates with isolated GBM8 EVs and confirmed proper vesicle coating by detection with the marker CD63 (Fig. 6c and Supplementary Fig. 8c). This system also allowed us to detect endogenous CCL18 on GBM8 EVs (Fig. 6d and Supplementary Fig. 8d). To further confirm CCL18 presence on GBM8 EVs, we performed immunogold EM on isolated EVs, observing exosome-like vesicles with strong immunoreactivity against CCL18 and CD63 (Fig. 6f, g).

Next, we validated the presence of glycans on GBM EV membranes. As shown in **Fig. 7a-c**, GBM8 EVs are rich in heparan sulfate, chondroitin sulfate and dermatan sulfate, the main GAGs produced by eukaryotic cells [383–385]. Chemokine-glycan interactions occur mainly by electrostatic forces and heparin. Heparin is a soluble and highly sulfated GAG, capable of displacing chemokine-glycan interactions due to its high negative charge density [381,382,386]. We reasoned that if CCL18 binding to EVs is needed for cellular uptake, pretreatment of EVs with heparin should cause CCL18 to be displaced from the EV membrane consequently, resulting in diminished uptake. Indeed, heparin pretreatment reduced EV uptake by 80% (Fig. 7d). This result is in agreement with a previous report from Paggetti and colleagues in which heparin treatment of chronic lymphoid leukemia-derived EVs caused a strong reduction in EV uptake [355]. Furthermore, heparin has been shown to efficiently bind and capture EVs [387]. To further demonstrate the involvement of GAGs in the uptake process, we treated purified EVs with Heparinase III (H'se III), which cleaves 1-4 linkages between hexosamine and glucuronic acid residues in heparan sulfate molecules. H'se III treatment reduced EV uptake by approximately 40%, confirming that glycans exposed on the EV membrane facilitate EV uptake (Fig. 7e). Collectively, these results reveal an EV uptake model in which CCL18 acts as a "connectokine" between glycans decorated on the EV membrane and the cellular receptor CCR8 (Fig. 7f).

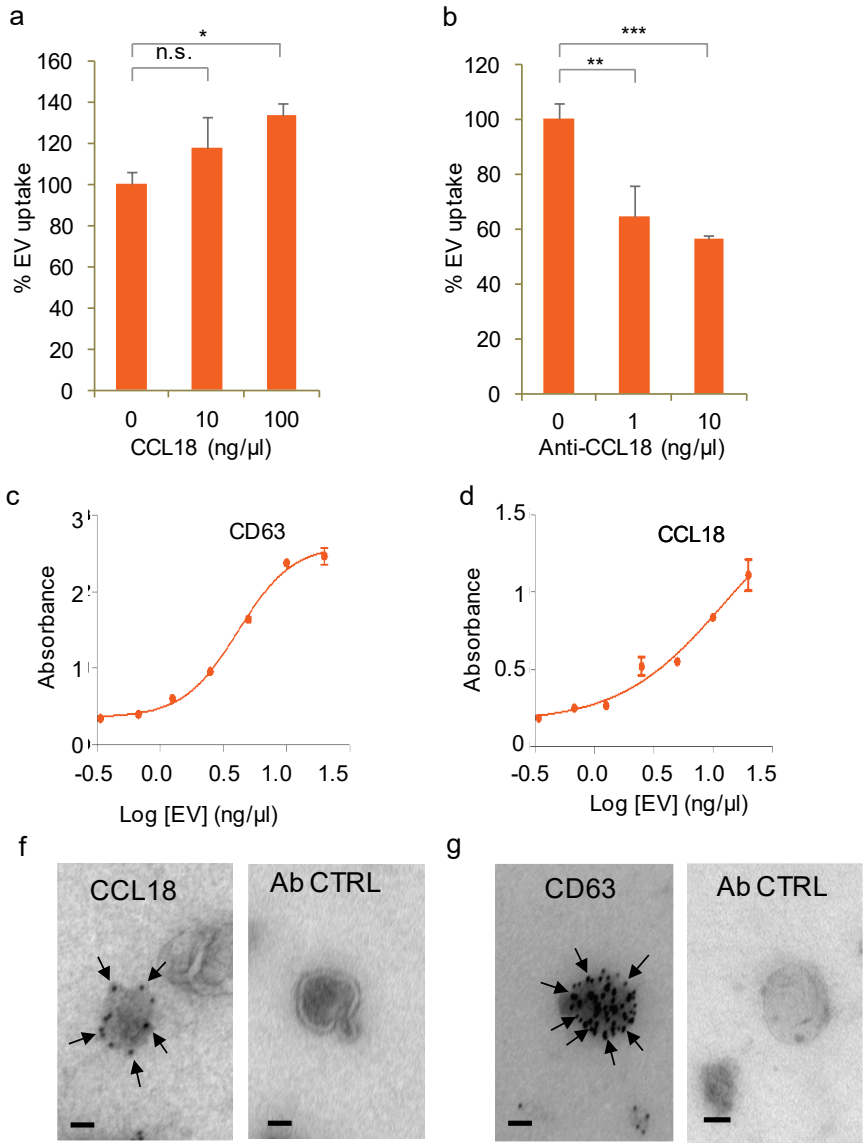

Figure 6. CCL18 enhances EV uptake. (**a**) EV uptake analysis on GBM8 cells incubated with recombinant CCL18 prior PKH67-EV addition. (**b**) EV uptake analysis on EVs pre-incubated with CCL18 neutralizing antibody. In both (**a**) and (**b**), * indicates p-value ≤0.05, ** indicates p-value ≤0.01, *** indicates p-value ≤0.001 as determined by ANOVA. (**c,d**) ELISA results on EVs plates coated with dilutions of isolated EVs and incubated with anti-CD63 (**c**) or anti-CCL18 (**d**). Both incubations displayed dose-dependent signal. (**e**) Immunogold EM pictures showing GBM EVs with strong reactivity against endogenous CCL18. (**f**) Positive control: Immunogold staining against the exosomal marker CD63. Ab control: No primary antibody (Scale bars: 25 µm).

Figure 7

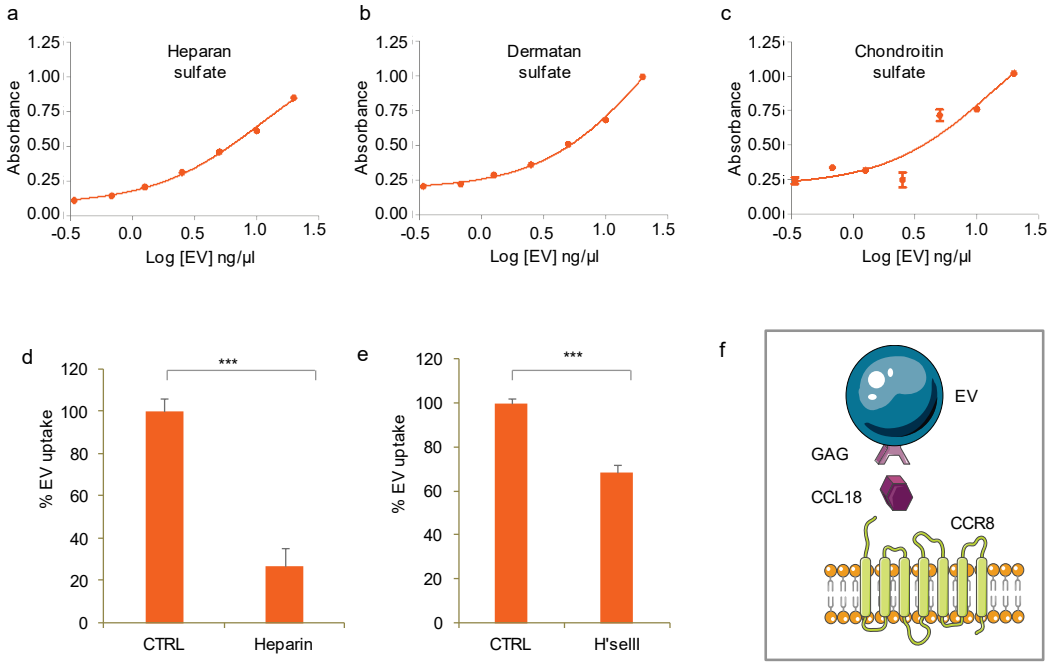

Figure 7. CCL18 acts as a bridging molecule between GAGs on EVs and cellular CCR8 (**a-c**) Heparan sulfate (**a**), dermatan sulfate (**b**) and chondroitin sulfate (**c**) GAGs are present on EV membranes, as determined by ELISA. (**d**) EV uptake is prevented by heparin (25 µg/ml) and by (**e**) Heparinase III (H'se III) (2 miU every 2 h for 6 h at 37ºC) treatment of EV isolates. *** indicates p-value ≤0.001 as determined by t-test. (**f**) Proposed model: GAGs present on the EV membrane bind CCL18 which connects with cellular CCR8 promoting EV uptake. Error bars represent SD of three independent experiments.

DISCUSSION

We present three main findings related to EV uptake by GBM cells: i) GBM EVs can be transferred between GBM cells *in vitro* and *in vivo*, stimulating GBM cell growth and protecting against TMZ; ii) CCR8 acts as an EV receptor on GBM cells and binds to CCL18, which acts as a bridging molecule to GAGs exposed on EVs, and iii) Pharmacological inhibition of CCR8 with the small molecule R243 inhibits EV uptake by GBM cells, resulting in sensitization of GBM cells to TMZ *in vitro* and *in vivo*.

Uptake of GBM EVs can induce cell growth in recipient cells, confirming previous reports [338,339], but seemed to have even stronger phenotypic effects on TMZ resistance in GBM, in particular *in vivo*. Tumor-derived EVs have been implicated in resistance to other types of therapy in various tumor types [344–348]. The Cre-based color switch model allowed us to demonstrate that GBM-derived EVs are capable of transferring active Cre mRNA molecules at physiological levels *in vitro* and *in vivo*. We identified a set of miRNAs in GBM EVs that have strong implications in the process of TMZ resistance. Among the most abundant miRNAs in GBM EVs we observed a majority of pro-tumoral, proliferation-inducing miRNAs, such as miR-10b-5p, miR-92 and miR-21(Supplementary Fig. 9a, b) [388–391]. Although this is an interesting observation, more research is needed to fully understand the mechanisms involved in the capacity of GBM EVs to induce TMZ resistance. TMZ is an alkylating agent that transfers a methyl group to purine bases in cellular DNA, causing incorrect pairing and triggering the mismatch repair system (MMR), resulting in cell cycle arrest and apoptosis in proliferating cells [392–394]. Tumor cells become resistant to TMZ by different mechanisms, including overexpression of DNA repair mechanisms and multidrug efflux transporters such as P-gp, mutations in p53 and phosphatase and tensin homolog (PTEN), and altered RNA expression patterns [395–397]. The main inducer of TMZ resistance is the DNA repair enzyme O6-methyl-guanidine methyltransferase (MGMT). MGMT counteracts TMZ effects by direct removal of the O6-methyl group from alkylated guanines [398]. Interestingly, it was reported that GBM EVs from cell lines resistant to TMZ as well as from treatment-refractory patients carry elevated levels of MGMT mRNA and these levels are predictive for patient outcome [399], and we do not exclude that EV transfer of MGMT mRNA molecules at least partly facilitates the TMZ resistance observed. (60–63).

Here we propose a model in which the chemokine CCL18, a natural ligand of the CCR8 receptor, connects glycans exposed on the EV membrane to the CCR8 receptor expressed on GBM cells. Virus and EVs can have similar biophysical characteristics and routes of biogenesis and uptake [358,359,400]. For instance, it was reported that certain strains of HIV can bind oligomers of CCL5 via glycans exposed on the viral envelope, allowing viral attachment to the

plasma membrane of the target cell. CCL5 was also shown to strongly induce uptake of (cellular, non-viral) EVs from uninfected T lymphocytes [401]. Of note, it was reported that enveloped viruses, like HIV, can use chemokine receptors as co-receptors, including CCR8 [371,402–404]. Moreover, natural ligands can compete with these viruses for the co-receptors, inhibiting viral uptake [405,406]. Exploring other viral co-receptors as potential EV receptors could be of interest.

Myanishi et al. demonstrated that Tim1 and Tim4 can act as EV receptors by binding to phosphatidylserine exposed on EVs. However, EV uptake by a certain cell may not only depend on the presence of specific cellular receptors, but in the case of bridging uptake mechanisms also on the availability of adaptor ligands, either secreted by the recipient or donor cell, or by other cells in the microenvironment. Here we show that CCL18 functions as bridging adaptor for GBM EVs, and CCL18 expression has been identified as an important prognostic factor in GBM [407]. Recently it was shown that EVs can also be decorated by autotaxin resulting in binding to integrins expressed on cell surfaces [361]. Similarly it was reported that heparan sulfates exposed on EVs can bind to fibronectin, serving as a bridging molecule to heparan sulfates expressed on cell membranes [363]. Christianson *et al*. previously showed that heparan sulfate molecules expressed on cell surfaces can function as EV receptors on GBM cells [362], and others demonstrated that heparin treatment reduces EV uptake by recipient cells, including GBM cells [355,363,408–411]. Here we observed that pretreatment of cells with heparin reduces EV uptake to a lesser extent than pretreatment of EVs with heparin (data not shown), suggesting that both mechanisms (direct heparin sulfate- and CCR8-mediated endocytosis) can occur simultaneously. An important consequence of the "connectokine" model is that it implies a complex level of regulation of EV transfer, perhaps similarly as observed for decoration of EVs with autotoxin [361] or fibronectin.

Interfering with selective EV uptake may be a promising approach to attack cancer cells, given the numerous potential protumoral effects EVs can exert. Here, we show that R243, a small molecule inhibitor of CCR8, inhibits EV uptake and counteracts EV-induced responses in recipient GBM cells *in vitro* and *in vivo*. R243 did not only influence the interaction of EVs and the GBM8 cell line, but had similar effects in 2 other GBM cell lines and in a melanoma cell line, suggesting a general role of CCR8-EV interaction, although the exact role of CCR8 expression on other non-cancerous cells – remains to be investigated. For instance, Th2 lymphocytes are known to express high levels of CCR8 [370,412–414], which we were not able to analyze in our nude mouse xenograft models with primary human GBM stem-like brain tumors. Also, we do not exclude that other receptors can function in the uptake of GBM EVs, and perhaps additional chemokine/chemokine receptor pairs play a role in the tropism determination of EVs. Complex networks of chemokine/chemokine receptor pairs are known

to induce tumor cell survival, angiogenesis, invasion as well as recruitment to metastatic niches. These networks act in both autocrine and paracrine fashion, establishing virtual reciprocal dialogues between the tumor and its environment. The CCR8 axis has been related to several cancer progression-related processes in lymphoma, urothelial and renal carcinomas, breast, and pancreatic cancers [373,374,415–418]. Noteworthy, in melanoma, where EV-mediated communication has been shown to be key for metastasis [334,419], highly malignant cells express elevated levels of CCR8 and migrate to the lymph node in response to the secretion of the ligand by lymphatic endothelial cells. Blocking of the CCR8 axis resulted in strong reduction of metastatic transit through the lymph node in xenograft models [375], suggestive of a potential role of EV uptake via CCR8 during melanoma metastasis.

In summary, we describe a mechanism of EV uptake involving a chemokine receptor and its natural ligand acting as a bridging adaptor. Inhibition of CCR8 decreased EV-induced phenotypes in GBM *in vitro* and *in vivo* models, opening the door to new anticancer approaches based on chemokine-receptor targeting of tumor EV crosstalk.

ACKNOWLEDGEMENTS

The authors would like to thank M. H. Meel for his help with FACS sorting and J. W. van Weering for his assistance with electron microscopy. The plasmids Puro.Cre (Addgene plasmid # 17408) and ROSA26 mT/mG (Addgene plasmid # 17787) were a kind gift from Dr. T. Jacks and Dr. L. Luo. Financial support was provided by European Research Council 336540 (TW) and Stichting STOPhersentumoren.nl (JB and TW). This work is part of the research program Vernieuwingsimpuls with project number 016.116.366 financed by the Netherlands Organization for Scientific Research (TW).

Supplementary Figures

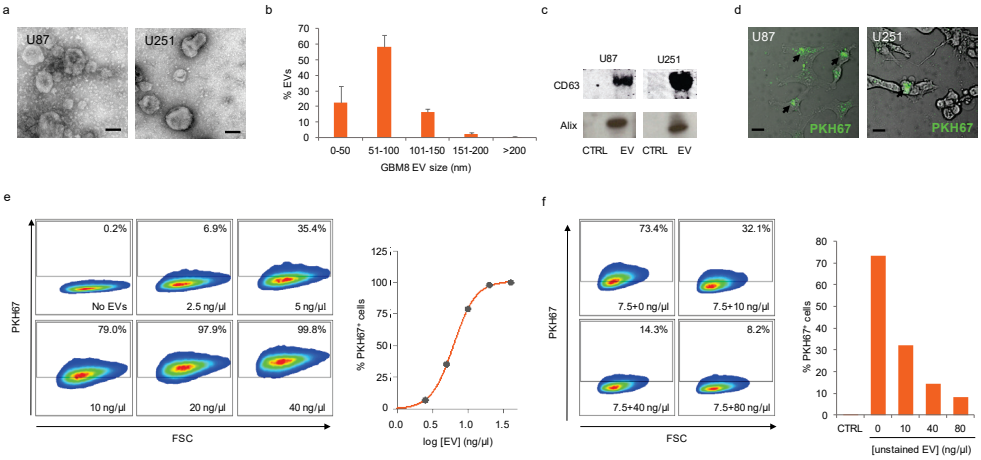

Supplementary Fig 1. (**a**) EM image of EVs isolated from U87 (left) and U251 (right) cells (scale bar: 100 nm). (**b**) Size distribution of isolated GBM8 EVs as determined by manual measuring of EVs on EM images. Bars represent the mean of three independent preparations. Error bars represent the standard deviation of the three measurements. (**c**) Western blot analysis of CD63 and Alix on EVs isolated from U87 (left) and U251 cells (right). Control: supernatant from the 70000g centrifugation. (**d**) U87 (left) and U251 (right) cells incubated with overnight with PKH67-labelled EVs from the same cell lines (scale bars: 10 µm). (**e**) FACS analysis of GBM8 cells incubated with increasing concentrations of PKH67-labelled GBM8 EVs. Left panel: scatterplots. Right graph: Dose-response curve of PKH67 fluorescence with the amount of EVs added showing saturation around 20 ng/µl of pKH67-labelled EVs. (**f**) FACS analysis of GBM8 cells incubated with a fixed concentration of stained EVs (7.5 ng/µl) and increasing concentrations of unstained EVs. Left: scatterplots. Right bar graphs showing the percentage of $PKH67^+$ cells.

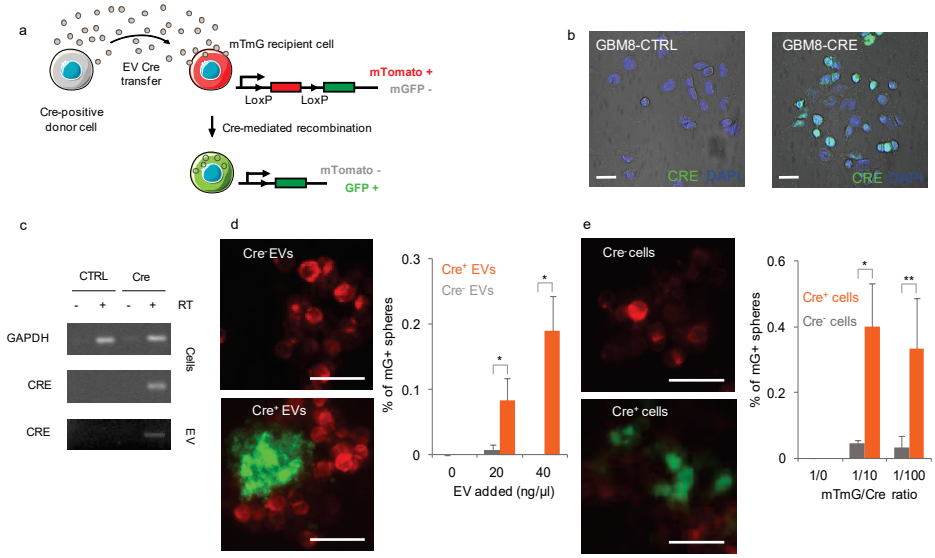

Supplementary Fig 2. (**a**) Schematic of Cre-mT/mG EV transfer reporter system. (**b**) Immunocytochemistry against Cre protein (green) on control (parental cells, left) or Cre-transduced GBM8 cells (right). DAPI (4',6-diamidino-2-phenylindole, blue) was used to stain the nuclei (scale bars: 10 µm). (**c**) Cre RT-PCR on Cre donor cells and their isolated EVs (**d**) Addition of EVs isolated from Cre^+ donor cells resulted in appearance of mG^+ patches in mT/mG spheres, as compared with addition of vesicles from non-Cre-expressing cells (left: representative pictures (scale bars: 25 µm); right: quantification of mG^+ spheres). (**e**) Co-culture of mT/mG cells with Cre donor cells (left: representative pictures (scale bars: 25 µm); right: quantification of mG^+ spheres). Bar graphs in (**e**) and (**f**) show the means ± SD of three independent experiments. * indicates p-value ≤0.05, ** indicates p-value ≤0.005. (t-test).

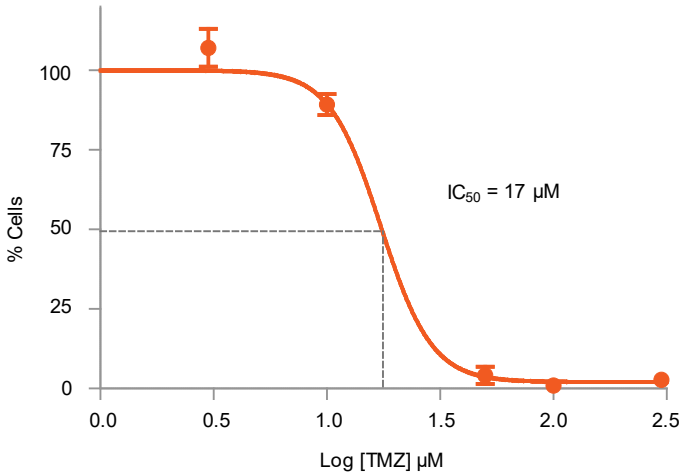

Supplementary Fig 3. TMZ IC_{50} determination on GBM8 cells (17 µM). Relative cell number was determined by calculating GBM8 sphere volumes (see methods).

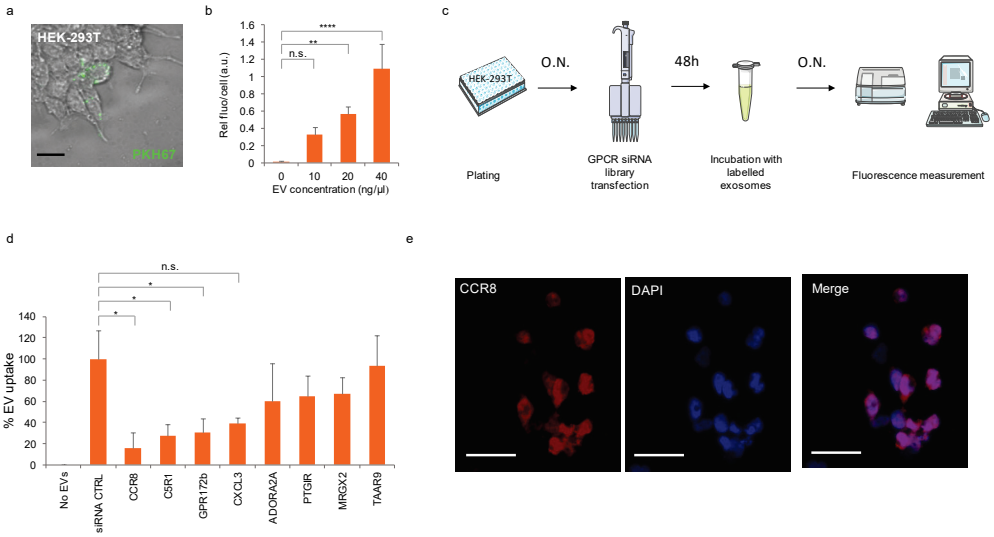

Supplementary Fig 4. (**a**) Image of uptake of PKH67-labelled GBM EVs by HEK-293T cells (scale bar: 25 µm). (**b**) EV uptake assay showing dose-dependent uptake of PKH67 GBM EVs by HEK-293T. ** indicates p-value ≤0.01 and **** indicates p-value ≤0.0001, as determined by ANOVA. (**c**) Experimental setup of the GPCR siRNA screening. At day 0, 5 x 10^3 HEK-293T cells were seeded in 96-well plates. The day after, a GPCR siRNA library was transfected and 48 h later cells were incubated with 20 ng/µl of fluorescent EVs. The day after, cell nuclei were stained with Hoechst dye and fluorescence was read with an automated plate reader. (**d**) siRNA screen validation on HEK-293T cells with an independent set of siRNAs on the 8 siRNAs which caused the strongest reduction in PKH67 fluorescence. * indicates p-value ≤0.05 as determined by ANOVA. (**e**) Immunocytochemistry against CCR8 (red) on GBM8 cells. Nuclei were stained with DAPI (blue) (scale bars: 50 µm).

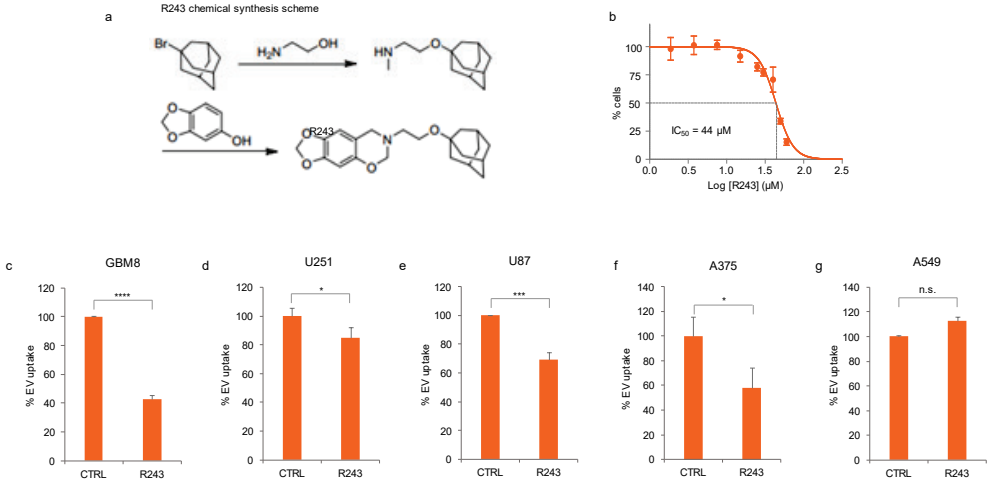

Supplementary Fig 5. (**a**) Chemical synthesis scheme of R243. (**b**) R243 IC_{50} determination on GBM8 cells (44 µM). Cell viability was estimated by CellTiter-Glo ssay (Promega). (**c-g**) EV uptake analysis in the presence of R243 on GBM8, U251, U87, A375 and A549cell lines * indicates p-value ≤0.05, ** indicates p-value ≤0.01 and *** indicates p-value ≤0.001 as determined by t-tests.

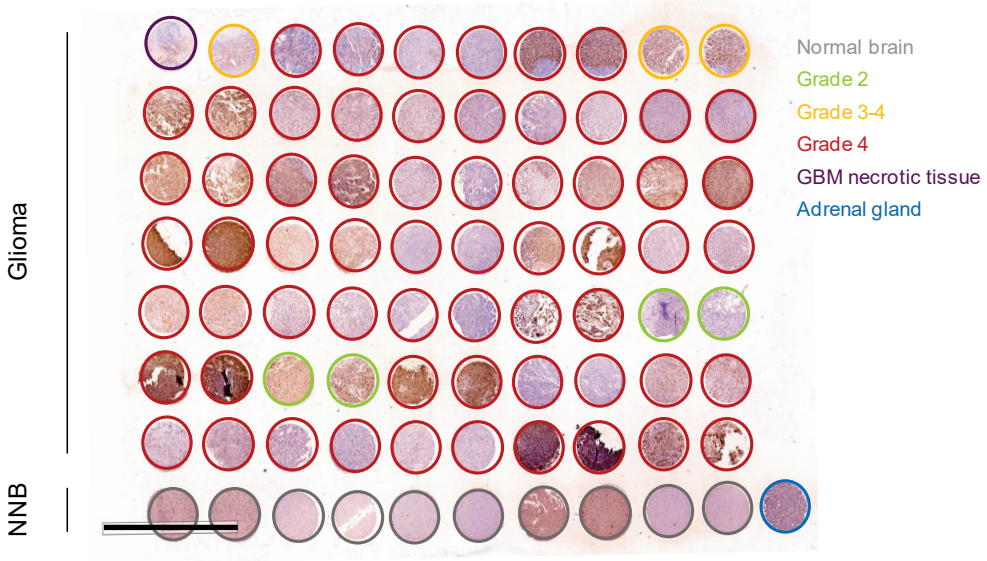

Supplementary Fig 6. Glioma TMA immunostained against CCR8 (scale bar: 5 mm). Specimens are included in a colored circle to indicate sample type and tumor grade, as indicated in the legend on the right.

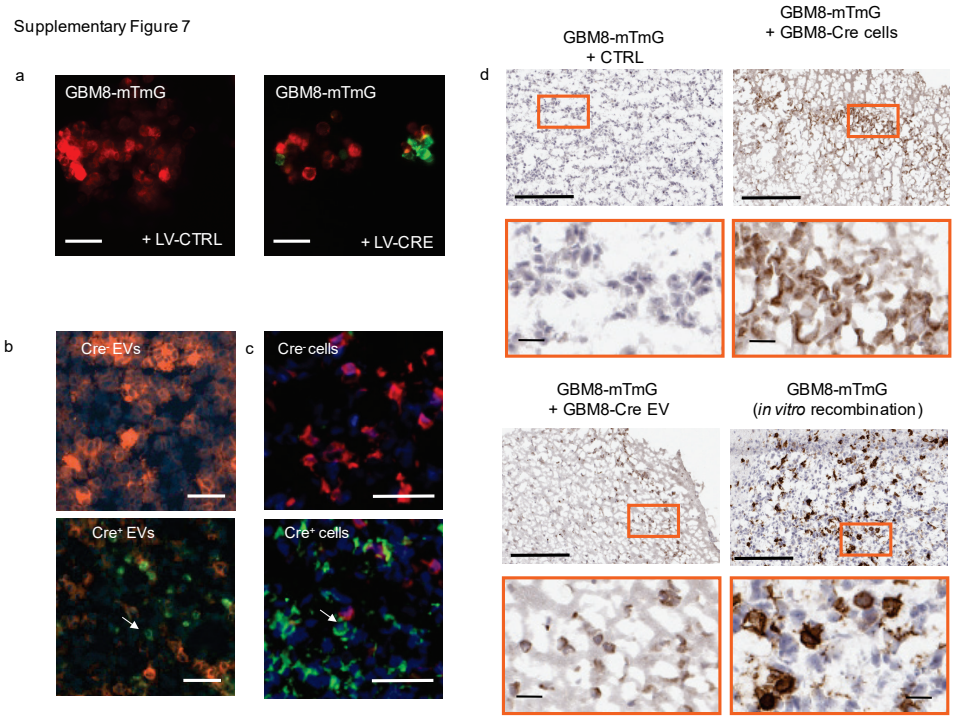

Supplementary Fig 7. (a) Functionality test of GBM8 mG/mT reporter cells: mG/mT cells were incubated with a lentivirus expressing Cre recombinase (LV-CRE) or non-Cre-expressing lentivirus (LV-CTRL). Images were taken after 24 h incubation. (scale bars: 25 µm). **(b)** Direct injection of Cre^+ EVs (bottom), but not control EVs (top) resulted in mT to mG color switch in GBM8-mT/mG mouse xenografts (scale bars: 50 µm). (**c**) Orthotopic injection of mT/mG cells combined with injection of Cre^+ cells (bottom), but not Cre^- cells (top) in opposite hemispheres resulted in mT to mG color switch in mT/mG cells (scale bars: 50 µm). For all experiments 1 x 10^5 cells resuspended in PBS were injected. **(d)** GFP immunostaining confirming presence of recombined GBM8 mG+ cells in mouse injected with mT/mG recipient cells co-injected either with Cre donor cells or with Cre^+ EVs.Negative control: mT/mG Cells co-injected with non-Cre expressing GBM8 cells. Positive control *in vitro* recombined GBM8 mT/mG cells as in **Supplementary Fig. 1g**. Squares in pictures on the top indicate the magnified areas shown in the pictures at the bottom. Scale bars: 200 µm (top), 20 µm (bottom).

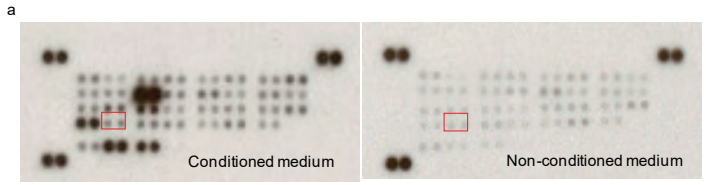

Chemokine	Fold	Chemokine	Fold	Chemokine	Fold	Chemokine	Fold	Chemokine	Fold
CCL21	2.96	CXCL1	6.46	XCL1	2.93	CCL15	2.67	CXCL12	2.78
CCL28	5.64	CCL14	3.97	CCL2	3.34	CCL20	3.79	CCL17	2.18
CXCL16	4.49	CCL1	4.25	CCL7	4.18	CCL19	2.96	CXCL17	2.96
Chemerin	3.43	CXCL8	36.26	CCL22	6.51	CXCL7	15.74		
CXCL5	2.36	IL-16	3.87	Midkine	13.96	CCL18	3.29		
CCL26	2.18	CXCL10	2.00	CXCL9	6.16	CXCL4	3.93		
CX3CL1	2.81	CXCL11	2.18	CCL3	2.72	CCL5	5.13		

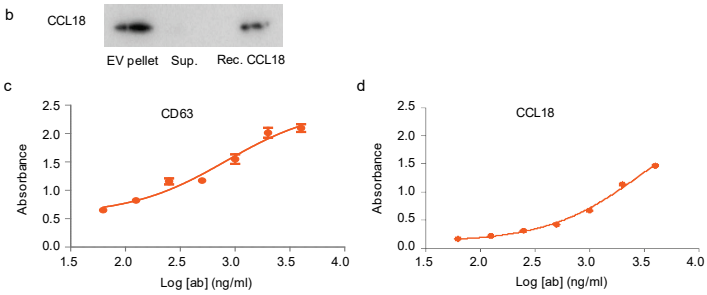

Supplementary Fig 8. (**a**) Chemokine array of overnight GBM8 conditioned medium (left). Non-conditioned medium was used as a negative control (right). Red square indicates the position of the anti-CCL18 antibody. Fold increase in band signal is indicated in the table below. (**b**) Western blot analysis against CCL18 on the 70,000 x g pellet or the supernatant derived from GBM8 EVs incubated overnight with recombinant CCL18, washed with PBS and re-pelleted. Positive control: Recombinant CCL18. (**c**) ELISA results on plates coated with a fixed concentration of EVs (5 ng/µl) incubated with serial dilutions of anti-CD63 antibody. (**d**) ELISA results on plates coated with a fixed concentration of EVs (5 ng/µl) incubated with serial dilutions anti-CCL18 antibody.

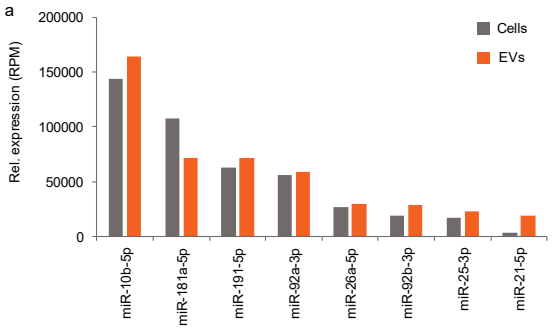

b

miRNA	GBM proliferation	Chemo resistance
miR-10b	(Gabriely 2011)	(Nishida 2012)
miR-181 a	n.a.	(Chen 2014)
miR-191	(Li 2014)	(Nagpal 2013)
miR-92a	(Niu 2012)	(Shuang 2013)
miR-26a	(Huse 2009)	n.a.
miR-92b	(Wang 2013)	(Li 2013)
miR-25	(Peng 2015)	(Zhou 2014)
miR-21	(Chan 2005)	(Shi 2010)

Supplementary Fig 9. (**a**) small RNA sequencing data of GBM8 cells and EVs. Over-represented miRNAs in GBM8 cells and EVs previously described as inducers of proliferation. Bars represent reads per million (RPM) in cells (grey bars) and in EVs (orange bars). (**b**) references relating miRNA sequencing results with induction of proliferation in GBM (left) and chemo resistance in several types of cancer (right). n.a: not applicable.

CHAPTER 7 |

Optical clearing and fluorescence deep-tissue imaging for 3D quantitative analysis of the brain tumor microenvironment

Tonny Lagerweij*, Sophie A. Dusoswa*, Adrian Negrean, Esther M.L. Hendrikx, Helga E. de Vries, Jeroen Kole, Juan J. Garcia-Vallejo, Huibert D. Mansvelder, W. Peter Vandertop, David P. Noske, Bakhos A. Tannous, René J.P. Musters, Yvette van Kooyk, Pieter Wesseling, Xi Wen Zhao, Thomas Wurdinger

Published in: Angiogenesis 2017; Nov; 20(4): 533-546

* These authors contributed equally to this work

ABSTRACT

Three-dimensional visualization of the brain vasculature and its interactions with surrounding cells may shed light on diseases where aberrant microvascular organization is involved, including glioblastoma (GBM). Intravital confocal imaging allows 3D visualization of microvascular structures and migration of cells in the brain of mice, however, with limited imaging depth. To enable comprehensive analysis of GBM and the brain microenvironment, in-depth 3D imaging methods are needed. Here we employed methods for optical tissue clearing prior to 3D microscopy to visualize the brain microvasculature and routes of invasion of GBM cells.

We present a workflow for *ex vivo* imaging of optically-cleared brain tumor tissues, and subsequent computational modeling. This workflow was used for quantification of the microvasculature in relation to nuclear or cellular density in healthy mouse brain tissues and in human orthotopic, infiltrative GBM8 and E98 glioblastoma models.

Ex vivo cleared mouse brain tissues had a >10-fold increased imaging depth as compared to intravital imaging of mouse brain *in vivo.* Imaging of optically-cleared brain tissue allowed quantification of the 3D microvascular characteristics in healthy mouse brains and in tissues with diffuse, infiltrative growing GBM8 brain tumors. Detailed 3D visualization revealed the organization of tumor cells relative to the vasculature, in both grey- and white matter regions, and patterns of multicellular GBM networks collectively invading the brain parenchyma.

Optical tissue clearing opens new avenues for combined quantitative and 3D microscopic analysis of the topographical relationship between GBM cells and their microenvironment.

INTRODUCTION

Glioblastomas (GBMs) remain incurable, partly because of extensive, diffuse infiltration of the GBM cells into their surrounding microenvironment. GBM cell invasion and proliferation leads to changes in the microvasculature, tissue perfusion, and brain architecture. Increased awareness of spatial heterogeneity of the GBM cells, in relation to the microvasculature, and intervascular tissue microenvironment [67,420–422], has raised the need for 3D analyses of brain tumor tissues.

Optical 3D analysis allows imaging of brain structures at cellular resolution and may serve as a bridge between CT, PET, or MRI and classical microscopic histology and immunohistochemistry [165,423]. Intravital confocal microscopy enables 3D fluorescence imaging on a cellular level [131,424], but its use is hampered by sedation time of the animal, limited imaging depth, small field of view, and limitations associated with fluorescent labeling [131]. These limitations do not apply to *ex vivo* optical imaging. For a long time, optical imaging of 3D structures was dependent on histological sectioning [147,148,421]. This sectioning is, however, a laborious and challenging task, since at least several dozens of histological slices have to be obtained and properly aligned for the creation of an informative 3D image. To avoid these laborious and error-prone approach, optical slicing methods were developed. Optical slicing involves clearing of tissues to make them transparent, thus enabling deep tissue fluorophore excitation and detection. Although optical clearing techniques were described already more than a century ago [425], the interest in this approach was boosted by the development of more advanced clearing techniques such as 3DISCO/iDISCO/uDISCO, *Scale,* SeeDB and CLARITY [156,161,426–432], which all have their specific advantages and disadvantages[156,158]. Besides new clearing techniques, other major contributions to optical slicing methods were the development and improvement of equipment such as multi-photon microscopes and lightsheet microscopes. Furthermore, numerous relevant software tools have been developed, including ImageJ, VAA3D, FARSIGHT, NeuronStudio, AMIRA and IMARIS [433–436].

Here we employed optical clearance methods to study GBM cells in the mouse brain microenvironment. We demonstrate that optically-cleared tissues can be imaged up to at least 2000 µm depth, at subcellular resolution. This allowed detailed 3D visualization of the brain tumor microenvironment and revealed patterns of networks of collectively invading GBM cells.

MATERIALS and METHODS

Animal care guidelines

All animal experiments were approved by the VU University Medical Center Animal Welfare review board. Female, specific pathogen-free, athymic nude-Foxn1^{nu} mice (6-8 weeks; Harlan/Envigo, The Netherlands) were kept in filter top cages and received food and water ad libitum.

Intravital confocal imaging

Application of a cranial window for intravital imaging of the mouse brain was based on the method as described by Mostany et al.[126]. Three mice were anesthetized by isoflurane inhalation and received temgesic (0.05 mg/kg) pre-operatively and dexamethasone (0.2 mg/kg) with carprufen (5 mg/kg) post-operatively to prevent edema. With a 0.8 mm cutter, an area with a diameter of 5 mm in the skull was opened at the designated location. After hemostasis, a drop of silicon oil was placed onto the dura and a glass coverslip was glued on top of the craniotomy. Blood vessels were fluorescently stained by intravenous injection of Lycopersicon esculentum (*tomato)* lectin^{tomato}-FITC. Images with a diameter of 350 µm were captured at 50 µm depth intervals.

Orthotopic GBM xenograft models

Human GBM8 glioblastoma cells [437] and human E98 glioblastoma cells were lentivirally transduced with a lentivirus vector to stably express the mCherry fluorescent protein and firefly luciferase (Fluc) [111]. GBM8-FM cells were cultured as neurospheres in serum-free medium, supplemented with growth factors (2% of B27 supplement, 1% of N2 supplement, 2 µg/ml heparin, 20 ng/ml recombinant human EGF, 10 ng/ml recombinant human bFGF). E98-FM cells were injected subcutaneously in a donor mouse. When the tumor reached a diameter of 1 cm, the tumor was removed and a single cell suspension was prepared. The harvested GBM cells were washed once with PBS and concentrated by centrifugation to a concentration of $1x10^5$ cells per µl. Mice were stereotactically injected with $5x10^5$ tumor cells into the striatum. Intracranial injections were performed under isoflurane anesthesia and systemic and topical analgesia (buprenophine, 0.1 mg/kg; lidocaine 0.5%). The coordinates used for injections were 0.5 mm X, 2 mm Y, and -3 mm Z from the bregma [200] Tumor progression was confirmed by Fluc *in vivo* bioluminescence imaging (BLI) after i.p. injection of D-luciferin (100 mg/kg) and acquiring the photon flux (p/s) using the Xenogen-IVIS Lumina system under isoflurane anesthesia.

Photoacoustic Imaging (PAI)

Three mice with GBM8-FM tumors were used to evaluate photoacoustic imaging. PAI was performed on a Vevo LAZR imaging station (FUJIFILM Visualsonics Inc. Toronto, ON, Canada) which features a hybrid ultrasound and photoacoustic transducer with a tunable nanosecond pulsed laser. Photoacoustic oxygenation signals were collected at 750 and 850 nm and with the provided FIJIFILM Visualsonics imaging analysis software the average oxygen saturation of the hemoglobulin was calculated and visualized [438].

CLARITY optical clearing and immunolabeling

Mice were perfused with CLARITY hydrogel according to the protocol described by Chung et al. [429]. Animals were deeply anesthetized with an overdose of ketamin/xylazin, and perfused with ice-cold PBS to remove highly auto-fluorescent hemoglobin, followed by perfusion with hydrogel solution (4% PFA, 4% acrylamide, 0.05% bis-acrylamide, 0.25% VA044 initiator in PBS). Brains were incubated for 24-72 hours in hydrogel at 4°C, and polymerization of the hydrogel was accomplished by deoxygenation, followed by thermal initiation of the polymerization reaction. Polymerized mouse brains were cut into 3-5 mm slices and washed to remove free monomers and PFA. An electrophoretic tissue chamber (ETC) was made, based on reported specifications [149] (Supplementary Figure S2A). SDS-clearing buffer (200 mM sodium borate, 4% SDS, pH8.5), was kept at 37ºC and pumped through the ETC chamber at a speed of 0.6-1.2 l/min. Tissues were electrophorized during 3-5 days at a constant voltage of 20V. The SDS-clearing solution was replaced if pH dropped below pH 8. After electrophoretic lipid removal, tissues were washed for 24 hours in PBS containing 0.1% Triton-X100 at 37°C. Tissue samples were stained, depending on their sizes, for 1-7 days in PBS containing DAPI and lectin^{tomato}-Dylight488 or lectin^{tomato}-Dylight594 (Vector Laboratories, dilution 1:500) or lectin^{tomato}-FITC (Vector Laboratories, dilution 1:500). Subsequently, samples were washed 24 hours in PBS and finally incubated for 6-24 hours in 80% glycerol to match refractive indices, resulting in transparency of the samples.

iDISCO immunolabeling and optical clearing

Brains of mice with established tumor progression were fixed and stored in 4% buffered formalin for at least 24 hours, up to more than two years. These brains were sliced into 3-5 mm thick sections and processed for immunolabeling and optical clearing with the methanol iDISCO procedure [439]. Samples were permeabilized with increasing methanol concentrations to a final concentration of 100% methanol. Next, the brain sections were bleached overnight at 4°C in hydrogen peroxide:methanol (ratio of 1:5), after which tissues were gradually rehydrated to PBS and washed in PBS with 0.2% Triton-X100. To block residual binding sides, tissues were incubated for three days at room temperature (RT) with antibody diluent (DAKO). Following blocking, the samples were stained for seven days with primary antibody (anti-RFP, which binds the mCherry reporter protein expressed in tumor cells) and Dylight488

conjugated lectin^{tomato} at RT. Excess primary antibodies or lectins were washed away during three days. Tissues were incubated with the secondary antibody (AlexaFluor594 conjugated anti-rabbit) for seven days. Unbound antibody was washed away with PBS-Triton during three days, after which tissues were dehydrated by gradually increasing methanol concentrations to a final solution of 100% methanol. Next, remaining lipids were removed by incubation in dichloromethane (DCM)/methanol and one hour incubation with 100% DCM. To make the samples transparent, samples were incubated in dibenzyl ether (DBE) for refractive index matching. It is important to use fresh DCM and DBE as oxidation of these reagents may result in suboptimal clearing and a brownish color of the tissues. Transparent samples were stored in the dark in a closed vial completely filled with DBE until image acquisition for a period up to 6 months.

3D Image acquisition

Intravital imaging was performed on a custom-built two-photon laser scanning microscope using Olympus objectives [153]. *Ex vivo* two-photon images were captured on a LaVision BioTec microscope system, based on an Olympus BX51WI microscope, connected to a pulsed tunable (740-1070 nm) laser (Chameleon, Coherent). CLARITY-cleared tissues were mounted in an imaging chamber filled with 80% glycerol whereas iDISCO-cleared tissues were mounted in a flexible imaging chamber, created with adhesive poster pads, which was filled with DBE (Supplementary Figure 3B). Images were acquired with a water immersion objective (20x magnification, NA 1.00, maximum working distance 2000 µm) at a voxel size of 0.54x0.54x1-5 µm. Epifluorescence signals were separated by dichroic mirrors and filters (DAPI: 420/50, FITC/Dylight488: 525/50), and collected by a photomultiplier tube (PMT). Laser power was set with an automatic laser power increment, which increased laser power gradually from 5 to 20% over a depth of maximum 2000 µm. Lectin^{tomato} labeled microvasculature and DAPI-stained nuclei were imaged at an excitation wavelength of 800 nm, which simultaneously excites all fluorophores. Alternatively, images were acquired with a Leica SP8 confocal microscope, equipped with a pulsed white light laser and a 10x 0.4NA air objective or a NIKON A1R confocal microscope with a 20x 0.8NA air objective. These images were taken with a voxel size of 1 μm^3 and fluorescent signals were recorded using gated hybrid detectors.

Data processing

Image reconstruction of the 2-photon images was performed using FIJI with the "Stitch Sequence of Grids of Images" plugin of FIJI [440]. Background subtraction was performed by application of a Gaussian filter. Images obtained with the other microscopes were imported directly into IMARIS software (version 7, Bitplane) and stitched automatically.

Quantification of signal intensity

Quantification of signal intensity was performed using FIJI. Epifluorescent signal intensity as a function of imaging depth was determined by measurement of median signal intensity at all imaging depths. Median fluorescence was normalized to the intensity of the most superficial slide.

3D-modeling of the vasculature and cell density

Fluorescently-stained vessel surfaces were detected and converted into a mask. This mask was used to create a new, binary, channel in which the voxels outside the mask were set to zero and inside the mask to a fixed value. This binary mask was used to trace blood vessels by the 'Filaments Tracer' option of IMARIS, which is a tool developed for the automatic detection of filament-like structures. Although this 'Filaments Tracer' tool is not completely compatible for the detection of vessel structures, as it does not allow the formation of loops, the detected structures co-localized with most of the fluorescently labeled vessels. During the detection process, vascular modeling required assignment of minimal (2 µm) and maximal (10 µm) vessel diameter, and manual definition of the thresholds for starting points and seeding points. Nuclei or RFP-positive cells were rendered using the "Spots Rendering" application of IMARIS. This application visualized the nuclei or cells as artificial solid objects, enabling quantification of number of nuclei per ROI and distance of the cells to the nearest blood vessel. All computational modeling was done 'unbiased', e.g. without additional improvement of the modeling by manual deletion or insertion of vessel parts.

2D Immunohistochemistry

Sections of 5 µm FFPE tumor containing brain tissues were processed after heat-induced antigen retrieval with Tris-EDTA (pH 9.0). Sections were stained with Dylight488-labeled lectin^{tomato} together with rabbit anti-CD31 antibody (Abcam, ab 28364; dilution 1:1000) or rabbit anti-RFP antibody (Tebu-Bio, cat. no. 600-901-397; dilution 1:500). The rabbit antibodies were detected with AlexaFluor594 labeled anti-rabbit as secondary antibody. Alternatively, slides were stained with hematoxylin/eosin. Image acquisition was done with a Zeiss Axio Scan Z1 slide scanner.

Statistical analysis

Statistical analyses were performed using GraphPad Prism 5 (GraphPad Software). Data were presented as mean ± SD. Unpaired student t-tests were used to test differences between spatial characteristics of different ROIs. P-values <0.05 were considered statistically significant.

RESULTS

High-resolution intravital imaging of the mouse brain vasculature is limited to a depth of 200 µm

Intravital imaging of the mouse cerebral vasculature was performed by two-photon imaging through a cranial window as schematically shown in Figure 1A. Through this window the superficial blood vessels, which can be used for orientation, are easily recognized (Fig. 1B). Blood vessels, fluorescently-stained with lectin^{tomato}-FITC, were imaged at 50 µm intervals. Under these conditions the maximal imaging depth was limited to 200 µm (Fig. 1C,H). Because this imaging depth was insufficient to image relevant locations deep into the brain, we decided to further explore *ex vivo* imaging methods for the visualization and quantification of the relation between tumor cells and the brain microenvironment, with a focus on the brain tumor vasculature.

Ex vivo two-photon imaging of optically-cleared brain tissue

In order to microscopically visualize regions throughout the entire mouse brain, optically clearing methods of mouse brain tissue were employed. Brains were stained and cleared by either the CLARITY [429] procedure or the methanol-based iDISCO method [439]. Brain slides of 3-5 mm thickness were processed to render transparent tissue, as shown for the iDISCO procedure in Figures 1D and 1E. Whereas iDISCO leads to a stable shrinkage of approximately 1.2x of the original tissue diameter (Fig. 1E), the CLARITY procedure resulted in an expansion of approximately 1.5x the tissue size. This tissue expansion continued after prolonged storage of the tissue in 80% glycerol, which complicates re-analysis of CLARITY cleared tissues, whereas tissues which were previously cleared and stained could be re-imaged for subsequent analyses months later (data not shown). Within the parietal cortex, lectin^{tomato} -stained microvessels could be imaged by 2-photon-microscopy down to a depth of 2000 µm after CLARITY optical clearing (Fig. 1F-H, Supplementary Fig. S1 and Supplementary Movie S1). In contrast to the rapid loss of signal intensity at increasing depth during intravital imaging, fluorescent signal intensity was well maintained in optically-cleared tissues. In optically-cleared tissues, signal intensity remained above 65% of superficial signal intensity along the complete working distance of the lens of 2000 µm (Fig. 1H).

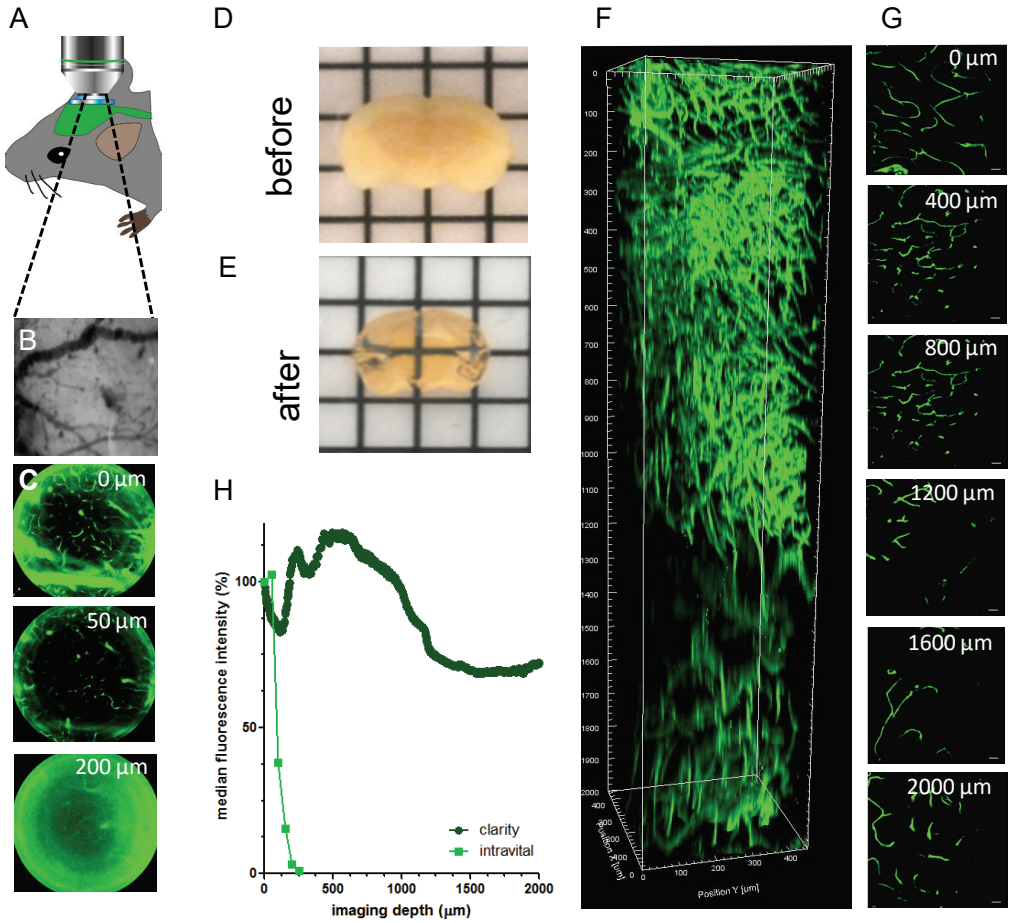

Figure 1. Intravital and *ex vivo* two-photon imaging of mouse cerebral microvasculature. (A) Schematic representation of intravital two-photon imaging setup. **(B)** Superficial blood vessels of the dura mater, observed through a cranial window. **(C)** 2D x-y plains obtained by intravital two-photon-imaging of lectin-FITC-labeled cerebral mouse vasculature at 50 µm depth intervals (n=1). Scale bars 100 µm. **(D)** 3mm thick slide of mouse brain, before optical clearing. **(E)** Transparent mouse brain after optical clearing with the iDISCO-procedure. **(F)** 2-photon imaging of lectin-FITC-labeled brain tissue, cleared with the CLARITY-procedure. Lateral view of a 3D-reconstruction of composed of 1001 pictures, starting at the parietal cortical surface to 2000 µm below, see also Supplementary Movie S1. **(G)** 2D x-y plains of *ex vivo* two-photon imaging of vasculature in CLARITY-cleared mouse brain tissue at 400 µm depth intervals. Scale bars 100 µm. **(H)** Relative fluorescence intensity as a function of imaging depth for intravital 2-photon imaging (n=1) and *ex vivo* two-photon-imaging of CLARITY-cleared mouse cerebral microvasculature (n=1).

Computational modeling of vasculature in healthy mouse brain tissue

Understanding the relation between glioblastoma cells and the vasculature would benefit from quantification of different aspects of their relationship. With the use of healthy mouse

brain tissue, a workflow for the quantification of the vasculature was developed (Supplementary Fig. S2). In a stack of lectin^{tomato} –FITC-stained vessels (Fig. 2A, green), different regions of interest (ROIs) were selected for computational modeling (Fig. 2A, red regions). Fluorescently-stained blood vessels (Fig. 2B, green, upper panel) were converted to computationally-modeled vessels (Fig. 2B, red, middle panel). Because these computational models were unbiased, i.e. without manual post-processing, the overlay of the modeled vessels showed a high degree of concordance, but was not perfect. (Fig. 2B overlay, bottom panel). By using 2D-orthogonal planes we estimated the concordance of the fluorescently labeled vasculature with the computational modeled vasculature to be approximately 80% (Fig. 2C, Supplementary Fig. S4). Next, the combination of lectin^{tomato}-FITC-labeled microvasculature and counter-stained nuclei (DAPI) was imaged using two-photon microscopy (Fig. 2D). These large, tiled image files show a striking vignetting at the borders of each acquired imaging field. This vignetting is due to the fact that standard water immersion or air objectives - which are not corrected for the high refractive indexes of the embedding medium - were used for the acquisition. Because this could potentially result in artifacts in the stitching and consequent quantification, selected ROIs were centered within the tiles. ROIs were selected within the granular layer (GL, green rectangles) and in the molecular layer (ML, blue rectangles) of the cerebellum (Fig. 2D). The obtained 3D stack with lectin^{tomato}-stained microvessels and DAPI-stained nuclei enabled detailed fluorescently imaging (Fig. 2E), and allowed computational modeling (Fig. 2F). After such computational modeling, the number of DAPI-stained nuclei, and quantitative data of the vasculature, such as number of branches, total vessel length, volume, area, and diameter of single segments per volume of 100x100x100 µm (=10^6 µm^3), were calculated. These analyses revealed large differences in the vasculature of the GL versus the ML of the cerebellum (Fig. 2G, Supplementary Movie S2). These observed differences corroborates findings of previous studies reporting that, within different brain regions, large differences in vasculature are present [441]. Thus emphasizing that only identical, anatomically well-defined, areas should be compared to evaluate spatial relations between cells and their brain microenvironment.

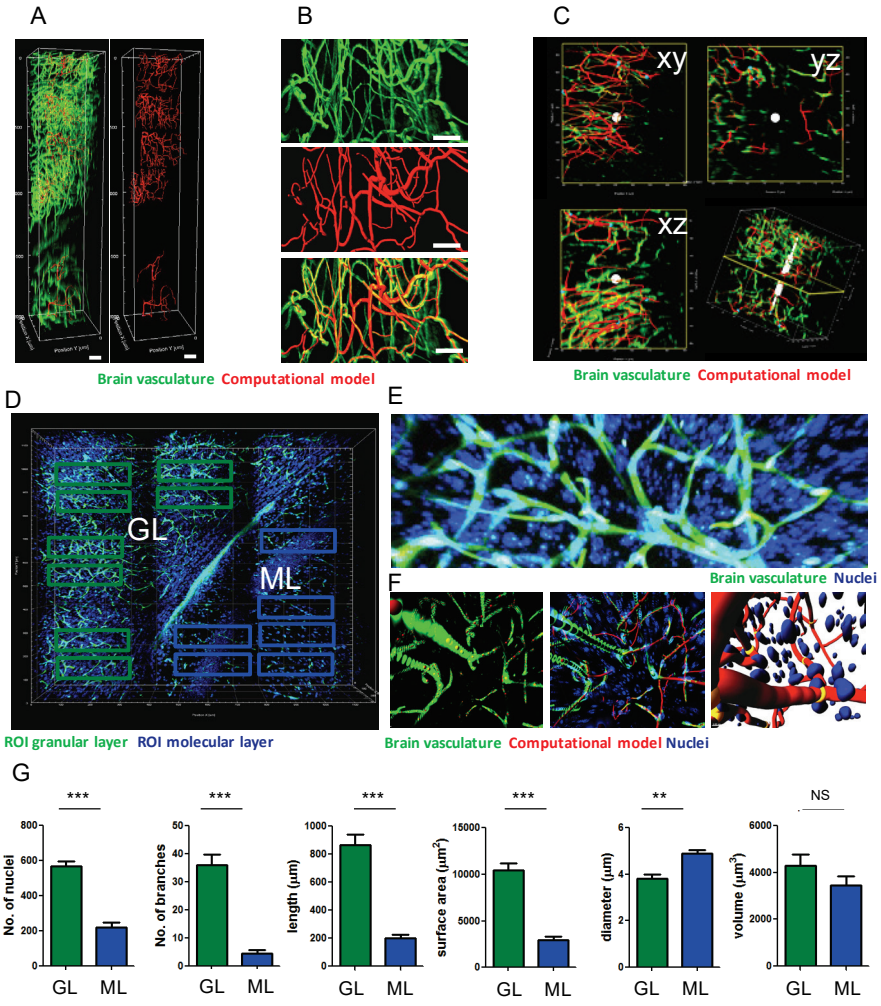

Figure 2. 3D representation and computational reconstruction of cerebral microvasculature and surrounding cells. (A) Computational modeling (red) of 3D cerebral-vasculature fluorescently labeled with lectin^{tomato}-Dylight488 (green). Scale bars 100 µm. **(B)** Upper panel: Fluorescently labeled vasculature (green), mid panel: computational reconstruction modeled with IMARIS Filaments tool (red), bottom: overlay of the fluorescent signal with the computational reconstruction. Scale bar: 25µm. **(C)** 2D orthogonal images of computational reconstruction (red) and fluorescent signal (green). **(D)** Areas in the granular layer of the cerebellum (gl, green rectangles) and the molecular layer of the cerebellum (ml, blue rectangles) are selected for quantification. Scale bar 100 µm. **(E)** Detail of a granular layer region, showing the spatial relation of the nuclei (blue) to the vessels (green). Scale bar 25 µm.**(F)** Computational modeling of vasculature (red) and nuclei (blue) of the microvascular and surrounding cells. Scale bars 10 µm. **(G)** Quantification of number of nuclei, number of vessel branches, total vessel length, total surface area, mean vessel diameter and total vessel volume in the granular layer and molecular layer regions of the cerebellar cortex. All quantifications are normalized to a volume of 10^6 um^3. ** p<0.01, *** p<0.001, t-test.

The lectin^{tomato}-staining pattern of the microvasculature is not affected by GBM cells

Because tumor cells are known to alter the endothelial glycocalyx [442], we confirmed the binding of lectin^{tomato} to blood vessels in tumor containing tissue. Brain tumors were induced by orthotopic xenograft transplantation of human GBM8-FM cells into nude mice. First, the presence of a GBM8-FM tumor was detected by photoacoustic imaging, which revealed increased oxygenation levels in the tumor areas, indicative for a change in the vasculature (Fig. 3A). Tumor growth was confirmed by bioluminescence imaging (Fig. 3B), and H&E staining of the brain clearly indicated the presence of tumor in the striatum (Fig. 3C). Furthermore, tumor was easily identified on tissue slides stained with lectin^{tomato} and anti-RFP antibody, which stains the GBM8-FM cells (Fig. 3D). Combined staining with lectin^{tomato} and anti-CD31 (Fig. 3E-G) demonstrated overlay of lectin^{tomato}-stained and CD31-stained microvasculature, indicating that tumor growth does not significantly influence the lectin-binding pattern of brain microvasculature.

Computational modeling of the GBM vasculature in mouse brain

As the iDISCO method allowed easy processing of already formalin-fixed materials, this method was employed for optically clearing of the formalin fixed tumor bearing brain tissues. The optically clearing procedures were performed with GBM8-FM xenografted brain tissues which were fixed for less than 2 months and with E98-FM xenografted brain tissues which were fixed for over two years. Tissue stained for tumor cells (anti-RFP-Ax594, red) and vasculature (lectin^{tomato}-DL488, green) revealed the presence of large, diffuse infiltrative tumors in the GBM8-FM glioblastoma xenograft models (Fig. 4A, Supplementary Movie S3). GBM cells have migrated away from the tumor core (TC) into the deep grey (DGM), and white (WM) matter areas, and even to the contralateral side (CL). Also, migration into the subarachnoid space was observed (arrow). Figure 4B shows that large numbers of GBM cells migrated collectively through white matter tracts such as the corpus callosum (CC), but both in the hemisphere where the tumor was transplanted as in the contralateral hemisphere, solitary cells can be identified, especially in close proximity to blood vessels (arrows). In the tumor core, changes in the vasculature where shown (Fig. 4C) as compared to the vasculature in the corresponding region on the contralateral side (Fig. 4D). Striking is the binding of lectin^{tomato} on cell-like structures in the tumor core (Fig. 4C), where these lectin-stained cells are virtually absent in the contralateral side (Fig. 4D). Computational modeling of the vasculature in these lectin-positive cell-rich areas was feasible, because the filament tracer detects tube-like structures (Supplemental Fig. S6). Quantifications of GBM8 and E98 tumors was performed by comparing contralateral brain areas within the same brain. The control area was normalized to 100% to allow a pair-wise comparison of the tumor versus control area. The quantifications revealed an increase in the number of vessel branches, increase in total vessel length and an increase in surface area of these vessels within the tumor regions. The mean vessel diameter was slightly lower in the tumor core as compared

to the same region of the contralateral side, resulting in comparable vessel volume in both areas for both the GBM8 tumor and the E98FM tumor (Fig. 4E).

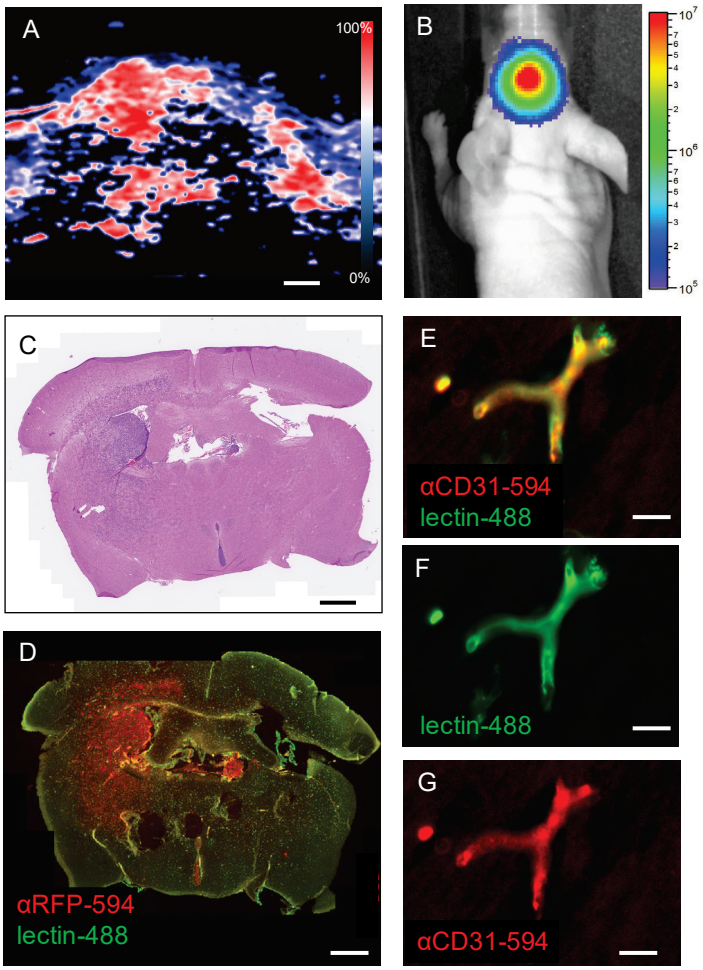

Figure 3. Lectin^{tomato} binding to the microvasculature in the presence of tumor cells. (A) Photoacoustic coronal image of an intracranial GBM8-FM tumor with highly-oxygenated, vascular regions indicated in red. **(B)** BLI image showing the presence of the GBM8-FM tumor. **(C)** Hematoxylin/eosin stained section of the same tumor as depicted in (A) and (B) showing the association between highly-vascularized/ oxygenated areas and the presence of tumor. **(D)** Brain tissue with GBM8-FM tumor stained with lectin^{tomato}-Dylight488 (green) directed against blood vessels, and with an anti-RFP-AlexaFluor594 antibody directed against the GBM8-FM cells. **(E-G)** Details of (D) showing that in the presence of tumor, lectin^{tomato} (green) and anti-CD31 antibody (red) stain the same microvessels. Scale bars A, C, D: 700 µm; Scale bars E, F, G: 10 µm.

GBM cell distribution in the brain microenvironment

We quantified the number of GBM cells in three different anatomical areas (TC, DGM, WM), as illustrated in Fig. 4A. The number of GBM8 cells per 10^6 µm^3 in the tumor core was significantly higher as compared to the infiltrative fronts in both the deep grey and the white matter regions (Fig. 5A). Similar as shown in Fig. 2G, large differences in vessel characteristics were observed between distinct anatomical regions, as shown for the number of vessel branches (Fig. 5B), and other parameters (Supplementary Fig. S7).

Next, we calculated the distance of the GBM8 tumor cells to the microvessels in the three anatomical areas. In the observed E98-FM tumor xenografts, infiltration was less pronounced as compared to the GBM8 tumors (Supplementary Fig. 5), which limited the quantitation of the E98 tumor cells to the tumor core and the grey matter areas. In the tumor core, 29.8% of the GBM8 tumor cells were located at a distance of >20 µm from the nearest blood vessel. Tumor cells in the infiltrative front within the deep grey matter were more closely located to the blood vessels; in this grey matter area, only 9.5% of the GBM8 tumor cells was located at a distance of >20 µm from their nearest blood vessel (Fig. 5C). The E98 tumor cells were even more closely associated to the vasculature, with >99% of the invasive GBM cells in the deep grey matter located at a distance of <20 µm from the nearest blood vessel (Fig. 5C).

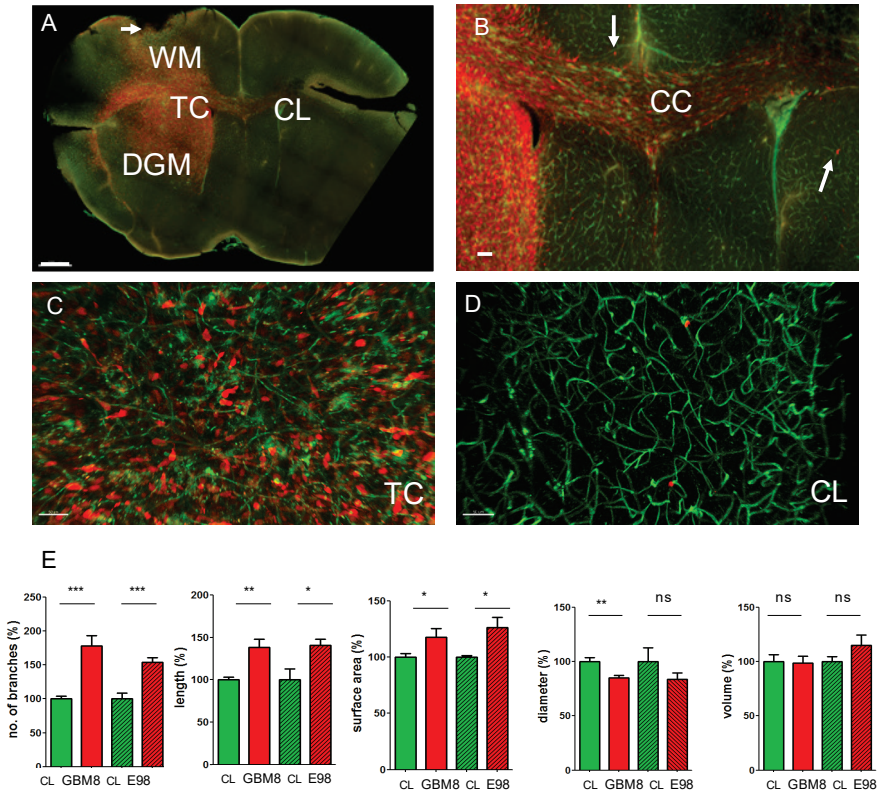

Figure 4. Microvascular reconstruction in GBM infiltrated areas. (A) Typical example of a diffuse, invasively growing GBM8-FM tumor (anti-RFP-Ax594, red) with its microvasculature (lectin^{tomato}-Dylight488, green). Tumor cells have migrated into the healthy brain parenchyma, away from the tumor core (TC) into the contralateral (CL) hemisphere, into the deep gray matter (DGM), and into the subarachnoid space (arrows). **(B)** Detail of (A) showing the abundant presence of GBM-cells in the corpus callosum (CC). **(C)** Detail of the TC, with tumor cells (red) in close proximity to blood vessels (green). **(D)** Detail of (A) showing distantly migrated solitary tumor cells (red) in close proximity to blood vessels (green). **(E)** Quantification of number of vessel branches, vessel length, surface, diameter and vessel volume in the tumor core of GBM8 tumors (n=7) and E98 (n=2) tumors. Values are normalized

to comparable control areas (CL) within the same brain where no evident tumor formation was detected. * p<0.05, ** p<0.01, *** p<0.001, t-test. Scale bars A: 700 µm; B: 250 µm; C, D: 50 µm.

These results may suggest some preference for perivascular migration of GBM cells in the deep grey matter, whereas in the tumor core use of alternative migration routes, such as through the brain parenchyma, are used. An alternative explanation is that proliferation of the GBM cells in the tumor core has resulted in an expansion of the intervascular compartment, thus resulting in larger distances of the tumor cells from the microvasculature. Interestingly, in the white matter regions, the distance distribution of the GBM cells to the nearest blood vessels was comparable to the tumor core regions, suggesting that tumor cell migration in the white matter area does not solely depend on blood vessel co-option, but may also occur via white matter tracts. Another striking observation is the presence of a subset of tumor cells that are interconnected by cellular processes similar as the multicellular networks as postulated by Osswald et al. [443]. Groups of approximately 4-6 cells were interconnected by tubular, 'dendrite-like' structures (Fig. 5D, arrows). These results demonstrate that optically cleared tissues can be used to detect subtle changes in the brain tumor microvasculature, allow visualization and quantitation of GBM cells, and quantitation of the relative position of GBM cells to the brain microvasculature. The proposed workflow (Supplementary Fig. S2) offers an attractive additional method for 3D histology (Supplementary Movie S3), complementary to traditional histological methods.

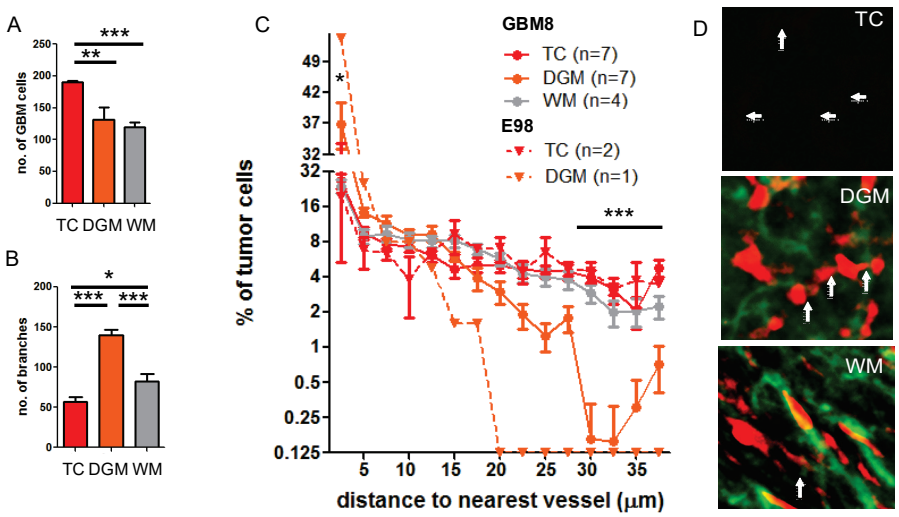

Figure 5. Topographical characteristics of GBM cells distant from the tumor core. (A) GBM cell density (per volume of 10^6 µm^3) was calculated in the tumor core (TC, n=7), and invasive fronts within the deep grey matter (DGM, n=7) and white matter (WM, n=4) of GBM8 tumors. **(B)** Number of vessel branches (per volume of 10^6 µm^3 in the three aforementioned areas in GBM8 xenografted brains. **(C)** Proportion of GBM8 and E98 cells at indicated distance (µm) of the nearest vessel at distribution intervals of 2.5

µm. **(D)** GBM8 cells are interconnected via cell processes (arrows). * p<0.05, ** p<0.01, *** p<0.001, t-test. Scale bars 10 µm. Samples were cleared with iDISCO.

DISCUSSION

In the present study, we show the use of optically-cleared brain tissues to allow visualization of cerebral microvasculature and the organization of nuclei or tumor cells in the brain tumor microenvironment. For this, we developed an effective workflow, which was explored to quantify subtle changes in the vasculature, and moreover, to visualize and measure the topographical relationship between GBM cells and their microenvironment in an invasive orthotopic GBM model in mice. Transparent adult mouse brain tissues were prepared with the CLARITY-protocol or the iDISCO-procedure. Both methods allowed detailed optical imaging and 3D-reconstruction of the microvasculature and distribution of cells or nuclei. Computational modeling allowed quantitative analysis, showing differences in the GBM cell distribution in distinct regions of the brain.

Intravital imaging was not suitable to image relevant regions of intracranial tumor due to its limited imaging depth and small fields of view. Therefore, we extended our methods to study the tumor microenvironment to *ex vivo* 3D imaging of transparent brain tissues. *Ex vivo* 3D whole tissue imaging has become a maturing field of research [444] and many tissue-clearing protocols have been developed recently. Most of these clearing protocols focus on improvement of fluorescence signal intensity because conventional clearing protocols caused quenching of fluorescence signal. CLARITY- and iDISCO-procedures have been reported to be compatible with fluorescently stained tissues [156,429,432,439]. Both procedures remove the highly abundant lipids in myelin rich brain tissue [155], which is an important step to obtain optically-transparent tissues, but also improves antibody penetration. Improvement of antibody penetration is important because immunofluorescent staining of large tissues is still a challenge [162,445]. Furthermore, we noticed that certain antibodies require further optimization for staining of large tissues. For example, anti-vimentin staining, which was successfully used to visualize E98FM tumor cells on traditional 5 µm sections[446], did not result in detection of tumor cells in our iDISCO processed samples, and the CD31 staining was hampered by low signal to noise ratio (data not shown). For the use of antibodies for additional markers, optimization steps such as titration of the antibody concentrations, and tissue pre-treatment, needs to be validated for each antibody [156]. Besides the use of antibodies to obtain clear structure information, these antibodies could also be validated for their use to provide functional information. These could include the staining of IgG leakiness [447] or the use of other proteins which leak out of the vasculature after BBB disruption. To ensure complete and consistent tissue staining, we limited the thickness of the tissue slides to approximately 3-5 mm and explored the use of lectins, which have a low molecular weight

(71 kD), as compared to antibodies (150 kD). The used lectin, isolated from Lycopersiconesculentum (*tomato)*, has a high affinity for glycan epitopes on endothelial cells [447–449], and on ramified and activated microglia[448,450], which might explain the observed binding of lectin^{tomato} to non-endothelial cells within the brain tumor. In addition, to quantify the cerebral vasculature and surrounding cells, we have extended the possibilities of 3D-visualization of cleared brain tissue by the addition of computational modeling with the commercial software package IMARIS.

For imaging of optically cleared tissues, numerous microscopical techniques have been developed, including two-photon imaging, light-sheet microscopy and confocal imaging, which all have their own advantages and limitations (Supplementary Fig. S8). All used microscopes in this manuscript were equipped with standard air or water lenses. Hence, vignetting is visible on the edges of all acquired images which leads to artifacts in the stitching of the tiled images. To prevent these artifacts, special lenses tailored for CLARITY are developed which could further improve the quality of tiled images [451].

The whole process, from tissue collection to sample preparation, image acquisition, reconstruction, post-processing, analysis and 3D-image acquisition takes approximately one month for both the CLARITY procedure and the iDISCO procedure (Figure 6). This processing time is highly influenced by the thickness of the tissue as diffusion of antibodies through the tissue is a time-consuming process. However, although these methods to prepare tissue for optical-sectioning are still time-consuming, they are not as labor-intensive as compared to traditional methods of mechanically, histological sectioning.

GBM is still incurable, partly because of its invasive character, but also because interactions with its microenvironment and intra-tumoral communication. The invasive character of GBM was already thoroughly described in the 1930's. In that work, four pathways of glioma cell invasion were recognized: through the brain parenchyma, along pre-existing blood vessels, through white matter tracts and via the subarachnoid space [452,453]. The distribution of GBM cells we observed are fully compatible with those four migratory patterns. We hypothesized that these migration patterns will be reflected by the distance of the tumor cells to the microvasculature. Indeed, we found that in grey areas, tumor cells migrated mainly in close proximity of the vasculature. In contrast, in the white matter a bigger proportion of the GBM cells were located at a larger distance from the microvasculature, suggestive for migration following the tracts of the white matter. In GBM, intra-tumoral communication may take place via secreted factors, including exosomes [454], or by direct cell-cell contact of the tumor cells via an interconnected GBM cell network [125,443,455]. In line with this, we observed the presence of interconnected GBM cells, similar as suggested by Osswald *et al.*[443]. These cell clusters were present in the tumor core, but also in the infiltrative fronts in the deep grey matter and the white matter.

In conclusion, we demonstrate the use of optically-cleared, transparent tissues to study in 3D the architecture of the brain microvasculature as well as the topographical relationship

of GBM cells to the microvasculature. Detailed 3D-visualization and quantitation revealed differences in organization of tumor cells relative to the vasculature in grey matter regions versus white matter regions, and patterns of GBM cell networks collectively invading the brain parenchyma. This deep-fluorescence-imaging and 3D quantitative approach opens new avenues to study the pathobiology of brain cancer cells and their microenvironment.

Conflict of interests

None declared.

Acknowledgments

We thank the Technical Department of the VU University for construction of the ETC chambers. Jithin Jose of FIJIFILM Visualsonics for support with photoacoustic imaging and Johan van Meerlo of VU University Medical Center for assistance with confocal imaging. Financial support was provided by the European Research Council 336540 (TW) and the Dutch Organization of Scientific Research 91711366 (TW).

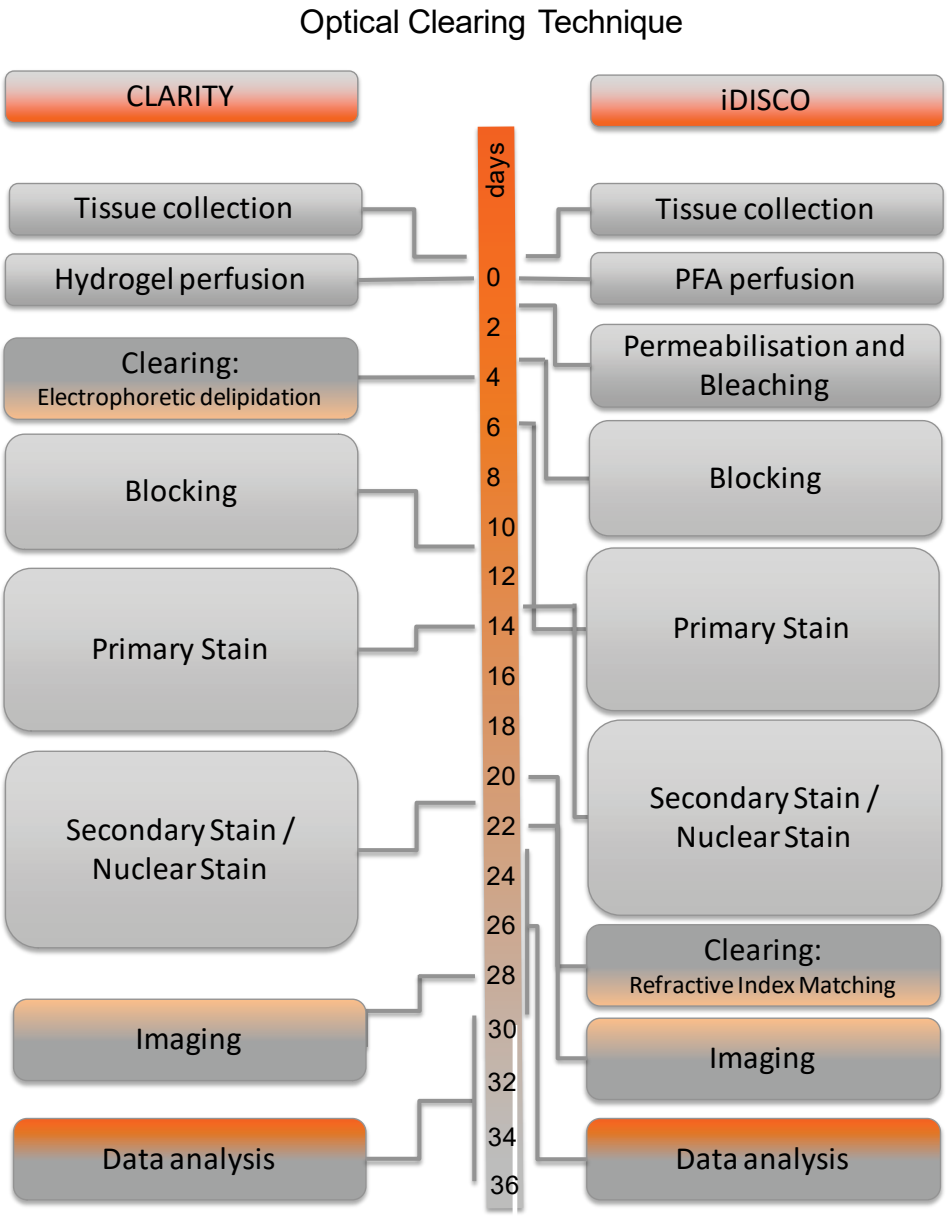

Figure 6. Timelines for the process from tissue collection to data analysis. This figure represents typical timelines for tissue of 5 mm thickness, which requires approximately one week for each antibody or lectin staining. Because the incubation steps are not very labor-intensive, it is feasible to process several tissues simultaneously.

Supplementary Figures.

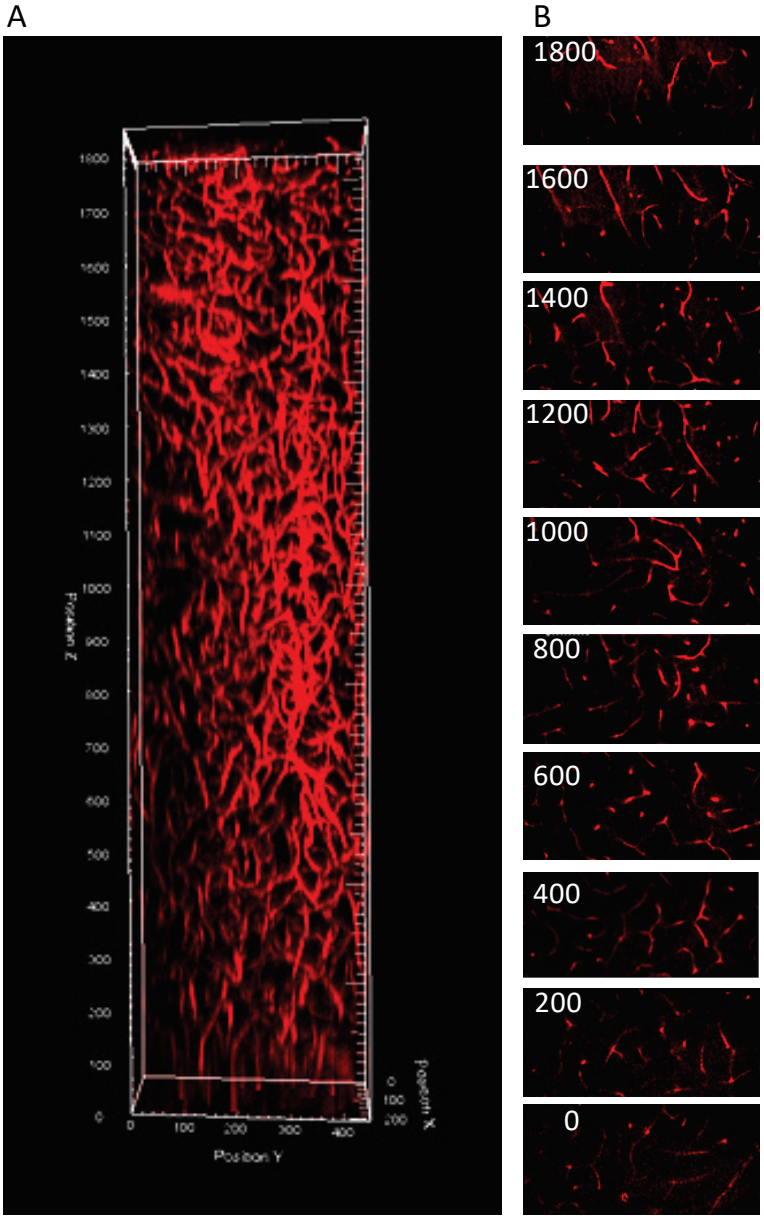

Supplementary Figure S1. (A) Two-photon imaging of lectin^{tomato}-Dylight594 labeled brain tissue, cleared with the CLARITY-procedure. Lateral view of a 3D-reconstruction of composed of 1850 pictures acquired at 1 µm interval. **(B)** 2D x-y plains of *ex vivo* two-photon imaging of vasculature in CLARITY-cleared mouse brain tissue at 200 µm depth intervals.

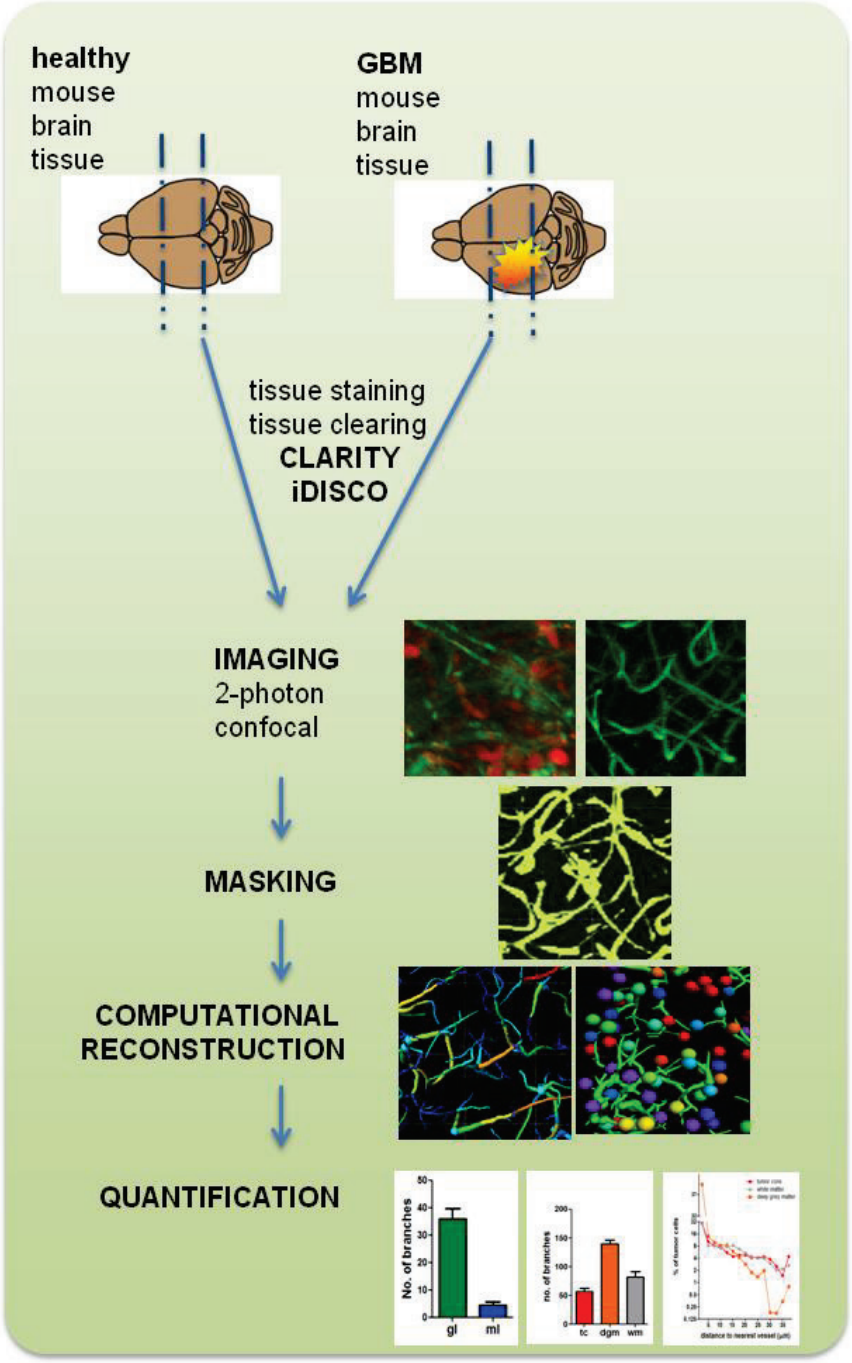

Supplementary Figure S2. Graphical abstract illustrating the workflow to quantify vessel and tumor characteristics in optically-cleared, transparent, tissues.

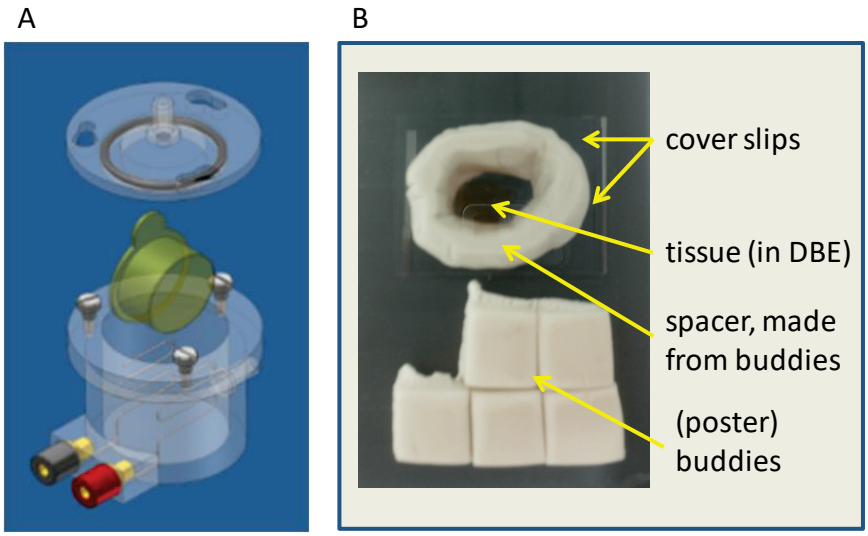

Supplementary Figure S3. (A) Design of CLARITY-electrophoresis chamber. **(B)** Example of a flexible imaging chamber.

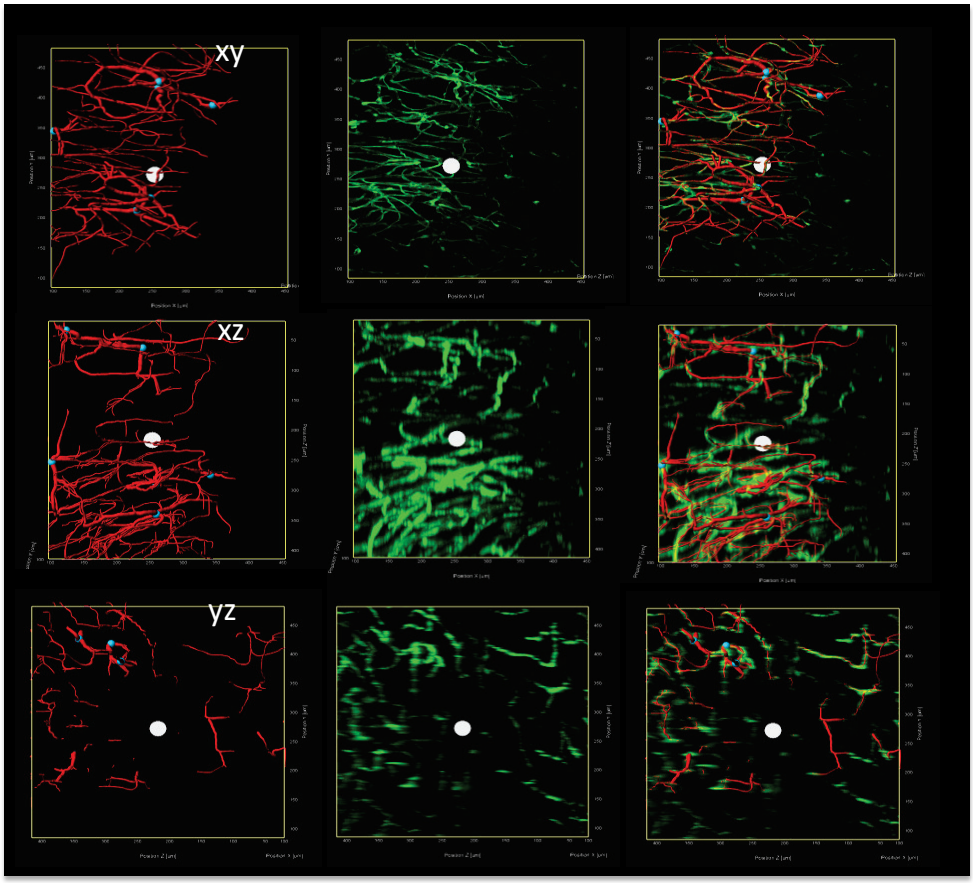

Supplementary Figure S4. 2D orthogonal representation of XY, XZ and YZ planes in iDISCO cleared tissues to illustrate the concordance between the computational vessel model and imaged fluorescence signal. This figures also illustrates the poor resolution in the Z-direction in relation to the XY resolution.

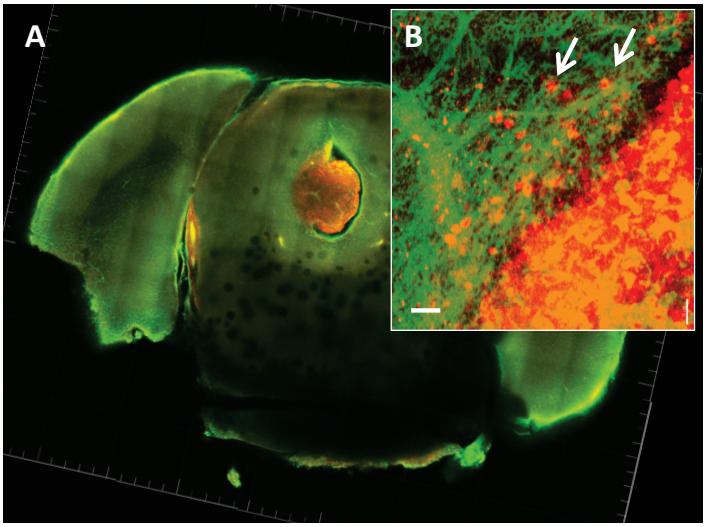

Supplementary Figure S5. (A) Example of an E98-FM tumor, this tumor has engrafted in the 3d ventricle and shows a more compact phenotype as compared to GBM8 tumors. **(B)** Detail of (A), arrows indicate infiltrating E98-FM cells. Scale bar: 30 µm

Online supplementary movies

Supplementary Movie S1. Vasculature of healthy mouse brain.
Supplementary Movie S2. Computational modeling of the mouse brain vasculature
Supplementary Movie S3. Vasculature and tumor cell distribution in human orthotopic GBM8 glioblastoma mouse model.

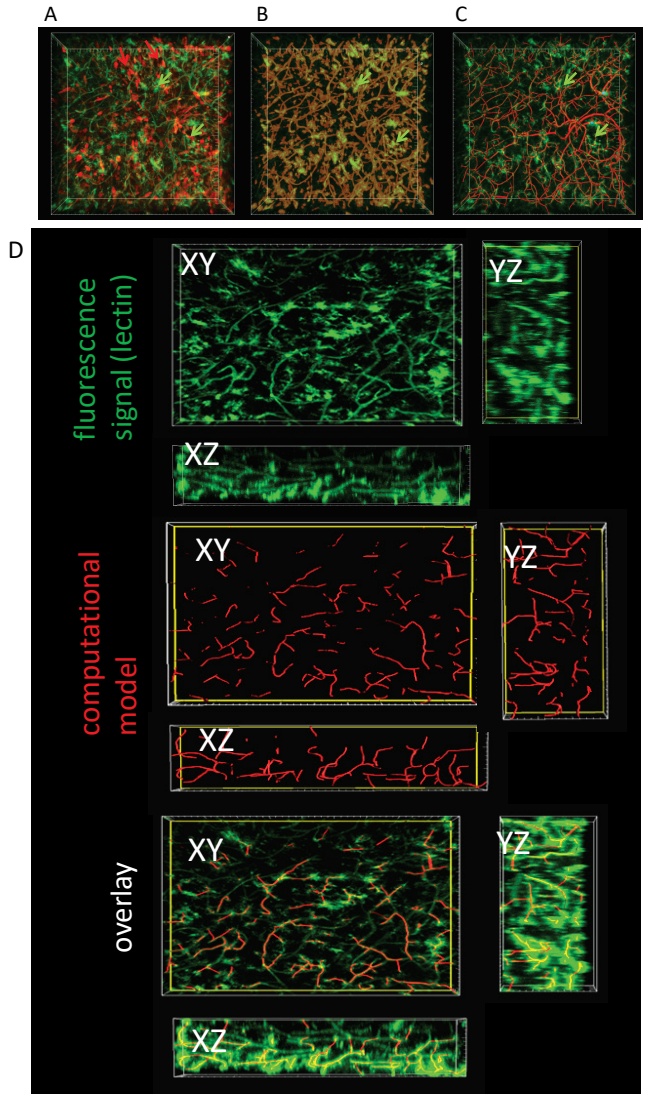

Supplementary Figure S6. Computational vessel reconstruction. **(A)** Tumor cells are stained with anti-RFP antibody (red, red arrows). The vasculature is stained with lectin (green), but also distinct cells are stained with this lectin (green arrow). **(B)** When a mask is applied to the green channel, these lectin stained cells are also included in the mask (arrow). **(C).** After use of the 'filament tracer' tool, most of the vessels are correctly identified while cell like structures are ignored. **(D).** 2D Orthogonal cross planes showing the vessel reconstruction in GBM infiltrated tissue.

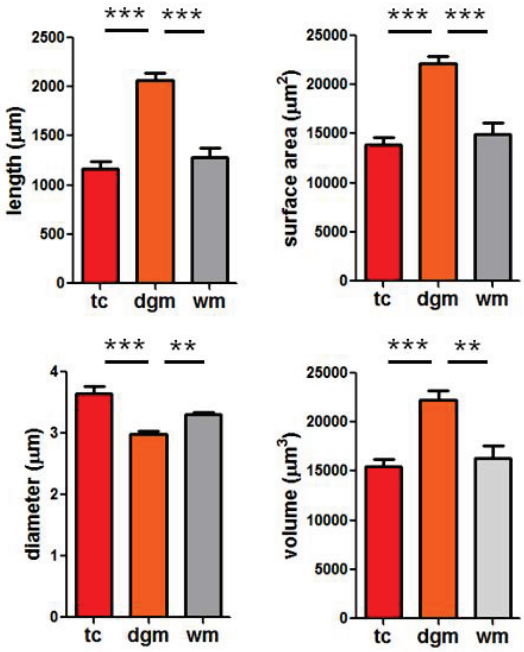

Supplementary Figure S7. Quantification of vessel length, surface area, diameter and volume within a ROI of 10^6 µm^3 in tumor core (TC), deep grey matter (DGM) and white matter (WM).

Imaging Technique

	Speed	Resolution	Photo Bleaching	Imaging Depth	Dependence on clearing
2-photon	+/-	++	+/-	++	+
confocal	+	++	+	+	++
lightsheet	+++	+/-	+/-	+++	+++

Supplementary Figure S8. Characteristics of suitable imaging techniques for advanced 3D-microscopy. Lightsheet microscopy offers the highest speed and imaging depth, but is very dependent on successful clearing efficacy and has limited magnification. Two-photon imaging has the lowest imaging speed but high magnification, good resolution, and good imaging depth. Because of the high wavelengths, 2-photon microscopy is less dependent on clearing efficacy. Confocal microscopes are available at many research labs. They allow reasonable to good imaging speed, good resolution but their imaging depth is limited. .

CHAPTER 8 |

GENERAL DISCUSSION AND FUTURE DIRECTIONS

Brain tumors and therapy

Currently, the most effective treatment regimens for primary high-grade brain tumors include surgical resection and radiotherapy, often supplemented with chemotherapy such as temozolomide for the treatment of GBM [49,456]. But, despite these therapeutic strategies, the relative survival estimates for GBM remain low with a median survival of only 5.5% five years post diagnosis [14]. This poor patient outcome is related to several reasons which are discussed in this thesis, such as the tumor location within the brain, the blood-brain-barrier (BBB) which limits the effective dose of the therapeutic agents, the infiltrative properties of these tumors, which prevents the complete resection of the tumor, and the tumor-heterogeneity that causes drug resistance.

Drug delivery across the BBB

Drug discovery programs have identified many therapeutic agents aimed against tumor cells. However, most of these therapeutics are not useful for the treatment of brain tumors because the compounds do not reach their targets within the brain [457]. This is due to several factors including metabolic instability of the drug, and the rate and extent of transport across the BBB [458]. In normal situations, the BBB protects the brain by limiting the access of micro-organisms and large molecules, and by actively pumping out foreign agents. In brain cancer however, the BBB also prevents therapeutic agents to reach sufficient high concentrations at the tumor site. To reach clinically effective concentrations of active drugs at the tumor location within the brain, several strategies are explored. These strategies involve either the increase of transport rate over the BBB into the brain, or the prevention of removal of the compound from the brain, bypassing the BBB, or combinations of these strategies.

To increase transport over the BBB, pharmaceutical characteristics including the polarity and molecular size of the compound are important. Because the BBB prevents large compounds to enter the brain, small-molecule drugs, with a molecular mass under a 400- to 500-Da threshold, are more likely to pass the BBB than larger drugs [312,457,459]. But, even if the drugs can pass the BBB, many will not reach pharmacologically relevant dosages at the tumor location because the drugs are actively pumped out of the brain. This drug removal is achieved by a range of ATP-binding cassette (ABC) efflux transporters such as ABCB1 (also known as multidrugresistance protein1 (MDR1) or P-glycoprotein) [63,460]. Therefore, inhibition of these drug efflux pumps would be a logical step to increase the drug concentration at the target location.

Inhibition of drug efflux pumps has been studied in the context of overcoming multidrug resistance (MDR). MDR is associated with the overexpression of efflux transporters on the tumor cells. Inhibition of these transporters could reverse the poor treatment outcome in the therapy resistant cancers, but so far clinical trials of inhibitors of ABCB1 have only been

moderately successful. The first and second generations of these inhibitors suffered from severe systemic toxicity, because efflux pumps are also present in tissues such as the liver and have important physiologic roles. In the third generation of ABCB1 modulators, the systemic toxicity of the inhibitors themselves is low. But these inhibitors are so effective that they frequently necessitate a reduction in the dose of anticancer agents [461]. Thus, although efflux transporter inhibitors efficiently increase drug concentrations within the brain in laboratory settings, animal models, and even in clinical studies, common practice of their use in combination therapies is still limited, due to concerns previously raised by these MDR studies.

If transport across the intact BBB after systemic administration is ineffective, other ways to deliver the drugs to the brain tumor are needed. One approach to bypass the BBB is local delivery of the compound directly into the brain, or even the tumor. This could be done by intracavitary chemotherapy such as the insertion of carmustine wafers in the resection area [194,462], intrathecal- or lumbar injections, or the intratumorally delivery by convection-enhanced delivery (CED). CED is the continuous infusion of the infusate by a positive-pressure. This technique allows distribution of the infusate into the tumor and its surrounding micro-environment. This infusion results in pharmaceutical relevant drug concentrations within the tumor, orders of magnitudes greater than systemic levels. Because drug distribution is not diffusion-mediated, there is not a steep concentration gradient required, thus limiting local toxicity of the initial dose [176]. With this convected delivery into the tumor, or tumor region, compounds can exert their effects locally on the tumor, without the severe systemical toxicity associated to systemic administration.

Besides the choice of therapeutic agents, therapy outcome via CED is also largely dependent on distribution and composition of the infusate. This distribution volume should cover the complete tumor area, including the invasive cells, to prevent tumor regrowth by untreated cells. This distribution volume of the infusate is highly dependent on technical variables, such as placement and design of the catheters, volume of infusion (Vi) and the infusion rate. But also properties, such as polarity and lipophilicity, of the drug.

In **Chapter 2** and **Chapter 3,** we employed CED for the administration of carmustine and doxorubicin in the treatment of diffuse intrinsic pontine glioma (DIPG). The intraparenchymal delivery approach resulted in locally high, but systemically low, concentrations of these chemotherapeutics. Unfortunately, although systemic toxicity was not observed with this administration route, the effects on survival in our animal tumor models were only modest. This because CED treatment resulted in only a temporary remission of the tumor progression, and moreover, damage to the surrounding brain tissue. Other therapeutics which have less effect on the healthy brain tissue might therefore be more suitable for the treatment of high-grade brain tumors.

Tumor biology and anti-cancer treatment

To avoid local toxicity as we observed with the broad-spectrum therapeutics which were used in our projects, such as carmustine and doxorubicin, more specific therapeutics could be used. Attractive candidate are drugs against specific epigenetic dysregulations which are found frequently in DIPG and GBM patients. In this approach, therapies are targeted against enzymes which affect the use of genes by histone modification. Recent studies suggest that EZH2 (enhancer of zeste homolog 2) and bromodomain proteins are promising therapeutic targets for DIPG and GBM treatment strategies [463–466]. EZH2 participates in DNA methylation, and bromodomain proteins recognize acetylated lysine residues on the N-terminal tails of histones, thus affecting gene activity and expression. However, systemic administration of these compounds for the treatment of brain tumors is not very effective, as the EZH2 inhibitors show restricted brain penetration, due to interaction with the drug efflux transporters ABCB1 and ABCG2 [464]. These drug characteristics -specific inhibition of the DIPG-targets and limited BBB-passage- make these drugs attractive candidates for CED administration. Besides these specific epigenetic dysregulations, also other cancer specific therapies could be explored for the treatment of brain tumors, such as the targeting of cell-cycle specific processes by interfering with the centrosome [467], MPS1 [468], WEE1 kinase [38,262], or Ape1 [469].

Another attractive approach, is the local delivery of immune-checkpoint inhibitors such as programmed death cell receptor (PD1/PDL1), cytotoxic T lymphocyte associated antigen 4 (CTLA-4) of indoleamine 2,3-dioxygenase (IDO) [81,470]. This could result in an alteration of the local immune system thereby limiting the tumor-promoting effects of the microenvironment and might even result in an anti-tumor response of the immune system.

Tumor heterogeneity and drug resistance

Even if the drug distribution to the tumor is adequate and the drug reaches clinically effective concentrations, treatment-effects are often only temporarily. These short-lived effects could partly be contributed to heterogeneity of brain tumors. This heterogeneity is due to the fact that cancer is not a single disease entity, but rather a whole family of diseases. The main characteristic of cancer is the pathological proliferation of cells. This uncontrolled growth of cells starts typically in a single cell due to genetic or epigenetic mutations caused by environmental factors, heredity or deviant cell division [471]. In normal situations, these mutations are corrected by the cells' repair machinery or the mutated cells are removed by the immune system. However, some mutations might escape these cell-cycle checkpoints or immune-cycle checkpoints which could result in initiation of cancer [472]. When these mutated cells start to multiply, every generation goes through a little evolutionary cycle, resulting in more evolved cells. These relentless cycles of mutation, selection and survival of cancer cells results in the generation of new cancer cells with the capacity to resist death signals, incite growth of blood vessels and ability to invade tissues.

Although the main tumor characteristic of uncontrolled proliferation of cells suggest a high commonality between cancers, most cancers, and thus most cancer patients are unique [471]. For high grade brain tumors, the situation is even more complex because tumor heterogeneity is not only observed between patients but also within the tumor of an individual patient. The strongest example of this is GBM where each cell might bear varying degrees of cellular and nuclear polymorphisms, as shown by the establishment of several subclones from a single tumor [473]. This indicates the presence of heterogeneous populations of cells within the tumor, where each cell may present its own potential target for therapeutic intervention [64]. This tumor heterogeneity contributes largely to the therapy resistance of brain tumors as the therapeutic agent initially kills only a proportion of the tumor cells. But after the initial therapeutic effect, remaining resistant cells, which have a different molecular identity, will continue to proliferate, thus resulting in recurrence of a therapy resistant tumor. To optimize current therapies, we evaluated the use different therapeutic strategies via three distinct mechanisms, namely 1) to improve radiotherapy, 2) anti-VEGF treatment for DIPG and 3) by diminishing cell-to-cell communication.

Radiotherapy

Radiotherapy is still an important aspect in the treatment of brain tumor patients. Radiation will not only affect the tumor tissue but also surrounding non-neoplastic tissues [47]. Because the brain of children under 3 years of age is still under development these brains are very sensitive to radiation, thus limiting the radiation dose is crucial in the treatment of young children. Therefore, methods to improve radiation efficiency and thus limiting the radiation are needed, especially for this group of young patients.

Sensitization of the tumor cells to radiotherapy could be a way to reduce the radiation dose as demonstrated in **Chapter 5** with the radio-sensitizing effect of quercetin. The role of quercetin in the treatment of brain tumor patients is probably not only limited to the radiotherapy, but could also be of value in the enhancement of chemotherapy, as quercetin has also been reported to exert synergistic effects when combined with temozolomide (TMZ), a FDA-approved drug for brain cancer treatment [474–479].

Angiogenesis inhibition

Treatment such as chemotherapy and radiotherapy are mainly aimed to kill the tumor cells directly. However, besides the direct attack of the tumor cells, it was hypothesized already in the 1970s that anti-angiogenic treatments could result in shrinkage of solid tumors. This led to development of anti-angiogenic agents, such as bevacizumab, which are directed against the vascular endothelial growth factor (VEGF) [253,480]. Targeting VEGF inhibits the process of new blood vessel formation and promotes regression of existing vessels. As high-grade brain tumors are highly vascularized [481], and VEGF is overexpressed in GBM, anti-angiogenic therapies were widely explored for these patients. These anti-VEGF therapies

resulted in inhibition of endothelial outgrow, which led to vascular normalization, and apparent improvement on contrast-enhanced MRI (pseudoresponse) [482–484]. However, this improvement of progression free survival was not reflected by an increase of the overall survival.

In chapter 4, we have demonstrated that in GBM this lack of efficacy of treatment with anti-VEGF antibodies can be partly explained by an absent VEGF upregulation on diffuse infiltrative tumor cells, and the inability of the antibody against VEGF to pass the BBB. These results, strengthened by a clinical study performed in children with DIPG [485], shows the importance of drug imaging to avoid treatment with compounds which are irrelevant for that specific type of tumor or for that specific patient.

Cell-to-cell communication

Intercellular communication might play a role in therapy resistance. This communication can be via direct cell-cell contact or via communication via excreted components. Examples for the role for direct cell-cell contact include the observation that clustered cancer cells are more resistant than single cells to apoptosis and that circulating tumor cell (CTC) clusters have increased metastatic potential compared to single CTCs [486,487]. Cell-cell contact of GBM stem cells was also demonstrated after xenografting in a mouse brain. In this study by Osswald *et al.* they showed that GBM cells formed multicellular networks by ultra-long cellular protrusions (length > 500 um). These multicellular networks were resistant to selective single cell ablation by application of a fatal laser dose [443].

Besides direct cell-cell contact, cells can communicate with each other via excreted components, including extracellular vesicles (EVs). EVs are membrane surrounded structures released by cells in an evolutionally conserved manner [488]. Tumor cells, including GBMs, are known to release vast amount of heterogenous populations of EVs, but also normal cells can produce significant amounts of EVs [339,489]. These EVs have the potential to migrate throughout the body and they are taken up by other cells. The uptake of the EV cargo could result in phenocopying tumor characteristics or alterations of the micro-environment [125,340] which result in the transfer of therapy resistance from one cell to another (Chapter 6).

PRECLINICAL RESEARCH and IMAGING

Animal models for brain tumors

Research into the mechanisms behind the onset and progression of brain tumors needs complex test systems, which should represent important aspects such as the BBB, tumor heterogeneity and the tumor micro-environment. Currently most *in vitro* assays -including advanced assays such as the culture of organoids or 'lab-on-a-chip' devices- are not sufficient to represent all these aspects. This lack of *in vitro* systems justifies the use of animal experiments to study brain tumors [490–493]. Before employing these complex animal experiments, data about efficacy, feasibility, and drug safety data are collected by iterative *in vitro* assays. Often, such *in vitro* tests start by administration of the compounds of interest to established cell lines to validate their effect on these cells. However, one cell line never reflects all the characteristics of a heterogeneous tumor. Therefore, to cover a large part of GBM heterogeneity, initiatives like the Human Glioblastoma Cell Culture (HGCC) resource were initiated. This HGCC collection aims to represent the four main GBM subtypes, namely proneural, neural, classical and mesenchymal [494]. Obtained cell lines can thus be used to identify novel therapeutics against the different GBM subclones. By screening drug libraries on cultured tumor cell lines in comparison with a range of normal –healthy- cells, compounds can be identified which have a toxic effect towards the tumor cells whilst normal cells are not, or minimally, affected.

Animal disease models are still crucial to study complex interactions such as the role of the immune system; the role of the BBB on brain tumor progression; to study the interaction of a tumor cell with its micro-environment, and to study the dependency of tumor cells on a wide range of physiological stimuli including cells, proteins and RNAs. Moreover, besides the need of animal experiments to advance scientific knowledge, the use of animal models is often demanded by regulatory authorities to identify adverse effects of therapies.

In our studies, we used xenograft models to study brain tumors. To enable the intracranial injection of human tumor cells, these cells were cultured *in vitro.* Many of these cell lines, including GBM lines U87MG, U251, and medulloblastoma lines DAOY and D283-med were established already decades ago [495–497]. Although these cell lines are generally used, their clinical relevance is questionable because the lack of infiltrative growth of the GBM cells and their relative sensitivity towards many drugs. Also, the authenticity of the cell lines with respect to the tumor where they were obtained from is questionable for a number of these cell lines.

Although not many cell lines can be authenticated with their original tumor anymore, it was shown for the widely used U87MG glioma cell line, that the DNA profile of the cell line was different from that of the original tumor [498]. Furthermore, established cell lines have evolved from their primary cell line. Every *in vitro* passage of the cell line represents a selection pressure on the cell line, resulting in a genetic drift in the cancer cells and even loss of typical GBM profiles in long-term subclones [499]. The authentication and characterization of the used cell lines, prior to start of the animal models would improve the translation of the obtained results. Further refinement of the xenograft models could be achieved by the use of primary cells which better reflect the tumor heterogeneity than established cell lines.

But not only the tumor should represent the human situation, also treatment options should reflect clinical practice closely. Although efforts are being made to treat mice similar as human patients [97], this is rarely the case as explained by some examples: Firstly, surgery is an important treatment option in human patients. Although tumor resection of intracranial tumors is feasible both in mice [500] and rats [115], not many studies consider the use of surgical resection of the brain tumor within preclinical settings of rodent studies. Secondly, for preclinical radiation therapy, often the whole head is irradiated [39] as opposed to localized, field radiation as used in the clinic. Thirdly, when novel treatments against human specific targets are being tested in xenograft models, these human targets might be absent in the animal tissues, thereby underestimating unwanted systemic side effects. But also wanted effects might be missed due to the species differences: Although a tumor microenvironment is present in the animal models, this microenvironment is of rodent origin and therefore not the same as in human patients. Finally, in preclinical research, therapy is often started at early time points at which the tumor is hardly detectable, whereas in humans the tumors are often at a much more advanced stage before therapy is started. Because now the tumors are small and not well-evolved yet, treatment is relatively easy at this time.

Imaging tools

Since cancer cells evolve during their relentless cycles of mutation and selection, anti-tumor therapies are most effective when a tumor is detected early after its initiation. For this early detection, imaging of tumor biomarkers is indispensable in current clinical oncology practice. Biomarkers are defined as 'characteristics that are objectively measured and evaluated as in indicators of normal biological processes, pathological processes or pharmaceutical responses to a therapeutic intervention' [501]. In contrast to previous definitions, these markers are not limited to biological molecules, as the FDA-NIH Biomarker Working Group explicitly states that 'molecular, histologic, radiographic, or physiologic characteristics are types of biomarkers' [502]. Imaging biomarkers are important to test hypotheses *in vitro* and on tissues; but their real value is in imaging of whole organisms during *in vivo* research and subsequently in early phase clinical trials [503].

Grading of brain tumors is mainly based on histological characteristics such as the presence of mitotic activity, nuclear atypia, microvascular, proliferation, and coagulation or pseudopalisading necrosis. All these observations are done *ex vivo* on tissue pieces or biopsies, as microscopical evaluation in living tissues is still at its infancy. In humans, intravital microscopy is feasible in only superficial tissues, as demonstrated by confocal endomicroscopy [504], in which microscopy is combined with colonoscopy. Intravital imaging has also been demonstrated on *in vivo* cleared skin tissues. These skin tissues were made somewhat transparent with the use of hyperosmotic agents [505,506]. For brain imaging, intravital imaging through a cranial window is feasible in preclinical animal research [128,507] and techniques to visualize unstained tissues with the use of second and third harmonic signaling are being explored for utilization in clinical practice [120]. Although microscopical techniques have their specific advantages, especially with respect to resolution, the availability of many specific stainings, and the cultivated histopathological knowledge, a major disadvantage of all these techniques is that only small fields of view or thin histological slides can be imaged. Imaging of optical cleared tissues allows imaging of larger tissues and is not restricted to 5 - 10 µm slides as commonly used for diagnosis by a pathologist. We employed these optically clearing techniques to visualize the tumor micro-environment and the topological orientation of tumor cells relative to the vasculature **(Chapter 7).**

A wide variety of preclinical imaging tools are available to detect a tumor, to monitor tumor growth, and to get insight in the processes involved in tumor progression. Obviously, mice are much smaller than men. This implicates that preclinical imaging equipment needs high-resolution to detect alterations in mice. For preclinical PET-scanners, a three-fold reduction of the spatial resolution was obtained as compared to clinical scanners. But this improvement is still insufficient to reach an equal sampling size as in humans, because a mouse brain is approximately 3000 times smaller than a human. Many of these imaging techniques which are used for preclinical research, such as PET, CT, and MRI, have proven their use in clinical practice, which simplifies translation of preclinically obtained results to the clinic. Others, like bioluminescent imaging and 3D-microscopy are still limited to preclinical research. In preclinical research, bioluminescent imaging is a valuable tool to establish the engraftment of tumor cells, tumor progression and the formation of distant metastasis. While bioluminescence imaging is widely used in a laboratory setting, the challenge to translate this imaging technique to the clinic is still unattainable due to the potential toxicity of luciferin as well as the potential immunogenicity of luciferases [508].

FUTURE DIRECTIONS

Early detection of cancer will save lives. By the time symptoms appear, cancer might already have spread and evolved, thus complicating effective treatment. Imaging remains a powerful, non-invasive tool to positively impact the management of patients with a brain tumor. Detection of the tumor is often dependent on imaging tools such as MR and CT. For some brain tumors, such as DIPG, even the diagnosis could be solely based on these imaging methods. But these conventional imaging methods are not very sensitive and have significant limitations in assessing treatment response and monitoring of disease progression. Both 'pseudoprogression' after chemoradiation and 'pseudoresponse' after anti-angiogenesis treatments are well-known radiological entities which are difficult to dissect from actual tumor progression [509]. Liquid biopsies could be a way to detect tumors even before a patient has symptoms. Techniques which enable these screening methods include the detection of circulating tumor cells, circulating biomarkers, or profiling of tumor-educated platelets [481,510–514]. Furthermore, these techniques might provide molecular subtyping of the tumor, thus allowing a personalized based targeted therapy.

Nowadays cancer treatment is not limited to chemotherapy and radiation, but also immunotherapy plays a limited, but increasingly important role in treatment of cancer. Cancer immunotherapies make use of the body's own immune system to attack and remove the cancer cells as it is based on stimulation of the body's own immune system in order to amplify both a humoral and cytotoxic immune response to target tumor cells [515]. Immunotherapies for brain cancer include the use of cancer vaccines, where tumor-associated antigens are used to elicit an immune response to attack cancer cells with these antigens [516–519]; skewing the immune response from tumor promoting to antitumoral, for example with anti-PD-1 and anti-CTLA-4 antibodies [520–522]; therapy with oncolytic viruses to cause lysis of the tumor cells and consequently generate an immune response against this cancer [523–525]; adoptive cell therapy where immune cells from the patient are activated or modified *in vitro* and re-injected into the patient to result in an anti-cancer response [526–531]; adjuvant immunotherapies and monoclonal antibodies [532].

Initially immunotherapy was not considered to be an option for brain cancer due to the BBB as well as the absence of the conventional lymphatic drainage system [533]. However, these opinions changed after demonstration that active immunotherapy with autologous dendritic cells (DCs) loaded with autologous tumor cells or lysates did improve median overall survival for both recurrent- and newly diagnosed GBM patients as compared to non-DC treated GBM patients [527]. Novel approaches, specifically aimed at the treatment of brain cancer are to adapt the innate immunity-mediated inflammation by depletion of tumor associated

microglia/macrophages (TAMs). TAMs are tumor promoting and can form up to 30% of the tumor mass in GBM. Moreover, TAMs can inhibit adaptive anti-tumor responses by the expression of cytokines and certain receptors. Targeting the CSF-1 receptor (CSF-1R) results both in removal of TAMs and skewing of TAMs to elicit an anti-tumor response [76,80,534].

As stated before, immunosuppressive checkpoints, including IDO, CTLA-4 and PD1/PDL1, have critical roles in tumor progression. Unfortunately, the efficacy of immune-checkpoint inhibitors is still limited for the treatment of brain tumors. This is illustrated by the treatment with nivolumab, an anti-PD-1 monoclonal antibody. Although this offers a superior survival benefit over docetaxel treatment in patients with non-small-cell lung cancer (NSCLC), the effect of nivolumab on brain tumor metastasis is limited.
Although the promising results and ongoing trials with CED [535], other approaches to pass the BBB are being explored. One of such approaches is the use of targeted ultrasound together with microbubbles [59–61]. The high energetic movement of the microbubbles results in a temporary opening of the BBB, thus allowing systemically administered therapeutics to enter the brain and exerts their effects onto the tumor cells. The main advantage of this ultrasound technique as compared to CED is the lack of invasive placement of catheters. However, due to the systemic administration of the compound, relatively high systemic concentrations of the therapeutic are needed, thus limiting the use of this technique to compounds with low systemic toxicity.

The procedures described in this thesis could be employed to improve the efficacy of these immune-checkpoint inhibitor treatments. CED could be a way to pass the BBB; PET-imaging to visualize the uptake of the compound in the brain tumor; 3D imaging to analyze changes in the tumor micro-environment and a change in the immune cell composition. The described techniques are not only useful to study brain tumors, but could also be extended to other tumor types as we have shown for the preclinically visualization and quantification of tumor progression in xenograft models of pancreatic ductal adenocarcinoma (PDAC), osteosarcoma, and prostate cancer [340,467,536].

Concluding remarks

Despite continuing advances in radiation therapy, neurosurgical techniques and chemotherapies, prognosis of high-grade primary brain tumor patients remains poor. In this thesis, we show the feasibility of CED to deliver pharmaceutical compounds into the brain, the use of a radiosensitizer to limit the radiation dose in pediatric patients and a novel target to inhibit the interaction of EVs with tumor cells. Furthermore, PET-imaging revealed that bevacizumab, an antibody against VEGF, does not reach its target within the brain. Finally, we have used 3D-microscopical techniques to visualize the topological orientation of tumor

cells and the brain vasculature. These insights and techniques could be a start of many new research projects, aiming at the improvement of brain tumor patients.

CHAPTER 9 |

SUMMARY

SUMMARY

In the human brain, a wide variety of primary tumors can be encountered, both in adults and in children. Due the infiltrative growth pattern of many of these tumors, complete surgical resection is often impossible. Furthermore, eradication of tumor cells by chemotherapy and radiotherapy without damaging the surrounding brain parenchyma is difficult to achieve, and these therapies often result in severe treatment-related side effects. The main obstacles which impair treatment efficacy in these patients are the presence of the blood-brain-barrier (BBB), which prevents drugs to reach clinically-effective concentrations at the tumor location, and the resistance to therapy. In this thesis, we aim to evaluate novel therapeutic strategies to improve the treatment of high grade brain tumors. We explored the use of convection-enhanced delivery (CED) to circumvent the BBB, the use of radiosensitizers to improve radiotherapy and the use of CCR8 inhibition to prevent therapy resistance. Furthermore, we employed a wide range of preclinical imaging techniques to monitor tumor progression.

In chapter 2 we developed a method to perform CED into the murine brainstem, and to test this method using the chemotherapeutic agent carmustine. We designed a stepped CED-catheter for the delivery of compounds into the brainstem of mice. This CED-catheter was used to treat mice with VUMC-DIPG-3 and E98FM brainstem tumors. Administration of the vehicle solutions (5% dextrose water, *or* 10% ethanol) into the brainstem was well tolerated. CED of carmustine increased median survival of the tumor bearing mice.

Chapter 3 describes the use of this CED method for local delivery of the anthracycline doxorubicin to treat pediatric DIPG and thalamic high-grade gliomas. First, the sensitivity of the tumor cells to a panel of anthracyclines was tested *in vitro*. From this panel, doxorubicin was selected for further evaluation. Doxorubicin was formulated either as free doxorubicin (i.e. dissolved directly in the vehicle solution) or in PEGylated liposomes (PEGylated liposomal doxorubicin, PLD). The maximum tolerated dose of these compounds into the thalamus was 10-times higher as compared to delivery into the brainstem. Local delivery of both doxorubicin formulations into the brainstem caused severe toxicity, even at concentrations which were safe when administered into the thalamus.

In chapter 4, we show by PET-imaging and distribution studies in orthotopically (intracranial) and heterotopic (subcutaneous) DIPG and high-grade glioma animal models that VEGF expression is dependent on the tumor microenvironment. Tumor cells were injected into different locations, and tumor progression was monitored by bioluminescence imaging and MRI. Although the tumors which were placed subcutaneously showed high accumulation of

^{89}Zr-bevacizumab, an antibody against VEGF, no accumulation of ^{89}Zr-bevacizumab was observed in any of the orthotopically located tumors. *In situ* hybridization demonstrated the presence of VEGF in the perinecrotic regions of subcutaneous E98-FM tumors whereas the VEGF-expression in the intracranial tumors was below detection limit.

In **chapter 5**, screening of a library of small-molecule compounds identified the flavonoid quercetin as a radiosensitizer. Radiosensitizing effects were confirmed on medulloblastoma cell lines D283 and D458. Quercetin was shown to sensitize these cells to radiation at low micromolar concentrations. Moreover, quercetin did not affect proliferation of normal human fibroblasts or neural precursor cells. In an orthotopic xenograft model for medulloblastoma, we confirmed that administration of quercetin around the time of radiation increases the radiation efficacy and increased survival of the tumor bearing mice.

Chapter 6 focuses on the role of extracellular vesicles (EVs). We show that glioblastoma EVs are transferred to recipient tumor cells and can promote tumor progression and resistance to the alkylating agent temozolomide (TMZ). Through RNAi screening, we identified that chemokine receptor CCR8 is involved in EV interaction. We discovered a novel EV-uptake mechanism which involves a triple interaction between the chemokine receptor CCR8 on the cell, glycans exposed on EVs and the soluble ligand CCL18. We demonstrate that EV-induced phenotypes are neutralized by the R243, a small-molecule inhibitor of CCR8. Administration of this compound R243 in combination with TMZ, to mice with orthotopically transplanted glioblastoma, prolongs progression-free survival and prevents TMZ resistance.

In **chapter 7,** we describe the use of optically-cleared, transparent tissues to study the topographical relationship between GBM cells and their microenvironment. We present a workflow for *ex vivo* imaging of optically-cleared brain tumor tissues, and subsequent computational modeling. This workflow was used for quantification of the microvasculature in relation to tumor-cell location in infiltrative GBM models. The detailed 3D-visualization revealed differences of organization of tumor cells relative to the vasculature between grey- and white matter regions. We identified GBM cells co-opting the brain vasculature, cells invading along white matter tracts, and groups of infiltrative, interconnected GBM cells.

In **chapter 8,** we discuss the results of these studies and the relevance of the use of preclinical animal models and imaging techniques in the field of brain tumor research. The insights and techniques described in this thesis could be a start of many new research projects, aiming at the improved treatment of brain tumor patients.

CHAPTER 10 |

SAMENVATTING

SAMENVATTING

Er zijn vele vormen van kwaadaardige hersentumoren, zowel bij volwassenen als ook bij kinderen. Deze tumoren zijn vaak slecht te behandelen, onder andere omdat de tumorcellen de hersenen infiltreren. Hierdoor zijn ze onbereikbaar voor de chirurg waardoor er na een operatie altijd tumorcellen achterblijven. Om deze achtergebleven tumorcellen te verwijderen, kan er gebruik gemaakt worden van chemotherapie en bestraling. Deze therapieën beschadigen echter ook vaak het omliggende hersenweefsel. Met name bij jonge kinderen kan bestraling daarom niet worden toegepast. Maar ook bij volwassenen zijn de behandelingsmethoden niet efficiënt en leiden ze vaak tot ernstige bijwerkingen. Eén van de factoren die de behandeling van hersentumoren bemoeilijkt, is de aanwezigheid van de bloed-hersen-barrière. Deze barrière voorkomt normaal gesproken dat schadelijke stoffen de hersenen bereiken. Bij de behandeling van hersentumoren voorkomen ze echter ook dat de geneesmiddelen de tumor bereiken. Hierdoor zijn hersentumoren vaak niet gevoelig voor behandeling met geneesmiddelen die wel bij andere tumoren effectief zijn gebleken.

In dit proefschrift testen we de mogelijkheid van 'convection-enhanced delivery' (CED) om geneesmiddelen toch bij de tumor te krijgen. CED wil zeggen dat je onder een lichte druk, het geneesmiddel direct in het tumorgebied injecteert. Met deze techniek hoeft het geneesmiddel dus niet in staat te zijn om zelfstandig over de bloed-hersen-barrière te gaan, maar wordt het geneesmiddel direct op de juiste locatie geïnjecteerd. Door deze manier van toedienen zijn de bijwerkingen vaak minder dan wanneer het geneesmiddelen via een infuus of als pil wordt toegediend.

Verder wordt in dit proefschrift een methode beschreven om de effecten van bestraling te versterken en we beschrijven hoe we een nieuw principe hebben gevonden dat we kunnen gebruiken om te voorkomen dat een tumor ongevoelig wordt voor behandeling met chemotherapeutica.

Voor al deze onderzoeken hebben we gebruik gemaakt van proefdiermodellen. Om te kunnen vaststellen of de therapie effectief was, hebben we gebruik gemaakt van beeldvormende technieken zoals bioluminescentie (waarbij we cellen voorzien hebben van een enzym uit een vuurvliegje zodat de tumor licht geeft), MRI, PET (injectie van radio-actieve signaalstoffen) en geavanceerde microscopische technieken.

In hoofdstuk 2 beschrijven we de techniek om CED in de hersenstam van de muis te kunnen uitvoeren. Omdat deze hersenstam heel klein is, hebben we zelf een CED-catheter ontwikkeld. Deze catheter hebben we vervolgens gebruikt om de chemotherapie,

carmustine, toe te dienen in de hersenstamtumor. Eerst hebben we bepaald of de techniek veilig was. Dit hebben we gedaan door alleen het oplosmiddel toe te dienen. Nadat dit veilig was gebleken hebben we vervolgens carmustine toegediend. Het bleek dat dieren die met de CED-methode met carmustine waren behandeld langer in leven bleven dan de dieren die alleen het oplosmiddel toegediend hadden gekregen.

Hoofdstuk 3 beschrijft vervolgens het gebruik van dezelfde CED-techniek om een ander geneesmiddel toe te dienen. In dit hoofdstuk wordt bepaald of de toediening van doxorubicine effectief is voor de behandeling van twee verschillende soorten hersentumoren die veel bij kinderen voorkomen, namelijk diffuus intrinsiek pons glioom (DIPG) welke in de hersenstam ontstaat en hoog-gradige gliomen (hGG) welke in de grote hersenen ontstaan. Eerst hebben we met behulp van een panel van geneesmiddelen bepaald voor welke behandelingen deze tumorcellen gevoelig zijn. Doxorubicine kwam uit deze testen naar voren als een geschikt geneesmiddel voor deze vormen van kanker. Doxorubicine kan toegediend worden als 'vrij-doxorubicine' -direct opgelost in het oplosmiddel- of in 'PEGylated liposomes' -hierbij zit het doxorubicine verpakt in liposomen, een soort kleine blaasjes. We toonden aan dat beide toedieningsvormen van doxorubicine zeer schadelijk waren wanneer het middel toegediend werd in de hersenstam. Wanneer dezelfde middelen werden toegediend in de grote hersenen, waren de bijwerkingen milder. Hierdoor kon er in de grote hersenen een 10x hogere dosis worden toegediend. Door deze schadelijke bijwerkingen was de effectiviteit van doxorubicine afwezig in de hersenstamtumoren en waren de gunstige effecten in hGG-tumoren in de grote hersenen zeer beperkt.

In hoofdstuk 4 beschrijven we het gebruik van een PET-scan. Dit is een positron emitting tomography; je kunt hiermee zien waar een radioactieve signaalstof aanwezig is. We hebben deze techniek gebruikt om vast te stellen of bevacizumab, een geneesmiddel gericht tegen VEGF -een signaalstof waarmee de tumor zorgt dat er nieuwe bloedvaten worden gevormd-, aankomt bij de tumorcellen. We konden vaststellen dat de hoeveelheid VEGF die tumorcellen produceren afhankelijk is van de locatie waarin deze tumor zich bevindt. Hiervoor hadden we tumorcellen onderhuids geïnjecteerd, of dezelfde tumorcellen in de hersenen. De radioactieve signaalstof, ^{89}Zr-bevacizumab, was aantoonbaar in de onderhuids geïnjecteerde tumoren, maar niet in de tumoren welke in de hersenen zaten. Vervolgens hebben we met een *in situ* hybridisatie techniek vastgesteld dat in de onderhuids geïnjecteerde tumoren het VEGF aanwezig was, maar dat in de tumoren in de hersenen dit VEGF niet geproduceerd werd. In deze experimenten hebben we gebruik gemaakt van diverse beeldvormende technieken zoals MRI om te zien of de bloed-hersen-barrière nog intact was en bioluminescentie om de tumorgroei te kunnen vaststellen.

In hoofdstuk 5 hebben we van 960-verschillende stoffen getest of ze in staat zijn om de effecten van bestraling te versterken. Uit deze testen kwam de stof quercetine naar voren als een effective 'radiosensitizer'. Dit 'radiosensitizerende' effect werd bevestigd in een aantal andere cellijnen voor een kinderhersentumor: medulloblastoma cellijnen D283 en D458. Het bleek dat quercetine al in zeer lage concentraties in staat was om de cellen te sensitiseren voor bestraling. Bovendien bleek dat quercetine geen invloed had op de celdeling van normale humane fibroblast cellen of neurale precursor cellen. Met behulp van een proefdiermodel, waarbij we menselijke medulloblastome tumorcellen in de hersenen van een muis hadden geïnjecteerd, hebben we vervolgens vastgesteld dat wanneer je quercetine toedient rondom het moment van bestraling, dit een versterking van het bestralingseffect geeft en de dieren langer blijven leven dan een controle groep die geen quercetine heeft gehad.

Hoofdstuk 6 behandelt de rol van 'extracellular vesicles' (EVs). EVs zijn kleine blaasjes die door alle cellen worden uitgescheiden. Eerst tonen we aan dat glioblastoma EVs van de ene cel, kunnen worden opgenomen door een andere cel. Deze opname van EVs zorgt voor een toename van het aantal tumorcellen en dat de tumorcellen minder gevoelig worden voor behandeling met temozolomide chemotherapie. Vervolgens hebben we een RNAi screenings techniek gebruikt om te bepalen via welke receptoren de tumorcellen EVs kunnen binden. Uit deze screenings techniek kwam het chemokine CCR8 naar voren als een effectieve receptor voor EVs. We hebben vastgesteld dat deze binding van EVs verloopt via een drie-staps interactie tussen het CCR8 op de tumorcellen, glycanen op de EVs en het chemokine CCL18 wat uitgescheiden wordt door de tumorcellen en hun omgeving. Deze interactie kan worden geremd met een stof genaamd R243. Dit is een 'small-molecule inhibitor' van CCR8. Wanneer we R243 toedienden in combinatie met temozolomide in een muismodel werd voorkomen dat de tumor ongevoelig werd voor temozolomide behandeling en leefden de dieren langer dan wanneer ze maar één van de middelen toegediend kregen.

In hoofdstuk 7 beschrijven we het gebruik van doorzichtig weefsel om de topografische relatie tussen tumorcellen en hun omgeving te bestuderen. We presenteren eerst een schema waarbij we weefsels doorzichtig kunnen maken, structuren kunnen bestuderen met behulp van geavanceerde microscopische technieken en de verschillende structuren kunnen detecteren met behulp van computermodellen. Deze proefopzet hebben we gebruikt om de afstand tussen tumorcellen en bloedvaten te kunnen meten in verschillende delen van de hersenen, namelijk de witte- en de grijze stof gebieden. Ook hebben we met deze techniek kunnen bevestigen dat glioblastoma tumorcellen voor hun migratie door de hersenen gebruik maken van de bloedvaten en de witte stof banen. Ook hebben we waargenomen dat er groepen van onderling met elkaar verbonden glioblastoma cellen aanwezig zijn.

In hoofdstuk 8 bespreken we de resultaten van de studies uit dit proefschrift en de relevantie van proefdiermodellen en beeldvormende technieken in het veld van hersentumor onderzoek. De verkregen inzichten en technieken vormen een mooi startpunt voor nieuwe onderzoeksprojecten gericht op de verbetering van de behandeling van hersentumor patiënten.

.

CHAPTER 11 |

REFERENCES

1. Louis DN, Ohgaki H, Wiestler OD, et al. The 2007 WHO classification of tumours of the central nervous system. *Acta Neuropathol.* 2007;114(2):97-109. doi:10.1007/s00401-007-0243-4.
2. McLendon R, Friedman A, Bigner D, et al. Comprehensive genomic characterization defines human glioblastoma genes and core pathways. *Nature* 2008;455(7216):1061-8. doi:10.1038/nature07385.
3. Verhaak RGW, Hoadley KA, Purdom E, et al. Integrated genomic analysis identifies clinically relevant subtypes of glioblastoma characterized by abnormalities in PDGFRA, IDH1, EGFR, and NF1. *Cancer Cell* 2010;17(1):98-110. doi:10.1016/j.ccr.2009.12.020.
4. Sturm D, Witt H, Hovestadt V, et al. Hotspot mutations in H3F3A and IDH1 define distinct epigenetic and biological subgroups of glioblastoma. *Cancer Cell* 2012;22(4):425-37. doi:10.1016/j.ccr.2012.08.024.
5. Sturm D, Bender S, Jones DTW, et al. Paediatric and adult glioblastoma: multiform (epi)genomic culprits emerge. *Nat. Rev. Cancer* 2014;14(2):92-107. doi:10.1038/nrc3655.
6. Schwartzentruber J, Korshunov A, Liu X-Y, et al. Driver mutations in histone H3.3 and chromatin remodelling genes in paediatric glioblastoma. *Nature* 2012;482(7384):226-31. doi:10.1038/nature10833.
7. Rushing EJ, Wesseling P. Towards an integrated morphological and molecular WHO diagnosis of central nervous system tumors: a paradigm shift. *Curr. Opin. Neurol.* 2015;28(6):628-32. doi:10.1097/WCO.0000000000000258.
8. Louis DN, Perry A, Reifenberger G, et al. The 2016 World Health Organization Classification of Tumors of the Central Nervous System: a summary. *Acta Neuropathol.* 2016;131(6):803-20. doi:10.1007/s00401-016-1545-1.
9. Northcott PA, Shih DJH, Peacock J, et al. Subgroup-specific structural variation across 1,000 medulloblastoma genomes. *Nature* 2012;488(7409):49-56. doi:10.1038/nature11327.
10. Taylor MD, Northcott PA, Korshunov A, et al. Molecular subgroups of medulloblastoma: The current consensus. *Acta Neuropathol.* 2012;123(4):465-472. doi:10.1007/s00401-011-0922-z.
11. Inda M, Bonavia R, Mukasa A, et al. Tumor heterogeneity is an active process maintained by a mutant EGFR-induced cytokine circuit in glioblastoma. 2010:1731-1745. doi:10.1101/gad.1890510.themselves.
12. Sottoriva A, Spiteri I, Piccirillo SGM, et al. Intratumor heterogeneity in human glioblastoma reflects cancer evolutionary dynamics. *Proc. Natl. Acad. Sci. U. S. A.* 2013;110(10). doi:10.1073/pnas.1219747110.
13. Singh AK, Arya RK, Maheshwari S, et al. Tumor heterogeneity and cancer stem cell paradigm: Updates in concept, controversies and clinical relevance. *Int. J. Cancer* 2015;136(9):1991-2000. doi:10.1002/ijc.28804.
14. Ostrom QT, Gittleman H, Xu J, et al. CBTRUS statistical report: Primary brain and other central nervous system tumors diagnosed in the United States in 2009-2013. *Neuro. Oncol.* 2016;18(suppl_5):v1-v75. doi:10.1093/neuonc/now207.
15. Merchant TE, Pollack IF, Loeffler JS. Brain Tumors Across the Age Spectrum: Biology, Therapy, and Late Effects. *Semin. Radiat. Oncol.* 2010;20(1):58-66. doi:10.1016/j.semradonc.2009.09.005.
16. Silber JH, Radcliffe J, Peckham V, et al. Whole-brain irradiation and decline in intelligence: the influence of dose and age on IQ score. *J. Clin. Oncol.* 1992;10(9):1390-6.
17. Ris MD, Packer R, Goldwein J, Jones-Wallace D, Boyett JM. Intellectual outcome after reduced-dose radiation therapy plus adjuvant chemotherapy for medulloblastoma: a Children's Cancer Group study. *J. Clin. Oncol.* 2001;19(15):3470-6.
18. Palmer SL, Reddick WE, Gajjar A. Understanding the cognitive impact on children who are treated for medulloblastoma. *J. Pediatr. Psychol.* 2007;32(9):1040-9. doi:10.1093/jpepsy/jsl056.
19. Kallappagoudar S, Yadav RK, Lowe BR, Partridge JF. Histone H3 mutations--a special role for H3.3 in tumorigenesis? *Chromosoma* 2015;124(2):177-89. doi:10.1007/s00412-015-0510-4.
20. Veldhuijzen van Zanten SEM, Jansen MHA, Sanchez Aliaga E, van Vuurden DG, Vandertop WP, Kaspers GJL. A twenty-year review of diagnosing and treating children with diffuse intrinsic pontine glioma in The Netherlands. *Expert Rev. Anticancer Ther.* 2015;15(2):157-64. doi:10.1586/14737140.2015.974563.
21. Donaldson SS, Laningham F, Fisher PG. Advances toward an understanding of brainstem gliomas. *J. Clin. Oncol.* 2006;24(8):1266-72. doi:10.1200/JCO.2005.04.6599.
22. Hargrave D, Chuang N, Bouffet E. Conventional MRI cannot predict survival in childhood diffuse intrinsic pontine glioma. *J. Neurooncol.* 2008;86(3):313-319. doi:10.1007/s11060-007-9473-5.
23. Wu G, Broniscer A, McEachron TA, et al. Somatic histone H3 alterations in pediatric diffuse intrinsic pontine gliomas and non-brainstem glioblastomas. *Nat. Genet.* 2012;44(3):251-3. doi:10.1038/ng.1102.
24. Grasso CS, Tang Y, Truffaux N, et al. Functionally defined therapeutic targets in diffuse intrinsic pontine glioma. *Nat. Med.* 2015;21(6):555-9. doi:10.1038/nm.3855.

25. Castel D, Philippe C, Calmon R, et al. Histone H3F3A and HIST1H3B K27M mutations define two subgroups of diffuse intrinsic pontine gliomas with different prognosis and phenotypes. *Acta Neuropathol.* 2015;130(6):815-827. doi:10.1007/s00401-015-1478-0.
26. Ramaswamy V, Remke M, Bouffet E, et al. Risk stratification of childhood medulloblastoma in the molecular era: the current consensus. *Acta Neuropathol.* 2016;131(6):821-31. doi:10.1007/s00401-016-1569-6.
27. Pizer B, Clifford S. Medulloblastoma: new insights into biology and treatment. *Arch. Dis. Child. Educ. Pract. Ed.* 2008;93(5):137-44. doi:10.1136/adc.2007.136655.
28. Tamayo-Orrego L, Swikert SM, Charron F. Evasion of cell senescence in SHH medulloblastoma. *Cell Cycle* 2016:1-6. doi:10.1080/15384101.2016.1189044.
29. de Haas T, Hasselt N, Troost D, et al. Molecular Risk Stratification of Medulloblastoma Patients Based on Immunohistochemical Analysis of MYC, LDHB, and CCNB1 Expression. *Clin. Cancer Res.* 2008;14(13):4154-4160. doi:10.1158/1078-0432.CCR-07-4159.
30. Kool M, Korshunov A, Remke M, et al. Molecular subgroups of medulloblastoma: an international meta-analysis of transcriptome, genetic aberrations, and clinical data of WNT, SHH, Group 3, and Group 4 medulloblastomas. *Acta Neuropathol.* 2012;123(4):473-84. doi:10.1007/s00401-012-0958-8.
31. Gottardo NG, Gajjar A. Chemotherapy for malignant brain tumors of childhood. *J. Child Neurol.* 2008;23(10):1149-59. doi:10.1177/0883073808321765.
32. Lafay-Cousin L, Smith A, Chi SN, et al. Clinical, Pathological, and Molecular Characterization of Infant Medulloblastomas Treated with Sequential High-Dose Chemotherapy. *Pediatr. Blood Cancer* 2016;63(9):1527-34. doi:10.1002/pbc.26042.
33. Palmer SL, Goloubeva O, Reddick WE, et al. Patterns of intellectual development among survivors of pediatric medulloblastoma: a longitudinal analysis. *J. Clin. Oncol.* 2001;19(8):2302-8.
34. Mueller S, Chang S. Pediatric brain tumors: current treatment strategies and future therapeutic approaches. *Neurotherapeutics* 2009;6(3):570-86. doi:10.1016/j.nurt.2009.04.006.
35. von Bueren AO, von Hoff K, Pietsch T, et al. Treatment of young children with localized medulloblastoma by chemotherapy alone: results of the prospective, multicenter trial HIT 2000 confirming the prognostic impact of histology. *Neuro. Oncol.* 2011;13(6):669-79. doi:10.1093/neuonc/nor025.
36. Chang JE, Khuntia D, Robins HI, Mehta MP. Radiotherapy and radiosensitizers in the treatment of glioblastoma multiforme. *Clin. Adv. Hematol. Oncol.* 2007;5(11):894-915.
37. Lin C, Yu Y, Zhao H-G, Yang A, Yan H, Cui Y. Combination of quercetin with radiotherapy enhances tumor radiosensitivity in vitro and in vivo. *Radiother. Oncol.* 2012;104(3):395-400. doi:10.1016/j.radonc.2011.10.023.
38. Caretti V, Hiddingh L, Lagerweij T, et al. WEE1 kinase inhibition enhances the radiation response of diffuse intrinsic pontine gliomas. *Mol. Cancer Ther.* 2013;12(2):141-50. doi:10.1158/1535-7163.MCT-12-0735.
39. Markowitz D, Powell C, Tran NL, et al. Pharmacological inhibition of the protein kinase MRK/ZAK radiosensitizes medulloblastoma. *Mol. Cancer Ther.* 2016. doi:10.1158/1535-7163.MCT-15-0849.
40. Kleihues P, Burger PC, Scheithauer BW. The New WHO Classification of Brain Tumours. *Brain Pathol.* 1993;3(3):255-268. doi:10.1111/j.1750-3639.1993.tb00752.x.
41. Li B, Senbabaoglu Y, Peng W, Yang M-L, Xu J, Li JZ. Genomic estimates of aneuploid content in glioblastoma multiforme and improved classification. *Clin. Cancer Res.* 2012;18(20):5595-605. doi:10.1158/1078-0432.CCR-12-1427.
42. Mizoguchi M, Yoshimoto K, Ma X, et al. Molecular characteristics of glioblastoma with 1p/19q co-deletion. *Brain Tumor Pathol.* 2012;29(3):148-53. doi:10.1007/s10014-012-0107-z.
43. Leone PE, González MB, Elosua C, et al. Integration of global spectral karyotyping, CGH arrays, and expression arrays reveals important genes in the pathogenesis of glioblastoma multiforme. *Ann. Surg. Oncol.* 2012;19(7):2367-79. doi:10.1245/s10434-011-2202-5.
44. Li L, Chakraborty S, Yang C-R, et al. An EGFR wild type-EGFRvIII-HB-EGF feed-forward loop regulates the activation of EGFRvIII. *Oncogene* 2014;33(33):4253-64. doi:10.1038/onc.2013.400.
45. Montano N, Cenci T, Martini M, et al. Expression of EGFRvIII in glioblastoma: prognostic significance revisited. *Neoplasia* 2011;13(12):1113-21.
46. Eskilsson E, Rosland G V, Talasila KM, et al. EGFRvIII mutations can emerge as late and heterogenous events in glioblastoma development and promote angiogenesis through Src activation. *Neuro. Oncol.* 2016. doi:10.1093/neuonc/now113.
47. Adamson C, Kanu OO, Mehta AI, et al. Glioblastoma multiforme: a review of where we have been and where we are going. *Expert Opin. Investig. Drugs* 2009;18(8):1061-83. doi:10.1517/13543780903052764.

48. Stupp R, Taillibert S, Kanner AA, et al. Maintenance Therapy With Tumor-Treating Fields Plus Temozolomide vs Temozolomide Alone for Glioblastoma. *JAMA* 2015;314(23):2535. doi:10.1001/jama.2015.16669.
49. Stupp R, Mason WP, van den Bent MJ, et al. Radiotherapy plus concomitant and adjuvant temozolomide for glioblastoma. *N. Engl. J. Med.* 2005;352(10):987-96. doi:10.1056/NEJMoa043330.
50. Hegi ME, Diserens A-C, Gorlia T, et al. MGMT gene silencing and benefit from temozolomide in glioblastoma. *N. Engl. J. Med.* 2005;352(10):997-1003. doi:10.1056/NEJMoa043331.
51. Cominelli M, Grisanti S, Mazzoleni S, et al. EGFR amplified and overexpressing glioblastomas and association with better response to adjuvant metronomic temozolomide. *J. Natl. Cancer Inst.* 2015;107(5). doi:10.1093/jnci/djv041.
52. Yin D, Forsayeth J, Bankiewicz KS. Optimized cannula design and placement for convection-enhanced delivery in rat striatum. *J. Neurosci. Methods* 2010;187(1):46-51. doi:10.1016/j.jneumeth.2009.12.008.
53. Lonser RR, Warren KE, Butman JA, et al. Real-time image-guided direct convective perfusion of intrinsic brainstem lesions. Technical note. *J. Neurosurg.* 2007;107(1):190-7. doi:10.3171/JNS-07/07/0190.
54. Chen X, Astary GW, Sepulveda H, Mareci TH, Sarntinoranont M. Quantitative assessment of macromolecular concentration during direct infusion into an agarose hydrogel phantom using contrast-enhanced MRI. *Magn. Reson. Imaging* 2008;26(10):1433-41. doi:10.1016/j.mri.2008.04.011.
55. Sugiyama S, Yamashita Y, Kikuchi T, Saito R, Kumabe T, Tominaga T. Safety and efficacy of convection-enhanced delivery of ACNU, a hydrophilic nitrosourea, in intracranial brain tumor models. *J. Neurooncol.* 2007;82(1):41-7. doi:10.1007/s11060-006-9247-5.
56. Rip J, Chen L, Hartman R, et al. Glutathione PEGylated liposomes: pharmacokinetics and delivery of cargo across the blood-brain barrier in rats. *J. Drug Target.* 2014;22(5):460-7. doi:10.3109/1061186X.2014.888070.
57. Kang Y-S, Jung H-J, Oh J-S, Song D-Y. Use of PEGylated Immunoliposomes to Deliver Dopamine Across the Blood-Brain Barrier in a Rat Model of Parkinson's Disease. *CNS Neurosci. Ther.* 2016;22(10):817-23. doi:10.1111/cns.12580.
58. Fu H, McCarty DM. Crossing the blood-brain-barrier with viral vectors. *Curr. Opin. Virol.* 2016;21:87-92. doi:10.1016/j.coviro.2016.08.006.
59. Shen Y, Guo J, Chen G, et al. Delivery of Liposomes with Different Sizes to Mice Brain after Sonication by Focused Ultrasound in the Presence of Microbubbles. *Ultrasound Med. Biol.* 2016;42(7):1499-511. doi:10.1016/j.ultrasmedbio.2016.01.019.
60. Sheikov N, McDannold N, Vykhodtseva N, Jolesz F, Hynynen K. Cellular mechanisms of the blood-brain barrier opening induced by ultrasound in presence of microbubbles. *Ultrasound Med. Biol.* 2004;30(7):979-89. doi:10.1016/j.ultrasmedbio.2004.04.010.
61. Alonso A. Ultrasound-induced blood-brain barrier opening for drug delivery. *Front. Neurol. Neurosci.* 2015;36:106-115. doi:10.1159/000366242.
62. Connell JJ, Chatain G, Cornelissen B, et al. Selective permeabilization of the blood-brain barrier at sites of metastasis. *J. Natl. Cancer Inst.* 2013;105(21):1634-43. doi:10.1093/jnci/djt276.
63. Van Tellingen O, Yetkin-Arik B, De Gooijer MC, Wesseling P, Wurdinger T, De Vries HE. Overcoming the blood-brain tumor barrier for effective glioblastoma treatment. *Drug Resist. Updat.* 2015;19:1-12. doi:10.1016/j.drup.2015.02.002.
64. Hanahan D, Weinberg RA. Hallmarks of cancer: the next generation. *Cell* 2011;144(5):646-74. doi:10.1016/j.cell.2011.02.013.
65. Vander Heiden MG, Cantley LC, Thompson CB. Understanding the Warburg effect: the metabolic requirements of cell proliferation. *Science* 2009;324(5930):1029-33. doi:10.1126/science.1160809.
66. Leenders WPJ, Küsters B, de Waal RMW. Vessel co-option: how tumors obtain blood supply in the absence of sprouting angiogenesis. *Endothelium* 2002;9(2):83-87. doi:10.1080/10623320290016537.
67. Lu K V, Chang JP, Parachoniak CA, et al. VEGF inhibits tumor cell invasion and mesenchymal transition through a MET/VEGFR2 complex. *Cancer Cell* 2012;22(1):21-35. doi:10.1016/j.ccr.2012.05.037.
68. Miletic H, Niclou SP, Johansson M, Bjerkvig R. Anti-VEGF therapies for malignant glioma: treatment effects and escape mechanisms. *Expert Opin. Ther. Targets* 2009;13(4):455-68. doi:10.1517/14728220902806444.
69. Ziegler J, Pody R, Coutinho de Souza P, et al. ELTD1, an effective anti-angiogenic target for gliomas: preclinical assessment in mouse GL261 and human G55 xenograft glioma models. *Neuro. Oncol.* 2016:now147. doi:10.1093/neuonc/now147.

70. Phillips HS, Kharbanda S, Chen R, et al. Molecular subclasses of high-grade glioma predict prognosis, delineate a pattern of disease progression, and resemble stages in neurogenesis. *Cancer Cell* 2006;9(3):157-73. doi:10.1016/j.ccr.2006.02.019.
71. Rood BR, Zhang H, Cogen PH. Intercellular heterogeneity of expression of the MGMT DNA repair gene in pediatric medulloblastoma. *Neuro. Oncol.* 2004;6(3):200-7. doi:10.1215/S1152851703000565.
72. Munoz JL, Rodriguez-Cruz V, Greco SJ, Ramkissoon SH, Ligon KL, Rameshwar P. Temozolomide resistance in glioblastoma cells occurs partly through epidermal growth factor receptor-mediated induction of connexin 43. *Cell Death Dis.* 2014;5:e1145. doi:10.1038/cddis.2014.111.
73. Hirata E, Girotti MR, Viros A, et al. Intravital imaging reveals how BRAF inhibition generates drug-tolerant microenvironments with high integrin β1/FAK signaling. *Cancer Cell* 2015;27(4):574-88. doi:10.1016/j.ccell.2015.03.008.
74. Inukai M, Toyooka S, Ito S, et al. Presence of epidermal growth factor receptor gene T790M mutation as a minor clone in non-small cell lung cancer. *Cancer Res.* 2006;66(16):7854-8. doi:10.1158/0008-5472.CAN-06-1951.
75. Bodogai M, Moritoh K, Lee-Chang C, et al. Immune suppressive and pro-metastatic functions of myeloid-derived suppressive cells rely upon education from tumor-associated B cells. *Cancer Res.* 2015;75(17):3456-65. doi:10.1158/0008-5472.CAN-14-3077.
76. Pyonteck SM, Akkari L, Schuhmacher AJ, et al. CSF-1R inhibition alters macrophage polarization and blocks glioma progression. *Nat. Med.* 2013;19(10):1264-72. doi:10.1038/nm.3337.
77. Quail DF, Joyce JA. Microenvironmental regulation of tumor progression and metastasis. *Nat. Med.* 2013;19(11):1423-37. doi:10.1038/nm.3394.
78. Zhou W, Ke SQ, Huang Z, et al. Periostin secreted by glioblastoma stem cells recruits M2 tumour-associated macrophages and promotes malignant growth. *Nat. Cell Biol.* 2015;17(November 2014):170-182. doi:10.1038/ncb3090.
79. Hambardzumyan D, Gutmann DH, Kettenmann H. The role of microglia and macrophages in glioma maintenance and progression. *Nat. Neurosci.* 2015;19(1). doi:10.1038/nn.4185.
80. Coniglio SJ, Eugenin E, Dobrenis K, et al. Microglial stimulation of glioblastoma invasion involves epidermal growth factor receptor (EGFR) and colony stimulating factor 1 receptor (CSF-1R) signaling. *Mol. Med.* 2012;18:519-27. doi:10.2119/molmed.2011.00217.
81. Patel MA, Kim JE, Ruzevick J, Li G, Lim M. The future of glioblastoma therapy: synergism of standard of care and immunotherapy. *Cancers (Basel).* 2014;6(4):1953-85. doi:10.3390/cancers6041953.
82. de Jong M, Essers J, van Weerden WM. Imaging preclinical tumour models: improving translational power. *Nat. Rev. Cancer* 2014;14(7):481-93. doi:10.1038/nrc3751.
83. Dickinson PJ, LeCouteur RA, Higgins RJ, et al. Canine spontaneous glioma: A translational model system for convection-enhanced delivery. *Neuro. Oncol.* 2010;12(9):928-940. doi:10.1093/neuonc/noq046.
84. Warnock G, Turtoi A, Blomme A, et al. In vivo PET/CT in a human glioblastoma chicken chorioallantoic membrane model: a new tool for oncology and radiotracer development. *J. Nucl. Med.* 2013;54(10):1782-8. doi:10.2967/jnumed.112.117150.
85. Lokman NA, Elder ASF, Ricciardelli C, Oehler MK. Chick chorioallantoic membrane (CAM) assay as an in vivo model to study the effect of newly identified molecules on ovarian cancer invasion and metastasis. *Int. J. Mol. Sci.* 2012;13(8):9959-70. doi:10.3390/ijms13089959.
86. Fomchenko EI, Holland EC. Mouse models of brain tumors and their applications in preclinical trials. *Clin. Cancer Res.* 2006;12(18):5288-97. doi:10.1158/1078-0432.CCR-06-0438.
87. Lesniak MS. Development of preclinical models for immunogene therapy of brain cancer: it's not monkey business! *Mol. Ther.* 2014;22(2):247-9. doi:10.1038/mt.2013.298.
88. Lee H. Genetically engineered mouse models for drug development and preclinical trials. *Biomol. Ther. (Seoul).* 2014;22(4):267-74. doi:10.4062/biomolther.2014.074.
89. Kucherlapati R. Genetically modified mouse models for biomarker discovery and preclinical drug testing. *Clin. Cancer Res.* 2012;18(3):625-30. doi:10.1158/1078-0432.CCR-11-2021.
90. Anderson A. Oncomouse released. *Nature* 1988;336(6197):300.
91. de Vries NA, Bruggeman SW, Hulsman D, et al. Rapid and Robust Transgenic High-Grade Glioma Mouse Models for Therapy Intervention Studies. *Clin. Cancer Res.* 2010;16(13):3431-3441. doi:10.1158/1078-0432.CCR-09-3414.
92. Sauer B, Henderson N. Site-specific DNA recombination in mammalian cells by the Cre recombinase of bacteriophage P1. *Proc. Natl. Acad. Sci. U. S. A.* 1988;85(14):5166-70.

93. Huijbers IJ, Del Bravo J, Bin Ali R, et al. Using the GEMM-ESC strategy to study gene function in mouse models. *Nat. Protoc.* 2015;10(11):1755-85. doi:10.1038/nprot.2015.114.
94. Ren Y, Qiu L, Lü F, et al. TALENs-directed knockout of the full-length transcription factor Nrf1α that represses malignant behaviour of human hepatocellular carcinoma (HepG2) cells. *Sci. Rep.* 2016;6:23775. doi:10.1038/srep23775.
95. Uhrbom L, Hesselager G, Nister M, Westermark B. Induction of Brain Tumors in Mice Using a Recombinant Platelet-derived Growth Factor B-Chain Retrovirus. *Cancer Res.* 1998;58(23):5275-5279.
96. Barth RF. Rat brain tumor models in experimental neuro-oncology: the 9L, C6, T9, F98, RG2 (D74), RT-2 and CNS-1 gliomas. *J. Neurooncol.* 1998;36(1):91-102.
97. Townsend EC, Murakami MA, Christodoulou A, et al. The Public Repository of Xenografts Enables Discovery and Randomized Phase II-like Trials in Mice. *Cancer Cell* 2016;29(4):574-586. doi:10.1016/j.ccell.2016.03.008.
98. Cekanova M, Rathore K. Animal models and therapeutic molecular targets of cancer: utility and limitations. *Drug Des. Devel. Ther.* 2014;8:1911-21. doi:10.2147/DDDT.S49584.
99. Kerbel RS. Human tumor xenografts as predictive preclinical models for anticancer drug activity in humans: better than commonly perceived-but they can be improved. *Cancer Biol. Ther.* 2003;2(4 Suppl 1):S134-9. doi:213 [pii].
100. Teicher BA. Tumor models for efficacy determination. *Mol. Cancer Ther.* 2006;5(10):2435-2443. doi:10.1158/1535-7163.MCT-06-0391.
101. Shapiro WR, Basler GA, Chernik NL, Posner JB. Human brain tumor transplantation into nude mice. *J. Natl. Cancer Inst.* 1979;62(3):447-53.
102. Horten BC, Basler GA, Shapiro WR. Xenograft of human malignant glial tumors into brains of nude mice. A histopatholgical study. *J. Neuropathol. Exp. Neurol.* 1981;40(5):493-511.
103. Garcia C, Dubois L, Xavier A, et al. The orthotopic xenotransplant of human glioblastoma successfully recapitulates glioblastoma-microenvironment interactions in a non-immunosuppressed mouse model. *BMC Cancer* 2014;14(1):923. doi:10.1186/1471-2407-14-923.
104. Borges AR, Lopez-Larrubia P, Marques JB, Cerdan SG. MR imaging features of high-grade gliomas in murine models: how they compare with human disease, reflect tumor biology, and play a role in preclinical trials. *AJNR. Am. J. Neuroradiol.* 2012;33(1):24-36. doi:10.3174/ajnr.A2959.
105. Oh T, Fakurnejad S, Sayegh ET, et al. Immunocompetent murine models for the study of glioblastoma immunotherapy. *J. Transl. Med.* 2014;12(1):107. doi:10.1186/1479-5876-12-107.
106. Wang H, Cai S, Bailey BJ, et al. Combination therapy in a xenograft model of glioblastoma: enhancement of the antitumor activity of temozolomide by an MDM2 antagonist. *J. Neurosurg.* 2016;13(13):1-14. doi:10.3171/2016.1.JNS152513.
107. Shultz LD, Ishikawa F, Greiner DL. Humanized mice in translational biomedical research. *Nat. Rev. Immunol.* 2007;7(2):118-30. doi:10.1038/nri2017.
108. Cunha L, Horvath I, Ferreira S, et al. Preclinical imaging: an essential ally in modern biosciences. *Mol. Diagn. Ther.* 2014;18(2):153-73. doi:10.1007/s40291-013-0062-3.
109. Richmond J. Refinement, reduction, and replacement of animal use for regulatory testing: future improvements and implementation within the regulatory framework. *ILAR J.* 2002;43 Suppl:S63-8.
110. Medvedeva SE, Boyandin A, Lankin Y, Kotov D, Rodicheva E, Popova L. BIOLUMBASE - The database of natural and transgenic bioluminescent organisms. *Luminescence* 2005;20(2):90-96.
111. Wurdinger T, Badr C, Pike L, et al. A secreted luciferase for ex vivo monitoring of in vivo processes. *Nat. Methods* 2008;5(2):171-173. doi:10.1038/nmeth.1177.
112. de Wet JR, Wood K V, DeLuca M, Helinski DR, Subramani S. Firefly luciferase gene: structure and expression in mammalian cells. *Mol. Cell. Biol.* 1987;7(2):725-37.
113. Edinger M, Cao Y -a., Hornig YS, et al. Advancing animal models of neoplasia through in vivo bioluminescence imaging. *Eur. J. Cancer* 2002;38(16):2128-2136. doi:10.1016/S0959-8049(02)00410-0.
114. Dinca EB, Voicu R V., Ciurea A V. Bioluminescence imaging of invasive intracranial xenografts: implications for translational research and targeted therapeutics of brain tumors. *Neurosurg. Rev.* 2010;33(4):385-394. doi:10.1007/s10143-010-0275-4.
115. Sweeney KJ, Jarzabek MA, Dicker P, et al. Validation of an imageable surgical resection animal model of Glioblastoma (GBM). *J. Neurosci. Methods* 2014;233:99-104. doi:10.1016/j.jneumeth.2014.05.006.
116. Rehemtulla A, Stegman LD, Cardozo SJ, et al. Rapid and quantitative assessment of cancer treatment response using in vivo bioluminescence imaging. *Neoplasia* 2000;2(6):491-495. doi:10.1038/sj.neo.7900121.

117. Ray P, Wu AM, Gambhir SS. Optical bioluminescence and positron emission tomography imaging of a novel fusion reporter gene in tumor xenografts of living mice. *Cancer Res.* 2003;63(6):1160-5.
118. Heuveling DA, Visser GWM, de Groot M, et al. Nanocolloidal albumin-IRDye 800CW: a near-infrared fluorescent tracer with optimal retention in the sentinel lymph node. *Eur. J. Nucl. Med. Mol. Imaging* 2012;39(7):1161-8. doi:10.1007/s00259-012-2080-5.
119. van den Berg NS, Miwa M, KleinJan GH, et al. (Near-Infrared) Fluorescence-Guided Surgery Under Ambient Light Conditions: A Next Step to Embedment of the Technology in Clinical Routine. *Ann. Surg. Oncol.* 2016. doi:10.1245/s10434-016-5186-3.
120. Kuzmin N V, Wesseling P, Hamer PC de W, et al. Third harmonic generation imaging for fast, label-free pathology of human brain tumors. *Biomed. Opt. Express* 2016;7(5):1889-904. doi:10.1364/BOE.7.001889.
121. Li JL, Goh CC, Keeble JL, et al. Intravital multiphoton imaging of immune responses in the mouse ear skin. *Nat. Protoc.* 2012;7(2):221-34. doi:10.1038/nprot.2011.438.
122. Egawa G, Kabashima K. In Vivo Imaging of Cutaneous DCs in Mice. *Methods Mol. Biol.* 2016;1423:269-74. doi:10.1007/978-1-4939-3606-9_19.
123. Uchugonova A, Hoffman RM, Weinigel M, Koenig K. Watching stem cells in the skin of living mice noninvasively. *Cell Cycle* 2011;10(12):2017-20. doi:10.4161/cc.10.12.15895.
124. Pineda CM, Park S, Mesa KR, et al. Intravital imaging of hair follicle regeneration in the mouse. *Nat. Protoc.* 2015;10(7):1116-30. doi:10.1038/nprot.2015.070.
125. Zomer A, Maynard C, Verweij FJ, et al. In Vivo Imaging Reveals Extracellular Vesicle-Mediated Phenocopying of Metastatic Behavior. *Cell* 2015;161(5):1046-1057. doi:10.1016/j.cell.2015.04.042.
126. Mostany R, Portera-Cailliau C. A craniotomy surgery procedure for chronic brain imaging. *J. Vis. Exp.* 2008;5(12):2-3. doi:10.3791/680.
127. Tozer GM, Ameer-Beg SM, Baker J, et al. Intravital imaging of tumour vascular networks using multi-photon fluorescence microscopy. *Adv. Drug Deliv. Rev.* 2005;57(1):135-52. doi:10.1016/j.addr.2004.07.015.
128. Holtmaat A, Bonhoeffer T, Chow DK, et al. Long-term, high-resolution imaging in the mouse neocortex through a chronic cranial window. *Nat. Protoc.* 2009;4(8):1128-44. doi:10.1038/nprot.2009.89.
129. Bayerl SH, Niesner R, Cseresnyes Z, et al. Time lapse in vivo microscopy reveals distinct dynamics of microglia-tumor environment interactions - a new role for the tumor perivascular space as highway for trafficking microglia. *Glia* 2016. doi:10.1002/glia.22994.
130. Lohela M, Casbon A-J, Olow A, et al. Intravital imaging reveals distinct responses of depleting dynamic tumor-associated macrophage and dendritic cell subpopulations. *Proc. Natl. Acad. Sci. U. S. A.* 2014;111(47):E5086-95. doi:10.1073/pnas.1419899111.
131. Kobat D, Horton NG, Xu C. In vivo two-photon microscopy to 1.6-mm depth in mouse cortex. *J. Biomed. Opt.* 2011;16(10):106014. doi:10.1117/1.3646209.
132. Horton NG, Wang K, Kobat D, et al. In vivo three-photon microscopy of subcortical structures within an intact mouse brain. *Nat. Photonics* 2013;7(3). doi:10.1038/nphoton.2012.336.
133. Bloomfield PM, Rajeswaran S, Spinks TJ, et al. The design and physical characteristics of a small animal positron emission tomograph. *Phys. Med. Biol.* 1995;40(6):1105-26.
134. Watanabe M, Uchida H, Okada H, et al. A high resolution PET for animal studies. *IEEE Trans. Med. Imaging* 1992;11(4):577-80. doi:10.1109/42.192694.
135. Cutler PD, Cherry SR, Hoffman EJ, Digby WM, Phelps ME. Design features and performance of a PET system for animal research. *J. Nucl. Med.* 1992;33(4):595-604.
136. Kenny L. The Use of Novel PET Tracers to Image Breast Cancer Biologic Processes Such as Proliferation, DNA Damage and Repair, and Angiogenesis. *J. Nucl. Med.* 2016;57 Suppl 1:89S-95S. doi:10.2967/jnumed.115.157958.
137. Puttick S, Bell C, Dowson N, Rose S, Fay M. PET, MRI, and simultaneous PET/MRI in the development of diagnostic and therapeutic strategies for glioma. *Drug Discov. Today* 2015;20(3):306-17. doi:10.1016/j.drudis.2014.10.016.
138. Das NM, Hatsell S, Nannuru K, et al. In Vivo Quantitative Microcomputed Tomographic Analysis of Vasculature and Organs in a Normal and Diseased Mouse Model. *PLoS One* 2016;11(2):e0150085. doi:10.1371/journal.pone.0150085.
139. Varoquaux A, Rager O, Poncet A, et al. Detection and quantification of focal uptake in head and neck tumours: (18)F-FDG PET/MR versus PET/CT. *Eur. J. Nucl. Med. Mol. Imaging* 2014;41(3):462-75. doi:10.1007/s00259-013-2580-y.

140. Baumann BC, Benci JL, Santoiemma PP, et al. An integrated method for reproducible and accurate image-guided stereotactic cranial irradiation of brain tumors using the small animal radiation research platform. *Transl. Oncol.* 2012;5(4):230-7.
141. Radaelli E, Ceruti R, Patton V, et al. Immunohistopathological and neuroimaging characterization of murine orthotopic xenograft models of glioblastoma multiforme recapitulating the most salient features of human disease. *Histol. Histopathol.* 2009;24(7):879-91.
142. Ramasawmy R, Johnson SP, Roberts TA, et al. Monitoring the Growth of an Orthotopic Tumour Xenograft Model: Multi-Modal Imaging Assessment with Benchtop MRI (1T), High-Field MRI (9.4T), Ultrasound and Bioluminescence. *PLoS One* 2016;11(5):e0156162. doi:10.1371/journal.pone.0156162.
143. Nagy K, Toth M, Major P, et al. Performance Evaluation of the Small-Animal nanoScan PET/MRI System. *J. Nucl. Med.* 2013;54(10):1825-32. doi:10.2967/jnumed.112.119065.
144. De Souza R, Spence T, Huang H, Allen C. Preclinical imaging and translational animal models of cancer for accelerated clinical implementation of nanotechnologies and macromolecular agents. *J. Control. Release* 2015;219:313-30. doi:10.1016/j.jconrel.2015.09.041.
145. Stein EW, Maslov K, Wang L V. Noninvasive, in vivo imaging of blood-oxygenation dynamics within the mouse brain using photoacoustic microscopy. *J. Biomed. Opt.* 2009;14(2):20502. doi:10.1117/1.3095799.
146. Griffini P, Smorenburg SM, Verbeek FJ, van Noorden CJ. Three-dimensional reconstruction of colon carcinoma metastases in liver. *J. Microsc.* 1997;187(Pt 1):12-21.
147. Gijtenbeek JMM, Wesseling P, Maass C, Burgers L, van der Laak JAWM. Three-dimensional reconstruction of tumor microvasculature: simultaneous visualization of multiple components in paraffin-embedded tissue. *Angiogenesis* 2005;8(4):297-305. doi:10.1007/s10456-005-9019-4.
148. Gilhuis HJ, van der Laak JAWM, Pomp J, Kappelle AC, Gijtenbeek JMM, Wesseling P. Three-dimensional (3D) reconstruction and quantitative analysis of the microvasculature in medulloblastoma and ependymoma subtypes. *Angiogenesis* 2006;9(4):201-8. doi:10.1007/s10456-006-9054-9.
149. Chung K, Wallace J, Kim S-Y, et al. Structural and molecular interrogation of intact biological systems (supp). *Nature* 2013;497(7449):332-7. doi:10.1038/nature12107.
150. Chieco P, Jonker A, De Boer BA, Ruijter JM, Van Noorden CJF. Image Cytometry: Protocols for 2D and 3D Quantification in Microscopic Images. *Prog. Histochem. Cytochem.* 2013;47(4):211-333. doi:10.1016/j.proghi.2012.09.001.
151. Weissleder R, Nahrendorf M. Advancing biomedical imaging. *Proc. Natl. Acad. Sci. U. S. A.* 2015;112(47):14424-8. doi:10.1073/pnas.1508524112.
152. Mauch CP, Dodt H, Leischner U, et al. Ultramicroscopy : three-dimensional visualization of neuronal networks in the whole mouse brain. *Nat. Methods* 2007;4(4):331-336. doi:10.1038/NMETH1036.
153. Negrean A, Mansvelder HD. Optimal lens design and use in laser-scanning microscopy. *Biomed. Opt. Express* 2014;5(5):1588. doi:10.1364/BOE.5.001588.
154. Susaki E a, Tainaka K, Perrin D, et al. Whole-Brain Imaging with Single-Cell Resolution Using Chemical Cocktails and Computational Analysis. *Cell* 2014;157(3):726-739. doi:10.1016/j.cell.2014.03.042.
155. Yang B, Treweek JB, Kulkarni RP, et al. Single-Cell Phenotyping within Transparent Intact Tissue through Whole-Body Clearing. *Cell* 2014:1-14. doi:10.1016/j.cell.2014.07.017.
156. Renier N, Wu Z, Simon DJ, Yang J, Ariel P, Tessier-lavigne M. Resource iDISCO : A Simple , Rapid Method to Immunolabel Large Tissue Samples for Volume Imaging. *Cell* 2014;Im:1-15. doi:10.1016/j.cell.2014.10.010.
157. Lee E, Choi J, Jo Y, et al. ACT-PRESTO: Rapid and consistent tissue clearing and labeling method for 3-dimensional (3D) imaging. *Sci. Rep.* 2016;6:18631. doi:10.1038/srep18631
158. Azaripour A, Lagerweij T, Scharfbillig C, Jadczak AE, Willershausen B, Van Noorden CJF. A survey of clearing techniques for 3D imaging of tissues with special reference to connective tissue. *Prog. Histochem. Cytochem.* 2016. doi:10.1016/j.proghi.2016.04.001.
159. Panchuk-Voloshina N, Haugland RP, Bishop-Stewart J, et al. Alexa dyes, a series of new fluorescent dyes that yield exceptionally bright, photostable conjugates. *J. Histochem. Cytochem.* 1999;47(9):1179-1188. doi:10.1177/002215549904700910.
160. Chen AK, Cheng Z, Behlke MA, Tsourkas A. Assessing the sensitivity of commercially available fluorophores to the intracellular environment. *Anal. Chem.* 2008;80(19):7437-44. doi:10.1021/ac8011347.
161. Liu H, Kao WWY. A novel protocol of whole mount electro-immunofluorescence staining. *Mol. Vis.* 2009;15(7449):505-517. doi:10.1038/nature12107.

162. Kim S-Y, Cho JH, Murray E, et al. Stochastic electrotransport selectively enhances the transport of highly electromobile molecules. *Proc. Natl. Acad. Sci. U. S. A.* 2015;112(46):E6274-83. doi:10.1073/pnas.1510133112.
163. Strack R. Protein labeling in cells. *Nat. Methods* 2015;13(1):33-33. doi:10.1038/nmeth.3702.
164. Lyons SK. Advances in imaging mouse tumour models in vivo. *J. Pathol.* 2005;205(2):194-205. doi:10.1002/path.1697.
165. Weissleder R. Scaling down imaging: molecular mapping of cancer in mice. *Nat. Rev. Cancer* 2002;2(1):11-8. doi:10.1038/nrc701.
166. Massoud TF, Gambhir SS. Molecular imaging in living subjects: Seeing fundamental biological processes in a new light. *Genes Dev.* 2003;17(5):545-580. doi:10.1101/gad.1047403.
167. Kherlopian AR, Song T, Duan Q, et al. A review of imaging techniques for systems biology. *BMC Syst. Biol.* 2008;2(1):74. doi:10.1186/1752-0509-2-74.
168. Hargrave D, Bartels U, Bouffet E. Diffuse brainstem glioma in children: Critical review of clinical trials. *Lancet Oncol.* 2006;7(3):241-248. doi:10.1016/S1470-2045(06)70615-5.
169. Jansen MH, van Vuurden DG, Vandertop WP, Kaspers GJL. Diffuse intrinsic pontine gliomas: A systematic update on clinical trials and biology. *Cancer Treat. Rev.* 2012;38(1):27-35. doi:10.1016/j.ctrv.2011.06.007.
170. Veringa SJE, Biesmans D, van Vuurden DG, et al. In Vitro Drug Response and Efflux Transporters Associated with Drug Resistance in Pediatric High Grade Glioma and Diffuse Intrinsic Pontine Glioma. Ulasov I, ed. *PLoS One* 2013;8(4):e61512. doi:10.1371/journal.pone.0061512.
171. Bradley KA, Pollack IF, Reid JM, et al. Motexafin gadolinium and involved field radiation therapy for intrinsic pontine glioma of childhood: a Children's Oncology Group phase I study. *Neuro. Oncol.* 2008;10(5):752-8. doi:10.1215/15228517-2008-043.
172. Smirniotopoulos JG, Murphy FM, Rushing EJ, Rees JH, Schroeder JW. Patterns of Contrast Enhancement in the Brain and Meninges. *RadioGraphics* 2007;27(2):525-551. doi:10.1148/rg.272065155.
173. Deeken JF, Löscher W. The Blood-Brain Barrier and Cancer: Transporters, Treatment, and Trojan Horses. *Clin. Cancer Res.* 2007;13(6).
174. Bartels U, Hawkins C, Vézina G, Kun L, Souweidane M, Bouffet E. Proceedings of the diffuse intrinsic pontine glioma (DIPG) Toronto Think Tank: advancing basic and translational research and cooperation in DIPG. *J. Neurooncol.* 2011;105(1):119-125. doi:10.1007/s11060-011-0704-4.
175. Song DK, Lonser RR. Convection-enhanced delivery for the treatment of pediatric neurologic disorders. *J. Child Neurol.* 2008;23(10):1231-7. doi:10.1177/0883073808321064.
176. Bobo RH, Laske DW, Akbasak A, Morrison PF, Dedrick RL, Oldfield EH. Convection-enhanced delivery of macromolecules in the brain. *Proc. Natl. Acad. Sci. U. S. A.* 1994;91(6):2076-80.
177. Groothuis DR, Ward S, Itskovich AC, et al. Comparison of 14C-sucrose delivery to the brain by intravenous, intraventricular, and convection-enhanced intracerebral infusion. *J Neurosurg* 1999;90(2):321-331. doi:10.3171/jns.1999.90.2.0321.
178. Bidros DS, Liu JK, Vogelbaum MA. Future of convection-enhanced delivery in the treatment of brain tumors. *Futur. Oncol.* 2010;6(1):117-125. doi:10.2217/fon.09.135.
179. Groothuis DR. The blood-brain and blood-tumor barriers: a review of strategies for increasing drug delivery. *Neuro. Oncol.* 2000;2(1):45-59.
180. Pardridge WM. Drug Delivery to the Brain. *J. Cereb. Blood Flow Metab.* 1997:713-731. doi:10.1097/00004647-199707000-00001.
181. Sandberg DI, Edgar MA, Souweidane MM. Convection-enhanced delivery into the rat brainstem. *J. Neurosurg.* 2002;96(5):885-891. doi:10.3171/jns.2002.96.5.0885.
182. Thomale UW, Tyler B, Renard VM, et al. Local chemotherapy in the rat brainstem with multiple catheters: a feasibility study. *Childs. Nerv. Syst.* 2009;25(1):21-8. doi:10.1007/s00381-008-0684-7.
183. Lonser RR, Walbridge S, Garmestani K, et al. Successful and safe perfusion of the primate brainstem: in vivo magnetic resonance imaging of macromolecular distribution during infusion. *J. Neurosurg.* 2002;97(4):905-913. doi:10.3171/jns.2002.97.4.0905
184. Yin D, Richardson RM, Fiandaca MS, et al. Cannula placement for effective convection-enhanced delivery in the nonhuman primate thalamus and brainstem: implications for clinical delivery of therapeutics. *J. Neurosurg.* 2010;113(2):240-248. doi:10.3171/2010.2.JNS091744.
185. Murad GJA, Walbridge S, Morrison PF, et al. Image-guided convection-enhanced delivery of gemcitabine to the brainstem. *J. Neurosurg.* 2007;106(2):351-356. doi:10.3171/jns.2007.106.2.351.

186. Anderson RCE, Kennedy B, Yanes CL, et al. Convection-enhanced delivery of topotecan into diffuse intrinsic brainstem tumors in children. *J. Neurosurg. Pediatr.* 2013;11(3):289-295. doi:10.3171/2012.10.PEDS12142.
187. Barua NU, Lowis SP, Woolley M, O'Sullivan S, Harrison R, Gill SS. Robot-guided convection-enhanced delivery of carboplatin for advanced brainstem glioma. *Acta Neurochir. (Wien).* 2013;155(8):1459-1465. doi:10.1007/s00701-013-1700-6.
188. Saito R, Sonoda Y, Kumabe T, Nagamatsu K, Watanabe M, Tominaga T. Regression of recurrent glioblastoma infiltrating the brainstem after convection-enhanced delivery of nimustine hydrochloride. *J. Neurosurg. Pediatr.* 2011;7(5):522-6. doi:10.3171/2011.2.PEDS10407.
189. Becher OJ, Hambardzumyan D, Walker TR, et al. Preclinical Evaluation of Radiation and Perifosine in a Genetically and Histologically Accurate Model of Brainstem Glioma. *Cancer Res.* 2010;70(6).
190. Monje M, Mitra SS, Freret ME, et al. Hedgehog-responsive candidate cell of origin for diffuse intrinsic pontine glioma. *Proc. Natl. Acad. Sci. U. S. A.* 2011;108(11):4453-8. doi:10.1073/pnas.1101657108.
191. Silvani A, Gaviani P, Lamperti EA, et al. Cisplatinum and BCNU chemotherapy in primary glioblastoma patients. *J. Neurooncol.* 2009;94(1):57-62. doi:10.1007/s11060-009-9800-0.
192. Buonerba C, Di Lorenzo G, Marinelli A, et al. A comprehensive outlook on intracerebral therapy of malignant gliomas. *Crit. Rev. Oncol. Hematol.* 2011;80(1):54-68. doi:10.1016/j.critrevonc.2010.09.001.
193. Engelhard HH. The role of interstitial BCNU chemotherapy in the treatment of malignant glioma. *Surg. Neurol.* 2000;53(5):458-64.
194. Sardi I, Sanzo M, Giordano F, et al. Intracavitary chemotherapy (Gliadel) and oral low-dose etoposide for recurrent anaplastic ependymoma. *Oncol. Rep.* 2008;19(5):1219-23.
195. Layton PB, Greenberg HS, Stetson PL, Ensminger WD, Gyves JW. BCNU solubility and toxicity in the treatment of malignant astrocytomas. *J. Neurosurg.* 1984;60(6):1134-1137. doi:10.3171/jns.1984.60.6.1134.
196. Caretti V, Sewing ACPCP, Lagerweij T, et al. Human pontine glioma cells can induce murine tumors. *Acta Neuropathol.* 2014;127(6):897-909. doi:10.1007/s00401-014-1272-4.
197. Caretti V, Zondervan I, Meijer DH, et al. Monitoring of tumor growth and post-irradiation recurrence in a diffuse intrinsic pontine glioma mouse model. *Brain Pathol.* 2011;21(4):441-451. doi:10.1111/j.1750-3639.2010.00468.x.
198. Chen Z-J, Gillies GT, Broaddus WC, et al. A realistic brain tissue phantom for intraparenchymal infusion studies. *J. Neurosurg.* 2004;101(2):314-322. doi:10.3171/jns.2004.101.2.0314.
199. Caretti V, Bugiani M, Freret M, et al. Subventricular spread of diffuse intrinsic pontine glioma. *Acta Neuropathol.* 2014;128(4):605-607. doi:10.1007/s00401-014-1307-x.
200. Paxinos GKF. The Mouse Brain in Stereotaxic Coordinates, Compact, 3rd Edition | George Paxinos, Keith Franklin | ISBN 9780123742445. *Mouse Brain Stereotaxic Coord. Compact. 3rd Ed.* 2008.
201. Saito R, Krauze MT, Noble CO, et al. Tissue affinity of the infusate affects the distribution volume during convection-enhanced delivery into rodent brains: Implications for local drug delivery. *J. Neurosci. Methods* 2006;154(1):225-232. doi:10.1016/j.jneumeth.2005.12.027.
202. Caretti V, Jansen MHA, Van Vuurden DG, et al. Implementation of a Multi-Institutional Diffuse Intrinsic Pontine Glioma Autopsy Protocol and Characterization of a Primary Cell Culture. *Neuropathol. Appl. Neurobiol.* 2012. doi:10.1111/j.1365-2990.2012.01294.x.
203. Occhiogrosso G, Edgar MA, Sandberg DI, Souweidane MM. Prolonged Convection-enhanced Delivery into the Rat Brainstem. *Neurosurgery* 2003;52(2):388-394. doi:10.1227/01.NEU.0000043696.83722.8D.
204. Solomon DA, Wood MD, Tihan T, et al. Diffuse Midline Gliomas with Histone H3-K27M Mutation: A Series of 47 Cases Assessing the Spectrum of Morphologic Variation and Associated Genetic Alterations. *Brain Pathol.* 2016;26(5):569-580. doi:10.1111/bpa.12336.
205. Eisenstat DD, Pollack IF, Demers A, et al. Impact of tumor location and pathological discordance on survival of children with midline high-grade gliomas treated on Children's Cancer Group high-grade glioma study CCG-945. *J. Neurooncol.* 2015;121(3):573-581. doi:10.1007/s11060-014-1669-x.
206. Jansen MH, Veldhuijzen van Zanten SE, Sanchez Aliaga E, et al. Survival prediction model of children with diffuse intrinsic pontine glioma based on clinical and radiological criteria. *Neuro. Oncol.* 2015;17(1):160-166. doi:10.1093/neuonc/nou104.
207. Buczkowicz P, Hoeman C, Rakopoulos P, et al. Genomic analysis of diffuse intrinsic pontine gliomas identifies three molecular subgroups and recurrent activating ACVR1 mutations. *Nat. Genet.* 2014;46(5):451-456. doi:10.1038/ng.2936.

208. Buczkowicz P, Hawkins C. Pathology, Molecular Genetics, and Epigenetics of Diffuse Intrinsic Pontine Glioma. *Front. Oncol.* 2015;5:147. doi:10.3389/fonc.2015.00147.
209. Morales La Madrid A, Hashizume R, Kieran MW. Future Clinical Trials in DIPG: Bringing Epigenetics to the Clinic. *Front. Oncol.* 2015;5:148. doi:10.3389/fonc.2015.00148.
210. Salloum R, DeWire M, Lane A, et al. Patterns of progression in pediatric patients with high-grade glioma or diffuse intrinsic pontine glioma treated with Bevacizumab-based therapy at diagnosis. *J. Neurooncol.* 2014;121:591-598. doi:10.1007/s11060-014-1671-3.
211. Kaspers GJ, Jansen MH. A new era for children with diffuse intrinsic pontine glioma: hope for cure? *Expert Rev. Anticancer Ther.* 2012;12(9):1109-1112. doi:10.1586/era.12.95.
212. van Dalen EC, Raphaël MF, Caron HN, Kremer LC. Treatment including anthracyclines versus treatment not including anthracyclines for childhood cancer. In: van Dalen EC, ed. *Cochrane Database of Systematic Reviews*. Chichester, UK: John Wiley & Sons, Ltd; 2014. doi:10.1002/14651858.CD006647.pub4.
213. Lipshultz SE, Karnik R, Sambatakos P, Franco VI, Ross SW, Miller TL. Anthracycline-related cardiotoxicity in childhood cancer survivors. *Curr. Opin. Cardiol.* 2014;29(1):103-112. doi:10.1097/HCO.0000000000000034.
214. Austin Doyle L, Ross DD. Multidrug resistance mediated by the breast cancer resistance protein BCRP (ABCG2). *Oncogene* 2003;22(47):7340-7358. doi:10.1038/sj.onc.1206938.
215. Qosa H, Miller DS, Pasinelli P, Trotti D. Regulation of ABC efflux transporters at blood-brain barrier in health and neurological disorders. *Brain Res.* 2015;1628:298-316. doi:10.1016/j.brainres.2015.07.005.
216. Chittiboina P, Heiss JD, Warren KE, Lonser RR. Magnetic resonance imaging properties of convective delivery in diffuse intrinsic pontine gliomas. *J. Neurosurg. Pediatr.* 2014;13(3):276-82. doi:10.3171/2013.11.PEDS136.
217. Barua NU, Gill SS, Love S. Convection-Enhanced Drug Delivery to the Brain: Therapeutic Potential and Neuropathological Considerations. *Brain Pathol.* 2014;24(2):117-127. doi:10.1111/bpa.12082.
218. Lonser RR, Sarntinoranont M, Morrison PF, Oldfield EH. Convection-enhanced delivery to the central nervous system. *J. Neurosurg.* 2015;122(3):697-706. doi:10.3171/2014.10.JNS14229.
219. Allard E, Passirani C, Benoit J-P. Convection-enhanced delivery of nanocarriers for the treatment of brain tumors. *Biomaterials* 2009;30(12):2302-2318. doi:10.1016/j.biomaterials.2009.01.003.
220. Kikuchi T, Saito R, Sugiyama S, et al. Convection-enhanced delivery of polyethylene glycol–coated liposomal doxorubicin: characterization and efficacy in rat intracranial glioma models. *J. Neurosurg.* 2008;109(5):867-873. doi:10.3171/JNS/2008/109/11/0867.
221. Krauze MT, Noble CO, Kawaguchi T, et al. Convection-enhanced delivery of nanoliposomal CPT-11 (irinotecan) and PEGylated liposomal doxorubicin (Doxil) in rodent intracranial brain tumor xenografts. *Neuro. Oncol.* 2007;9(4):393-403. doi:10.1215/15228517-2007-019.
222. Zhou J, Patel TR, Sirianni RW, et al. Highly penetrative, drug-loaded nanocarriers improve treatment of glioblastoma. *Proc. Natl. Acad. Sci. U. S. A.* 2013;110(29):11751-6. doi:10.1073/pnas.1304504110.
223. Di Leo A, Gancberg D, Larsimont D, et al. HER-2 amplification and topoisomerase IIalpha gene aberrations as predictive markers in node-positive breast cancer patients randomly treated either with an anthracycline-based therapy or with cyclophosphamide, methotrexate, and 5-fluorouracil. *Clin. Cancer Res.* 2002;8(5):1107-16.
224. Di Leo A, Biganzoli L, Claudino W, Licitra S, Pestrin M, Larsimont D. Topoisomerase II alpha as a marker predicting anthracyclines' activity in early breast cancer patients: Ready for the primetime? *Eur. J. Cancer* 2008;44(18):2791-2798. doi:10.1016/j.ejca.2008.09.014.
225. Paugh BS, Broniscer A, Qu C, et al. Genome-wide analyses identify recurrent amplifications of receptor tyrosine kinases and cell-cycle regulatory genes in diffuse intrinsic pontine glioma. *J. Clin. Oncol.* 2011;29(30):3999-4006. doi:10.1200/JCO.2011.35.5677.
226. Paugh BS, Qu C, Jones C, et al. Integrated molecular genetic profiling of pediatric high-grade gliomas reveals key differences with the adult disease. *J. Clin. Oncol.* 2010;28(18):3061-3068. doi:10.1200/JCO.2009.26.7252.
227. Harris LW, Lockstone HE, Khaitovich P, Weickert CS, Webster MJ, Bahn S. Gene expression in the prefrontal cortex during adolescence: implications for the onset of schizophrenia. *BMC Med. Genomics* 2009;2:28. doi:10.1186/1755-8794-2-28.
228. Gravendeel L a M, Kouwenhoven MCM, Gevaert O, et al. Intrinsic gene expression profiles of gliomas are a better predictor of survival than histology. *Cancer Res.* 2009;69(23):9065-9072. doi:10.1158/0008-5472.CAN-09-2307.

229. Boult JKR, Taylor KR, Vinci M, et al. Abstract 3271: Novel orthotopic pediatric high grade glioma xenografts evaluated with magnetic resonance imaging mimic human disease. *Cancer Res.* 2015;75(15 Supplement):3271-3271. doi:10.1158/1538-7445.AM2015-3271.
230. Jansen MHA, Lagerweij T, Sewing ACP, et al. Bevacizumab targeting diffuse intrinsic pontine glioma: results of 89Zr-bevacizumab PET imaging in brain tumor models. *Mol. Cancer Ther.* 2016;15(September):2166-2174. doi:10.1158/1535-7163.MCT-15-0558.
231. Gaillard PJ, Appeldoorn CCM, Dorland R, et al. Pharmacokinetics, Brain Delivery, and Efficacy in Brain Tumor-Bearing Mice of Glutathione Pegylated Liposomal Doxorubicin (2B3-101). Velasco G, ed. *PLoS One* 2014;9(1):e82331. doi:10.1371/journal.pone.0082331.
232. Barenholz Y (Chezy). Doxil® — The first FDA-approved nano-drug: Lessons learned. *J. Control. Release* 2012;160(2):117-134. doi:10.1016/j.jconrel.2012.03.020.
233. Claes A, Schuuring J, Boots-Sprenger S, et al. Phenotypic and genotypic characterization of orthotopic human glioma models and its relevance for the study of anti-glioma therapy. *Brain Pathol.* 2008;18(3):423-433. doi:10.1111/j.1750-3639.2008.00141.x.
234. Sewing ACPCP, Caretti V, Lagerweij T, et al. Convection Enhanced Delivery of Carmustine to the Murine Brainstem: a feasibility study. *J. Neurosci. Methods* 2014;238:88-94. doi:10.1016/j.jneumeth.2014.09.020.
235. Chastagner P, Sudour H, Mriouah J, Barberi-Heyob M, Bernier-Chastagner V, Pinel S. Preclinical Studies of Pegylated- and Non-Pegylated Liposomal Forms of Doxorubicin as Radiosensitizer on Orthotopic High-Grade Glioma Xenografts. *Pharm. Res.* 2015;32(1):158-166. doi:10.1007/s11095-014-1452-x.
236. Lippens RJ. Liposomal daunorubicin (DaunoXome) in children with recurrent or progressive brain tumors. *Pediatr. Hematol. Oncol.* 16(2):131-9.
237. Wagner S, Peters O, Fels C, et al. Pegylated-liposomal doxorubicin and oral topotecan in eight children with relapsed high-grade malignant brain tumors. *J. Neurooncol.* 2008;86(2):175-181. doi:10.1007/s11060-007-9444-x.
238. Wolff JE, Trilling T, Mölenkamp G, Egeler RM, Jürgens H. Chemosensitivity of glioma cells in vitro: a meta analysis. *J. Cancer Res. Clin. Oncol.* 125(8-9):481-6.
239. Chan K-M, Fang D, Gan H, et al. The histone H3.3K27M mutation in pediatric glioma reprograms H3K27 methylation and gene expression. *Genes Dev.* 2013;27(9):985-990. doi:10.1101/gad.217778.113.
240. Fontebasso AM, Liu X-Y, Sturm D, Jabado N. Chromatin Remodeling Defects in Pediatric and Young Adult Glioblastoma: A Tale of a Variant Histone 3 Tail. *Brain Pathol.* 2013;23(2):210-216. doi:10.1111/bpa.12023.
241. Pang B, Qiao X, Janssen L, et al. Drug-induced histone eviction from open chromatin contributes to the chemotherapeutic effects of doxorubicin. *Nat. Commun.* 2013;4:1908. doi:10.1038/ncomms2921.
242. Zhang R, Saito R, Mano Y, et al. Concentration rather than dose defines the local brain toxicity of agents that are effectively distributed by convection-enhanced delivery. *J. Neurosci. Methods* 2014;222:131-137. doi:10.1016/j.jneumeth.2013.11.004.
243. Kakee A, Terasaki T, Sugiyama Y. Brain efflux index as a novel method of analyzing efflux transport at the blood-brain barrier. *J. Pharmacol. Exp. Ther.* 1996;277(3):1550-9.
244. Zhou Z, Ho SL, Singh R, Pisapia DJ, Souweidane MM. Toxicity evaluation of convection-enhanced delivery of small-molecule kinase inhibitors in naïve mouse brainstem. *Child's Nerv. Syst.* 2015;31(4):557-562. doi:10.1007/s00381-015-2640-7.
245. Siepmann J, Siepmann F, Florence AT. Local controlled drug delivery to the brain: Mathematical modeling of the underlying mass transport mechanisms. *Int. J. Pharm.* 2006;314(2):101-119. doi:10.1016/j.ijpharm.2005.07.027.
246. Ferrara N. Vascular endothelial growth factor: Basic science and clinical progress. *Endocr. Rev.* 2004;25(4):581-611. doi:10.1210/er.2003-0027.
247. Shibuya M. Differential roles of vascular endothelial growth factor receptor-1 and receptor-2 in angiogenesis. *J. Biochem. Mol. Biol.* 2006;39(5):469-478. doi:10.5483/BMBRep.2006.39.5.469.
248. Friedman HS, Prados MD, Wen PY, et al. Bevacizumab alone and in combination with irinotecan in recurrent glioblastoma. *J. Clin. Oncol.* 2009;27(28):4733-40. doi:10.1200/JCO.2008.19.8721.
249. Vredenburgh JJ, Desjardins A, Herndon JE, et al. Phase II trial of bevacizumab and irinotecan in recurrent malignant glioma. *Clin. Cancer Res.* 2007;13(4):1253-1259. doi:10.1158/1078-0432.CCR-06-2309.
250. Vredenburgh JJ, Desjardins A, Herndon JE, et al. Bevacizumab plus irinotecan in recurrent glioblastoma multiforme. *J. Clin. Oncol.* 2007;25(30):4722-4729. doi:10.1200/JCO.2007.12.2440.
251. Chinot OL, Wick W, Mason W, et al. Bevacizumab plus radiotherapy-temozolomide for newly diagnosed

glioblastoma. *N. Engl. J. Med.* 2014;370(8):709-22. doi:10.1056/NEJMoa1308345.
252. Gilbert MR, Dignam JJ, Armstrong TS, et al. A randomized trial of bevacizumab for newly diagnosed glioblastoma. *N. Engl. J. Med.* 2014;370(8):699-708. doi:10.1056/NEJMoa1308573.
253. Khasraw M, Ameratunga MS, Grant R, Wheeler H, Pavlakis N. Antiangiogenic therapy for high-grade glioma. *Cochrane database Syst. Rev.* 2014;9:CD008218. doi:10.1002/14651858.CD008218.pub3.
254. Gururangan S, Chi SN, Young Poussaint T, et al. Lack of efficacy of bevacizumab plus irinotecan in children with recurrent malignant glioma and diffuse brainstem glioma: a Pediatric Brain Tumor Consortium study. *J. Clin. Oncol.* 2010;28(18):3069-3075. doi:10.1200/JCO.2009.26.8789.
255. Aguilera DG, Mazewski C, Hayes L, et al. Prolonged survival after treatment of diffuse intrinsic pontine glioma with radiation, temozolamide, and bevacizumab: report of 2 cases. *J. Pediatr. Hematol. Oncol.* 2013;35(1):e42-6. doi:10.1097/MPH.0b013e318279aed8.
256. Zaky W, Wellner M, Brown RJ, Blüml S, Finlay JL, Dhall G. Treatment of children with diffuse intrinsic pontine gliomas with chemoradiotherapy followed by a combination of temozolomide, irinotecan, and bevacizumab. *Pediatr. Hematol. Oncol.* 2013;30(7):623-32. doi:10.3109/08880018.2013.829895.
257. Hummel TR, Salloum R, Drissi R, et al. A pilot study of bevacizumab-based therapy in patients with newly diagnosed high-grade gliomas and diffuse intrinsic pontine gliomas. *J. Neurooncol.* 2016;127(1):53-61. doi:10.1007/s11060-015-2008-6.
258. Roodink I, Van Der Laak J, Kusters B, et al. Development of the tumor vascular bed in response to hypoxia-induced VEGF-A differs from that in tumors with constitutive VEGF-A expression. *Int. J. Cancer* 2006;119(9):2054-2062. doi:10.1002/ijc.22072.
259. Verel I, Visser GWM, Boellaard R, Stigter-van Walsum M, Snow GB, van Dongen G a MS. 89Zr immuno-PET: comprehensive procedures for the production of 89Zr-labeled monoclonal antibodies. *J. Nucl. Med.* 2003;44(8):1271-1281.
260. Taylor KR, Mackay A, Truffaux N, et al. Recurrent activating ACVR1 mutations in diffuse intrinsic pontine glioma. *Nat. Genet.* 2014;46(5):457-61. doi:10.1038/ng.2925.
261. Bernsen HJJ a, Rijken PFJW, Peters H, Bakker H, van der Kogel a. J. The effect of the anti-angiogenic agent TNP-470 on tumor growth and vascularity in low passaged xenografts of human gliomas in nude mice. *J. Neurooncol.* 1998;38(1):51-57. doi:10.1023/A:1005957201431.
262. Mir SE, De Witt Hamer PC, Krawczyk PM, et al. In silico analysis of kinase expression identifies WEE1 as a gatekeeper against mitotic catastrophe in glioblastoma. *Cancer Cell* 2010;18(3):244-57. doi:10.1016/j.ccr.2010.08.011.
263. de Weger RA, Tilanus MG, Scheidel KC, van den Tweel JG, Verdonck LF. Monitoring of residual disease and guided donor leucocyte infusion after allogeneic bone marrow transplantation by chimaerism analysis with short tandem repeats. *Br. J. Haematol.* 2000;110(3):647-53.
264. Verel I, Visser GWM, Boellaard R, et al. Quantitative 89Zr immuno-PET for in vivo scouting of 90Y-labeled monoclonal antibodies in xenograft-bearing nude mice. *J. Nucl. Med.* 2003;44(10):1663-1670.
265. de Jong HWAM, van Velden FHP, Kloet RW, Buijs FL, Boellaard R, Lammertsma AA. Performance evaluation of the ECAT HRRT: an LSO-LYSO double layer high resolution, high sensitivity scanner. *Phys. Med. Biol.* 2007;52(5):1505-26. doi:10.1088/0031-9155/52/5/019.
266. Loening AM, Gambhir SS. AMIDE: a free software tool for multimodality medical image analysis. *Mol. Imaging* 2003;2(3):131-7.
267. Papadopoulos N, Martin J, Ruan Q, et al. Binding and neutralization of vascular endothelial growth factor (VEGF) and related ligands by VEGF Trap, ranibizumab and bevacizumab. *Angiogenesis* 2012;15(2):171-185. doi:10.1007/s10456-011-9249-6.
268. Jacobs VL, Valdes PA, Hickey WF, De Leo JA. Current review of in vivo GBM rodent models: emphasis on the CNS-1 tumour model. *ASN Neuro* 2011;3(3):e00063. doi:10.1042/AN20110014.
269. Johansson M, Brännström T, Bergenheim a T, Henriksson R. Spatial expression of VEGF-A in human glioma. *J. Neurooncol.* 2002;59(1):1-6.
270. Navis AC, Hamans BC, Claes A, et al. Effects of targeting the VEGF and PDGF pathways in diffuse orthotopic glioma models. *J. Pathol.* 2011;223(5):626-634. doi:10.1002/path.2836.
271. Yu L, Wu X, Cheng Z, et al. Interaction between bevacizumab and murine VEGF-A: A reassessment. *Investig. Ophthalmol. Vis. Sci.* 2008;49(2):522-527. doi:10.1167/iovs.07-1175.
272. Paugh BS, Qu C, Jones C, et al. Integrated molecular genetic profiling of pediatric high-grade gliomas reveals key differences with the adult disease. *J. Clin. Oncol.* 2010;28(18):3061-8. doi:10.1200/JCO.2009.26.7252

.
273. Zhao L, Yang Z, Liu Y, Ying H, Zhang H, Xue Y. Vascular endothelial growth factor increases permeability of the blood-tumor barrier via caveolae-mediated transcellular pathway. *J. Mol. Neurosci.* 2011;44(2):122-9. doi:10.1007/s12031-010-9487-x.
274. Pàez-Ribes M, Allen E, Hudock J, et al. Antiangiogenic therapy elicits malignant progression of tumors to increased local invasion and distant metastasis. *Cancer Cell* 2009;15(3):220-31. doi:10.1016/j.ccr.2009.01.027.
275. Gomez-Manzano C, Holash J, Fueyo J, et al. VEGF Trap induces antiglioma effect at different stages of disease. *Neuro. Oncol.* 2008;10(6):940-945. doi:10.1215/15228517-2008-061.
276. Wesseling P, Ruiter DJ, Burger PC. Angiogenesis in brain tumors; pathobiological and clinical aspects. *J. Neurooncol.* 1997;32(3):253-65.
277. Gagner J-P, Law M, Fischer I, Newcomb EW, Zagzag D. Angiogenesis in gliomas: imaging and experimental therapeutics. *Brain Pathol.* 2005;15(4):342-363. doi:10.1111/j.1750-3639.2005.tb00119.x.
278. Jubb AM, Harris AL. Biomarkers to predict the clinical efficacy of bevacizumab in cancer. *Lancet. Oncol.* 2010;11(12):1172-83. doi:10.1016/S1470-2045(10)70232-1.
279. Jubb AM. Impact of Vascular Endothelial Growth Factor-A Expression, Thrombospondin-2 Expression, and Microvessel Density on the Treatment Effect of Bevacizumab in Metastatic Colorectal Cancer. *J. Clin. Oncol.* 2005;24(2):217-227. doi:10.1200/JCO.2005.01.5388.
280. Shih T, Lindley C. Bevacizumab: an angiogenesis inhibitor for the treatment of solid malignancies. *Clin. Ther.* 2006;28(11):1779-802. doi:10.1016/j.clinthera.2006.11.015.
281. Ostrom QT, Gittleman H, Farah P, et al. CBTRUS statistical report: Primary brain and central nervous system tumors diagnosed in the United States in 2006-2010. *Neuro. Oncol.* 2013;15 Suppl 2(suppl 2):ii1-56. doi:10.1093/neuonc/not151.
282. Gibson P, Tong Y, Robinson G, et al. Subtypes of medulloblastoma have distinct developmental origins. *Nature* 2010;468(7327):1095-9. doi:10.1038/nature09587.
283. Grammel D, Warmuth-Metz M, von Bueren AO, et al. Sonic hedgehog-associated medulloblastoma arising from the cochlear nuclei of the brainstem. *Acta Neuropathol.* 2012;123(4):601-14. doi:10.1007/s00401-012-0961-0.
284. Packer RJ, Zhou T, Holmes E, Vezina G, Gajjar A. Survival and secondary tumors in children with medulloblastoma receiving radiotherapy and adjuvant chemotherapy: results of Children's Oncology Group trial A9961. *Neuro. Oncol.* 2013;15(1):97-103. doi:10.1093/neuonc/nos267.
285. Massimino M, Cefalo G, Riva D, et al. Long-term results of combined preradiation chemotherapy and age-tailored radiotherapy doses for childhood medulloblastoma. *J. Neurooncol.* 2012;108(1):163-71. doi:10.1007/s11060-012-0822-7.
286. Gajjar A, Packer RJ, Foreman NK, Cohen K, Haas-Kogan D, Merchant TE. Children's Oncology Group's 2013 blueprint for research: central nervous system tumors. *Pediatr. Blood Cancer* 2013;60(6):1022-6. doi:10.1002/pbc.24427.
287. Toogood AA. Endocrine consequences of brain irradiation. *Growth Horm. IGF Res.* 2004;14 Suppl A:S118-24. doi:10.1016/j.ghir.2004.03.038.
288. Armstrong GT, Whitton JA, Gajjar A, et al. Abnormal timing of menarche in survivors of central nervous system tumors: A report from the Childhood Cancer Survivor Study. *Cancer* 2009;115(11):2562-70. doi:10.1002/cncr.24294.
289. Kieffer-Renaux V, Viguier D, Raquin M-A, et al. Therapeutic schedules influence the pattern of intellectual decline after irradiation of posterior fossa tumors. *Pediatr. Blood Cancer* 2005;45(6):814-9. doi:10.1002/pbc.20329.
290. Miralbell R, Lomax A, Russo M. Potential role of proton therapy in the treatment of pediatric medulloblastoma/primitive neuro-ectodermal tumors: spinal theca irradiation. *Int. J. Radiat. Oncol. Biol. Phys.* 1997;38(4):805-11.
291. Lee CT, Bilton SD, Famiglietti RM, et al. Treatment planning with protons for pediatric retinoblastoma, medulloblastoma, and pelvic sarcoma: how do protons compare with other conformal techniques? *Int. J. Radiat. Oncol. Biol. Phys.* 2005;63(2):362-72. doi:10.1016/j.ijrobp.2005.01.060.
292. Fossati P, Ricardi U, Orecchia R. Pediatric medulloblastoma: toxicity of current treatment and potential role of protontherapy. *Cancer Treat. Rev.* 2009;35(1):79-96. doi:10.1016/j.ctrv.2008.09.002.
293. Luttjeboer M, Kaspers GJL. Medulloblastoma: need for targeted treatment. *Expert Rev. Anticancer Ther.* 2006;6(5):649-52. doi:10.1586/14737140.6.5.649.

294. Vuurden DG Van, Hulleman E, Meijer OLM, et al. PARP inhibition sensitizes childhood high grade medulloblastoma and ependymoma to radiation. *Oncotarget* 2011;2(12):984-996.
295. Zhao X, Liu Z, Yu L, et al. Global gene expression profiling confirms the molecular fidelity of primary tumor-based orthotopic xenograft mouse models of medulloblastoma. *Neuro. Oncol.* 2012;14(5):574-83. doi:10.1093/neuonc/nos061.
296. Pollastri MP. Overview on the Rule of Five. *Curr. Protoc. Pharmacol.* 2010;Chapter 9:Unit 9.12. doi:10.1002/0471141755.ph0912s49.
297. Badr CE, Wurdinger T, Tannous BA. Functional drug screening assay reveals potential glioma therapeutics. *Assay Drug Dev. Technol.* 2011;9(3):281-9. doi:10.1089/adt.2010.0324.
298. Zhao X, Liu Z, Yu L, et al. Global gene expression profiling confirms. 2012.
299. Paxinos G, Franklin K. *The Mouse Brain in Stereotaxic Coordinates: Second Edition (Deluxe)*. Academic Press, New York; 2001.
300. Zhang J, Chung T, Oldenburg K. A Simple Statistical Parameter for Use in Evaluation and Validation of High Throughput Screening Assays. *J. Biomol. Screen.* 1999;4(2):67-73.
301. van Rijn J, van den Berg J. Flavonoids as enhancers of x-ray-induced cell damage in hepatoma cells. *Clin. Cancer Res.* 1997;3(10):1775-9.
302. Luttjeboer M, Lafleur MVM, Kwidama ZJ, et al. Strategies for the analysis of in vitro radiation sensitivity and prediction of interaction with potential radiation modifying agents. *Int. J. Radiat. Biol.* 2010;86(6):458-66. doi:10.3109/09553000903568019.
303. Ishisaka A, Ichikawa S, Sakakibara H, et al. Accumulation of orally administered quercetin in brain tissue and its antioxidative effects in rats. *Free Radic. Biol. Med.* 2011;51(7):1329-36. doi:10.1016/j.freeradbiomed.2011.06.017.
304. Ferrer P, Asensi M, Segarra R, et al. Association between pterostilbene and quercetin inhibits metastatic activity of B16 melanoma. *Neoplasia* 2005;7(1):37-47.
305. Aghdassi A, Phillips P, Dudeja V, et al. Heat shock protein 70 increases tumorigenicity and inhibits apoptosis in pancreatic adenocarcinoma. *Cancer Res.* 2007;67(2):616-25. doi:10.1158/0008-5472.CAN-06-1567.
306. Aalinkeel R, Bindukumar B, Reynolds JL, et al. The dietary bioflavonoid, quercetin, selectively induces apoptosis of prostate cancer cells by down-regulating the expression of heat shock protein 90. *Prostate* 2008;68(16):1773-89. doi:10.1002/pros.20845.
307. Lugli E, Ferraresi R, Roat E, et al. Quercetin inhibits lymphocyte activation and proliferation without inducing apoptosis in peripheral mononuclear cells. *Leuk. Res.* 2009;33(1):140-50. doi:10.1016/j.leukres.2008.07.025.
308. Harwood M, Danielewska-Nikiel B, Borzelleca JF, Flamm GW, Williams GM, Lines TC. A critical review of the data related to the safety of quercetin and lack of evidence of in vivo toxicity, including lack of genotoxic/carcinogenic properties. *Food Chem. Toxicol.* 2007;45(11):2179-205. doi:10.1016/j.fct.2007.05.015.
309. Conquer JA, Maiani G, Azzini E, Raguzzini A, Holub BJ. Supplementation with quercetin markedly increases plasma quercetin concentration without effect on selected risk factors for heart disease in healthy subjects. *J. Nutr.* 1998;128(3):593-7.
310. Manach C, Williamson G, Morand C, Scalbert A, Rémésy C. Bioavailability and bioefficacy of polyphenols in humans. I. Review of 97 bioavailability studies. *Am. J. Clin. Nutr.* 2005;81(1 Suppl):230S-242S.
311. Faria A, Pestana D, Teixeira D, et al. Flavonoid transport across RBE4 cells: A blood-brain barrier model. *Cell. Mol. Biol. Lett.* 2010;15(2):234-41. doi:10.2478/s11658-010-0006-4.
312. Yang Z-H, Sun X, Mei C, Sun X-B, Liu X-D, Chang Q. An in vitro transport model for rapid screening and predicting the permeability of candidate compounds at blood-brain barrier. *J. Asian Nat. Prod. Res.* 2011;13(12):1087-97. doi:10.1080/10286020.2011.599958.
313. Agarwal S, Sane R, Oberoi R, Ohlfest JR, Elmquist WF. Delivery of molecularly targeted therapy to malignant glioma, a disease of the whole brain. *Expert Rev. Mol. Med.* 2011;13:e17. doi:10.1017/S1462399411001888.
314. Schültke E, Kamencic H, Zhao M, et al. Neuroprotection following fluid percussion brain trauma: a pilot study using quercetin. *J. Neurotrauma* 2005;22(12):1475-84. doi:10.1089/neu.2005.22.1475.
315. Pu F, Mishima K, Irie K, et al. Neuroprotective effects of quercetin and rutin on spatial memory impairment in an 8-arm radial maze task and neuronal death induced by repeated cerebral ischemia in rats. *J. Pharmacol. Sci.* 2007;104(4):329-34.

316. Lu J, Wu D-M, Zheng Y-L, et al. Quercetin activates AMP-activated protein kinase by reducing PP2C expression protecting old mouse brain against high cholesterol-induced neurotoxicity. *J. Pathol.* 2010;222(2):199-212. doi:10.1002/path.2754.
317. Singh A, Naidu PS, Kulkarni SK. Reversal of aging and chronic ethanol-induced cognitive dysfunction by quercetin a bioflavonoid. *Free Radic. Res.* 2003;37(11):1245-52.
318. Tota S, Awasthi H, Kamat PK, Nath C, Hanif K. Protective effect of quercetin against intracerebral streptozotocin induced reduction in cerebral blood flow and impairment of memory in mice. *Behav. Brain Res.* 2010;209(1):73-9. doi:10.1016/j.bbr.2010.01.017.
319. Tongjaroenbuangam W, Ruksee N, Chantiratikul P, Pakdeenarong N, Kongbuntad W, Govitrapong P. Neuroprotective effects of quercetin, rutin and okra (Abelmoschus esculentus Linn.) in dexamethasone-treated mice. *Neurochem. Int.* 2011;59(5):677-85. doi:10.1016/j.neuint.2011.06.014.
320. Russo M, Spagnuolo C, Tedesco I, Bilotto S, Russo GL. The flavonoid quercetin in disease prevention and therapy: facts and fancies. *Biochem. Pharmacol.* 2012;83(1):6-15. doi:10.1016/j.bcp.2011.08.010.
321. Perez-Vizcaino F, Duarte J. Flavonols and cardiovascular disease. *Mol. Aspects Med.* 2010;31(6):478-94. doi:10.1016/j.mam.2010.09.002.
322. Jagtap S, Meganathan K, Wagh V, Winkler J, Hescheler J, Sachinidis A. Chemoprotective mechanism of the natural compounds, epigallocatechin-3-O-gallate, quercetin and curcumin against cancer and cardiovascular diseases. *Curr. Med. Chem.* 2009;16(12):1451-62.
323. Lamson DW, Brignall MS. Antioxidants and cancer, part 3: quercetin. *Altern. Med. Rev.* 2000;5(3):196-208.
324. Zamin LL, Filippi-Chiela EC, Dillenburg-Pilla P, Horn F, Salbego C, Lenz G. Resveratrol and quercetin cooperate to induce senescence-like growth arrest in C6 rat glioma cells. *Cancer Sci.* 2009;100(9):1655-62. doi:10.1111/j.1349-7006.2009.01215.x.
325. Wang K, Liu R, Li J, et al. Quercetin induces protective autophagy in gastric cancer cells: involvement of Akt-mTOR- and hypoxia-induced factor 1α-mediated signaling. *Autophagy* 2011;7(9):966-78.
326. Donnini S, Finetti F, Lusini L, et al. Divergent effects of quercetin conjugates on angiogenesis. *Br. J. Nutr.* 2006;95(5):1016-23.
327. Chirumbolo S. The role of quercetin, flavonols and flavones in modulating inflammatory cell function. *Inflamm. Allergy Drug Targets* 2010;9(4):263-85.
328. Labbé D, Provençal M, Lamy S, Boivin D, Gingras D, Béliveau R. The flavonols quercetin, kaempferol, and myricetin inhibit hepatocyte growth factor-induced medulloblastoma cell migration. *J. Nutr.* 2009;139(4):646-52. doi:10.3945/jn.108.102616.
329. Pambid MR, Berns R, Adomat HH, et al. Overcoming resistance to Sonic Hedgehog inhibition by targeting p90 ribosomal S6 kinase in pediatric medulloblastoma. *Pediatr. Blood Cancer* 2014;61(1):107-15. doi:10.1002/pbc.24675.
330. Diaz R, Golbourn B, Faria C, et al. Mechanism of action and therapeutic application of aurora kinase B inhibition in c-MYC overexpressing medulloblastoma. *Oncotarget* 2015;6(5):i1-i51.
331. Wang Y, Yi J, Chen X, Zhang Y, Xu M, Yang Z. The regulation of cancer cell migration by lung cancer cell-derived exosomes through TGF-β and IL-10. *Oncol. Lett.* 2016;11(2):1527-1530. doi:10.3892/ol.2015.4044.
332. Liao J, Liu R, Shi YJ, Yin LH, Pu YP. Exosome-shuttling microRNA-21 promotes cell migration and invasion-targeting PDCD4 in esophageal cancer. *Int. J. Oncol.* 2016;48(6):2567-2579. doi:10.3892/ijo.2016.3453.
333. Hoshino A, Costa-Silva B, Shen T-L, et al. Tumour exosome integrins determine organotropic metastasis. *Nature* 2015;527(7578):329-35. doi:10.1038/nature15756.
334. Peinado H, Alečković M, Lavotshkin S, et al. Melanoma exosomes educate bone marrow progenitor cells toward a pro-metastatic phenotype through MET. *Nat. Med.* 2012;18(6):883-91. doi:10.1038/nm.2753.
335. Costa-Silva B, Aiello NM, Ocean AJ, et al. Pancreatic cancer exosomes initiate pre-metastatic niche formation in the liver. *Nat Cell Biol* 2015;17(6):816-826. doi:10.1038/ncb3169.
336. Hosseini-Beheshti E, Choi W, Weiswald LB, et al. Exosomes confer pro-survival signals to alter the phenotype of prostate cells in their surrounding environment. *Oncotarget* 2016;7(12):14639-14658. doi:10.18632/oncotarget.7052.
337. Rodríguez M, Silva J, Herrera A, et al. Exosomes enriched in stemness/metastatic-related mRNAS promote oncogenic potential in breast cancer. *Oncotarget* 2015;6(38):40575-87. doi:10.18632/oncotarget.5818.
338. Setti M, Osti D, Richichi C, et al. Extracellular vesicle-mediated transfer of CLIC1 protein is a novel mechanism for the regulation of glioblastoma growth. *Oncotarget* 2015;6(31):31413-27. doi:10.18632/oncotarget.5105.

339. Skog J, Würdinger T, van Rijn S, et al. Glioblastoma microvesicles transport RNA and proteins that promote tumour growth and provide diagnostic biomarkers. *Nat. Cell Biol.* 2008;10(12):1470-6. doi:10.1038/ncb1800.
340. Baglio SR, Lagerweij T, Pérez Lanzón M, et al. Blocking tumor-educated MSC paracrine activity halts osteosarcoma progression. *Clin. Cancer Res.* 2017.
341. Wendler F, Favicchio R, Simon T, Alifrangis C, Stebbing J, Giamas G. Extracellular vesicles swarm the cancer microenvironment: from tumor–stroma communication to drug intervention. *Oncogene* 2017;36(7):877-884. doi:10.1038/onc.2016.253.
342. Godlewski J, Krichevsky AM, Johnson MD, Chiocca EA, Bronisz A. Belonging to a network--microRNAs, extracellular vesicles, and the glioblastoma microenvironment. *Neuro. Oncol.* 2015;17(5):652-62. doi:10.1093/neuonc/nou292.
343. Godlewski J, Ferrer-Luna R, Rooj AK, et al. MicroRNA Signatures and Molecular Subtypes of Glioblastoma: The Role of Extracellular Transfer. *Stem cell reports* 2017;8(6):1497-1505. doi:10.1016/j.stemcr.2017.04.024.
344. Bebawy M, Combes V, Lee E, et al. Membrane microparticles mediate transfer of P-glycoprotein to drug sensitive cancer cells. *Leuk. Off. J. Leuk. Soc. Am. Leuk. Res. Fund, U.K* 2009;23(9):1643-1649. doi:10.1038/leu.2009.76.
345. Corcoran C, Rani S, O'Brien K, et al. Docetaxel-Resistance in Prostate Cancer: Evaluating Associated Phenotypic Changes and Potential for Resistance Transfer via Exosomes. *PLoS One* 2012;7(12). doi:10.1371/journal.pone.0050999.
346. Ma X, Chen Z, Hua D, et al. Essential role for TrpC5-containing extracellular vesicles in breast cancer with chemotherapeutic resistance. *Proc. Natl. Acad. Sci. U. S. A.* 2014;111(17):6389-94. doi:10.1073/pnas.1400272111.
347. Takahashi K, Yan IK, Kogure T, Haga H, Patel T. Extracellular vesicle-mediated transfer of long non-coding RNA ROR modulates chemosensitivity in human hepatocellular cancer. *FEBS Open Bio* 2014;4:458-467. doi:10.1016/j.fob.2014.04.007.
348. Sousa D, Lima RT, Vasconcelos MH. Intercellular Transfer of Cancer Drug Resistance Traits by Extracellular Vesicles. *Trends Mol. Med.* 2015;21(10):595-608. doi:10.1016/j.molmed.2015.08.002.
349. Wiklander OPB, Nordin JZ, O'Loughlin A, et al. Extracellular vesicle in vivo biodistribution is determined by cell source, route of administration and targeting. *J. Extracell. vesicles* 2015;4(2015 SRC-GoogleScholar FG-0):26316. doi:10.3402/jev.v4.26316.
350. Prada I, Meldolesi J. Binding and fusion of extracellular vesicles to the plasma membrane of their cell targets. *Int. J. Mol. Sci.* 2016;17(8). doi:10.3390/ijms17081296.
351. Mulcahy LA, Pink RC, Carter DRF. Routes and mechanisms of extracellular vesicle uptake. *J. Extracell. vesicles* 2014;3(2014 SRC-GoogleScholar FG-0):1-14. doi:10.3402/jev.v3.24641.
352. Parolini I, Federici C, Raggi C, et al. Microenvironmental pH is a key factor for exosome traffic in tumor cells. *J. Biol. Chem.* 2009;284(49):34211-34222. doi:10.1074/jbc.M109.041152.
353. Escrevente C, Keller S, Altevogt P, Costa J. Interaction and uptake of exosomes by ovarian cancer cells. *BMC Cancer* 2011;11(2011 SRC-GoogleScholar FG-0):108. doi:10.1186/1471-2407-11-108.
354. Smyth TJ, Redzic JS, Graner MW, Anchordoquy TJ. Examination of the specificity of tumor cell derived exosomes with tumor cells in vitro. *Biochim. Biophys. Acta* 2014;1838(11):2954-2965. doi:10.1016/j.bbamem.2014.07.026.
355. Paggetti J, Haderk F, Seiffert M, et al. Exosomes released by chronic lymphocytic leukemia cells induce the transition of stromal cells into cancer-associated fi broblasts. *Blood* 2015;126(9):1106-1118. doi:10.1182/blood-2014-12-618025.The.
356. Lässer C, Alikhani VS, Ekström K, et al. Human saliva, plasma and breast milk exosomes contain RNA: uptake by macrophages. *J. Transl. Med.* 2011;9(1):9. doi:10.1186/1479-5876-9-9.
357. Svensson KJ, Christianson HC, Wittrup A, et al. Exosome uptake depends on ERK1/2-heat shock protein 27 signaling and lipid raft-mediated endocytosis negatively regulated by caveolin-1. *J. Biol. Chem.* 2013;288(24):17713-17724. doi:10.1074/jbc.M112.445403.
358. van Dongen HM, Masoumi N, Witwer KW, Pegtel DM. Extracellular Vesicles Exploit Viral Entry Routes for Cargo Delivery. *Microbiol. Mol. Biol. Rev.* 2016;80(2):369-86. doi:10.1128/MMBR.00063-15.
359. Wurdinger T, Gatson NN, Balaj L, Kaur B, Breakefield XO, Pegtel DM. Extracellular Vesicles and Their Convergence with Viral Pathways. *Adv. Virol.* 2012;2012(2012 SRC-GoogleScholar FG-0). doi:10.1155/2012/767694.

360. Miyanishi M, Tada K, Koike M, Uchiyama Y, Kitamura T, Nagata S. Identification of Tim4 as a phosphatidylserine receptor. *Nature* 2007;450(7168):435-439. doi:10.1038/nature06307.
361. Jethwa SA, Leah EJ, Zhang Q, et al. Exosomes bind autotaxin and act as a physiological delivery mechanism to stimulate LPA receptor signalling in cells. *J. Cell Sci.* 2016;129(August):3948-3957. doi:10.1242/jcs.184424.
362. Christianson HC, Svensson KJ, van Kuppevelt TH, Li J-P, Belting M. Cancer cell exosomes depend on cell-surface heparan sulfate proteoglycans for their internalization and functional activity. *Proc. Natl. Acad. Sci. U. S. A.* 2013;110(43):17380-5. doi:10.1073/pnas.1304266110.
363. Purushothaman A, Bandari SK, Liu J, Mobley JA, Brown EA, Sanderson RD. Fibronectin on the surface of myeloma cell-derived exosomes mediates exosome-cell interactions. *J. Biol. Chem.* 2016;291(4):1652-1663. doi:10.1074/jbc.M115.686295.
364. Al-Nedawi K. Intercellular transfer of the oncogenic receptor EGFRvIII by microvesicles derived from tumour cells. *Nat. Cell Biol.* 2008;10:619-624.
365. Antonyak MA, Li B, Boroughs LK, et al. Cancer cell-derived microvesicles induce transformation by transferring tissue transglutaminase and fibronectin to recipient cells. *Proc. Natl. Acad. Sci.* 2011;108(12):4852-4857. doi:10.1073/pnas.1017667108.
366. Johnson DR, O'Neill BP. Glioblastoma survival in the United States before and during the temozolomide era. *J. Neurooncol.* 2012;107(2):359-364. doi:10.1007/s11060-011-0749-4.
367. Théry C, Amigorena S. Isolation and characterization of exosomes from cell culture supernatants and biological fluids. In: *Current Protocols in Cell Biology*.Vol supplement.; 2006:1-29.
368. Livshts MA, Khomyakova E, Evtushenko EG, et al. Isolation of exosomes by differential centrifugation: Theoretical analysis of a commonly used protocol. *Sci. Rep.* 2015;5(2015 SRC-GoogleScholar FG-0). doi:10.1038/srep17319.
369. Sato A, Sunayama J, Matsuda K, et al. MEK-ERK Signaling Dictates DNA-Repair Gene MGMT Expression and Temozolomide Resistance of Stem-Like Glioblastoma Cells via the MDM2-p53 Axis. *Stem Cells* 2011;29(12):1942-1951. doi:10.1002/stem.753.
370. Islam SA, Ling MF, Leung J, Shreffler WG, Luster AD. Identification of human CCR8 as a CCL18 receptor. *J. Exp. Med.* 2013;210 SRC-:1889-1898.
371. Lee S, Tiffany HL, King L, et al. CCR8 on Human Thymocytes Functions as a Human Immunodeficiency Virus Type 1 Coreceptor CCR8 on Human Thymocytes Functions as a Human Immunodeficiency Virus Type 1 Coreceptor. *J. Virol.* 2000;74 SRC-:6946-6952. doi:10.1128/JVI.74.15.6946-6952.2000.Updated.
372. Calado M. Coreceptor usage by HIV-1 and HIV-2 primary isolates: the relevance of CCR8 chemokine receptor as an alternative coreceptor. *Virology* 2010;408:174-182.
373. Eruslanov E. Expansion of CCR8(+) inflammatory myeloid cells in cancer patients with urothelial and renal carcinomas. *Clin. cancer Res. an Off. J. Am. Assoc. Cancer Res.* 2013;19 SRC-:1670-1680.
374. Louahed J. CCR8-dependent activation of the RAS/MAPK pathway mediates anti-apoptotic activity of I-309/CCL1 and vMIP-I. *Eur. J. Immunol.* 2003;33:494-501.
375. Das S. Tumor cell entry into the lymph node is controlled by CCL1 chemokine expressed by lymph node lymphatic sinuses. *J. Exp. Med.* 2013;210 SRC-:1509-1528.
376. Lüttichau HR, Stine J, Boesen TP, et al. A highly selective CC chemokine receptor (CCR)8 antagonist encoded by the poxvirus molluscum contagiosum. *J. Exp. Med.* 2000;191(1):171-80.
377. Oshio T, Kawashima R, Kawamura YI, Hagiwara T, Mizutani N. Chemokine Receptor CCR8 Is Required for Lipopolysaccharide-Triggered Cytokine Production in Mouse Peritoneal Macrophages. 2014;9(4). doi:10.1371/journal.pone.0094445.
378. Chou T, Talalay P. C. & Quantitative analysis of dose-effect relationships: the combined effects of multiple drugs or enzyme inhibitors. *Adv. Enzyme Regul.* 1984;22:27-55.
379. Escrevente C, Grammel N, Kandzia S, et al. Sialoglycoproteins and N-Glycans from Secreted Exosomes of Ovarian Carcinoma Cells. *PLoS One* 2013;8(10). doi:10.1371/journal.pone.0078631.
380. Batista BS, Eng WS, Pilobello KT, Mahal LK. Hendricks-Muñoz, K.D. & Identification of a Conserved Glycan Signature for Microvesicles. *J. Proteome Res.* 2011;10:4624-4633.
381. Fukui S, Feizi T, Galustian C, Lawson AM, Chai W. Oligosaccharide microarrays for high-throughput detection and specificity assignments of carbohydrate-protein interactions. *Nat. Biotechnol.* 2002;20:1011-1017.
382. Handel TM, Johnson Z, Crown SE, Lau EK, Proudfoot AE. Regulation of protein function by glycosaminoglycans-as exemplified by chemokines. *Annu. Rev. Biochem.* 2005;74 SRC-:385-410.

383. Raedts J, Kengen SW, der Oost J. van Occurrence of L-iduronic acid and putative D-glucuronyl C5-epimerases in prokaryotes. *Glycoconj. J.* 2011;28:57-66.
384. Bülow HE, Hobert O. The Molecular Diversity of Glycosaminoglycans Shapes Animal Development. *Annu. Rev. Cell Dev. Biol.* 2006;22(1):375-407. doi:10.1146/annurev.cellbio.22.010605.093433.
385. Hook M, Kjellen L, Johansson S. Cell-surface glycosaminoglycans. *Annu. Rev. Biochem.* 1984;53:847-869.
386. Kuschen GS V, Coulin F, Power CA, et al. Glycosaminoglycans interact selectively with chemokines and modulate receptor binding and cellular responses. *Biochemistry* 1999;38(39):12959-12968. doi:10.1021/bi990711d.
387. Balaj L. Heparin affinity purification of extracellular vesicles. *Sci Rep 5* 10266(2015 SRC-GoogleScholar FG-0).
388. Gabriely G, Yi M, Narayan RS, et al. Human glioma growth is controlled by microRNA-10b. *Cancer Res.* 2011;71(10):3563-72. doi:10.1158/0008-5472.CAN-10-3568.
389. Chan JA, Krichevsky AM, Kosik KS, Chan JA, Krichevsky AM, Kosik KS. MicroRNA-21 Is an Antiapoptotic Factor in Human Glioblastoma Cells MicroRNA-21 Is an Antiapoptotic Factor in Human. *Cancer Res.* 2005;65(14):6029-6033. doi:10.1158/0008-5472.CAN-05-0137.
390. Wang K, Wang X, Zou J, et al. MiR-92b controls glioma proliferation and invasion through regulating Wnt/beta-catenin signaling via Nemo-like kinase. *Neuro. Oncol.* 2013;15(5):578-588. doi:10.1093/neuonc/not004.
391. Niu H, Wang K, Zhang A, et al. miR-92a is a critical regulator of the apoptosis pathway in glioblastoma with inverse expression of BCL2L11. *Oncol. Rep.* 2012;28(5):1771-1777. doi:10.3892/or.2012.1970.
392. Denny BJ, Wheelhouse RT, Stevens MF, Tsang LL, Slack J a. NMR and molecular modeling investigation of the mechanism of activation of the antitumor drug temozolomide and its interaction with DNA. *Biochemistry* 1994;33:9045-9051. doi:10.1021/bi00197a003.
393. Drabløs, F. Alkylation damage in DNA and RNA—repair mechanisms and medical significance. 2004;3 SRC-G:1389-1407.
394. Friedman HS, Kerby T, Calvert H. Temozolomide and Treatment of Malignant Glioma. *Clin. Cancer Res.* 2000;6 SRC-G:2585-2597.
395. Messaoudi K, Clavreul A, Lagarce F. Toward an effective strategy in glioblastoma treatment. Part I: resistance mechanisms and strategies to overcome resistance of glioblastoma to temozolomide. *Drug Discov. Today* 2015;20(7):899-905. doi:10.1016/j.drudis.2015.02.011.
396. Hiddingh L. EFEMP1 induces gamma-secretase/Notch-mediated temozolomide resistance in glioblastoma. *Oncotarget* 2014;5 SRC-G:363-374.
397. Hiddingh L, Raktoe RS, Jeuken J, et al. Identification of temozolomide resistance factors in glioblastoma via integrative miRNA/mRNA regulatory network analysis. *Sci. Rep.* 2014;4(2014 SRC-GoogleScholar FG-0):5260. doi:10.1038/srep05260.
398. Kaina B, Christmann M, Naumann S, Roos WP. MGMT: Key node in the battle against genotoxicity, carcinogenicity and apoptosis induced by alkylating agents. *DNA Repair (Amst).* 2007;6(8):1079-1099. doi:10.1016/j.dnarep.2007.03.008.
399. Shao H, Chung J, Lee K, et al. Chip-based analysis of exosomal mRNA mediating drug resistance in glioblastoma. *Nat. Commun.* 2015;6(May):6999. doi:10.1038/ncomms7999.
400. Meckes DG, Raab-Traub N. Microvesicles and viral infection. *J. Virol.* 2011;85(24):12844-54. doi:10.1128/JVI.05853-11.
401. Trkola A, Gordon C, Matthews J, et al. The CC-chemokine RANTES increases the attachment of human immunodeficiency virus type 1 to target cells via glycosaminoglycans and also activates a signal transduction pathway that enhances viral infectivity. *J Virol* 1999;73(8):6370-6379.
402. Dragic T. HIV-1 entry into CD4+ cells is mediated by the chemokine receptor CC-CKR-5. *Nature* 1996;381 SRC-:667-673.
403. Feng Y, Broder CC, Kennedy PE, Berger EA. HIV-1 Entry Cofactor: Functional cof a Seven-Transmembrane, Receptor. Science . 1996;272 SRC-:872-877.
404. Deng H, Liu R, Ellmeier W, et al. Identification of a major co-receptor for primary isolates of HIV-1. *Nature* 1996;381(6584):661-666. doi:10.1038/381661a0.
405. Cocchi F, Devico AL, Garzinodemo A, Arya SK, Gallo RC, Lusso P. Identification of Rantes, Mip-1-Alpha, and Mip-1-Beta As the Major Hiv-Suppressive Factors Produced By Cd8(+) T-Cells. *Science (80-.).* 1995;270(5243):1811-1815.
406. Trkola A, Paxton WA, Monard SP, et al. Genetic subtype-independent inhibition of human immunodeficiency virus type 1 replication by CC and CXC chemokines. *J Virol* 1998;72(1):396-404.

407. Cheng W. Bioinformatic profiling identifies an immune-related risk signature for glioblastoma. *Neurology* 2016;86:2226-2234.
408. Atai NA, Balaj L, Van Veen H, et al. Heparin blocks transfer of extracellular vesicles between donor and recipient cells. *J. Neurooncol.* 2013;115(3):343-351. doi:10.1007/s11060-013-1235-y.
409. Franzen CA, Simms PE, Van Huis AF, Foreman KE, Kuo PC, Gupta GN. Characterization of uptake and internalization of exosomes by bladder cancer cells. *Biomed Res. Int.* 2014;2014(2014 SRC-GoogleScholar FG-0). doi:10.1155/2014/619829.
410. Sento S, Sasabe E, Yamamoto T, LoS ONE. Application of a Persistent Heparin Treatment Inhibits the Malignant Potential of Oral Squamous Carcinoma Cells Induced by Tumor Cell-Derived Exosomes. *P11 e* 148454(2016 SRC-GoogleScholar FG-0).
411. Sukreet S, Zhang H, Adamec J, Cui J, Zempleni J. Identification of Glycoproteins on the Surface of Cow's Milk Exosomes that Mediate the Uptake of Exosomes into Human Colon Carcinoma Caco-2 Cells. *30 125* 1(2016 SRC-GoogleScholar FG-0).
412. Soler D, Chapman TR, Poisson LR, et al. CCR8 Expression Identifies CD4 Memory T Cells Enriched for FOXP3+ Regulatory and Th2 Effector Lymphocytes. *J. Immunol.* 2006;177(10):6940-6951. doi:10.4049/jimmunol.177.10.6940.
413. Connolly S, Skrinjar M, Rosendahl A. Orally bioavailable allosteric CCR8 antagonists inhibit dendritic cell, T cell and eosinophil migration. *Biochem. Pharmacol.* 2012;83(6):778-787. doi:10.1016/j.bcp.2011.12.021.
414. De Monte L, Reni M, Tassi E, et al. Intratumor T helper type 2 cell infiltrate correlates with cancer-associated fibroblast thymic stromal lymphopoietin production and reduced survival in pancreatic cancer. *J. Exp. Med.* 2011;208(3):469-78. doi:10.1084/jem.20101876.
415. Hoelzinger DB, Smith SE, Mirza N, Dominguez AL, Manrique SZ, Lustgarten J. Blockade of CCL1 Inhibits T Regulatory Cell Suppressive Function Enhancing Tumor Immunity without Affecting T Effector Responses. *J. Immunol.* 2010;184(12).
416. Chen J, Yao Y, Gong C, et al. CCL18 from Tumor-Associated Macrophages Promotes Breast Cancer Metastasis via PITPNM3. *Cancer Cell* 2011;19(4):541-555. doi:10.1016/j.ccr.2011.02.006.
417. Li D, Duell EJ, Yu K, et al. Pathway analysis of genome-wide association study data highlights pancreatic development genes as susceptibility factors for pancreatic cancer. *Carcinogenesis* 2012;33(7):1384-1390. doi:10.1093/carcin/bgs151.
418. Burkholder B, Huang R-Y, Burgess R, et al. Tumor-induced perturbations of cytokines and immune cell networks. *Biochim. Biophys. Acta - Rev. Cancer* 2014;1845(2):182-201. doi:10.1016/j.bbcan.2014.01.004.
419. Hood JL, San Roman S, Wickline SA. Exosomes released by melanoma cells prepare sentinel lymph nodes for tumor metastasis. *Cancer Res.* 2011;71(11):3792-3801. doi:10.1158/0008-5472.CAN-10-4455.
420. Achyut BR, Shankar A, Iskander ASM, et al. Chimeric Mouse model to track the migration of bone marrow derived cells in glioblastoma following anti-angiogenic treatments. *Cancer Biol. Ther.* 2016;17(3):280-90. doi:10.1080/15384047.2016.1139243.
421. Wu J, He Y, Yang Z, et al. 3D BrainCV: simultaneous visualization and analysis of cells and capillaries in a whole mouse brain with one-micron voxel resolution. *Neuroimage* 2014;87:199-208. doi:10.1016/j.neuroimage.2013.10.036.
422. Wälchli T, Mateos JM, Weinman O, et al. Quantitative assessment of angiogenesis, perfused blood vessels and endothelial tip cells in the postnatal mouse brain. *Nat. Protoc.* 2015;10(1):53-74. doi:10.1038/nprot.2015.002.
423. Helmchen F, Denk W. Deep tissue two-photon microscopy. *Nat. Methods* 2005;2(12):932-940. doi:10.1038/nmeth818.
424. Kobat D, Durst ME, Nishimura N, Wong AW, Schaffer CB, Xu C. Deep tissue multiphoton microscopy using longer wavelength excitation. *Opt. Express* 2009;17(16):13354. doi:10.1364/OE.17.013354.
425. Spalteholz W. *Über Das Durchsichtigmachen von Menschlichen Und Tierischen Präparaten Und Seine Theoretischen Bedingungen*. Leipzig: Hierzel S, Leipzig; 1914.
426. Hama H, Hioki H, Namiki K, et al. ScaleS: an optical clearing palette for biological imaging. *Nat. Neurosci.* 2015;18(10):1518-1529. doi:10.1038/nn.4107.
427. Ertürk A, Becker K, Jährling N, et al. Three-dimensional imaging of solvent-cleared organs using 3DISCO. *Nat. Protoc.* 2012;7(11):1983-95. doi:10.1038/nprot.2012.119.
428. Ke M-T, Fujimoto S, Imai T. SeeDB: a simple and morphology-preserving optical clearing agent for neuronal circuit reconstruction. *Nat. Neurosci.* 2013;16(8):1154-61. doi:10.1038/nn.3447.
429. Chung K, Deisseroth K. CLARITY for mapping the nervous system. *Nat. Methods* 2013;10(6):508-13. doi:10.1038/nmeth.2481.

430. Tang JCY, Szikra T, Kozorovitskiy Y, et al. A Nanobody-Based System Using Fluorescent Proteins as Scaffolds for Cell-Specific Gene Manipulation. *Cell* 2013;154(4):928-939.
431. Costantini I, Ghobril J-P, Di Giovanna AP, et al. A versatile clearing agent for multi-modal brain imaging. *Sci. Rep.* 2015;5:9808. doi:10.1038/srep09808.
432. Pan C, Cai R, Quacquarelli FP, et al. Shrinkage-mediated imaging of entire organs and organisms using uDISCO. *Nat. Methods* 2016. doi:10.1038/nmeth.3964.
433. Peng H, Bria A, Zhou Z, Iannello G, Long F. Extensible visualization and analysis for multidimensional images using Vaa3D. *Nat. Protoc.* 2014;9(1):193-208. doi:10.1038/nprot.2014.011.
434. Bjornsson CS, Lin G, Al-Kofahi Y, et al. Associative image analysis: a method for automated quantification of 3D multi-parameter images of brain tissue. *J. Neurosci. Methods* 2008;170(1):165-78. doi:10.1016/j.jneumeth.2007.12.024.
435. de Chaumont F, Dallongeville S, Chenouard N, et al. Icy: an open bioimage informatics platform for extended reproducible research. *Nat. Methods* 2012;9(7):690-6. doi:10.1038/nmeth.2075.
436. Kutzing MK, Langhammer CG, Luo V, Lakdawala H, Firestein BL. Automated Sholl analysis of digitized neuronal morphology at multiple scales. *J. Vis. Exp.* 2010;(45). doi:10.3791/2354.
437. Wakimoto H, Kesari S, Farrell CJ, et al. Human glioblastoma-derived cancer stem cells: establishment of invasive glioma models and treatment with oncolytic herpes simplex virus vectors. *Cancer Res.* 2009;69(8):3472-81. doi:10.1158/0008-5472.CAN-08-3886.
438. Scheepbouwer C, Meyer S, Burggraaf MJ, Jose J, Molthoff CFM. A Multimodal Imaging Approach for Longitudinal Evaluation of Bladder Tumor Development in an Orthotopic Murine Model. *PLoS One* 2016;11(8). doi:10.1371/journal.pone.0161284.
439. Renier N, Adams EL, Kirst C, et al. Mapping of Brain Activity by Automated Volume Analysis of Immediate Early Genes. *Cell* 2016;165(7):1789-1802. doi:10.1016/j.cell.2016.05.007.
440. Preibisch S, Saalfeld S, Tomancak P. Globally optimal stitching of tiled 3D microscopic image acquisitions. *Bioinformatics* 2009;25(11):1463-5. doi:10.1093/bioinformatics/btp184.
441. Wesseling P, van der Laak JA, de Leeuw H, Ruiter DJ, Burger PC. Quantitative immunohistological analysis of the microvasculature in untreated human glioblastoma multiforme. Computer-assisted image analysis of whole-tumor sections. *J. Neurosurg.* 1994;81(6):902-9. doi:10.3171/jns.1994.81.6.0902.
442. Rai S, Nejadhamzeeigilani Z, Gutowski NJ, Whatmore JL. Loss of the endothelial glycocalyx is associated with increased E-selectin mediated adhesion of lung tumour cells to the brain microvascular endothelium. *J. Exp. Clin. Cancer Res.* 2015;34. doi:10.1186/s13046-015-0223-9.
443. Osswald M, Jung E, Sahm F, et al. Brain tumour cells interconnect to a functional and resistant network. *Nature* 2015;528(7580):93-98. doi:10.1038/nature16071.
444. Vogt N. Transparency in large tissue samples. *Nat. Methods* 2015;12(1):2015.
445. Hiromitsu S, Jin K, Emiko S, et al. Novel method for immunofluorescence staining of mammalian eggs using non-contact alternating-current electric-field mixing of microdroplets. *Sci. Rep.* 2015;5:15371. doi:10.1038/srep15371.
446. Caretti V, Sewing ACP, Lagerweij T, et al. Human pontine glioma cells can induce murine tumors. *Acta Neuropathol.* 2014;127(6):897-909. doi:10.1007/s00401-014-1272-4.
447. Michalak Z, Lebrun A, Miceli M Di, et al. IgG Leakage May Contribute to Neuronal Dysfunction in Drug-Refractory Epilepsies With Blood-Brain Barrier Disruption. *J. Neuropathol. Exp. Neurol.* 2012;71(9):826-838. doi:10.1097/NEN.0b013e31826809a6.
448. Jährling N, Becker K, Dodt H. 3D-reconstruction of blood vessels by ultramicroscopy. *Organogenesis* 2009;5(4):227-230. doi:10.4161/org.5.4.10403.
449. Minamikawa T, Miyake T, Takamatsu T, Fujita S. A new method of lectin histochemistry for the study of brain angiogenesis - Lectin angiography. *Histochemistry* 1987;87(4):317-320. doi:10.1007/BF00492584.
450. Robertson RT, Levine ST, Haynes SM, et al. Use of labeled tomato lectin for imaging vasculature structures. *Histochem. Cell Biol.* 2014;143(2):225-234. doi:10.1007/s00418-014-1301-3.
451. Villacampa N, Almolda B, González B, Castellano B. Tomato lectin histochemistry for microglial visualization. *Methods Mol. Biol.* 2013;1041:261-79. doi:10.1007/978-1-62703-520-0_23.
452. Marx V. Microscopy: seeing through tissue. *Nat. Methods* 2014;11(12):1209-1214. doi:10.1038/nmeth.3181.
453. Scherer HJ. Structural Development in Gliomas. *Am. J. Cancer* 1938;34(3).
454. Cuddapah VA, Robel S, Watkins S, Sontheimer H. A neurocentric perspective on glioma invasion. *Nat. Rev. Neurosci.* 2014;15(7):455-465. doi:10.1038/nrn3765.

455. Osswald M, Solecki G, Wick W, Winkler F. A malignant cellular network in gliomas: potential clinical implications. *Neuro. Oncol.* 2016;18(4):479-85. doi:10.1093/neuonc/now014.
456. Landelijke-Werkgroep-Neuro-Oncologie. Oncoline - richtlijnen oncologische zorg. 2017. Available at: www.oncoline.nl/gliomen.
457. Pardridge WM. The blood-brain barrier: bottleneck in brain drug development. *NeuroRx* 2005;2(1):3-14. doi:10.1602/neurorx.2.1.3.
458. Hoosain FG, Choonara YE, Tomar LK, et al. Bypassing P-Glycoprotein Drug Efflux Mechanisms: Possible Applications in Pharmacoresistant Schizophrenia Therapy. *Biomed Res. Int.* 2015;2015. doi:10.1155/2015/484963.
459. Martins IF, Teixeira AL, Pinheiro L, Falcao AO. A Bayesian approach to in Silico blood-brain barrier penetration modeling. *J. Chem. Inf. Model.* 2012;52:1686-1697. doi:10.1021/ci300124c.
460. de Gooijer MC, Zhang P, Thota N, et al. P-glycoprotein and breast cancer resistance protein restrict the brain penetration of the CDK4/6 inhibitor palbociclib. *Invest. New Drugs* 2015;33(5):1012-9. doi:10.1007/s10637-015-0266-y.
461. Callaghan R, Luk F, Bebawy M. Special Section on Transporters in Toxicity and Disease—Minireview Inhibition of the Multidrug Resistance P-Glycoprotein: Time for a Change of Strategy? *DRUG Metab. Dispos. Drug Metab Dispos* 2014;42:623-631. doi:10.1124/dmd.113.056176.
462. Chae GS, Lee JS, Kim SH, et al. Enhancement of the stability of BCNU using self-emulsifying drug delivery systems (SEDDS) and in vitro antitumor activity of self-emulsified BCNU-loaded PLGA wafer. *Int. J. Pharm.* 2005;301(1-2):6-14. doi:10.1016/j.ijpharm.2005.03.034.
463. Ridler C. Neuro-oncology: New therapeutic targets for diffuse intrinsic pontine glioma. *Nat. Rev. Neurol.* 2017. doi:10.1038/nrneurol.2017.39.
464. Mohammad F, Weissmann S, Leblanc B, et al. EZH2 is a potential therapeutic target for H3K27M-mutant pediatric gliomas. *Nat. Med.* 2017;23(4):483-492. doi:10.1038/nm.4293.
465. Piunti A, Hashizume R, Morgan MA, et al. Therapeutic targeting of polycomb and BET bromodomain proteins in diffuse intrinsic pontine gliomas. *Nat. Med.* 2017;23(4):493-500. doi:10.1038/nm.4296.
466. deVries NA, Hulsman D, Akhtar W, et al. Prolonged Ezh2 Depletion in Glioblastoma Causes a Robust Switch in Cell Fate Resulting in Tumor Progression. *Cell Rep.* 2015;10(3):383-397. doi:10.1016/j.celrep.2014.12.028.
467. Bijnsdorp I V, Hodzic J, Lagerweij T, et al. miR-129-3p controls centrosome number in metastatic prostate cancer cells by repressing CP110. *Oncotarget* 2016. doi:10.18632/oncotarget.7572.
468. Tannous BABA, Kerami M, Van Der Stoop PMPM, et al. Effects of the selective MPS1 inhibitor MPS1-IN-3 on glioblastoma sensitivity to antimitotic drugs. *J. Natl. Cancer Inst.* 2013;105(17):1322-1331. doi:10.1093/jnci/djt168.
469. Montaldi AP, Godoy PRD V, Sakamoto-Hojo ET. APE1/REF-1 down-regulation enhances the cytotoxic effects of temozolomide in a resistant glioblastoma cell line. *Mutat. Res. Genet. Toxicol. Environ. Mutagen.* 2015;793:19-29. doi:10.1016/j.mrgentox.2015.06.001.
470. De Felice F, Musio D, Cassese R, Gravina GL, Tombolini V. New approaches in glioblastoma multiforme: the potential role of immune-check point inhibitors. *Curr. Cancer Drug Targets* 2016.
471. Mukherjee S. *The Emperor of All Maladies*. First edit. London: Fourth Estate, HarperCollins publishers; 2011.
472. Vogelstein B, Kinzler KW. The Path to Cancer --Three Strikes and You're Out. *N. Engl. J. Med.* 2015;373(20):1895-8. doi:10.1056/NEJMp1508811.
473. Soeda A, Hara A, Kunisada T, Yoshimura S, Iwama T, Park DM. The Evidence of Glioblastoma Heterogeneity. *Sci. Rep.* 2015;5:7979. doi:10.1038/srep07979.
474. Jakubowicz-Gil J, Langner E, Rzeski W. Kinetic studies of the effects of Temodal and quercetin on astrocytoma cells. *Pharmacol. Rep.* 2011;63(2):403-16.
475. Hu J, Wang J, Wang G, Yao Z, Dang X. Pharmacokinetics and antitumor efficacy of DSPE-PEG2000 polymeric liposomes loaded with quercetin and temozolomide: Analysis of their effectiveness in enhancing the chemosensitization of drug-resistant glioma cells. *Int. J. Mol. Med.* 2016;37(3):690-702. doi:10.3892/ijmm.2016.2458.
476. Matias D, Balça-Silva J, Dubois LG, et al. Dual treatment with shikonin and temozolomide reduces glioblastoma tumor growth, migration and glial-to-mesenchymal transition. *Cell. Oncol.* 2017:1-15. doi:10.1007/s13402-017-0320-1.

477. Xavier CPR, Lima CF, Rohde M, Pereira-Wilson C. Quercetin enhances 5-fluorouracil-induced apoptosis in MSI colorectal cancer cells through p53 modulation. *Cancer Chemother. Pharmacol.* 2011;68(6):1449-1457. doi:10.1007/s00280-011-1641-9.
478. Siegelin MD, Reuss DE, Habel A, Rami A, von Deimling A. Quercetin promotes degradation of survivin and thereby enhances death-receptor-mediated apoptosis in glioma cells. *Neuro. Oncol.* 2009;11(2):122-31. doi:10.1215/15228517-2008-085.
479. Kim EJ, Choi CH, Park JY, Kang SK, Kim YK. Underlying mechanism of quercetin-induced cell death in human glioma cells. *Neurochem. Res.* 2008;33(6):971-979. doi:10.1007/s11064-007-9416-8.
480. Sherwood LM, Parris EE, Folkman J. Tumor Angiogenesis: Therapeutic Implications. *N. Engl. J. Med.* 1971;285(21):1182-1186. doi:10.1056/NEJM197111182852108.
481. Aldape K, Zadeh G, Mansouri S, Reifenberger G, von Deimling A. Glioblastoma: pathology, molecular mechanisms and markers. *Acta Neuropathol.* 2015;129(6):829-48. doi:10.1007/s00401-015-1432-1.
482. Rahmathulla G, Hovey EJ, Hashemi-Sadraei N, Ahluwalia MS. Bevacizumab in high-grade gliomas: a review of its uses, toxicity assessment, and future treatment challenges. *Onco. Targets. Ther.* 2013;6:371-89. doi:10.2147/OTT.S38628.
483. Wilson TA, Karajannis MA, Harter DH. Glioblastoma multiforme: State of the art and future therapeutics. *Surg. Neurol. Int.* 2014;5:64. doi:10.4103/2152-7806.132138.
484. Jain RK. Normalization of Tumor Vasculature: An Emerging Concept in Antiangiogenic Therapy. *Science (80-.).* 2005;307(5706):58-62. doi:10.1126/science.1104819.
485. Veldhuijzen van Zanten SEM, Jansen M, van Vuurden DG, et al. HG-009. MOLECULAR DRUG IMAGING: PIONEERING WORK IN CHILDREN WITH DIFFUSE INTRINSIC PONTINE GLIOMA. *Neuro. Oncol.* 2014;16 (Suppl:i40-59.
486. Friedl P, Gilmour D. Collective cell migration in morphogenesis, regeneration and cancer. *Nat. Rev. Mol. Cell Biol.* 2009;10(7):445-457. doi:10.1038/nrm2720.
487. Aceto N, Bardia A, Miyamoto DT, et al. Circulating Tumor Cell Clusters Are Oligoclonal Precursors of Breast Cancer Metastasis. *Cell* 2014;158(5):1110-1122. doi:10.1016/j.cell.2014.07.013.
488. Extracellular Vesicles. Available at: www.extracellularvesicles.org. Accessed June 20, 2012.
489. Nilsson RJA, Balaj L, Hulleman E, et al. Blood platelets contain tumor-derived RNA biomarkers. *Blood* 2011;118(13):3680-3. doi:10.1182/blood-2011-03-344408.
490. Bagley JA, Reumann D, Bian S, L?vi-Strauss J, Knoblich JA. Fused cerebral organoids model interactions between brain regions. *Nat. Methods* 2017. doi:10.1038/nmeth.4304.
491. Lancaster MA, Corsini NS, Wolfinger S, et al. Guided self-organization and cortical plate formation in human brain organoids. *Nat. Biotechnol.* 2017. doi:10.1038/nbt.3906.
492. Gruionu G, Bazou D, Maimon N, et al. Implantable tissue isolation chambers for analyzing tumor dynamics in vivo. *Lab Chip* 2016;16(10):1840-51. doi:10.1039/c6lc00237d.
493. Griep LM, Wolbers F, de Wagenaar B, et al. BBB ON CHIP: microfluidic platform to mechanically and biochemically modulate blood-brain barrier function. *Biomed. Microdevices* 2013;15(1):145-150. doi:10.1007/s10544-012-9699-7.
494. Xie Y, Bergström T, Jiang Y, et al. The Human Glioblastoma Cell Culture Resource: Validated Cell Models Representing All Molecular Subtypes. *EBioMedicine* 2015;2(10):1351-63. doi:10.1016/j.ebiom.2015.08.026.
495. Jacobsen PF, Jenkyn DJ, Papadimitriou JM. Establishment of a human medulloblastoma cell line and its heterotransplantation into nude mice. *J. Neuropathol. Exp. Neurol.* 1985;44(5):472-85.
496. Friedman HS, Burger PC, Bigner SH, et al. Establishment and characterization of the human medulloblastoma cell line and transplantable xenograft D283 Med. *J. Neuropathol. Exp. Neurol.* 1985;44(6):592-605.
497. Pontén J, Macintyre EH. Long term culture of normal and neoplastic human glia. *Acta Pathol. Microbiol. Scand.* 1968;74(4):465-86.
498. Allen M, Bjerke M, Edlund H, Nelander S, Westermark B. Origin of the U87MG glioma cell line: Good news and bad news. *Sci. Transl. Med.* 2016;8(354):354re3-354re3. doi:10.1126/scitranslmed.aaf6853.
499. Torsvik A, Stieber D, Enger PØ, et al. U-251 revisited: genetic drift and phenotypic consequences of long-term cultures of glioblastoma cells. *Cancer Med.* 2014;3(4):812-24. doi:10.1002/cam4.219.
500. Hingtgen S, Figueiredo J-L, Farrar C, et al. Real-time multi-modality imaging of glioblastoma tumor resection and recurrence. *J. Neurooncol.* 2013;111(2):153-61. doi:10.1007/s11060-012-1008-z.
501. Biomarkers Definitions Working Group. Biomarkers and surrogate endpoints: Preferred definitions and conceptual framework. *Clin. Pharmacol. Ther.* 2001;69(3):89-95. doi:10.1067/mcp.2001.113989.

502. Group F-NBW. *BEST (Biomarkers, EndpointS, and Other Tools) Resource*. Food and Drug Administration (US); 2016.
503. Skwarski M, Higgins GS. A new roadmap to improve translation of imaging biomarkers. *Br. J. Cancer* 2016;115(12):1443-1444. doi:10.1038/bjc.2016.374.
504. Ussui VM, Wallace MB, Ussui VM, Wallace MB. Confocal Endomicroscopy of Colorectal Polyps. *Gastroenterol. Res. Pract.* 2012;2012:1-6. doi:10.1155/2012/545679.
505. Yeh AT, Choi B, Nelson JS, Tromberg BJ. Reversible Dissociation of Collagen in Tissues. *J. Invest. Dermatol.* 2003;121(6):1332-1335. doi:10.1046/j.1523-1747.2003.12634.x.
506. Genina E a., Bashkatov AN, Tuchin V V. Glucose-Indused Optical Clearing Effects in Tissues and Blood. *Handb. Opt. Sens. Glucose Biol. Fluids Tissues Ser. Med. Phys. Biomed. Eng.* 2009:657-692.
507. Wilson CM, Gaber MW, Sabek OM, Zawaski J a, Merchant TE. Radiation-induced astrogliosis and blood-brain barrier damage can be abrogated using anti-TNF treatment. *Int. J. Radiat. Oncol. Biol. Phys.* 2009;74(3):934-41. doi:10.1016/j.ijrobp.2009.02.035.
508. Badr C. Bioluminescence imaging in glioblastoma: monitoring of biological processes and novel therapeutics. In: *PhD Thesis*.; 2010:10-29.
509. Hyare H, Thust S, Rees J. Advanced MRI Techniques in the Monitoring of Treatment of Gliomas. *Curr. Treat. Options Neurol.* 2017;19(3):11. doi:10.1007/s11940-017-0445-6.
510. Lombard A, Goffart N, Rogister B, Lombard A, Goffart N, Rogister B. Glioblastoma Circulating Cells: Reality, Trap or Illusion? *Stem Cells Int.* 2015;2015:182985. doi:10.1155/2015/182985.
511. Fabbri M, Paone A, Calore F, et al. MicroRNAs bind to Toll-like receptors to induce prometastatic inflammatory response. *Proc. Natl. Acad. Sci. U. S. A.* 2012;109(31):E2110-6. doi:10.1073/pnas.1209414109.
512. Best MG, Sol N, Kooi I, et al. RNA-Seq of Tumor-Educated Platelets Enables Blood-Based Pan-Cancer, Multiclass, and Molecular Pathway Cancer Diagnostics. *Cancer Cell* 2015;28(5):666-676. doi:10.1016/j.ccell.2015.09.018.
513. Saadatpour L, Fadaee E, Fadaei S, et al. Glioblastoma: exosome and microRNA as novel diagnosis biomarkers. *Cancer Gene Ther.* 2016;23(12):415-418. doi:10.1038/cgt.2016.48.
514. Lamb LS, Bowersock J, Dasgupta A, et al. Engineered drug resistant γδ T cells kill glioblastoma cell lines during a chemotherapy challenge: a strategy for combining chemo- and immunotherapy. *PLoS One* 2013;8(1):e51805. doi:10.1371/journal.pone.0051805.
515. Schuster M, Nechansky A, Kircheis R. Cancer immunotherapy. *Biotechnol. J.* 2006;1(2):138-147. doi:10.1002/biot.200500044.
516. Kindy MS, Yu J, Zhu H, Smith MT, Gattoni-Celli S. A therapeutic cancer vaccine against GL261 murine glioma. *J. Transl. Med.* 2016;14(1):1. doi:10.1186/s12967-015-0757-9.
517. Renner DN, Malo CS, Jin F, Parney IF, Pavelko KD, Johnson AJ. Improved Treatment Efficacy of Antiangiogenic Therapy when Combined with Picornavirus Vaccination in the GL261 Glioma Model. *Neurotherapeutics* 2016;13(1):226-236. doi:10.1007/s13311-015-0407-1.
518. Buonaguro L, Petrizzo A, Tornesello ML, Buonaguro FM. Translating Tumor Antigens into Cancer Vaccines. *Clin. Vaccine Immunol.* 2011;18(1):23-34. doi:10.1128/CVI.00286-10.
519. Sampson JH, Mitchell DA. Vaccination strategies for neuro-oncology. *Neuro. Oncol.* 2015;17 Suppl 7(suppl 7):vii15-vii25. doi:10.1093/neuonc/nov159.
520. Zeng J, See AP, Phallen J, et al. Anti-PD-1 Blockade and Stereotactic Radiation Produce Long-Term Survival in Mice With Intracranial Gliomas. *Int. J. Radiat. Oncol.* 2013;86(2):343-349. doi:10.1016/j.ijrobp.2012.12.025.
521. Hardcastle J, Mills L, Malo CS, et al. Immunovirotherapy with measles virus strains in combination with anti–PD-1 antibody blockade enhances antitumor activity in glioblastoma treatment. *Neuro. Oncol.* 2016:now179. doi:10.1093/neuonc/now179.
522. Wainwright DA, Chang AL, Dey M, et al. Durable Therapeutic Efficacy Utilizing Combinatorial Blockade against IDO, CTLA-4, and PD-L1 in Mice with Brain Tumors. *Clin. Cancer Res.* 2014;20(20):5290-5301. doi:10.1158/1078-0432.CCR-14-0514.
523. Verheije MH, Lamfers MLM, Wurdinger T, et al. Coronavirus Genetically Redirected to the Epidermal Growth Factor Receptor Exhibits Effective Antitumor Activity against a Malignant Glioblastoma. *J. Virol.* 2009;83(15):7507-7516. doi:10.1128/JVI.00495-09.
524. Todo T. Oncolytic virus therapy using genetically engineered herpes simplex viruses. *Front. Biosci.* 2008;13:2060-4.

525. Andreansky S, Soroceanu L, Flotte ER, et al. Evaluation of genetically engineered herpes simplex viruses as oncolytic agents for human malignant brain tumors. *Cancer Res.* 1997;57(8):1502-9.
526. Shah AH, Bregy A, Heros DO, Komotar RJ, Goldberg J. Dendritic cell vaccine for recurrent high-grade gliomas in pediatric and adult subjects: clinical trial protocol. *Neurosurgery* 2013;73(5):863-7. doi:10.1227/NEU.0000000000000107.
527. Bregy A, Wong TM, Shah AH, Goldberg JM, Komotar RJ. Active immunotherapy using dendritic cells in the treatment of glioblastoma multiforme. *Cancer Treat. Rev.* 2013;39(8):891-907. doi:10.1016/j.ctrv.2013.05.007.
528. Miao H, Choi BD, Suryadevara CM, et al. EGFRvIII-Specific Chimeric Antigen Receptor T Cells Migrate to and Kill Tumor Deposits Infiltrating the Brain Parenchyma in an Invasive Xenograft Model of Glioblastoma. Castro MG, ed. *PLoS One* 2014;9(4):e94281. doi:10.1371/journal.pone.0094281.
529. Gras Navarro A, Kmiecik J, Leiss L, et al. NK Cells with KIR2DS2 Immunogenotype Have a Functional Activation Advantage To Efficiently Kill Glioblastoma and Prolong Animal Survival. *J. Immunol.* 2014;193(12):6192-6206. doi:10.4049/jimmunol.1400859.
530. Polyzoidis S, Ashkan K. DCVax®-L—Developed by Northwest Biotherapeutics. *Hum. Vaccin. Immunother.* 2014;10(11):3139-3145. doi:10.4161/hv.29276.
531. Jarry U, Chauvin C, Joalland N, et al. Stereotaxic administrations of allogeneic human Vγ9Vδ2 T cells efficiently control the development of human glioblastoma brain tumors. *Oncoimmunology* 2016;5(6):e1168554. doi:10.1080/2162402X.2016.1168554.
532. Immuno therapy. Available at: www.cancerresearch.org. Accessed December 1, 2016.
533. McMahon EJ, Bailey SL, Miller SD. CNS dendritic cells: Critical participants in CNS inflammation? *Neurochem. Int.* 2006;49(2):195-203. doi:10.1016/j.neuint.2006.04.004.
534. Huang L, Xu X, Hao Y. The possible mechanisms of tumor progression via CSF-1/CSF-1R pathway activation. *Rom J Morphol Embryol* 2014;55(2):501-506.
535. Debinski W, Tatter SB. Convection-enhanced delivery for the treatment of brain tumors. *Expert Rev. Neurother.* 2009;9(10):1519-1527. doi:10.1586/ern.09.99.
536. Avan A, Caretti V, Funel N, et al. Crizotinib inhibits metabolic inactivation of gemcitabine in c-Met-driven pancreatic carcinoma. *Cancer Res.* 2013;73(22):6745-6756. doi:10.1158/0008-5472.CAN-13-0837.

ADDENDA |

CURRICULUM VITAE

CURRICULUM VITAE

Tonny Lagerweij is geboren op 10 december 1971 te Lunteren, gemeente Ede. Zijn jeugd heeft hij doorgebracht in het bosrijke Bennekom, waar hij zijn lagere school heeft gevolgd op de Nassauschool. In 1989 behaalde hij zijn H.A.V.O.-diploma aan het Christelijk Streeklyceum Ede. In datzelfde jaar begon hij zijn studie H.L.O. Biotechnologie aan de Hogeschool Gelderland in Arnhem en Nijmegen.

Met behulp van een verkregen Erasmus beurs, heeft hij zijn stage/afstudeeropdracht kunnen verrichten in het buitenland bij Zeneca Bioproducts in Billingham, Engeland, onder begeleiding van dr. Ian Hodgson. Aansluitend aan het verkrijgen van zijn H.L.O. diploma (1993) is hij Biomedische Gezondheidswetenschappen -met als specialisatie toxicologie- gaan studeren aan de Katholieke Universiteit Nijmegen. In het kader van zijn doctoraalexamen heeft hij zijn afstudeeropdracht gedaan bij de afdeling Longziekten van het St. Radboud Ziekenhuis Nijmegen onder supervisie van dr. Pascal Wielders. Tijdens deze studie heeft hij zijn aantekening proefdierdeskundige (ex. Art. 9 van de Wet op Dierproeven) behaald. Zijn doctoraal heeft hij in 1996 afgerond.

Van 1997 tot 2000 was hij werkzaam als Research Scientist en Quality Assurance Deputy bij de startup van het bedrijf Future Diagnostics in Wijchen. Dit bedrijf stond onder leiding van Frans Rosmalen en Mike Martens. Bij Future Diagnostics heeft hij zijn aantekening Internal Quality Auditor bij Llods Register in 1997 gehaald en vervolgens het ISO9001-kwaliteitssysteem bij dit bedrijf mede vormgegeven.

In 2000 verhuisde hij naar de Randstad en vervolgde zijn carrière in Leiden bij TNO Kwaliteit van Leven, afdeling Immunologische en Infectieziekten, onder leiding van Lex Nagelkerken. Tijdens zijn werkzaamheden bij TNO, heeft hij zijn certificaat International Project Management (IPMA-D) in 2008 behaald. Hij heeft met name gewerkt aan onderzoek naar auto-immuunziektes zoals multiple sclerosis en psoriasis en verschillende diermodellen opgezet voor chronische darmontstekingen.

Na 10 jaar met veel plezier bij TNO gewerkt te hebben, veranderde hij in 2010 van werkplek en ging werken bij de Neuro-oncologische Research Group van het VUmc te Amsterdam. Na eerst vier jaar als research technician gewerkt te hebben aan preklinisch onderzoek naar de vorming en behandeling van hersentumoren, is hij in 2014 gestart als promovendus en heeft hij in het lab van prof.dr. Tom Wurdinger het in dit proefschrift beschreven onderzoek verricht.

ADDENDA |

DANKWOORD | ACKNOWLEDGEMENTS

Het is gedaan! Het werk van bijna vier jaar onderzoek is gebundeld in een boekje en nu kan ik het gedeelte gaan schrijven dat wel door iedereen gelezen wordt. Want dit proefschrift was niet tot stand gekomen zonder de hulp en steun van een groot aantal mensen. Enkelen wil ik hier bij naam noemen.

Allereerst wil ik natuurlijk mijn begeleider en promotor, prof. dr. Wurdinger bedanken. Tom, jouw optimisme, enthousiasme en enorme gedrevenheid werken bijzonder stimulerend. Besprekingen met jou leveren altijd vele nieuwe ideeën op, waarvan sommigen zelfs uitvoerbaar blijken. Deze positieve insteek heeft er dan ook mede aan bijgedragen dat ik alsnog de stap heb gezet om een promotietraject te starten.

Ook mijn copromotor, dr, Esther Hulleman, wil ik graag bedanken voor alle hulp de afgelopen jaren. Esther, al voor mijn promotietraject begon onze samenwerking met de DIPG projecten. Maar gelukkig hebben we ook tijdens mijn AIO-schap nog samen kunnen werken en hopelijk blijft dat ook nog zo na mijn promotie.

.

Dr. Noske en prof.dr. Vandertop: Bedankt voor jullie kritische noten bij de manuscripten en voor alle hulp bij de organisatorische aspecten die zijn komen kijken bij de afronding van dit proefschrift.

Ook wil ik de leden van de leescommissie, prof.dr. Van Dongen, prof.dr. Van Noorden, prof.dr. Van Beusechem, dr. Wolf en dr. Walenkamp, bedanken voor het aandachtig lezen van alle hoofdstukken. Ik kijk uit naar de dag van de promotie, waarop ik met u van gedachten kan wisselen over de inhoud van dit proefschrift.

Nadat ik mijn werkzame leven begonnen ben bij Future Diagnostics, en vervolgens bij TNO, ben ik in 2010, via een sollicitatiegesprek met Jacqueline Cloos, als analist begonnen bij de Neuro-oncologische researchgroep (NRG). Viola Caretti tried to convince me that I should become a doctor, but only after she had left I realized that she was correct. Viola, thanks a lot for the nice cooperation during your PhD; and for the fact that you always believed in my capacities. And it was an honor to be, together with Marc, your paranymph during your promotion.

Tijdens mijn periode bij de NRG was het een komen-en-gaan van AIOs en analisten. Ik denk hierbij vooral aan Michiel, Jolien, Ravi, Magda, Dennis, Pepijn, Marcel, Sjoerd, Lotte, Dannis, Sharyar, Susanna. Voor de meeste van jullie was de NRG een leuke begin, maar hopelijk heeft jullie carrière hierna een echte start gemaakt.

Maar ook verschillende postdocs zijn er gepasseerd tijdens mijn verblijf bij de NRG: Petra, bedankt dat je vanuit je huidige functie bij de HLO Leiden nog regelmatig nieuwe studenten bij ons aanbeveelt. Jordi, and Xi Wen: Such a pity that you have left. We still have to get at least one manuscript published, but I hope that even after that we will find a way to continue our work together.

Nik, Myron, Ravi en Lot; Al zijn jullie al vertrokken uit de AIO-kamer, gelukkig komen jullie zo af-en-toe nog wel eens langs. Meestal voor borrels, of als er gebak te halen is, maar het is in ieder geval altijd gezellig als jullie er zijn.

Veel van mijn studies zijn voor een groot deel uitgevoerd in locaties buiten het Cancer Center Amsterdam. Heel veel tijd heb ik doorgebracht in het RNC. Marijke, Mariska en Ricardo waren altijd zeer betrokken bij het welzijn van de dieren. Carla, heeft de organisatie van de dierfaciliteit altijd strak in handen gehouden. Tjaard, Gertrude, en de technische dienst, met name Fred waren altijd in de buurt als er een probleem opgelost moest worden.

Maar ook heb ik vrij veel tijd doorgebracht bij de microscopen op het MCBI. Esther, Nanne, Jasper, Elga, Jeroen en René hebben me daarbij geholpen met het regelen van toegang tot de apparatuur, het instellen van de apparatuur, en met z'n allen hebben we heel veel tijd gestoken in het verkrijgen van schitterende microscopische opnames en de analyses achteraf.

Behalve aan de mensen binnen de VU, ben ik ook veel dank verschuldigd aan een groot aantal mensen buiten de VU met wie ik heb mogen samenwerken zoals Olaf van Tellingen en Mark de Gooijer van het NKI, jullie input was altijd geweldig, zowel qua discussies als met alle hulp wanneer ik weer eens iets nodig had; William Leenders, Kiek Verrijp en Anneke Navis van het Radboud UMC, Timo ten Hagen van het Erasmus MC. And of course I would also would like to thank Bakhos Tannous, for his help on many of our projects.

Alhoewel mijn proefschrift toegespitst is op hersentumoren, heb ik ook mogen bijdragen aan andere research projecten. Eén van de eerst samenwerkingen was in een project gericht tegen pancreas tumoren. Elisa, Amir, Rocco, Tessa, it was great to work with you. I was always amazed how quickly you were able to organize the projects and finish a paper. Another nice collaboration was (and still is) the work on osteosarcoma and extracellular vesicles together with Rubina, Maria and Michiel. Furthermore, I had the pleasure to join a project on gingiva together with Adriano, Mo, and Ron. From this project I learned especially how nice it is to present your work for an international audience. En ook ben ik blij dat ik heb mogen meewerken aan een prostaatkanker project waarbij onder anderen Irene, Jasmina en Ab betrokken waren.

En nu ga ik dan ook nog toekomen aan mijn huidige, zeer gewaardeerde collega's. Ten eerste natuurlijk Laurine, je organisatie skills zijn onovertroffen, maar ik denk dat vooral het feit dat je altijd voor iedereen klaar staat zorgt dat de NRG zo'n hechte club blijft. Piotr, fantastisch zoals jij ook altijd alles weet te plannen en klaar staat om alle collega's van advies en hulp te voorzien. Ed, Heleen, Francios, Aniska, heel erg bedankt voor jullie hulp in het lab en de vele verhalen tijdens de lunch. Ida, Jasmina, Wen, Terki, Maxime. Jullie waren geweldige buren op de derde verdieping.

Bart en Dani, bedankt voor al jullie support bij het opstellen van mijn eerste subsidieaanvragen. Nog niet succesvol, maar dat lag zeker niet aan jullie. Pieter¸ dank voor al je kritische noten bij de histologische beoordeling van de verschillende preparaten. Ik heb hier veel van geleerd.

Mijn huidige kamergenoten: Chantal, Sjors, Mo, Rianne, Dennis, Adrienne, en Hans. Wetenschappelijke discussie met jullie starten vaak op een hoog niveau, en zakken dan snel af tot een gesprek waarin ik ook kan meepraten. Door jullie was er een fantastische sfeer in de kamer, en tijdens de vele borrels buiten het CCA.

Ook wil ik alle studenten die bij onze afdeling stage liepen, waaronder Thijs, Bart, Sophie, Jurrien, Lieke, Jhon, Yanyan, en Naomi, bedanken voor alle gezelligheid. En ik ben stiekem toch wel blij dat de meeste van jullie, ondanks mijn advies om het niet te doen, toch hebben gekozen voor een carrière binnen de wetenschap.

Natuurlijk wil ik Hilde en Naomi bedanken dat ze mijn paranimfen willen zijn.

Paps en mams, dat hadden jullie toch ook nooit kunnen bedenken dat jullie zoon nog eens doctor zou worden. Bedankt voor al jullie liefde en steun.

Nicolette: Door jouw onvoorwaardelijke liefde was ik in staat om dit af te ronden. Het schrijven van dit proefschrift kostte toch wat meer uren dan dat er in een werkdag zaten. Al die avonden dat ik achter de computer heb gezeten, had ik liever samen met jou doorgebracht. Thijs en Daan, ik hou van jullie.

En dan nog iedereen die niet genoemd is, co-auteurs, medewerkers van andere afdelingen waar ik wel eens wat van geleend heb of mee samengewerkt heb, buren, vrienden en familie: Bedankt!

ADDENDA |

LIST OF PUBLICATIONS

Tonny Lagerweij[#] , Maria Pérez-Lanzón[#], S. Rubina Baglio. A preclinical mouse model of osteosarcoma to define the extracellular vesicle-mediated communication between tumor and mesenchymal stem cells. JoVE (*accepted)*

Adriano Azaripour, Tonny Lagerweij, Christina Scharfbillig, Anna Elisabeth Jadczak, Ard Jonker, Britt van der Swan,Manon Molenaar, Rens van der Waal, Karoline Kielbassa, Wikky Tigchelaar,Daisy L. Picavet, Esther M.L. Hendrikx, Vashendriya Hira, Mohammed Khurshed, Cornelis J.F. Van Noorden. Three-dimensional histochemistry and imaging of human gingiva (*under revision*)

Raimond Heukers, Tian Shu Fan, Raymond H. de Wit, Jeffrey R. van Senten, Timo W.M. De Groof, Maarten P. Bebelman, Tonny Lagerweij, Joao Vieira, Sabrina M. de Munnik, Laura Smits-de Vries, Jody van Offenbeek, Afsar Rahbar, Diane van Hoorick, Cecilia Söderberg-Naucler, Thomas Würdinger, Rob Leurs, Marco Siderius, Henry F. Vischer, Martine J. Smit. The constitutive activity of the virally-encoded chemokine receptor US28 accelerates glioblastoma growth (*under revision)*

Jordi Berenguer, Tonny Lagerweij, Xi Wen Zhao, Sophie Dusoswa, Petra van der Stoop, Bart Westerman, Danijela Koppers-Lalic, Mark C. de Gooijer, Marloes Zoetemelk, Anoek Zomer, Matheus H. W. Crommentuijn, Laurine E. Wedekind, Àlan López-López, Alberta Giovanazzi, Marina Bruch-Oms, Ida H. van der Meulen-Muileman, Rogier M. Reijmers, Toin H. van Kuppevelt, Juan-Jesús García-Vallejo, Yvette van Kooyk, Bakhos A. Tannous, Pieter Wesseling, W. Peter Vandertop, David P. Noske, Victor W. van Beusechem, Jacco van Rheenen, D. Michiel Pegtel, Olaf van Tellingen, Thomas Wurdinger. Glioblastoma-derived extracellular vesicles induce proliferation and temozolomide resistance via chemokine receptor CCR8 (*under revision*)

Narayan RS, Gasol A, Slangen PLG, Cornelissen FMG, Lagerweij T, Veldman HYYE, Dik R, van den Berg J, Slotman BJ, Wurdinger T, Haas-Kogan D, Stalpers LJA, Baumert BG, Westerman B, Theys J, Sminia P. Identification of MEK162 as a radiosensitizer for the treatment of glioblastoma. Mol Cancer Ther. 2017 Sep 27. pii: molcanther.0480.2017. doi: 10.1158/1535-7163.MCT-17-0480.

Nurten Saydam, Thomas Ströbel, Sibylle Madlener, Serkan Tuna, Sarah C Vose, T. Lagerweij, Thomas Würdinger, Klemens Vierlinger, Adelheid Wöhrer, Brendan D Price, Bruce Demple, Okay Saydam. Ape1/Ref-1 guides cellular decisions on DNA repair pathway choice. Sci Rep. 2017 Aug 29;7(1):9674. doi: 10.1038/s41598-017-10013-w.

Tonny Lagerweij[#], Sophie A. Dusoswa[#], Adrian Negrean, Esther M.L. Hendrikx, Helga E. de Vries, Jeroen Kole, Juan J. Garcia-Vallejo, Huibert D. Mansvelder, W. Peter Vandertop, David P. Noske, Bakhos A. Tannous, René J.P. Musters, Yvette van Kooyk, Pieter Wesseling, Xi Wen Zhao, Thomas Wurdinger. Optical clearing and fluorescence deep-tissue imaging for 3D quantitative analysis of the brain tumor microenvironment.
Angiogenesis. 2017 Jul 11. doi: 10.1007/s10456-017-9565-6

A. Charlotte P. Sewing, **Tonny Lagerweij**, Dannis G. van Vuurden, Michaël H. Meel, Susanna J. E. Veringa, Angel M. Carcaboso, Pieter J. Gaillard, W. Pieter Vandertop, Pieter Wesseling, David Noske, Gertjan J. L. Kaspers, MD, and Esther Hulleman. Preclinical evaluation of convection-enhanced delivery with liposomal doxorubicin to treat pediatric diffuse intrinsic pontine glioma and thalamic high-grade glioma. J. Neurosurgery Pediatrics. 2017 May;19(5):518-530. doi: 10.3171/2016.9.PEDS16152.

S. Rubina Baglio, **Tonny Lagerweij**, Maria Perez Lanzon, Xuan Dung Ho, Nicolas Leveille, Sonia A. Melo,Anne-Marie Cleton-Jansen, Ekaterina S. Jordanova, Laura Roncuzzi, Michelina Greco, Monique A. J. vanEijndhoven, Giulia Grisendi, Massimo Dominici, Roberta Bonafede, Sinead M. Lougheed, Tanja D. de Gruijl, Nicoletta Zini, Silvia Cervo, Agostino Steffan, Vincenzo Canzonieri, Aare Martson, Katre Maasalu, Sulev Koks, Tom Wurdinger, Nicola Baldini, D. Michiel Pegtel. Blocking tumor-educated MSC paracrine activity halts osteosarcoma Progression. Clin Cancer Res. 2017 Jul 15;23(14):3721-3733. doi: 10.1158/1078-0432.CCR-16-2726.

Jansen MH[#], **Lagerweij T[#]**, Sewing AC, Vugts DJ, van Vuurden DG, Molthoff CF, Caretti V, Veringa SJ, Petersen N, Montero-Carcaboso A, Noske DP, Vandertop WP, Wesseling P, van Dongen GA, Kaspers GJ, Hulleman E. Bevacizumab targeting diffuse intrinsic pontine glioma: results of 89Zr-bevacizumab PET imaging in brain tumor models. Mol Cancer Ther. 2016 Sep;15(9):2166-74. doi: 10.1158/1535-7163.MCT-15-0558.

Azaripour A, **Lagerweij T**, Scharfbillig C, Jadczak AE, Willershausen B, Van Noorden CJ. A survey of clearing techniques for 3D imaging of tissues with special reference to connective tissue. Prog Histochem Cytochem. 2016 Aug;51(2):9-23. doi: 10.1016/j.proghi.2016.04.001

Lagerweij T[#], Hiddingh L[#], Biesmans D, Crommentuijn MH, Cloos J, Li XN, Kogiso M, Tannous BA, Vandertop WP, Noske DP, Kaspers GJ, Würdinger T, Hulleman E. A chemical screen for medulloblastoma identifies quercetin as a putative radiosensitizer. Oncotarget. 2016 Jun 14;7(24):35776-35788. doi: 10.18632/oncotarget.7980.

Bijnsdorp IV, Hodzic J, **Lagerweij T**, Westerman B, Krijgsman O, Broeke J, Verweij F, Nilsson RJ, Rozendaal L, van Beusechem VW, van Moorselaar JA, Wurdinger T, Geldof AA. miR-129-3p controls centrosome number in metastatic prostate cancer cells by repressing CP110. Oncotarget. 2016 Mar 29;7(13):16676-87. doi: 10.18632/oncotarget.7572.

Sewing AC[#], Caretti V[#], **Lagerweij T[#]**, Schellen P, Jansen MH, van Vuurden DG, Idema S, Molthoff CF, Vandertop WP, Kaspers GJ, Noske DP, Hulleman E. Convection enhanced delivery of carmustine to the murine brainstem: a feasibility study. J Neurosci Methods. 2014 Dec 30;238:88-94. doi: 10.1016/j.jneumeth.2014.09.020.

Caretti V, Sewing AC, **Lagerweij T**, Schellen P, Bugiani M, Jansen MH, van Vuurden DG, Navis AC, Horsman I, Vandertop WP, Noske DP, Wesseling P, Kaspers GJ, Nazarian J, Vogel H, Hulleman E, Monje M, Wurdinger T. Human pontine glioma cells can induce murine tumors. Acta Neuropathol. 2014 ;127(6):897-909. doi: 10.1007/s00401-014-1272-4.

Giovannetti E, Wang Q, Avan A, Funel N, **Lagerweij T**, Lee JH, Caretti V, van der Velde A, Boggi U, Wang Y, Vasile E, Peters GJ, Wurdinger T, Giaccone G. Role of CYB5A in pancreatic cancer prognosis and autophagy modulation. J Natl Cancer Inst. 2014 Jan;106(1):djt346. doi: 10.1093/jnci/djt346.

Avan A, Caretti V, Funel N, Galvani E, Maftouh M, Honeywell RJ, **Lagerweij T**, Van Tellingen O, Campani D, Fuchs D, Verheul HM, Schuurhuis GJ, Boggi U, Peters GJ, Würdinger T, Giovannetti E. Crizotinib inhibits metabolic inactivation of gemcitabine in c-Met-driven pancreatic carcinoma. Cancer Res. 2013 Nov 15;73(22):6745-56. doi: 10.1158/0008-5472.CAN-13-0837.

Tannous BA, Kerami M, Van der Stoop PM, Kwiatkowski N, Wang J, Zhou W, Kessler AF, Lewandrowski G, Hiddingh L, Sol N, **Lagerweij T**, Wedekind L, Niers JM, Barazas M, Nilsson RJ, Geerts D, De Witt Hamer PC, Hagemann C, Vandertop WP, Van Tellingen O, Noske DP, Gray NS, Würdinger T. Effects of the selective MPS1 inhibitor MPS1-IN-3 on glioblastoma sensitivity to antimitotic drugs. J Natl Cancer Inst. 2013 Sep 4;105(17):1322-31. doi: 10.1093/jnci/djt168. Epub 2013 Aug 12.

Caretti V, Hiddingh L, **Lagerweij T**, Schellen P, Koken PW, Hulleman E, van Vuurden DG, Vandertop WP, Kaspers GJ, Noske DP, Wurdinger T. WEE1 kinase inhibition enhances the radiation response of diffuse intrinsic pontine gliomas. Mol Cancer Ther. 2013 Feb;12(2):141-50. doi: 10.1158/1535-7163.MCT-12-0735.

Kremer B, Mariman R, van Erk M, **Lagerweij T**, Nagelkerken L. Temporal colonic gene expression profiling in the recurrent colitis model identifies early and chronic inflammatory processes. PLoS One. 2012 7(11):e50388. doi: 10.1371/journal.pone.0050388.

Caretti V, Jansen MH, van Vuurden DG, **Lagerweij T**, Bugiani M, Horsman I, Wessels H, van der Valk P, Cloos J, Noske DP, Vandertop WP, Wesseling P, Wurdinger T, Hulleman E, Kaspers GJ. Implementation of a multi-institutional diffuse intrinsic pontine glioma autopsy protocol and characterization of a primary cell culture. Neuropathol Appl Neurobiol. 2013 Jun;39(4):426-36. doi: 10.1111/j.1365-2990.2012.01294.x.

Mariman R, Kremer B, van Erk M, **Lagerweij T**, Koning F, Nagelkerken L. Gene expression profiling identifies mechanisms of protection to recurrent trinitrobenzene sulfonic acid colitis mediated by probiotics. Inflamm Bowel Dis. 2012 Aug;18(8):1424-33. doi: 10.1002/ibd.22849.

Nagelkerken L, Verzaal P, **Lagerweij T**, Persoon-Deen C, Berbee JF, Prens EP, Havekes LM, Oranje AP. Development of atopic dermatitis in mice transgenic for human apolipoprotein C1. J Invest Dermatol. 2008 May;128(5):1165-72.

Eefting D, Schepers A, De Vries MR, Pires NM, Grimbergen JM, **Lagerweij T**, Nagelkerken LM, Monraats PS, Jukema JW, van Bockel JH, Quax PH. The effect of interleukin-10 knock-out and overexpression on neointima formation in hypercholesterolemic APOE*3-Leiden mice. Atherosclerosis. 2007 Aug;193(2):335-42

[#] Shared first author-ship

ADDENDA |

LIST OF DISSERTATIONS HERSENTUMORCENTRUM AMSTERDAM

10 Jun 2005	Carla Verstappen	Cancer therapy related neurotoxicity
28 Sep 2005	Maaike Vos	Evaluation of reponse, toxicity and outcome in glioma therapy
20 Dec 2005	Birgit Georger	Conditionally replicative adenoviruses for the treatment of malignant glioma and neuroblastoma
20 Dec 2005	Jacques Grill	Gene therapy and virotherapy of brain tumors with recombinant adenoviruses
19 Jun 2009	Fonnet Bleeker	Mutational profiling of glioblastoma
24 Nov 2009	Philip de Witt Hamer	Glioblastoma: between bed and bench
7 May 2010	Ingeborg Bosma	Cognitive dysfunction in glioma; underlying mechanisms and consequences
23 Sep 2010	Christian Badr	Bioluminescence imaging in glioblastom: monitoring of biological processes and novel therapeutics
8 Nov 2010	Linda Douw	Neural networks in brain tumors; the interplay between tumor, cognition, and epilepsy
10 Jun 2011	Sander Idema	Improving oncolytic viral therapy for glioma
5 Oct 2011	Anneke Niers	Novel biosensors for preclinical brain tumor analysis
3 Jul 2012	Viola Caretti	Pioneering preclinical research in diffuse intrinsic pontine glioma: towards new treatment strategies
29 Oct 2012	Leonora Balaj	Exosomes: the biological messengers
8 Feb 2013	Marjolein de Groot	Epilepsy in brain tumor patients; towards improved and personalized treatment
4 Jun 2013	Edwin van Dellen	Lesions in the connected brain; a network perspective on brain tumors and lesional epilepsy
4 Dec 2013	Michiel Smits	Micro-RNA and epigenetic signaling in glioma angiogenesis
11 Dec 2013	Eefje Sizoo	The end-of-life phase of high-grade glioma patients; towards a dignified death
17 Jun 2014	Dannis van Vuurden	Innovative treatment targets in pediatric high-grade brain tumors
7 Jan 2015	Lotte Hidding	Treatment sensitizers for high-grade tumors
17 Mar 2015	Marc Jansen	Diffuse Intrinsic Pontine Glioma: clinical aspects and imaging
11 May 2015	Florien Boele	Towards improving health-related quality of life in glioma patients and their informal caregivers
30 Sep 2015	Johan Koekkoek	Epilepsy in glioma patients; optimizing treatment until the end of life
19 Jan 2016	Sjoerd van Rijn	Functional molecular imaging of cancer development and stem cell regeneration in the nervous system
24 Mar 2016	Hinke van Thuijl	Molecular characterization of low-grade glial neoplasms
18 May 2016	Avanita Prabowo	Molecular Features of long-term epilepsy-associated tumours; focus on glioneural tumours
8 Jun 2016	Ronald Willemse	Functional mapping of the sensorimotor cortex: clinical studies with MEG and fMRI
21 Jun 2016	Sharyar Mir	Novel treatment targets in high-grade brain tumors
1 Jul 2016	Femke Froklage	The role of the blood-brain barrier in drug-resistance and central neurotoxicity
3 Nov 2017	Thijs Crommentuijn	Development of vector-based strategies against glioblastoma
28 Nov 2017	Sophie Veldhuijzen van Zanten	Diffuse Intrinsic Pontine Glioma: a multi-facetted view and global view
28 Nov 2017	Lot Sewing	Diffuse Intrinsic Pontine Glioma: disease models and translational research
23 Jan 2018	Tonny Lagerweij	Brain tumors: Preclinical imaging and novel therapies